Alaska Department of Transportation & Public Facilities

Research & Technology Transfer

ALASKA DEPARTMENT OF TRANSPORTATION

Seismic Behavior of Concrete Bridge Columns at Sub-Freezing Temperatures

Prepared by:

Constructed Facilities Laboratory
2414 Campus Shore Drive
North Carolina State University
Raleigh, NC 27695-7533

March 2008

Prepared for:
Alaska Department of Transportation
Statewide Research Office
3132 Channel Drive
Juneau, AK 99801-7898

FHWA-AK-RD-08-01

Notice

This document is disseminated under the sponsorship of the U.S. Department of Transportation in the interest of information exchange. The U.S. Government assumes no liability for the use of the information contained in this document.

The U.S. Government does not endorse products or manufacturers. Trademarks or manufacturers' names appear in this report only because they are considered essential to the objective of the document.

Quality Assurance Statement

The Federal Highway Administration (FHWA) provides high-quality information to serve Government, industry, and the public in a manner that promotes public understanding. Standards and policies are used to ensure and maximize the quality, objectivity, utility, and integrity of its information. FHWA periodically reviews quality issues and adjusts its programs and processes to ensure continuous quality improvement.

Author's Disclaimer

Opinions and conclusions expressed or implied in the report are those of the author. They are not necessarily those of the Alaska DOT&PF or funding agencies.

REPORT DOCUMENTATION PAGE

Form approved OMB No.

1. AGENCY USE ONLY (LEAVE BLANK)	2. REPORT DATE	3. REPORT TYPE AND DATES COVERED
FHWA-AK-RD-08-01	March 2008	Final

4. TITLE AND SUBTITLE

Seismic Behavior of Reinforced Concrete Bridge Columns at Sub-Freezing Temperatures

5. FUNDING NUMBERS

HPR-4000(48)/61378

6. AUTHOR(S)

Luis A. Montejo, Dr. Mervyn J. Kowalsky, Dr. Tasnim Hassan

7. PERFORMING ORGANIZATION NAME(S) AND ADDRESS(ES)

Constructed Facilities Laboratory
2414 Campus Shore Drive
North Carolina State University
Raleigh, NC 27695-7533

8. PERFORMING ORGANIZATION REPORT NUMBER

Technical Report No. RD-08-01

9. SPONSORING/MONITORING AGENCY NAME(S) AND ADDRESS(ES)

State of Alaska, Alaska Dept. of Transportation and Public Facilities
Research and Technology Transfer
2301 Peger Rd
Fairbanks, AK 99709-5399

10. SPONSORING/MONITORING AGENCY REPORT NUMBER

FHWA-AK-RD-08-01

11. SUPPLENMENTARY NOTES

Performed in cooperation with the U.S. Department of Transportation, Federal Highway Administration.
Research Project Title: “Influence of Low Temperatures on the Ductility of Bridge Structures in High Seismic Regions”

12a. DISTRIBUTION / AVAILABILITY STATEMENT

No restrictions.
This document is available to the public through the National Technical Information Service, Springfield, VA 22161

12b. DISTRIBUTION CODE

13. ABSTRACT (Maximum 200 words)

The final goal of this research was to develop recommendations for the future seismic design or assessment of reinforced concrete (RC) bridge bent structures in cold seismic regions. Ten large scale circular columns were constructed and tested under cyclic reversal of loads inside an environmental chamber in the North Carolina State University Constructed Facilities Laboratory (CFL). The columns were tested at freezing (-40°C, -40°F) and ambient (23°C, 74°F) temperatures. In order to characterize every aspect of the seismic response at low temperatures, the columns' design was governed by a desire behavior: shear dominated, flexural dominated and reinforced concrete filled steel tube columns (RCFST).

Results obtained show that RC member exposed to the combined effect of sub-freezing temperatures and cyclic loads undergo a gradual increase in strength and stiffness coupled with a reduction in displacement capacity. The experimental results were used to calibrate a fiber-based model and a series of static and inelastic analyses were performed to typical Alaska DOT bent configurations. Based on the results obtained from the experimental tests, the non-linear simulations and a moment-curvature parametric analyses, a simple methodology was developed to account for the low temperature flexural overstrength and reduction in ductility capacity.

14. KEYWORDS : Testing, Investigation of Structures, Structural Analysis, Structural Models, Structural Design, Earthquake Resistant Design, Bridge Foundations

15. NUMBER OF PAGES
388

16. PRICE CODE
N/A

17. SECURITY CLASSIFICATION OF REPORT	18. SECURITY CLASSIFICATION OF THIS PAGE	19. SECURITY CLASSIFICATION OF ABSTRACT	20. LIMITATION OF ABSTRACT
Unclassified	Unclassified	Unclassified	N/A

SI* (MODERN METRIC) CONVERSION FACTORS

APPROXIMATE CONVERSIONS TO SI UNITS

Symbol	When You Know	Multiply By	To Find	Symbol
		LENGTH		
in	inches	25.4	millimeters	mm
ft	feet	0.305	meters	m
yd	yards	0.914	meters	m
mi	miles	1.61	kilometers	km
		AREA		
in^2	square inches	645.2	square millimeters	mm^2
ft^2	square feet	0.093	square meters	m^2
yd^2	square yard	0.836	square meters	m^2
ac	acres	0.405	hectares	ha
mi^2	square miles	2.59	square kilometers	km^2
		VOLUME		
fl oz	fluid ounces	29.57	milliliters	mL
gal	gallons	3.785	liters	L
ft^3	cubic feet	0.028	cubic meters	m^3
yd^3	cubic yards	0.765	cubic meters	m^3
		NOTE: volumes greater than 1000 L shall be shown in m^3		
		MASS		
oz	ounces	28.35	grams	g
lb	pounds	0.454	kilograms	kg
T	short tons (2000 lb)	0.907	megagrams (or "metric ton")	Mg (or "t")
		TEMPERATURE (exact degrees)		
^oF	Fahrenheit	5 (F-32)/9 or (F-32)/1.8	Celsius	^oC
		ILLUMINATION		
fc	foot-candles	10.76	lux	lx
fl	foot-Lamberts	3.426	$candela/m^2$	cd/m^2
		FORCE and PRESSURE or STRESS		
lbf	poundforce	4.45	newtons	N
lbf/in^2	poundforce per square inch	6.89	kilopascals	kPa

APPROXIMATE CONVERSIONS FROM SI UNITS

Symbol	When You Know	Multiply By	To Find	Symbol
		LENGTH		
mm	millimeters	0.039	inches	in
m	meters	3.28	feet	ft
m	meters	1.09	yards	yd
km	kilometers	0.621	miles	mi
		AREA		
mm^2	square millimeters	0.0016	square inches	in^2
m^2	square meters	10.764	square feet	ft^2
m^2	square meters	1.195	square yards	yd^2
ha	hectares	2.47	acres	ac
km^2	square kilometers	0.386	square miles	mi^2
		VOLUME		
mL	milliliters	0.034	fluid ounces	fl oz
L	liters	0.264	gallons	gal
m^3	cubic meters	35.314	cubic feet	ft^3
m^3	cubic meters	1.307	cubic yards	yd^3
		MASS		
g	grams	0.035	ounces	oz
kg	kilograms	2.202	pounds	lb
Mg (or "t")	megagrams (or "metric ton")	1.103	short tons (2000 lb)	T
		TEMPERATURE (exact degrees)		
^oC	Celsius	1.8C+32	Fahrenheit	^oF
		ILLUMINATION		
lx	lux	0.0929	foot-candles	fc
cd/m^2	$candela/m^2$	0.2919	foot-Lamberts	fl
		FORCE and PRESSURE or STRESS		
N	newtons	0.225	poundforce	lbf
kPa	kilopascals	0.145	poundforce per square inch	lbf/in^2

*SI is the symbol for the International System of Units. Appropriate rounding should be made to comply with Section 4 of ASTM E380.
(Revised March 2003)

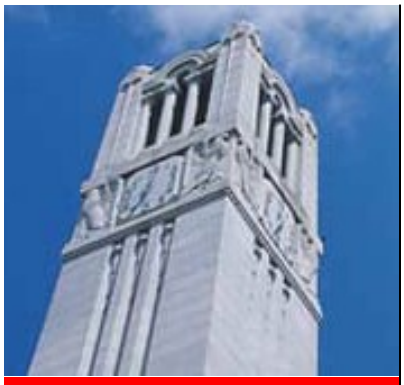

NC STATE UNIVERSITY

Constructed Facilities Laboratory
Department of Civil, Construction, and Environmental Engineering

Technical Report
No. RD-08-01

SEISMIC BEHAVIOR OF REINFORCED CONCRETE BRIDGE COLUMNS AT SUB-FREEZING TEMPERATURES

Prepared by:

Mr. Luis A. Montejo, ***Research Assistant***
Dr. Mervyn J. Kowalsky, ***Principle Investigator***
Dr. Tasnim Hassan, ***Principle Investigator***

Prepared for:

Alaska Department of Transportation
and Public Facilities
Juneau, Alaska

March 2008

Constructed Facilities Laboratory
2414 Campus Shore Drive
North Carolina State University
Raleigh, NC 27695-7533
Tel: (919) 513-1733
Fax: (919) 513-1765
Email: cfl@ncsu.edu
Web Site: www.cfl.ncsu.edu

ABSTRACT

The final goal of this research was to develop recommendations for the future seismic design or assessment of reinforced concrete (RC) bridge bent structures in cold seismic regions. Ten large scale circular columns were constructed and tested under cyclic reversal of loads inside an environmental chamber in the North Carolina State University Constructed Facilities Laboratory (CFL). The columns were tested at freezing (-40˚C, -40˚F) and ambient (23˚C, 74˚F) temperatures. In order to characterize every aspect of the seismic response at low temperatures, the columns' design was governed by a desire behavior: shear dominated, flexural dominated and reinforced concrete filled steel tube columns (RCFST).

Results obtained show that RC member exposed to the combined effect of sub-freezing temperatures and cyclic loads undergo a gradual increase in strength and stiffness coupled with a reduction in displacement capacity. The experimental results were used to calibrate a fiber-based model and a series of static and inelastic analyses were performed to typical Alaska DOT bent configurations. Based on the results obtained from the experimental tests, the non-linear simulations and a moment-curvature parametric analyses, a simple methodology was developed to account for the low temperature flexural overstrength and reduction in ductility capacity.

TABLE OF CONTENT

LIST OF FIGURES

LIST OF TABLES

CHAPTER I

INTRODUCTION

1.1 Problem description and scope of the research

Seismic design of reinforced concrete bridges is generally based on the principles of capacity design, where a strength hierarchy is established in the bridge to ensure that damage is controllable, and occurs only where the designer intends (Priestley et al., 1996). Special importance is then placed on the *ductility* of the structural members selected to develop plastic hinges, which should be specially detailed in order to sustain large inelastic deformations. All other members should be design to remain elastic while resisting the *overstrength* moments coming from adjacent members.

In freezing temperatures, the properties of construction materials and soil foundation are expected to vary and consequently, the response of the structure to a seismic excitation is also expected to change. The research described here aims to asses the influence of low temperatures on the strength and ductility of reinforced concrete structures in seismically active regions such as those found in Alaska. The final goal of this research is to develop recommendations for the future seismic design or assessment of bridge structures in cold seismic regions. In order to accomplish this objective, 10 large scale circular columns were constructed and tested under cyclic reversal of loads inside an environmental chamber in the North Carolina State University Construction Facilities Laboratory (CFL). The columns were tested at freezing (-40˚C, -40˚F) and ambient (23˚C, 74˚F) temperatures. With the information collected from those tests as well as the results obtained from a previous research performed at NCSU (Sloan, 2005), a series of non-linear time history analysis of typical Alaska Department of Transportation (DOT) bridge bent structures were performed in order to evaluate current designs.

Recommendations are provided around two alternative design strategies: the traditional forced-based design and the more recent displacement-based design.

1.2 Influence of low temperature in seismic behavior of reinforced concrete structures

The effects of low temperatures in construction materials have been very evident during world history. Take for example one of the worst maritime disasters in history: the 1912 sinking of the British luxury liner Titanic. After struck an iceberg, the cold water temperatures caused the steel to crack in a brittle manner killing 1513 people. Similar cases where reported in the 1940s when hundreds of ships experienced large cracks because the composition of the steel was such that the transition from ductile to brittle behavior occurred at temperatures that the ships experienced while in service, particularly in the cold waters of the North Atlantic (Sanford, 2003). Despite the historic evidence, a literature review seems to have identified a potential lack of information in the case of reinforced concrete structures exposed to freezing conditions and seismic actions. Most of the literature available comes from the 80's and is related to cryogenic applications of reinforced and prestressed concrete for storage of liquefied natural gas or liquefied petroleum gas and for barge hulls. Limited reversed cyclic tests on reinforced concrete members conducted at low temperatures are found in the literature. Since the majority of the research done have focused on the material level, past research is divided into four components: (1) low temperature effects on hardened concrete, (2) low temperature effects on reinforcing steel, (3) low temperatures effects on reinforced concrete members and (4) low temperature effects on soil-structure interaction.

1.2.1 Low temperature effects on hardened concrete

1.2.1.1 Compressive strength

Past research has indicated that cold temperatures cause a remarkable increase in compressive strength, see for example Kasami et al. (1981), Browne and Bamforth (1981), Berner et al. (1985), Rostàsy and Push (1987), Lee et al. (1988a, 1988b). This

increase will depend mainly in the moisture content and in a minor amount on the characteristics of the mix (i.e. w/c ratio, air content, etc). Saturated concretes will increase their compressive strength at low temperatures in a more dramatic way than partially dry concretes, but even oven dry concretes will see a small increase in strength when temperature drops below the freezing point. It is believed that this increase is due to water expansion when transformed into ice, filling the large capillary pores and closing the micro-cracks by some kind of microprestressing, thus delaying the process of cracking (Elices, 1987). In the same way concretes with a larger water cement ration will increase its strength in a larger proportion that concrete with a low water cement ratio (high strength concretes). In general, from the literature available the pattern for the range 0°C (-32°C) to -50°C (-58°C) (which is the range of interest for this research and for most common civil structures) seems to be an almost linear increase in compressive strength as show in Figure 1.1. The data used to generate this figure was extracted from the information presented by different authors and also from cylinders tested at low temperatures in this project. Data related to water-saturated concrete was extracted from Rostàsy and Wiedemann (1980) and Rostàsy and Sprenger (1984), data related to partially dry concrete was extracted from Nasser and Evans (1973), Sehnal et al. (1983), Filiatrault and Holleran (2001) and Sloan (2005).

Some researches have proposed equations to determine the compressive strength of concrete at low temperatures $\sigma_c(T)$ as a function of the compressive strength at room temperature $\sigma_c(T_R)$. Okada and Iguro (1978) proposed a predictive equation that is independent of the free water content (Equation 1.1). Goto and Miura (1979) proposed equations that are dependent on both, the temperature and the moisture content w (Equation 1.2). Browne and Bamforth (1981) have also proposed design curves that are function of the moisture content (Equation 1.3). Figure 1.2 evaluate these three equations with the data collected for partially dry concrete, the moisture content used to generate the graph was 3% (common of air exposed concrete) and the room temperature compressive strength was 28 MPa (4ksi). It can be noticed from this graph that for the temperature range under investigation the equation proposed by Browne and Bamforth is not only the simplest one but also the closest to the experimental data, followed closely

by the one proposed by Goto and Miura. The equation proposed by Okada and Iguro seriously over predicts the strength in the range of temperatures being evaluated.

$$\sigma_c(T) = \sigma_c(T_R) + 5.3 - 0.84T - 0.0027T^2 \qquad -10^\circ C > T > -100^\circ C \tag{1.1}$$

$$\sigma_c(T) = \sigma_c(T_R) - (2/15 + T/2700)wT \qquad 0^\circ C > T > -120^\circ C \tag{1.2}$$

$$\sigma_c(T) = \sigma_c(T_R) - Tw/12 \qquad 0^\circ C > T > -120^\circ C \tag{1.3}$$

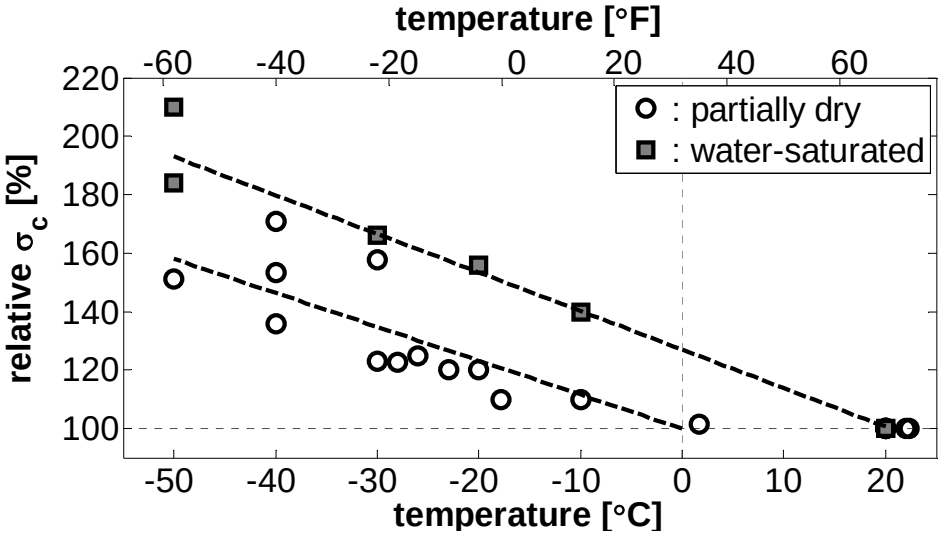

Figure 1.1. Effect of low temperatures in compressive strength of concrete

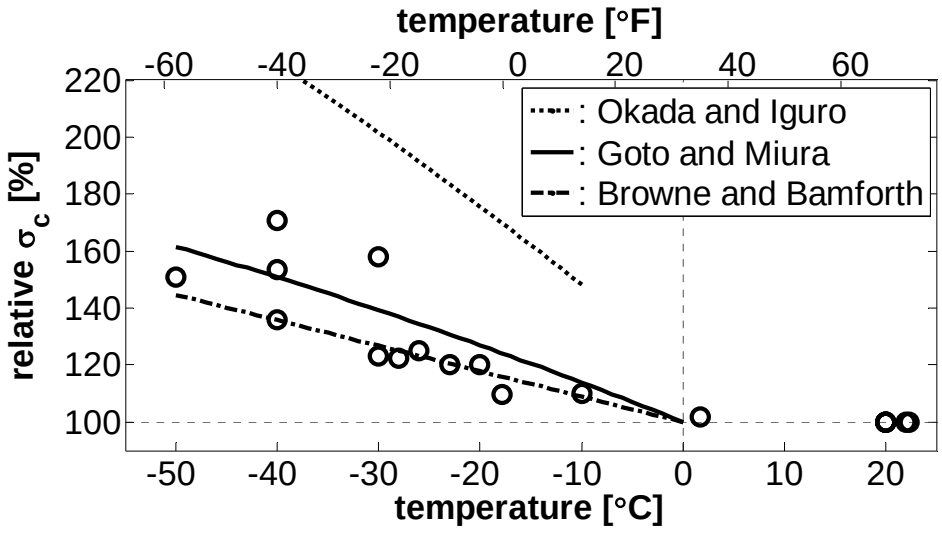

Figure 1.2. Predictive equations for low temperatures concrete compressive strength

1.2.1.2 Modulus of elasticity and Poisson's ratio

Modulus of elasticity and Poisson ratio also increase with low temperatures. Nonetheless, the rate of increase in the modulus of elasticity has been found to be smaller than that for the compressive strength (Figure 1.3). At normal temperatures, the modulus of elasticity of concrete is related to its compressive strength and is approximately proportional to its square root, the effect of low temperatures can be addressed by introducing a new variable k_2, as presented in Equation 1.4.

$$E(T) = k_2(T)k_1\sqrt{\sigma_c(T)} \tag{1.4}$$

where k_1 is the ratio between the square root of the compressive strength and modulus of elasticity at room temperature, and $\sigma_c(T)$ is the compressive strength at cold temperature *T*. Figure 1.4 show the experimental results obtained for k_2, the data used to generate this figure was extracted from Marshall (1982), Kasami et al. (1981), Lee et al. (1988a) and Filiatrault and Holleran (2001). From this figure can be seen that a value of $k_2 = 1$ can be used to predict the modulus of elasticity of concrete at low temperature, which means that the conventional equation of the type $E = k\sqrt{f_c^{'}}$ is still valid in low temperature conditions if the corresponding low temperature compressive strength is used.

Information regarding the influence of low temperature in Poisson's ratio of concrete is limited. Lee et al. (1988a) reported a linear increase in Poisson's ratio as the temperature decreases below freezing, at -40°C (-40°F) an increase of 40% was found. Approximately same increase is described in Marshall (1982).

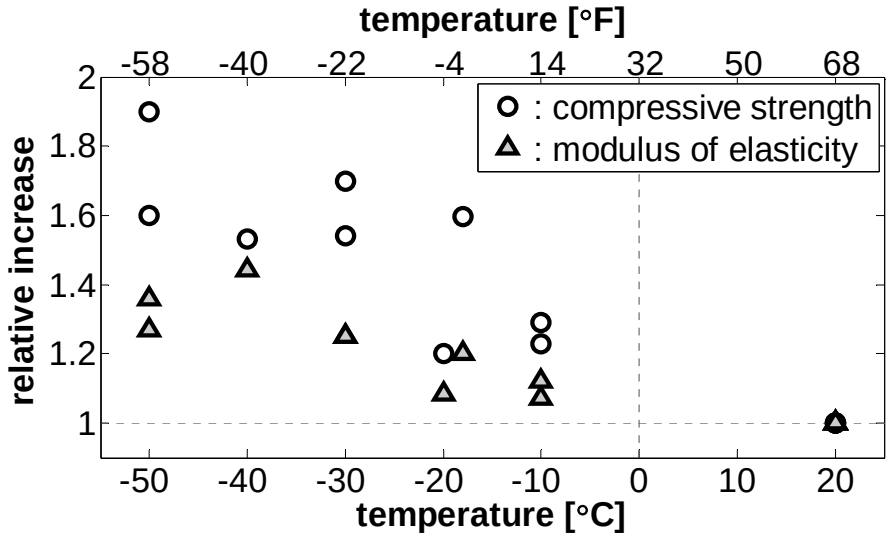

Figure 1.3. Effect of low temperatures in the modulus of elasticity of concrete

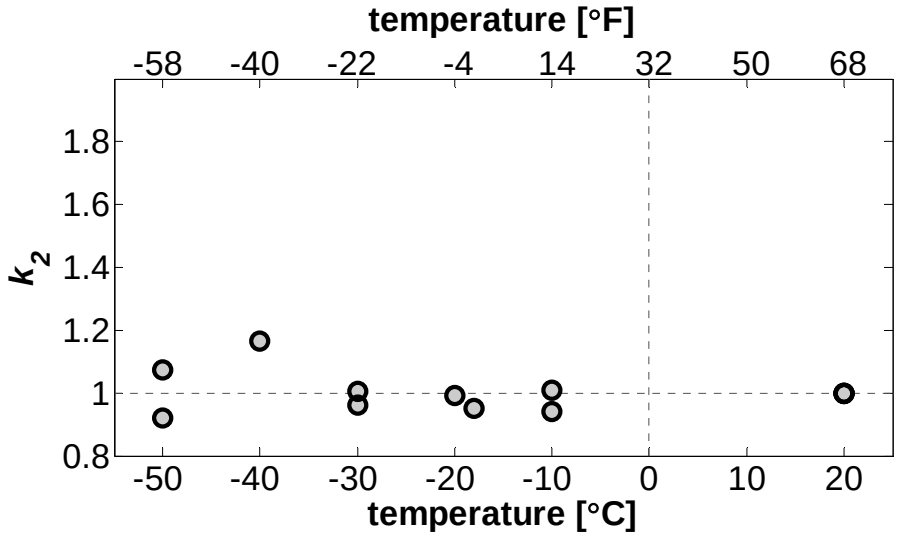

Figure 1.4. Experimental determination of K_2 for concrete modulus of elasticity

1.2.1.3 Stress-strain behavior

Just as the compressive strength, the stress-strain behavior of concrete is also highly influenced by the temperature and moisture of the specimen being tested. Rostàsy and Wiedemann (1980) showed how saturated concrete cooled at -170°C (-274°F) behaves purely elastic and brittle. Although the brittle behavior exhibit by the cold specimens, the strain at maximum stress ε_o was essentially the same as for the room

temperature specimen. From Rostàsy tests can also be noticed that the ultimate concrete strain increases linearly when the temperature decrease below freezing and until ~50°C (-58°F) where a maximum is attained (~160%) and then start decreasing. It should be remembered that Rostàsy's test were performed on saturated concrete. However, results obtained by Sloan (2005) on partially dry concrete exhibit the same behavior. Figure 1.5 display the results obtained by Sloan, it should be noticed that concrete cylinders at -40˚C (-40°F) failed abruptly without a softening portion of the stress-strain curve. Finally, Figure 1.6 is adapted from Rostàsy and Wiedemann (1980) and complemented for partially dry concrete with data provided by Sloan (2005). From this figure can be observed that, even taught it follows the same pattern, the effect of low temperatures in the strain at maximum stress ε_o of partially dry concrete is not as marked as for wet concrete.

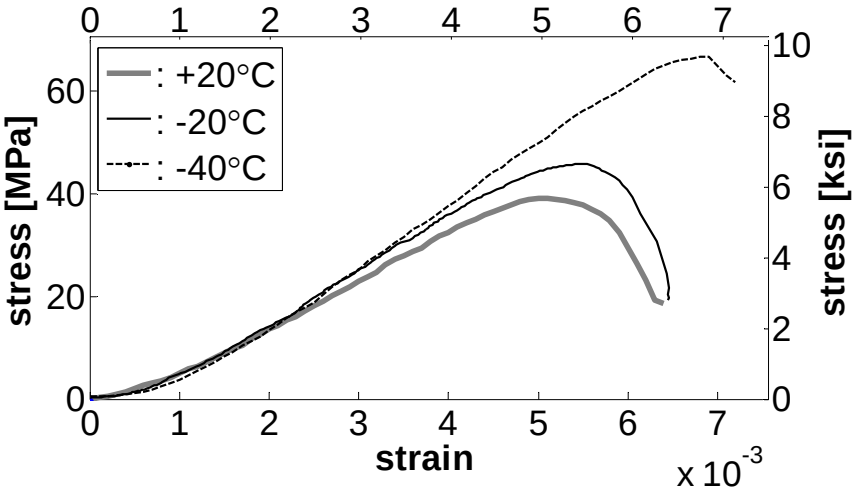

Figure 1.5. Concrete stress-strain response at different temperatures (from Sloan, 2005)

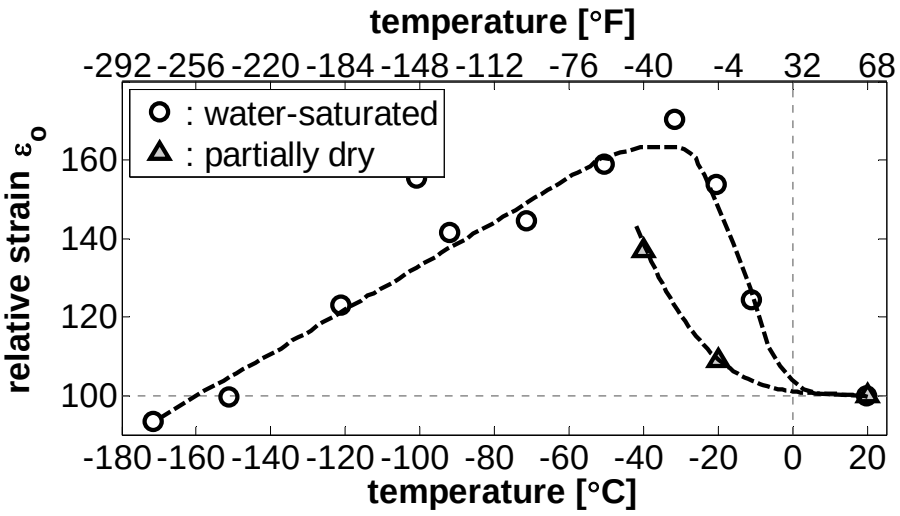

Figure 1.6. Low temperature effect on concrete strain at maximum stress

1.2.1.4 Tensile strength

Past research have shown that tensile strength of concrete, as determined from the splitting test, increase with low temperatures at a larger rate than the compressive strength. The results obtained from Nasser and Evans (1973), Kasami et al. (1981) and Lee et al. (1988a) are presented in Figure 1.7. Just as the modulus of elasticity, the tensile strength of concrete at normal temperatures is proportional to its compressive strength and is usually related to its square root. Therefore, we proceed here as for the modulus of elasticity and try to find a variable $k_{2T}(T)$ to account for the low temperature effect. Figure 1.8 displays the results obtained, in this case $k_{2T}(T)$ increase uniformly once the temperature drops below freezing. Based on the results displayed in Figure 1.8, the tensile strength of concrete at temperature below freezing can be estimated using Equation 1.5.

$$\sigma_t(T) = k_{2T}(T)k_{1T}\sqrt{\sigma_c(T)} = (1-0.0105T)k_{1T}\sqrt{\sigma_c(T)} \quad 0^\circ C > T > -50^\circ C \qquad (1.5)$$

where k_{1T} is the ratio between the square root of the compressive strength and tensile strength at room temperature.

Other researchers have found similar results when obtaining the tensile strength following different approaches. Cantin and Pigeon (1998) use the simple beam third-point load test and noticed an increase of ~35% in the peak load of specimens tested at -30°C (-22°F) when compared to specimens tested at room temperature. Elices and Planas (1982) used the double punch technique along with the traditional splitting test and found similar results at cryogenic temperatures. Nasser and Evans (1973) explain this increase as the result of additional adhesive forces developed in the ice formed in the capillary cavities of the concrete.

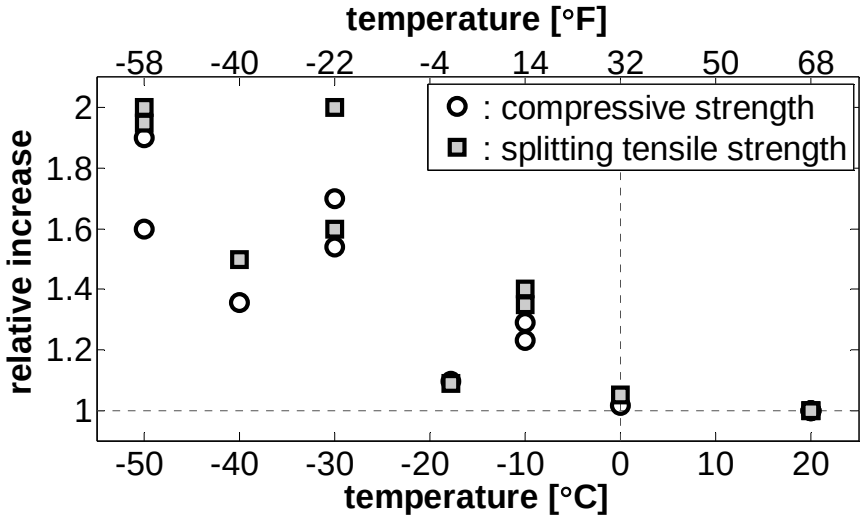

Figure 1.7. Effect of low temperatures in the tensile strength of concrete

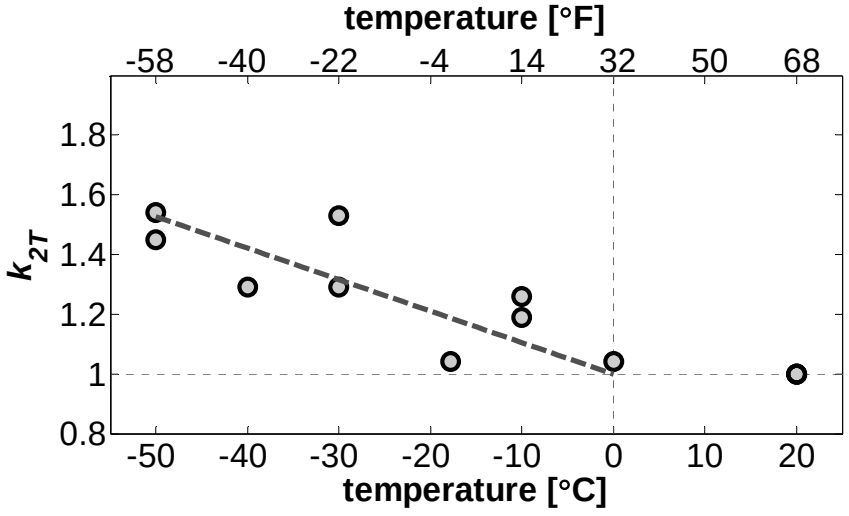

Figure 1.8. Experimental determination of K_{2T} for concrete tensile strength

1.2.1.5 Fracture properties

Past research has shown that the fracture energy of concrete specimens tested at low temperatures considerably increase when compared with specimens tested at room temperatures and this increase is larger in wet concrete. Ohlsson et al. (1990) reported an increase of 40 % in the peak load and an average 50% increase in the fracture energy when third point load notched beams where tested at -30°C (-22°F) with respect to the room temperature properties. Maturana et al. (1990) tested water-saturated specimens and report an increase of 200% in the fracture energy in specimens tested at -70°C (-94°F). Dubey and Banthia (1998) performed a series of tests in double cantilever beams instead of notched beams and come out with the same conclusion that earlier researchers. The explanation for this increase seems to be again in the formation of ice from the free water in the concrete. As postulated by Dubey and Banthia (1998) the high adhesive forces in the surface of the ice hold the crack faces together reducing the stress intensity at the crack tip.

1.2.1.6 Cyclic behavior

Information on cyclic behavior of concrete on freezing temperatures is very limited. Only two references were found that deal with this topic. Berner et al. (1985) tested lightweight concrete cylinders under compressive cycling load at temperatures ranging from 21°C (70°F) to -190°C (-310°F). The load protocol was intended to approximate the 20-year storm wave loading on a prestressed concrete floating cryogenic containment vessel. Each specimen was subjected to more of 10000 cycles with a nominal precompression of 37.5% the 28 days compressive strength to simulate the effect of the prestress. Results obtained indicate that effect of low temperatures on concrete subjected to cyclic loads is the same that for monotonic loads: concrete increase it compressive strength and modulus of elasticity, tough in a minor proportion. Ohlsson et al. (1990) performed cyclic tests on third point load notched beams and found that the fatigue strength also increase when the temperature is lowered.

1.2.1.7 Concrete-steel bond behavior

Concrete bond strength at low temperatures have been investigated by Lee et al. (1988a, 1988b) and Shih et al. (1988) based on pull out tests of reinforcing bars imbedded in normal and high strength concrete under monotonic, repeated cyclic and reverse cyclic loadings. Results obtained show that local bond strength increases at low temperatures for any type of load and concrete, however this increase is larger in normal strength concrete than in high strength concrete. Similar results were obtained by Vandewalle (1995), who used a beam-type test with monotonic loading and found the bond strength to increase uniformly when temperature was lowered in the range from 20°C (68°F) to -120°C (-184°F); for lower temperatures a slight decrease was noticed.

1.2.2 Low temperature effects on reinforcing steel

Past research has indicated that, as temperature reduces, the yield and tensile strength of reinforcing steel bars increase. Figure 1.9 was generated with information extracted from the works of Filiatrault and Holleran (2001) and Sloan (2005), points presented correspond to bars tested at a strain rate of $0.001s^{-1}$. It can be seen from this figure that, even the increase on yield strength seems to be slightly larger than the increase in tensile strength, both increases can be approximated to be of 10% in the range [-40°C (-40°F) -25°C (-13°F)] and then linearly decrease to zero at 0°C (32°F). It should be noticed that this approximation is valid only in the specified range, results obtained by Elices et al. (1986) show an increase of 80% and 36% in the yielding and tensile strength, respectively, of reinforcing bars tested at -180°C (-292°F). All abovementioned investigations agree that modulus of elasticity and ductility (measured as elongation under maximum load) are not affected by low temperatures, Figure 1.10 shows the stress-strain behavior of steel rebars at room and low temperatures. According with Elices et al. (1986) cold temperatures significantly reduce the ultimate strain only when the bar has surface defects (as cuts or notches). However, it should be noticed that all the results aforementioned were obtained from monotonic tests; therefore no conclusion regarding the strain capacity under cyclic loading typical of seismic excitation is possible.

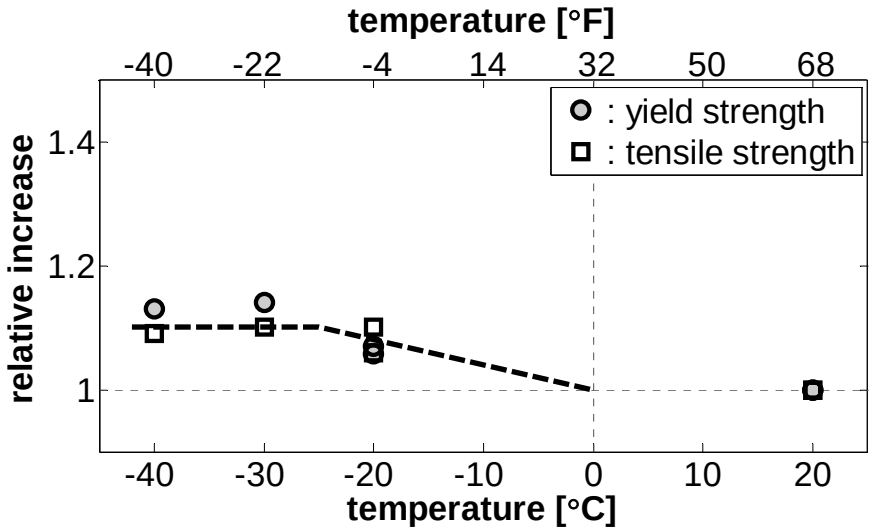

Figure 1.9. Effect of low temperatures in the yield and tensile strength of steel reinforcing bars

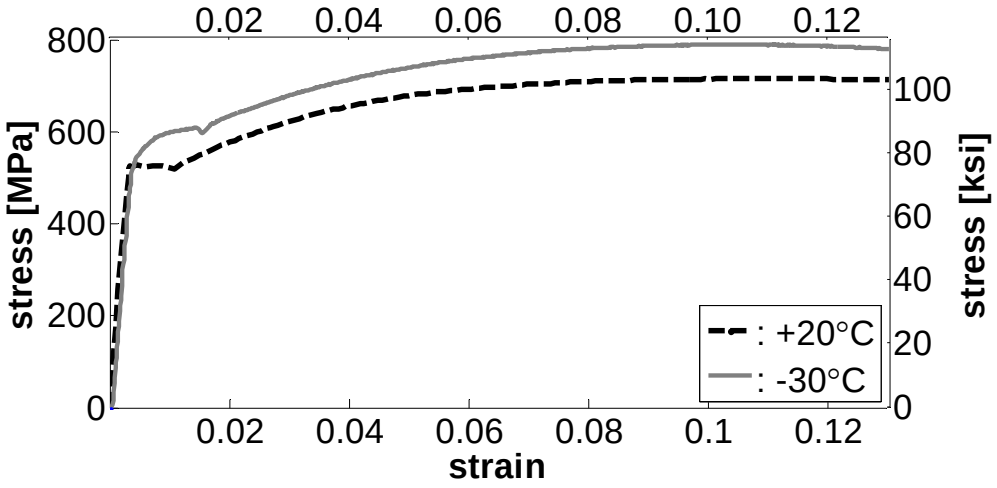

Figure 1.10. Stress-strain behavior of steel reinforcing bars at low temperatures (Sloan 2005)

1.2.3 Low temperature effect on reinforced concrete members

Information related to the effect of low temperatures in reinforced concrete structure is quite limited. The only large scale reversed cyclic tests on reinforced concrete members conducted at low temperature have been those by Sritharan et al (2007) and Sloan (2005). Sritharan's tests will be discussed in the next section since their main objective was to identify the effect of low temperatures in the soil-structure interaction. Sloan (2005) tested 4 identical reinforced concrete column-type members, 3 of them were

subjected to low temperatures {-20^{0}C (-4°F), -30^{0}C (-22°F), -40^{0}C (-40°F)} and the other one was tested at ambient laboratory temperature 23^{0}C (73°F). The columns were lightly reinforced, and were loaded in a reversed cyclic manner while inside of an environmental chamber. The results obtained indicate moderate increases in column strength as the temperature decreases, as well as moderate decreases in ultimate displacement capacity as the temperature decreases (Figure 1.11).

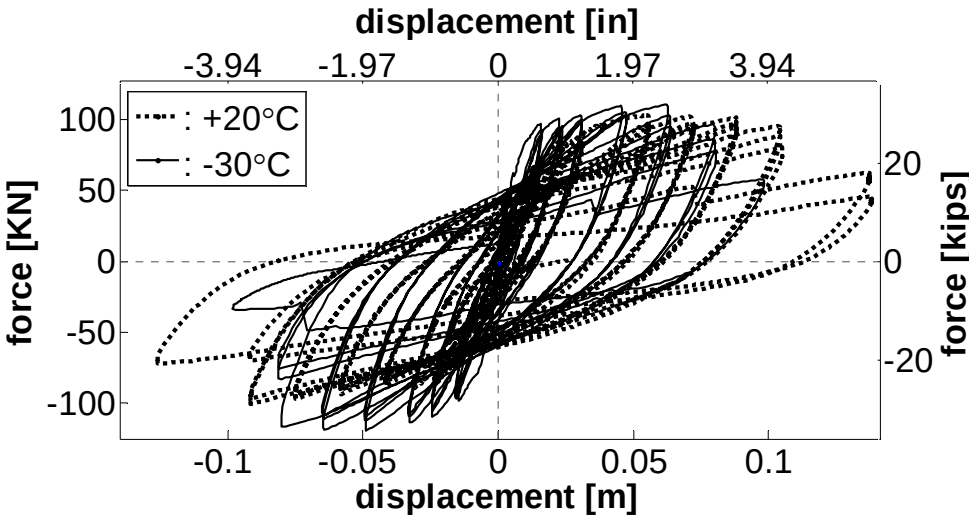

Figure 1.11. Reinforced concrete force-displacement response at different temperatures (Sloan, 2005)

1.2.4 Low temperature effects on soil-structure interaction

The effect of low temperatures in soil-structure interaction has been recently addressed by a research performed at Iowa State University. The results of this research are presented in Suleiman et al. (2006) and Sritharan et al. (2007). In this research the effect of seasonal freezing in bridge column foundation systems with a Cast-In-Drilled-Hole (CIDH) shaft was investigated using three outdoor large scale test units. Two of the units were identical having the columns and foundation shaft the same diameter, the third unit had an oversized foundation. One of the units was tested in summer conditions 23^{0}C (73°F) and the other two in winter conditions -10^{0}C (14°F). The results obtained showed that as temperature decreases, the depth of freezing soil increases. This provokes a migration of the plastic hinge towards the surface, accompanied by a significant increase

in the effective elastic stiffness and shear demand and a reduction in the displacement capacity.

1.3 General organization

Chapter I contains a general introduction to the research. The motivation and problem description are briefly discussed. The chapter continues with a review of the most relevant previous works on the subject of seismic behavior of reinforced concrete structures under freezing conditions. The scope and organization of the report are also included in the first chapter.

Chapter II presents the details of the design and construction of the specimens. The analytical models used to calculate the response of the specimens are concisely described and the initial member response predictions are presented. The chapter ends with a description of the construction process and the results of the material tests.

Chapter III contains a description of the test setup and the instrumentation used. Information related to the footing support and the application of the axial and lateral loads are presented in this chapter, as well as the load protocol and the instrumentation distribution.

Chapters IV, V and VI presents the results obtained from the tests of the flexural dominated columns, reinforced concrete filled steel tube columns and shear dominated columns, respectively. The results are analyzed in order to identify the effects of temperature in the strength and ductility of the members. The analytical models and material constitutive relations used to calculate the initial predictions are revised in order to account for the effect of temperature.

In Chapter VII the results obtained in Chapters IV to VI are implemented to model typical bridge bents used by the Alaska Department of Transportation. A series of dynamic inelastic time history analysis are conducted in order to determine the impact on the overall structural response.

Finally, Chapter VIII presents a summary of the main findings and achievements. Recommendations are given for the seismic design and assessment of bridges in cold regions. A list of areas and specific topics where it is deemed that more work would be beneficial is also provided.

CHAPTER II

THEORETICAL CONSIDERATIONS AND SPECIMEN DESIGN

2.1 Introduction

This chapter discusses the design of the test units. In order to understand every aspect of the seismic behavior of RC members under freezing temperatures, the design of each unit is motivated by a desired behavior. The test program was divided into three categories: (1) flexural dominated members, (2) reinforced concrete filled steel tube members typical of Alaska DOT design practice and (3) shear dominated members. In the shear dominated members, two different transverse reinforcement ratios were designed with the aim of achieving shear failures at low levels of ductility (brittle shear failure) and high levels of ductility (ductile shear failure).

In order to accommodate the need for temperatures down to –40^{o}C (-40°F), the tests were conducted with the specimens inside of an environmental chamber. The dimensions of the chamber made it necessary that the specimens be tested while lying in a horizontal position rather than standing vertically erect, this turned out to be the major limitation in the design of the cross section configurations, height of the column and the size of the footing. A summary of the test matrix is shown in Table 2.2. The specimens were initially designed using the analytical models presented in the next section and the expected material properties.

2.2 Analytical models

In order to design the specimens to fail in the desired mode, an iterative methodology was followed: First, a section configuration and member length are chosen and a section analysis is performed by tabulating moment and curvature of the member section for increasing levels of concrete strain. Then, the member response is obtained from the section moment-curvature results along with an equivalent plastic hinge length originally developed by Priestley and Park (1987) and recently updated by Priestley, Calvi and Kowalsky (2007). The shear strength envelope for the member is calculated using the revised UCSD shear model (Kowalsky and Priestley, 2000). The on set of buckling is checked according to two different models, one proposed by Moyer and Kowalsky (2003) and the other proposed by Berry and Eberhard (2005). If the resulting mode of failure is different from that which is intended, or if the levels of required force or displacement exceed the limits of the testing apparatus, changes are made to the section configuration and the member response is recalculated.

The constitutive models used for the unconfined and confined concrete are those proposed by Mander, Priestley and Park (1988). The constitutive model for the steel is that proposed by King (1986). With the aim of facilitating the implementation of the models and procedures mentioned above, a *Matlab*® based code, *CUMBIA* (Montejo and Kowalsky, 2007), was developed and used for the design and analysis of the specimens. In the next section, a concise description of the aforementioned analytical models aforementioned is presented.

2.2.1 Material models

2.2.1.1 Constitutive model for the confined concrete

Transverse reinforcement is placed to RC members in the form of spirals, hoops or jackets in order to provide confinement to the compressed concrete and to prevent buckling of the longitudinal reinforcement. Concrete expands when compression stresses are developed, provoking hoop tension in the transverse reinforcement (Paulay and

Priestley, 1992). The maximum lateral pressure f_l that can be induced in the concrete by the transverse reinforcement occurs when the transverse reinforcement reaches its yielding stress, Equations 2.1 and 2.2 are found from the equilibrium of the free bodies in Figure 2.1

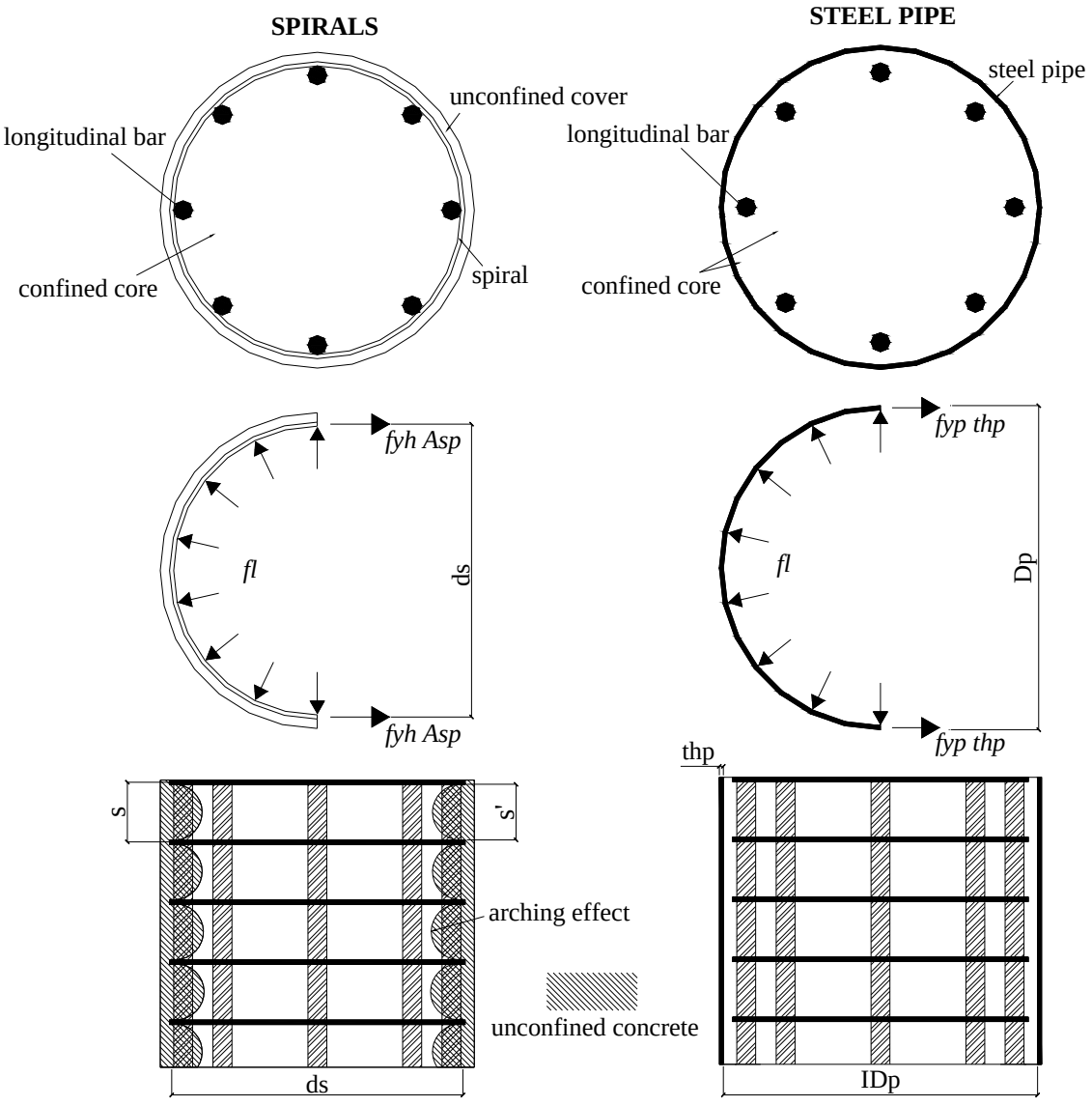

Figure 2.1. Confinement of concrete by spirals and steel pipes

$$f_l = {2 f_{yh} A_{sp}}/{d_s s} \text{ , for spirals or circular hoops} \qquad (2.1)$$

$$f_l = 2 f_{yp} th_p \Big/ \left(D_p - th_p\right), \text{ for steel pipe} \quad (2.2)$$

where d_s is the center-to-center diameter of the spiral and D_p is the outside diameter of the steel pipe; A_{sp} is the bar area of the spiral and th_p is the thickness of the steel pipe; f_{yh} and f_{yp} are the yielding stresses of the spirals and steel pipe, respectively. It should be noticed that Equation 2.1 does not account for the arching effect between transverse bars; midway between the layers of transverse reinforcement the area of ineffectively confined concrete is larger. In general, the effect of confinement is to increase the compression strength and ultimate strain of concrete. Different stress-strain relationships have been developed for confined concrete. The model proposed by Mander et al. (1988) is the one used in this research and is described below.

2.2.1.1.1 Members with spirals as transverse reinforcement

Mander et al. (1988) has proposed a unified stress-strain approach for confined concrete (Figure 2.2) applicable to circular and rectangular sections. In the Mander model, the compressive stress f_c for the confined concrete is given by:

$$f_c = \frac{f'_{cc}\, xr}{r - 1 + x^r} \quad (2.3)$$

$$r = \frac{E_c}{E_c - E_{\text{sec}}} \quad (2.4)$$

$$E_{\text{sec}} = \frac{f'_{cc}}{\varepsilon_{cc}} \quad (2.5)$$

where $x = \varepsilon_c / \varepsilon_{cc}$; ε_c is the compressive concrete strain of the confined concrete and ε_{cc} is the strain for maximum stress in the confined concrete which is given by:

$$\varepsilon_{cc} = \varepsilon_{co}\left[1 + 5\left(\frac{f'_{cc}}{f'_{co}} - 1\right)\right] \quad (2.6)$$

In Equation 2.6 ε_{co} is the strain for maximum stress in the unconfined concrete, f'_{co} is the unconfined concrete compressive strength (from cylinder test) and f'_{cc} is the maximum stress in the confined concrete and for circular sections is defined by Equation 2.7

$$f'_{cc} = f'_{co}\left(-1.254 + 2.254\sqrt{1+\frac{7.94 f'_l}{f'_{co}}} - 2\frac{f'_l}{f'_{co}}\right) \tag{2.7}$$

where f'_l is the effective confining stress as defined by:

$$f'_l = k_e f_l \tag{2.8}$$

In Equation 2.8 k_e is the confinement effective coefficient and f_l is the maximum lateral pressure previously defined in Equation 2.1.

$$k_e = \frac{1-\frac{s'}{2d_s}}{1-\rho_{cc}} \text{ , for circular spirals} \tag{2.9}$$

s': Clear distance between spirals or hoops

ρ_{cc}: Ratio of area of longitudinal reinforcement to area of core section

Equation 2.8 is commonly expressed in terms of the volumetric ratio of transverse confining steel and confined concrete core ρ_s:

$$f'_l = \frac{1}{2}k_e\rho_s f_{yh}, \quad \rho_s = \frac{4A_{sp}}{d_s s} \tag{2.10}$$

An energy balance approach is used in the Mander et al. (1988) model to predict the compressive strain in the concrete corresponding to first fracture of the transverse reinforcement by equating the strain energy capacity of the transverse reinforcement to the strain energy stored in the concrete as a result of the confinement. The ultimate concrete strain is then given by the expression between parentheses in Equation 2.11

where ε_{su} is the ultimate tensile strain of the transverse reinforcement. Since experimental results have shown that the ultimate concrete strain calculated based on the Mander model to be consistently conservative by 50% (Kowlasky, 2000), the original Mander expression for ε_{cu} is modified by a factor of 1.4 as shown in Equation 2.11.

$$\varepsilon_{cu} = 1.4\left(0.004 + \frac{1.4\rho_s f_{yh}\varepsilon_{su}}{f'_{cc}}\right) \tag{2.11}$$

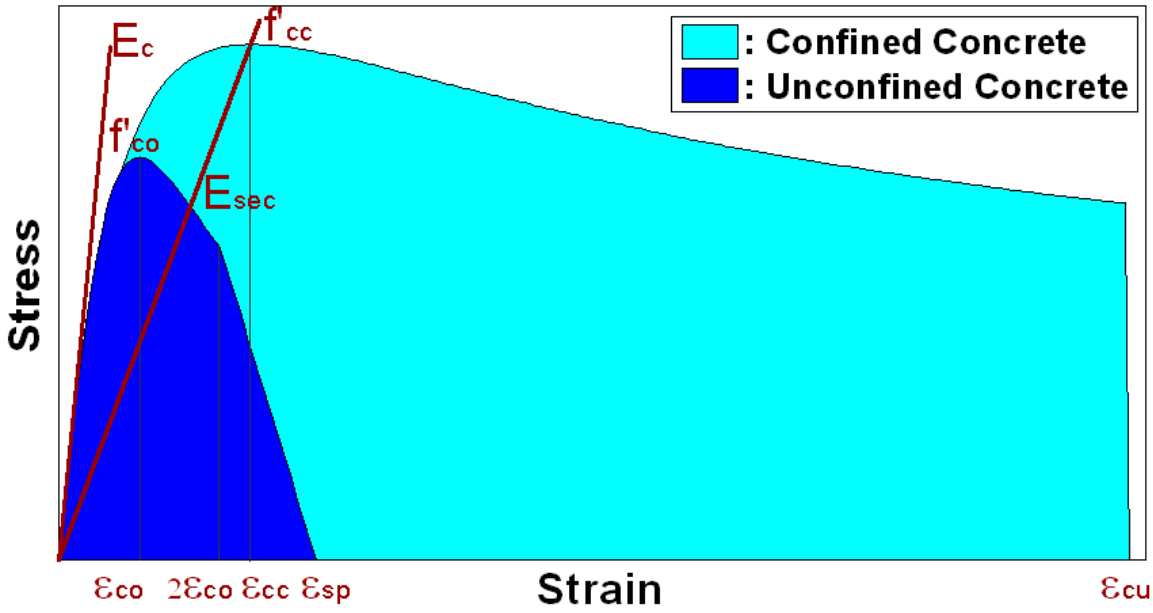

Figure 2.2. Mander model for confined and unconfined concrete

2.2.1.1.2 Members with a steel pipe as transverse reinforcement

Even tough the Mander et al. (1988) model was developed for RC member with confining steel in the form of spirals or hoops, the model can be easily modified to account for members with a steel pipe as transverse reinforcement (Chai et al. 1991). As illustrated in Figure 2.1, when using a steel pipe as confining reinforcement, the whole concrete area is effectively confined, which means that for reinforced concrete filled steel pipes (RCFSP) the confinement effective coefficient k_e is 1 and the effective confining stress is given by Equation 2.12. The stress strain relationship can then be found as usual by using Equations 2.3 to 2.7.

$$f_l^{'} = f_l = 2 f_{yp} th_p \Big/ \left(D_p - th_p\right) = \frac{1}{2} f_{yp} \rho_{sp} \left(\frac{D_p - 2th_p}{D_p - th_p} \right)^2 \tag{2.12}$$

where ρ_{sp} is the volumetric confinement ratio of the steel pipe.

$$\rho_{sp} = \frac{4th_p\left(D_p - th_p\right)}{\left(D_p - 2th_p\right)^2} \tag{2.13}$$

It should be noticed that the reinforced concrete filled steel tubes column tested in this research have both types of reinforcement: steel pipe and spirals. The volumetric confinement ratio in this case is then the sum of the ratios obtained from equations 2.10 and 2.13, as presented in Table 2.2.

2.2.1.2 Constitutive model for the unconfined concrete

The Mander et al. (1988) model for unconfined concrete follows the same curve as that for confined concrete (Equation 2.3) with a lateral confined stress of $f'_l = 0$. The falling branch (for strains larger than $2\varepsilon_{co}$) is assumed to be a straight line which reaches zero at the spalling strain ε_{sp} (Figure 2.2).

2.2.1.3 Constitutive model for the reinforcing steel

The stress-strain relation for the reinforcing steel (Figure 2.2) is the one proposed by Raynor et al. (2002):

$$\begin{aligned} f_s &= E_s \varepsilon_s && \varepsilon_s \le \varepsilon_y \\ f_s &= f_y + \left(\varepsilon_s - \varepsilon_y\right) E_y && \varepsilon_y < \varepsilon_s < \varepsilon_{sh} \\ f_s &= f_u - \left(f_u - f_{sh}\right)\left(\frac{\varepsilon_{sm} - \varepsilon_s}{\varepsilon_{sm} - \varepsilon_{sh}} \right)^{C1} && \varepsilon_{sh} < \varepsilon_s \le \varepsilon_{sm} \end{aligned} \tag{2.14}$$

$$\varepsilon_y = \frac{f_y}{E} \tag{2.15}$$

$$f_{sh} = f_y + \left(\varepsilon_{sh} - \varepsilon_y\right) E_y \tag{2.16}$$

where E_s is the steel modulus of elasticity, f_y is the steel yielding stress, ε_y is the steel yielding strain, ε_{sh} is the strain at which strain hardening starts, ε_{sm} is the ultimate steel strain, E_y is the slope of the yield plateau, *C1* is the parameter that defines the curvature of the strain hardening curve and, f_s and ε_s are the steel stress and strain at any point.

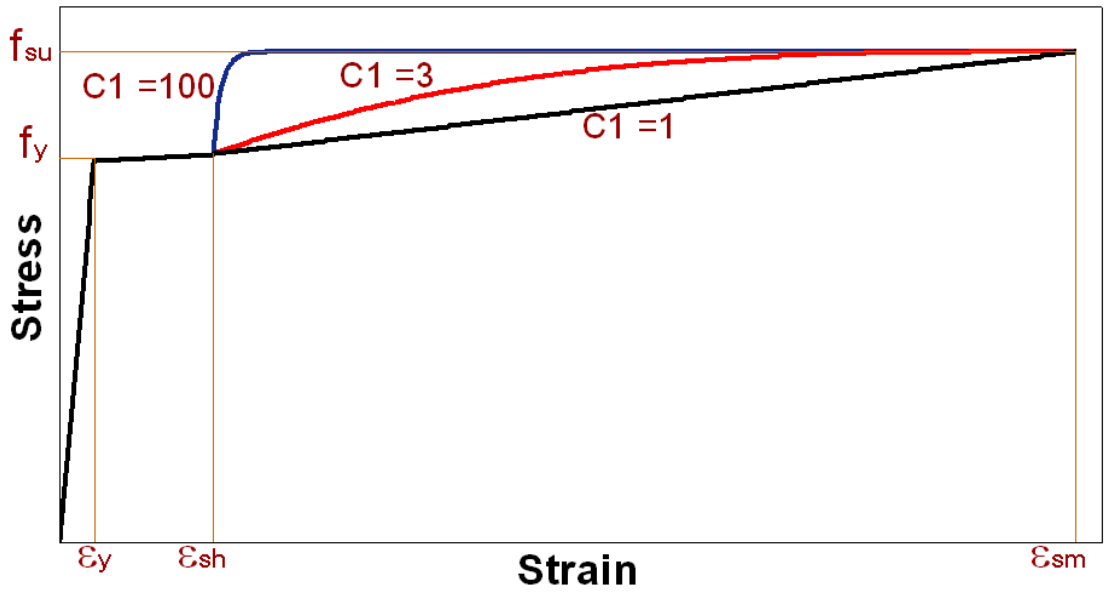

Figure 2.2. Constitutive model for the reinforcing steel

2.2.2 Section analysis and member response

The section analysis is performed by tabulating moment (M) and curvature (ϕ) of the member section for increasing levels of concrete strain. An iterative procedure is used in order to find the depth of the neutral axis to satisfy equilibrium at each level of concrete strain. The iterative process continues until the concrete strain in the core exceeds the maximum concrete compressive strain, the strain in the bottom steel bars exceeds the maximum steel strain or a drop of 20% in the moment capacity is observed.

The member response is obtained using the plastic hinge method as described in Priestley, Calvi and Kowalsky (2007). The plastic hinge method replaces the real curvature distribution with an equivalent curvature distribution in order to facilitate the application of the moment area method to find the displacements in the member (Figure

2.3). The length of the equivalent plastic hinge (L_p) is defined as the length over which the maximum curvature can be assumed to be constant. Equations 2.17 and 2.18 are used to calculate the equivalent plastic hinge length and the strain penetration length (L_{sp}), respectively.

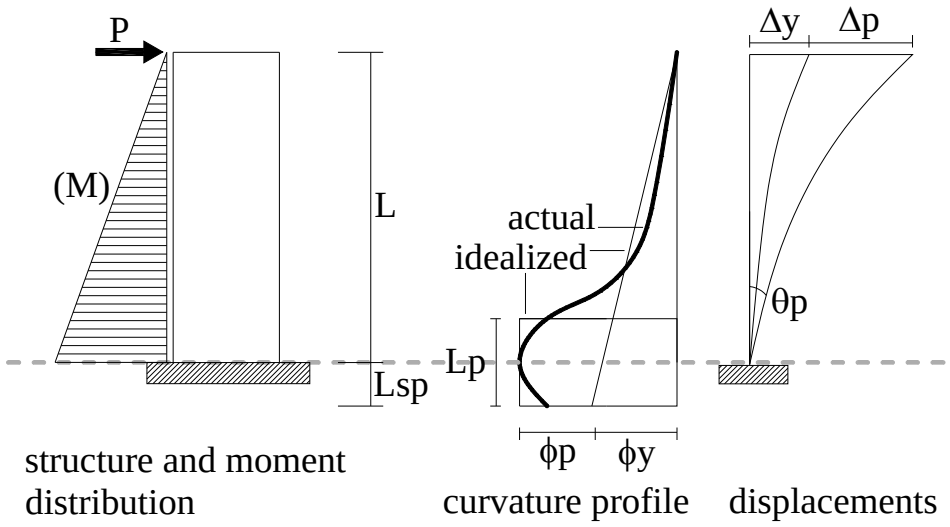

Figure 2.3. Plastic hinge method (column in single bending)

$$L_p = kL + L_{sp} \geq 2L_{sp} \tag{2.17}$$

$$L_{sp} = 0.022 f_s d_{bl} \quad f_s \leq fy \quad (MPa) \tag{2.18}$$

where:

$$k = 0.2\left(\frac{f_{su}}{f_y} - 1\right) \leq 0.08$$

L : clear length of the member

f_y : expected longitudinal bar yield stress

f_{su} : expected longitudinal bar maximum tensile stress

f_s : tensile stress in the longitudinal bars

d_{bl} : longitudinal bar diameter

In the case of reinforced concrete filled steel pipes the length of the equivalent plastic hinge is calculated using Equation 2.19 (Chai et al. 1991) where g is the gap between the steel pipe and the base of the column.

$$L_p = 2L_{sp} + g \tag{2.19}$$

An effective length of the member is then defined as:

$$L_{eff} = L + L_{sp}, \text{ for columns in single bending} \tag{2.20}$$

$$L_{eff} = L + 2L_{sp}, \text{ for columns in double bending} \tag{2.21}$$

Flexural displacement before cracking is calculated as $\Delta_f = L^2/3$ or $\Delta_f = L^2/6$ for single and double bending, respectively. The flexural displacement of the member before yielding and after cracking is calculated as:

$$\Delta_f = \frac{\phi L_{eff}^{\ 2}}{3}, \text{ single bending} \tag{2.22}$$

$$\Delta_f = \frac{\phi L_{eff}^{\ 2}}{6}, \text{ double bending} \tag{2.23}$$

The flexural displacement beyond yield is given by:

$$\Delta_f = \left[\phi - \phi_y^{'} \frac{M}{M_y^{'}}\right] L_p \left(L + L_{sp} - 0.5L_p\right) + \Delta_y^{'} \frac{M}{M_y^{'}} \tag{2.24}$$

where $\phi_y^{'}$, $M_y^{'}$ and $\Delta_y^{'}$ are the curvature, moment and displacement for the first yielding, respectively. Note that the yield displacement is scaled to the current moment, M, to account for additional column elastic flexibility.

A simplified approach for calculating the shear stiffness in the elastic range of response based on the cracked section stiffness is used to calculate the shear deformations. The premise of this approach is that the elastic shear stiffness is reduced approximately in proportion to the flexural stiffness. After shear cracking and before the section reaches its nominal moment, shear deflections are computed by considering the shear flexibility of an equivalent strut-and-tie model. The procedure is described in Equations 2.25 to 2.32 where A_g and I_g are the gross area and moment of inertia of the section.

$E_c = 5000\sqrt{f'c} \quad (MPa)$, concrete modulus of elasticity (2.25)

$G = 0.43E_c$, concrete shear modulus (2.26)

$A_s = 0.9A_g$, shear effective area (circular section) (2.27)

$I_{eff} = \frac{M'_y}{E_c \phi'_y}$, effective or moment of inertia (2.28)

$k_{sg} = \frac{GA_s}{L}$, shear stiffness (2.29)

$k_{seff} = k_{sg}\frac{I_{eff}}{I_g}$, effective shear stiffness (2.30)

The shear deformations of the columns before shear cracking are then calculated using Equation 2.31 where V is the shear force acting in the member. Shear cracking is assumed to occur when the applied shear is larger than the shear strength of the concrete V_c, which is obtained from Equation 2.36 with $\gamma = 0.29$ (i.e. the initial concrete strength).

$\Delta_s = \frac{V}{k_{seff}}, \quad V < V_c$ (2.31)

After shear cracking occurs and before the nominal moment is reached, the shear stiffness is calculated using Equation 2.32, where B and d are the effective width and depth of the section.

$$k_{scr} = \frac{0.25(\pi\rho_s/8)}{0.25+10(\pi\rho_s/8)} E_s 0.64D^2 \tag{2.32}$$

The shear displacement beyond yield is assumed to increase proportional to the flexural displacement. The total displacement in the member is given then by Equation 2.33.

$$\Delta = \Delta_f + \Delta_s \tag{2.33}$$

2.2.3 Shear capacity

The shear strength envelope for the member is calculated using the revised UCSD shear model (Kowalsky and Priestley, 2000). The original UCSD model for assessment of shear strength included: (1) the effect of the axial load separate from the concrete strength and (2) degradation of concrete strength with ductility. The revised model intends to take also into account: (1) the effect of concrete compression zone on the mobilization of transverse steel and (2) the influence of the aspect ratio and the longitudinal steel ratio in the shear strength of the concrete. The model expresses the shear strength capacity of the member as the sum of three separate components as shown in Equation 2.34 where V_s represents the shear capacity attributed to the steel truss mechanisms, V_c represents the strength of the concrete shear resisting mechanism and V_p represents the strength attributed to the axial load.

$$V = V_s + V_c + V_p \tag{2.34}$$

The shear resistance provided by the transverse reinforcement for a circular column with circular hoops or spirals is given by:

$$V_s = \frac{\pi}{2} A_{sp} f_{yh} \frac{D - clb + d_h - c}{s} \cot(\theta) \tag{2.35}$$

where clb is the cover to the longitudinal bar, d_h is the diameter of the transverse steel, c is the depth of the neutral axis at M_n and θ is the angle of the flexure-shear crack, for assessment of existing structure a value of $\theta = 30^o$ is recommended. The concrete shear resisting mechanism depends on the aspect ratio, the ratio of longitudinal reinforcement and the level of ductility. Equations 2.36 to 2.40 are used to calculate the shear strength provided by the concrete.

$$V_c = \alpha\beta\gamma\sqrt{f'_c}\left(0.8A_g\right) \tag{2.36}$$

$$1 \le \alpha = 3 - \frac{M}{VD} \le 1.5 \tag{2.37}$$

$$\beta = 0.5 + 20\rho_l \le 1 \tag{2.38}$$

$$0.05 \le \gamma = 0.37 - 0.04\mu_\Delta \le 0.29 \qquad \text{uniaxial ductility demand} \tag{2.39}$$

$$0.05 \le \gamma = 0.33 - 0.04\mu_\Delta \le 0.29 \qquad \text{biaxial ductility demand} \tag{2.40}$$

In Equations 2.38 to 2.40 the variables ρ_l and μ_Δ represent the longitudinal steel ratio and the displacement ductility, respectively. The yield displacement used to calculate the displacement ductility is calculated considering only the flexural deformation. However, the total displacement is calculated considering flexural and shear deformations. The variable *M/VD*, where *M* is the moment and *V* the shear at the critical section, is equivalent to the aspect ratio L_c/D, where L_c is the distance from the critical section to the point of contraflexure. For the single bending case $L_c=L$ and for the double bending case it is usually assumed that $L_c=L/2$. The axial load component can be obtained using Equations 2.41 to 2.44.

$$V_p = P\frac{D - c}{2L} \quad P > 0 \qquad \text{columns in single bending} \tag{2.41}$$

$$V_p = P\frac{D-c}{L} \quad P > 0 \qquad \text{columns in double bending} \tag{2.42}$$

$$V_p = 0 \quad P < 0 \tag{2.43}$$

Equations 2.34 to 2.43 are used for the assessment of the shear strength of existing structures. For the design of new structures a more conservative approach is used: the axial load is reduced by 15%, the angle of the flexure-shear crack is incremented to 35˚ and a shear strength reduction factor of 0.85 is applied.

2.2.3 Reinforcement buckling

The assessment of the reinforcement buckling limit state is determined following two different methodologies, one is the proposed by Moyer and Kowalsky (2003) and the other is the proposed by Berry and Eberhard (2005). In the Moyer-Kowalsky model, the characteristic compression strain capacity is defined by Equation 2.44. From experimental results the growth strain ε_{sgr} was determined to be 50% of the peak strain after a curvature ductility of 4, linear interpolation is used for the evaluation of growth strain between curvature ductilities of 1 (where growth strain is zero) and 4. The growth strain represents the amount of tension strain induced in the reinforcing bars due to cyclic loading. It was postulated that by subtracting the growth strain from the characteristic compression strain, the remaining strain would be available for flexure induced tension as shown in (Equation 2.45). As Equation 2.45 is a function of total member deformation, the on set of buckling is defined as the point where the tension strain in the column due to bending reaches the allowable tension strain from Equation 2.45. The model is presented graphically in (Figure 2.4).

$$\varepsilon_{scc} = -3\left(\frac{s}{d_{bl}}\right)^{-2.5} \tag{2.44}$$

$$\varepsilon_{sfl} = \varepsilon_{scc} - \varepsilon_{sgr} \tag{2.45}$$

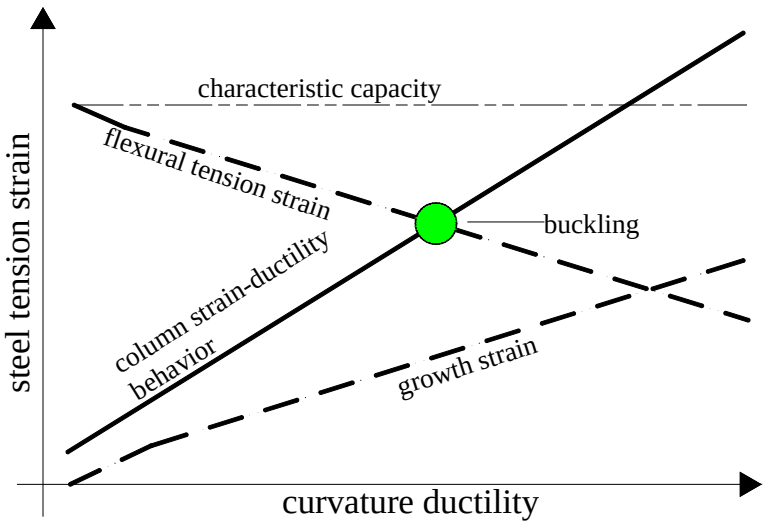

Figure 2.4. Assessment of reinforcement buckling limit state (from Moyer and Kowalsky, 2003)

The Berry-Eberhard model is an empirical model based on the existing database of column tests where the plastic rotation at the onset of bar buckling is expressed as:

$$\theta_{pbb} = C_0\left(1 + C_1\rho_{eff}\right)\left(1 + C_2\frac{P}{A_g f_c^{'}}\right)^{-1}\left(1 + C_3\frac{L}{D} + C_4\frac{f_y d_{bl}}{D}\right) \tag{2.46}$$

where $\rho_{eff} = \frac{f_{yh}}{f_c^{/}}\rho_s$ and buckling occurs when the plastic rotation in the member reaches the value of θ_{pbb}. For circular sections: $C_0 = 0.006$, $C_2 = 3.129$, $C_3 = 0.651$ and $C_4 = 0.227$

2.3 Specimen design

As mentioned before, the specimens were initially designed using the analytical models presented in section 2.2 and the expected material properties. The specified concrete strength (f'_c) was 4 ksi (27.6 MPa) for all the specimens, the reinforcing bars and spiral steel used was Grade 60 (f_y = 60 ksi, 414 MPa) and API5L X52 (f_{yp} = 52 ksi, 358 MPa) steel pipes with an outside diameter of 457mm (18in) and 9.5mm (0.375in) of thickness were used for the reinforced concrete filled steel tube columns (RCFST). Based on previous research the material properties used for the initial member response

predictions are presented in Table 2.1. Tables 2.2 and 2.3 present the test specimen matrix.

Table 2.1. Material properties values used for the design of the specimens

TEMP.	CONCRETE STRENGTH	YIELD STRESS [BARS AND SPIRALS]	TENSILE STRENGTH [BARS AND SPIRALS]	YIELD STRESS [STEEL PIPE]
74˚F/ 23˚C	4.4 ksi (30.3MPa)	70 ksi (483 MPa)	94 ksi (648 MPa)	60 ksi (414 MPa)
-40˚F/ -40˚C	7.5 ksi (51.7 MPa)	85 ksi (586 MPa)	115 ksi (791 Mpa)	72 ksi (500 MPa)

Table 2.2 Test specimen matrix (long columns*)

SPECIMEN	TEMP.	BEHAVIOR	LONG. STEEL/ RATIO	TRANSVERSE STEEL/RATIO	AXIAL LOAD/ RATIO
RCFST-89A	74˚F/ 23˚C	Steel pile column	8#9 3.1%	#3@63mm (2.5in) 9.5mm (3/8in) th. steel tube (1.2+8.5)%	231kN 52kips 4.6%
RCFST-89C	-40˚F/ -40˚C	Steel pile column	8#9 3.1%	#3@63mm (2.5in) 9.5mm (3/8in) th. steel tube (1.2+8.5)%	231kN 52kips 2.7%
RCFST-87A	74˚F/ 23˚C	Steel pile column	8#7 2.1%	#3@63mm (2.5in) 9.5mm (3/8in) th. steel tube (1.2+8.5)%	231kN 52kips 4.6%
RCFST-87C	-40˚F/ -40˚C	Steel pile column	8#7 2.1%	#3@63mm (2.5in) 9.5mm (3/8in) th. steel tube (1.2+8.5)%	231kN 52kips 2.7%
FL-89A	74˚F/ 23˚C	Flexure	8#9 3.1%	#3@63mm (2.5in) 1.2%	231kN 52kips 4.6%
FL-89C	-40˚F/ -40˚C	Flexure	8#9 3.1%	#3@63mm (2.5in) 1.2%	231kN 52kips 2.7%

* All the long columns have diameter 457mm (18in) and length 1651mm (65in)

Table 2.3 Test specimen matrix (short columns*)

SPECIMEN	TEMP.	BEHAVIOR	LONG. STEEL/ RATIO	TRANSVERSE STEEL/RATIO	AXIAL LOAD/ RATIO
DSH-87A	74˚F/ 23˚C	Ductile shear	8#7 2.2%	#3@100mm (4in) 0.8%	134kN 30kips 3.2%
DSH-87C	-40˚F/ -40˚C	Ductile shear	8#7 2.2%	#3@100mm (4in) 0.8%	134kN 30kips 1.9%
BSH-89A	74˚F/ 23˚C	Brittle shear	8#9 3.7%	#3@146mm (5.7in) 0.6%	134kN 30kips 3.2%
BSH-89C	-40˚F/ -40˚C	Brittle shear	8#9 3.7%	#3@146mm (5.7in) 0.6%	134kN 30kips 1.9%

* All the short columns have diameter 419mm (16.5in) and length 762mm (30in)

Figures 2.5 to 2.9 display the initial force-displacement response predictions obtained using the available analytical methods (section 2.2) along with the material properties displayed in Table 2.1. In the case of the RCFST columns a 1 in gap is left between the steel tube and the footing. The purpose of the steel tube is to improve the confinement and shear strength of the column and not (directly) the flexural and axial capacity. Geometric properties and reinforcement details of the specimens are presented in Figure 2.10.

Figures 2.5 to 2.7 present the response of the flexurally dominated members. Figures 2.8 and 2.9 display, along with the force-displacement responses, the shear strength envelopes. The shear critical members are expected to fail at the point where the force-displacement response intersects with the shear strength envelope. Two different types of shear dominated members where designed, one to obtain a shear failure at low levels of ductility (brittle shear failure, Figure 2.8) and the other to obtain a shear failure

at larger levels of ductility (ductile shear failure, Figure 2.9). It can be noticed that according to existing analytical models, the effect of freezing temperatures in the seismic behavior of reinforced concrete columns is to increase the flexural and shear strength of the column without any loss in the displacement capacity of the column.

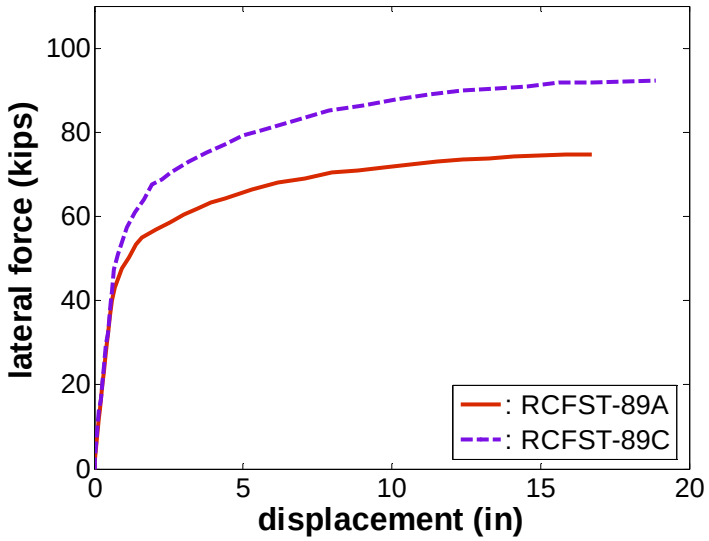

Figure 2.5. Initial member response prediction for RCFST-89A and RCFST-89C

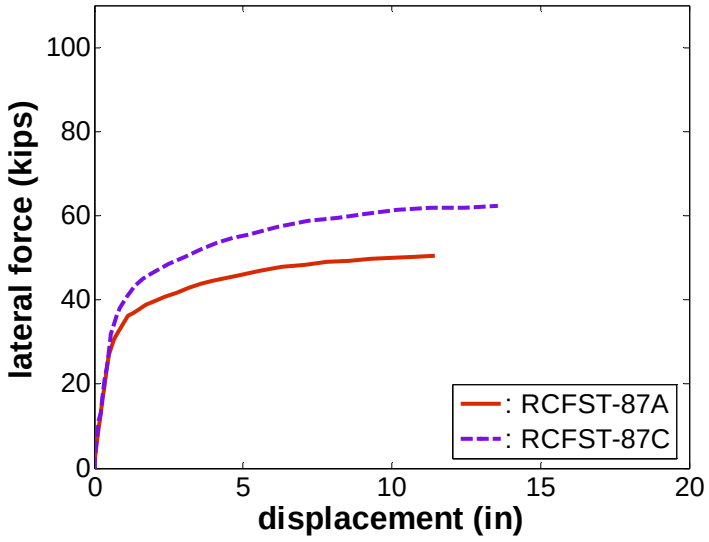

Figure 2.6. Initial member response prediction for RCFST-87A and RCFST-87C

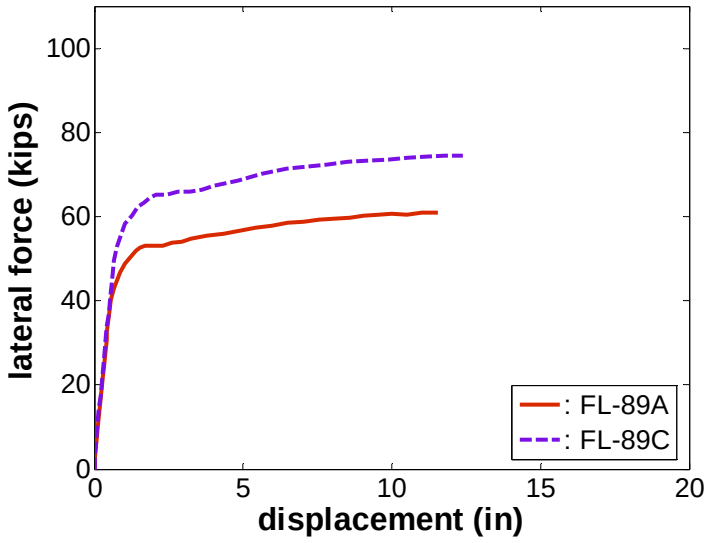

Figure 2.7. Initial member response prediction for FL-89A and FL-89C

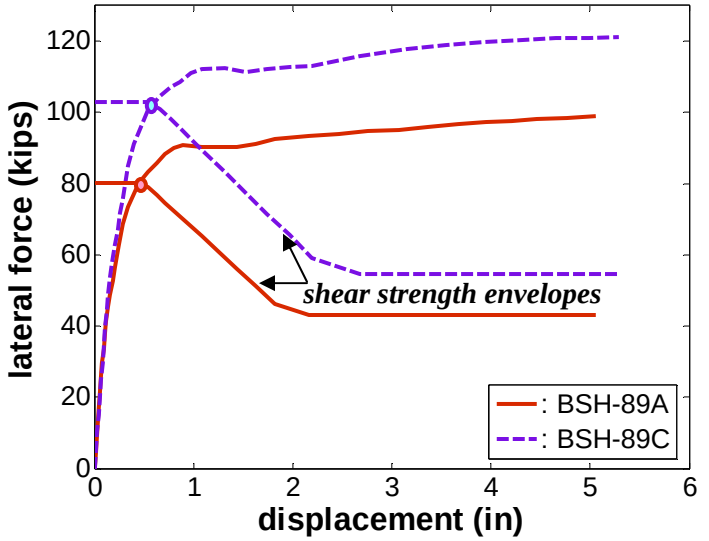

Figure 2.8. Initial member response prediction for BSH-89A and BSH-89C

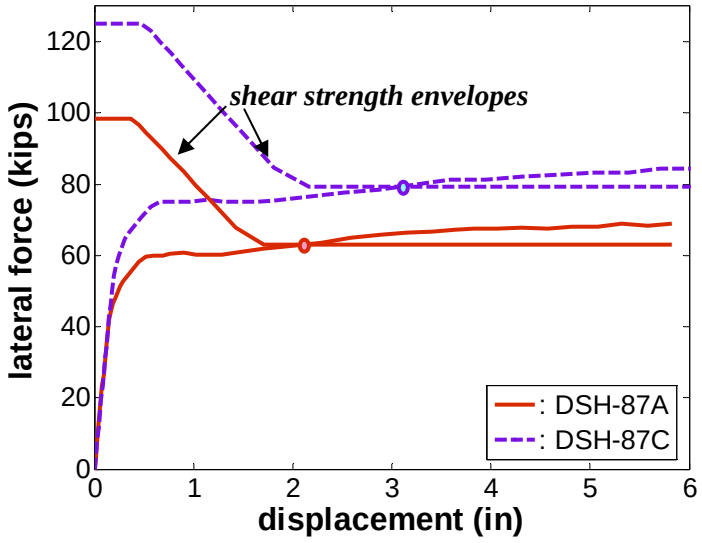

Figure 2.9. Initial member response prediction for DSH-87A and DSH-87C

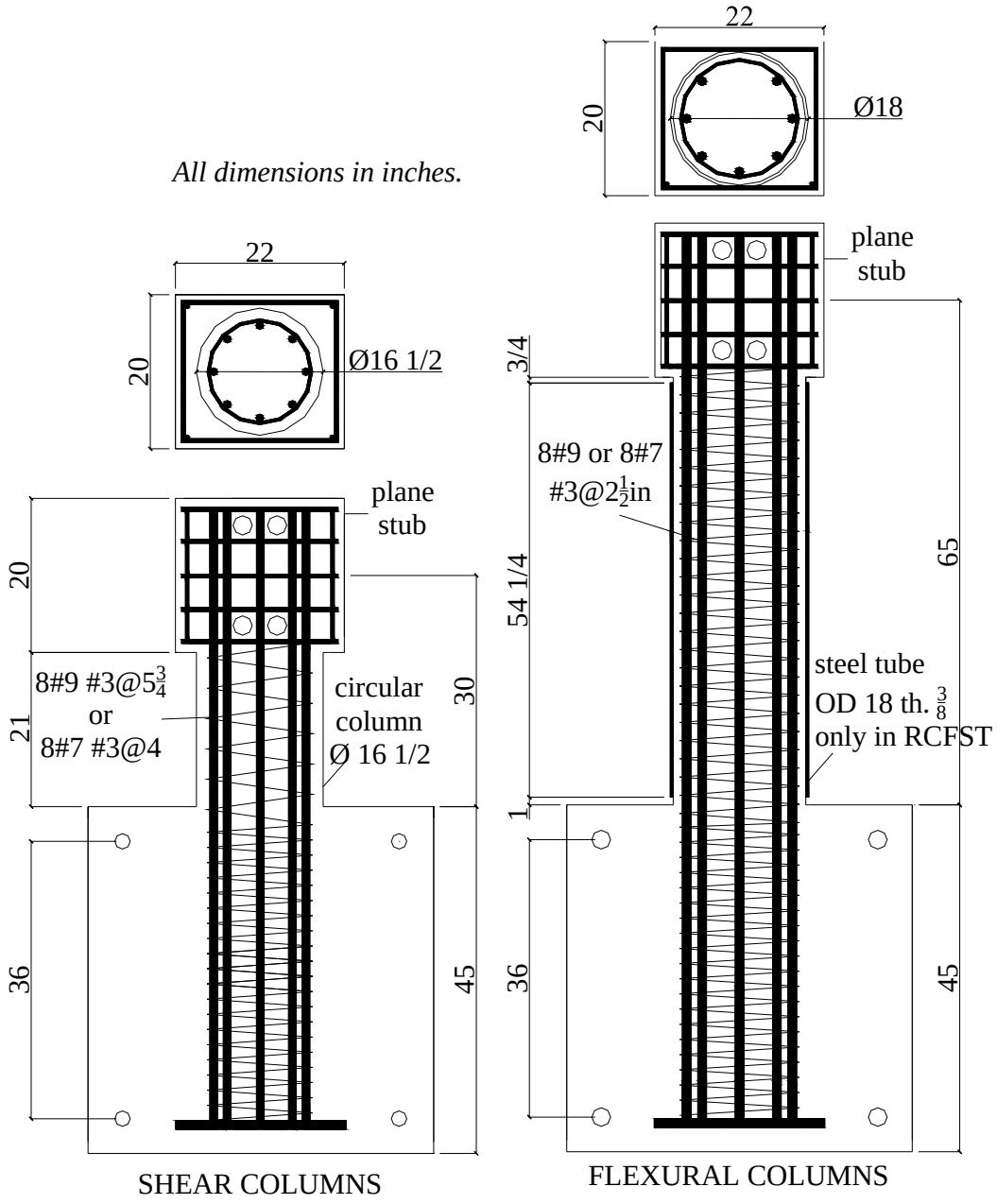

Figure 2.10. Geometric properties and reinforcement details of the specimens (footing reinforcement is omitted for the seek of clarity)

2.4 Footing design

The primary limitations in the design of the footing are (1) The environmental chamber, and (2) The distribution of holes in the strong floor. As a result the dimensions of the footing are relatively small and a large amount of steel was required to support the

large shear stresses developed. Inside the footing were four PVC tubes that allowed for the post-tensioning of the specimen to the strong floor. The tubes were two inches (50.8 mm) in diameter and were spaced in 36 inches by 36 inches (914 mm) on center, which matched the pattern of holes in the strong floor. The footing reinforcement consisted of 8#8 bars in the bottom and 8#8 bars in the top running parallel to the column reinforcement in the form of "c" facing each other, running perpendicular to the column reinforcement were 8#6 bar in the top and 8#6 bars in the bottom also in a "c" shape facing each other. Additional shear reinforcement included 4#5 bars in each side of the footing forming an "x" between them. The footing design is displayed in Figure 2.11.

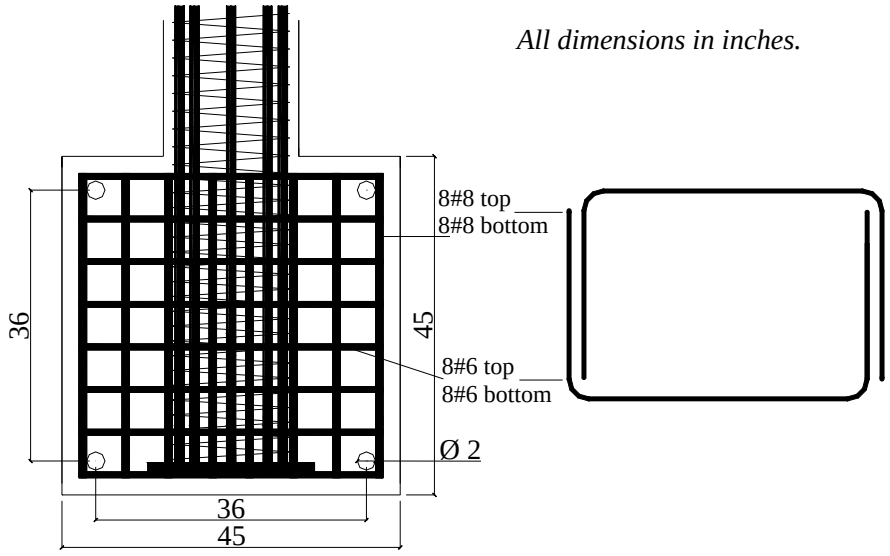

Figure 2.11. Geometric properties and reinforcement details of the footing

2.5 Construction process

The steel cages were tied trying to match as close as possible the specified design presented in Figures 2.10 and 2.11. For that reason, wood fixtures were fabricated in order to obtain the desired circular shape of the columns, as shown in Figure 2.12. After tying the column, the footing cage was tied, taking into account that the column reinforcement continues all the way down the footing, as shown in Figure 2.13.

After the steel cages were completely tied, strain gages were placed in the longitudinal and transverse reinforcement, as shown in Figure 2.14. The distribution of strain gages is discussed in Chapter III.

Figure 2.12. Tying of the circular columns

Figure 2.13. Footing steel cage

Figure 2.14. Strain gages on longitudinal and transverse reinforcement

The next step in the construction process is the casting of the concrete; this was performed in two stages. First, the footing was cast ensuring in this process the verticality of the column cage. Figure 2.15 shows 2 of the “steel tubed” specimens just after pouring of the footing concrete, PVC pipes were used to create the space for the prestressing bars to anchor the specimen to the floor.

After curing of the footings, the specimens are taking inside the lab where the column and load stub parts were cast. In the case of the “steel tubed” specimens, the steel tube was used as a form. Wood fixtures were fabricated to create the 1” and ¾” gaps between the steel tube and the footing and load stub, respectively (Figure 2.16). *Sonotube* was used to obtain the circular shape of the columns in the other specimens (Figures 2.17 and 2.18). Before pouring the concrete, three thermocouples wires were placed in each specimen in order to monitor the internal temperature when testing.

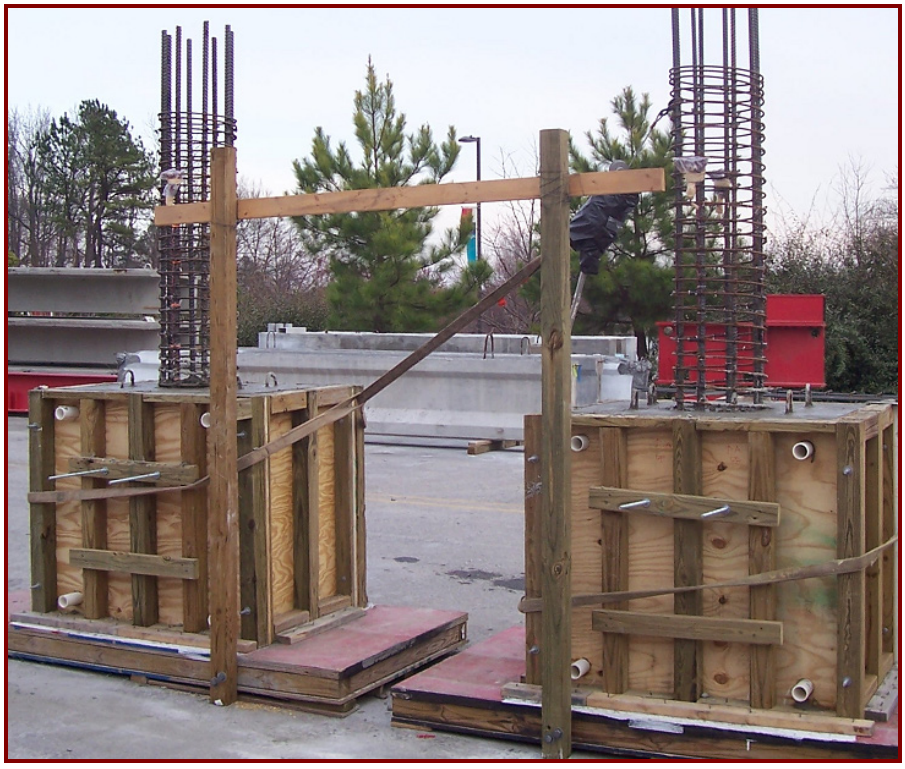

Figure 2.15. Casting of footings

Figure 2.16. Casting of the RCFST columns

Figure 2.17. Casting of the flexural columns

Figure 2.18. Casting of the shear columns

2.6 Material testing

2.6.1 Concrete cylinders

Several concrete cylinders (4” by 8”) were cast for each batch of concrete. The cylinders were tested at different ages and temperature conditions, Tables 2.4 to 2.6 present the results obtained. The average concrete strength is obtained from the tests of three cylinders. In the cold tests the temperature was monitored through a thermocouple wire imbedded in the concrete cylinder. Concrete cylinders were cooled in the environmental chamber together with its respective column, and then tested outside after being exposed to ~26 hours of freezing temperatures. Nonetheless, temperature in the cylinders increased quickly when taken out of the chamber. Since cylinders were tested an average of 8℃ (12℉) above the average temperature of the concrete in the column test, the value of compressive concrete strength to be used in the theoretical predictions needs to be adjusted by linear extrapolation as described in section 1.2.1. Table 2.4 to 2.6 also show the values of *f’c* used for the predictions.

Table 2.4 Average concrete strength for the RCFST columns

BATCH: RCFST COLUMNS		
Days after casting	Average strength / STDEV (psi)	Temperature
7	3465 / 70	Ambient (~74˚F/ 23˚C)
14	3585 / 230	Ambient (~74˚F/ 23˚C)
21	3510 / 205	Ambient (~74˚F/ 23˚C)
28	3595 / 230	Ambient (~74˚F/ 23˚C)
133 (RCFST-89A test day)	3750 / 165	Ambient (~74˚F/ 23˚C)
313 (RCFST-87A test day)	3855 / 150	Ambient (~74˚F/ 23˚C)
240 (RCFST-87C test day)	6000 / 175	-22˚F/ -30˚C
300 (RCFST-89C test day)	6045 / 170	-22˚F/ -30˚C
Warm test prediction	3800 (26.2MPa)	Ambient (~74˚F/ 23˚C)
Cold test prediction	6400 (44MPa)	-32˚F/ -36˚C

*STDEV: Standard deviation

Table 2.5 Average concrete strength for the flexural columns

BATCH: FLEXURAL COLUMNS		
Days after casting	Average strength / STDEV (psi)	Temperature
7	2750 / 130	Ambient (~74˚F/ 23˚C)
14	3090 / 105	Ambient (~74˚F/ 23˚C)
21	3140 / 75	Ambient (~74˚F/ 23˚C)
28	3145 / 70	Ambient (~74˚F/ 23˚C)
120 (FL-89A test day)	3145 / 70	Ambient (~74˚F/ 23˚C)
200 (FL-89C test day)	3800 / 110	-18˚F/ -28˚C
Warm test prediction	3100 (21.4MPa)	Ambient (~74˚F/ 23˚C)
Cold test prediction	4000 (27.6MPa)	-32˚F/ -36˚C

*STDEV: Standard deviation

Table 2.6 Average concrete strength for the shear columns

BATCH: SHEAR COLUMNS		
Days after casting	Average strength / STDEV (psi)	Temperature
7	2965 / 275	Ambient (~74˚F/ 23˚C)
14	3960 / 190	Ambient (~74˚F/ 23˚C)
21	4000 / 355	Ambient (~74˚F/ 23˚C)
28	4045 / 295	Ambient (~74˚F/ 23˚C)
250 (DSH-87A test day)	3985 / 60	Ambient (~74˚F/ 23˚C)
265 (BSH-89A test day)	4000 / 60	Ambient (~74˚F/ 23˚C)
274 (DSH-87C test day)	4845 / 20	-15˚F/ -26˚C
286 (DSH-89C test day)	5040 / 100	-15˚F/ -26˚C
287 (DSH-89C warm test)	3990 / 120	Ambient (~74˚F/ 23˚C)
Warm test prediction	4000 (27.6MPa)	Ambient (~74˚F/ 23˚C)
Cold test prediction	5400 (37.2MPa)	-32˚F/ -36˚C

*STDEV: Standard deviation

2.6.2 Reinforcing bars

Tension tests were performed on the longitudinal and transverse steel at room temperature. Figure 2.19 shows the results obtained for the longitudinal bars. While ASTM A706 steel was ordered for the research program, it was discovered much later that the steel was ASTM A615. As a result, even though both sizes of bars used (#7 and #9) were marked to be of the same type (ASTM A615), the stress-strain behavior is quit different. Fortunately, the steel still meets most of ACI 318 and ASTM requirements for seismic applications: (1) Yield strength should not exceed the specified yield strength by more than 124 MPa (18 ksi), i.e. for grade 60 steel the yield strength should not exceed 537 MPa (78 ksi). It is seen that this requirement is satisfied by the #7 bars, but not by the #9 bars which exhibited a yield strength (558 MPa / 81 ksi) slightly larger than the specified limit. (2) The tensile-yield ratio should not be less than 1.25, this requirement is fulfilled by the #7 and #9 bars with tensile-yield ratios of 1.26 and 1.44, respectively. And (3) the elongation at rupture of the monotonic tensile test should be at least 0.1. Elongation at rupture can not be properly measured during the tensile tests because of the

necking effect, however the required minimum elongation was reached by both size of bars before the onset of necking. Figure 2.20 shows the results obtained for the ASTM A706 spirals, note that there is no defined yield plateau for the spirals as they have been previously deformed past the onset of strain hardening in the bending process. Therefore, for analysis purposes a value of $f_y = f_u/1.4$ is used for the yield stress of the spirals. Finally, Table 2.7 shows the key properties obtained during the tests and the estimated values for cold temperatures based on the results obtained by other authors (section 1.2.2). Other values used for the steel model (Raynor et al. 2002) are: #9 bars: $\varepsilon_{sh} = 0.008$, $\varepsilon_{sm} = 0.10$, $E_y = 700 kips/in/in$ and $C1 = 3.3$, and for the #7 bars: $\varepsilon_{sh} = 0.009$, $\varepsilon_{sm} = 0.13$, $E_y = 350 kips/in/in$ and $C1 = 2.8$. The results obtained from the material tests were used to improve the analytical force-displacement predictions which are presented in Chapters IV to VI along with the experimental results.

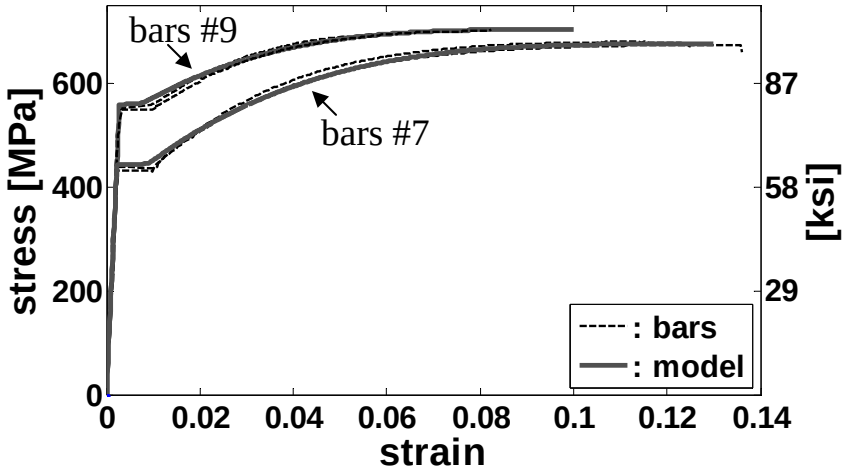

Figure 2.19. Stress-strain curves for the longitudinal bars

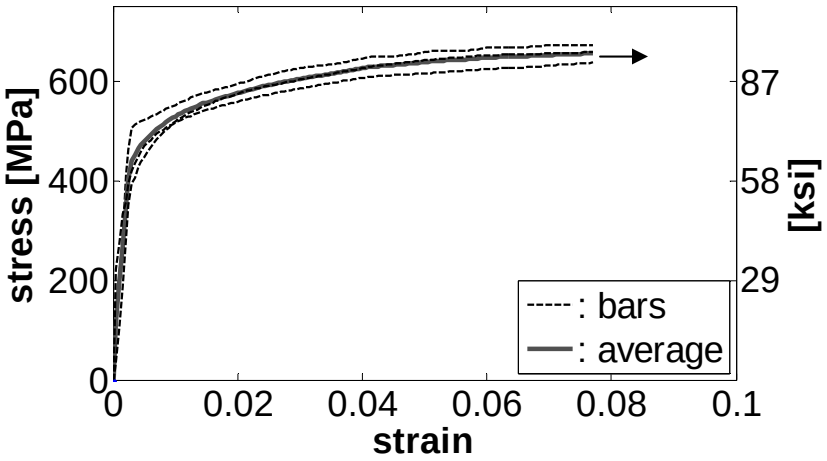

Figure 2.20. Stress-strain curves for the spirals

Table 2.7 Average reinforcement steel strength

	MEASURED AT ROOM TEMPERATURE		ESTIMATED FOR -37˚F/-38˚C	
Description	Yield strength	Ultimate strength	Yield strength	Ultimate strength
Long. Bars #9	558MPa (81ksi)	703MPa (102ksi)	627MPa (91ksi)	778MPa (113ksi)
Long. Bars #7	442MPa (64ksi)	675MPa (98ksi)	490Mpa (71ksi)	741MPa (108ksi)
Spirals	469MPa (68ksi)	655MPa (95ksi)	524MPa (76ksi)	723Mpa (105ksi)

CHAPTER III

TEST SETUP AND INSTRUMENTATION

3.1 Introduction

The test set up was designed to allow the application to the column of increasing cyclic reversal of lateral loads and a constant axial load while inside an environmental chamber that permits the control of the temperature during the test. The main components of the test are displayed in Figure 3.1. The four most important aspects of the test set up were the environmental chamber, the footing support and the application of the lateral and axial load.

3.2 The environmental chamber

In order to reach and maintain the desired low temperatures during the tests, the specimens were tested inside an environmental chamber. The environmental chamber, manufactured by Thermotron, is a model WP-1512-CHM-25-25 with a temperature range of –68˚C (–90˚F) to 85˚C (185˚F) and having dimensions of 7.4m (291in) long, 2m (82in) tall, and 2m (82in) wide. The dimensions of the chamber made it necessary to test in a horizontal position, as displayed in Figure 3.1. In the floor and roof of the chamber are a series of 6” diameter holes spaced every 3’ allowing for the anchorage of the specimen to the strong floor and for an actuator extension to enter the chamber from above. The hole used to test the large specimens was enlarged to 12” in diameter in a past research to allow for rotation of the actuator extension. In the case of the short columns the corresponding hole in the roof of the environmental chamber was enlarged to 9x9 in. Figure 3.2 shows the environmental chamber from outside, as well as the steel frame and the 110 kips (490kN) actuator used for the tests.

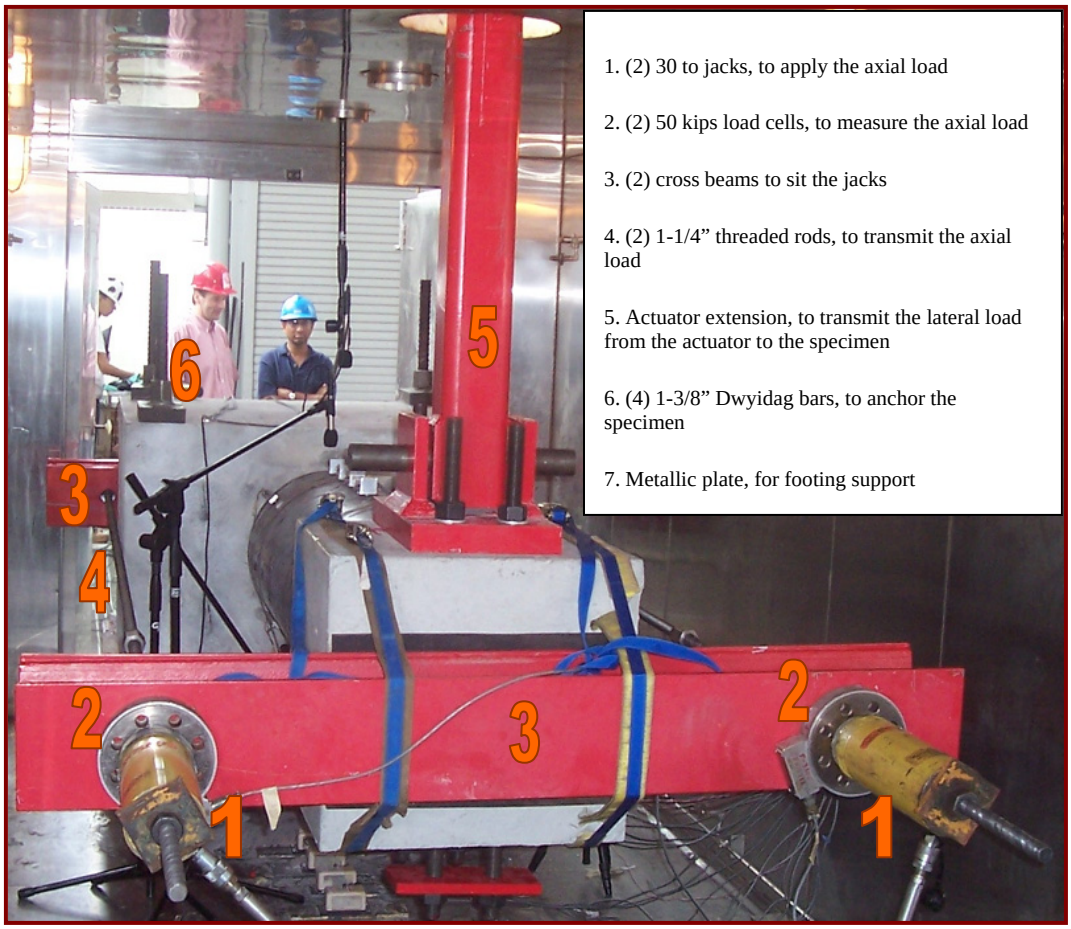

Figure 3.1. Test setup

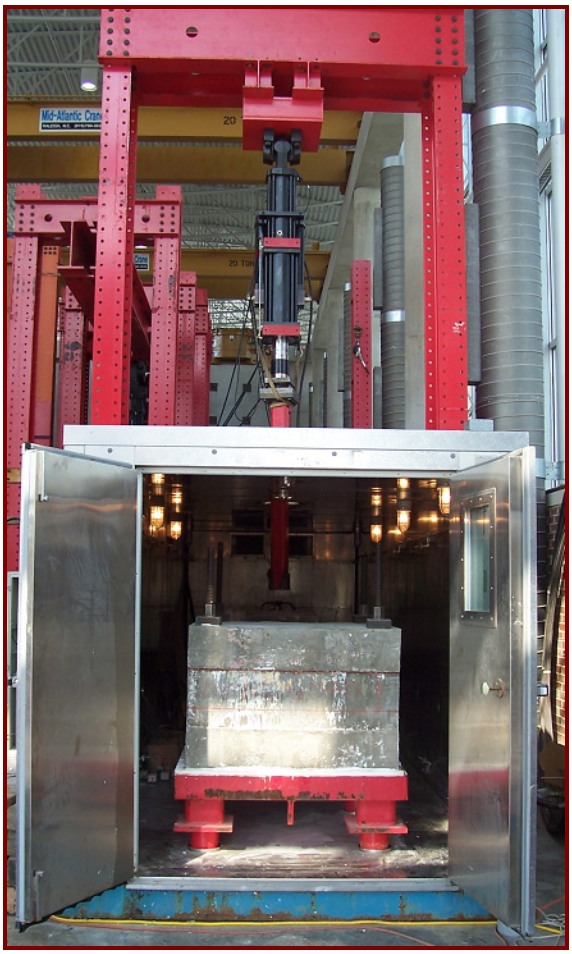

Figure 3.2. Environmental chamber, steel frame and actuator

3.3 Footing support setup

The footing of the column rested on a steel base plate that had 4 squat legs, since the footing face was not perfectly plane, the gap between the footing and the plate was filled with hydro-stone to guarantee a uniform distribution of the reaction forces at the supports, as shown in Figure 3.3. The legs of the base plate then rested on 4 steel tube sections that extended through the floor of the environmental chamber all the way down to the strong floor of the lab. Four Dywidag post-tensioning bars with a diameter of 1-3/8 inches were placed through the footing and the strong floor in order to anchor the specimen, each bar was postensioned to approximately 90 kips (400kN).

3.4 Application of the lateral load

As mentioned before due to the size of the environmental chamber the columns were tested in a horizontal position. The cyclic lateral load was applied using an actuator with a capacity of 110 kips (490kN). The actuator was vertically connected to a steel frame which was anchored to the strong floor, as shown in Figure 3.2. Due to the fact that the actuator could not properly operate at low temperatures inside the chamber, an actuator extension was fabricated to transmit the load to the column. The actuator extension was designed to support the full capacity of the actuator (110 kips in tension and compression) applied in a quasi-static mode. The extensions consist of three major parts (Figure 3.4): (1) a "*connection piece*" with a threaded rod in one side that can be screwed into the actuator, (2) a "*tube*" with a plate welded in one end with holes that match the connection piece and allows the tube to be bolted to the connection piece and (3) a metallic "*chair*" with slotted holes that match the holes in the loading stub of the column and is connected to the tube through a 2" pin. Four D1-1/4" threaded rods were used to fix the column to the actuator extension.

Figure 3.3. Foooting support setup

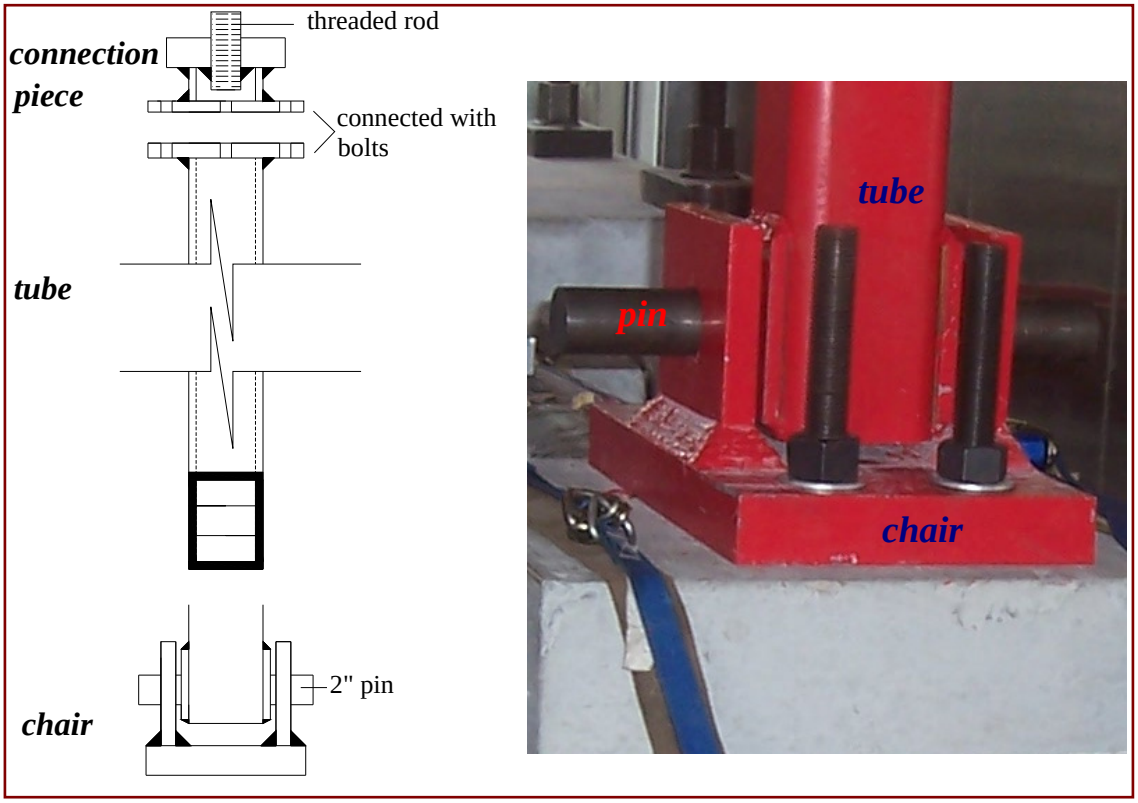

Figure 3.4. Actuator extension

3.5 Application of the axial load

The axial load was applied through 2 cross beams located one behind the footing and the other on top of the column (Figure 3.1). A neoprene bearing pad was placed between the steel beam and the top of the column to uniformly distribute the load. Two 1-1/4 inches diameter threaded rods were running parallel to the column and connecting the two cross beams. Two 30 ton capacity jacks were used to apply the axial load through the bars while two 50 kips (220kN) load cells were used to measure and control the level of axial load being applied. Both jacks were connected in parallel to a single pump in order to distribute the pressure uniformly in both sides of the column. A constant pressure valve maintained constant axial load during testing to within ±10% of the applied load.

3.6 Instrumentation

The sign convention to label the instrumentation was adopted in accordance with the direction of the lateral load. From the center of the column cross section, the “up” and “down” directions correspond to the pulling and pushing action of the actuator, respectively. The “left” and “right” directions are defined looking from the top of the column to the footing. To identify the location of the instruments in the horizontal direction, along the longitudinal axis of the column, they were labeled with their distance in inches from the base of the column. In general terms, the instrumentation used during the test consisted of thermocouples, string potentiometers, linear potentiometers, strain gauges and load cells.

3.6.1 Thermocouples

Three thermocouple wires were cast inside of each column in order to control the temperature in the specimen. The thermocouples were placed at the base of the column, one of them in the center of the cross section (*thcore*) and the other two in the main longitudinal bars (*threbar 1 and 2*), as shown in Figure 3.5.

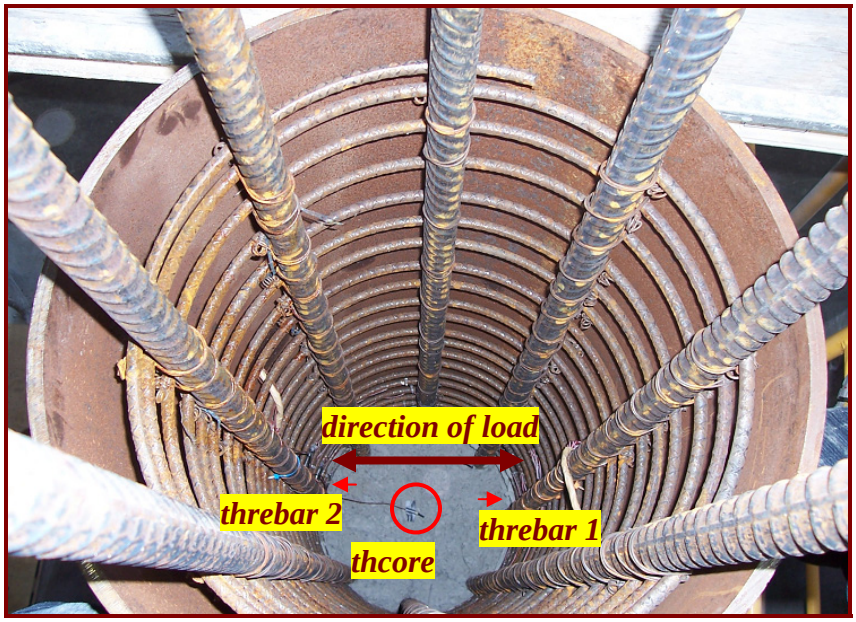

Figure 3.5. Thermocouples distribution

3.6.2 String potentiometers

String potentiometers ranging from 10 to 50 inches in length were mainly used to measure the displacement profile of the column. They were extended using a leader, and then attached to the specimen by an aluminum angle that was glued to the surface of the column. An average of 7 and 5 string potentiometers distributed along the column were used in the flexural and shear specimens, respectively. Two of them were placed at the top of the column. One was placed at the column centerline, and the other was offset horizontally by 8in. The offset potentiometer is used as a backup as well as an indicator of the top stub column-axis torsional rotation. The string potentiometers were labeled with the letters SP and a number in ascending order from the base of the column. The specific distribution is presented for each specimen in Chapters 4, 5 an 6. Figure 3.6 shows the placement and distribution of the string potentiometers in a long column.

With the information obtained from the string potentiometers displacement profiles of the column at different load and deformation stages can be generated. Also, the displacements measured by the string potentiometers in the top of the column along with the force applied by the actuator are used to generate the hysteretic force-displacement response of the column.

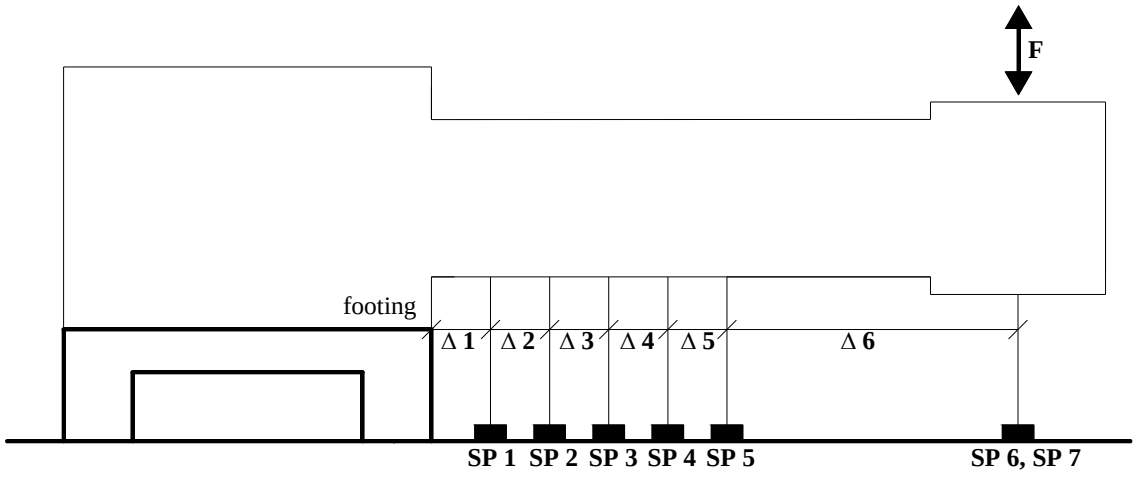

Figure 3.6. String potentiometers distribution

3.6.3 Linear potentiometers

Linear potentiometers (LPOTS) are used to measure displacement over a specified length. Depending on their placement configuration, the information obtained from the linear potentiometers are use to calculate average curvatures and flexural deformations or shear deformations. The potentiometers were screwed onto 1/4 inch threaded studs that were glued into the column with epoxy, and the landing point for each potentiometer was a small aluminum angle that was also attached to the threaded stud. Figure 3.7 and 3.8 show the linear potentiometers set up for the flexural and shear members, respectively.

3.6.3.1 Obtaining curvature and flexural deformation from Linear Potentiometers

Average rotation and curvatures in the $cell_i$ (Figure 3.7) are calculated using Equations 3.1 and 3.2, respectively.

$$\theta_i = \frac{XPU_i - XPD_i}{D_i} \tag{3.1}$$

$$\phi_i = \frac{\theta_i}{G_i} = \frac{XPU_i - XPD_i}{G_i D_i} \tag{3.2}$$

where XPU_i and XPD_i are the readings from the linear potentiometers in the top and bottom of the column at the level i. D_i is the vertical distance between the two transducers and G_i is the horizontal gauge length for the LPOTS in the $cell_i$. Once the average curvatures and rotations are calculated, the moment area method can be utilized to calculate the flexural displacement the top of the column. It should be noticed from Figure 3.7 that in the case of the large columns additional potentiometers PB1, PB2, PB3 and PB4 are placed in the base of the column, the information obtained from that potentiometers (together with the data from PU1 and PD1) are used to calculate the curvature in the base of the column.

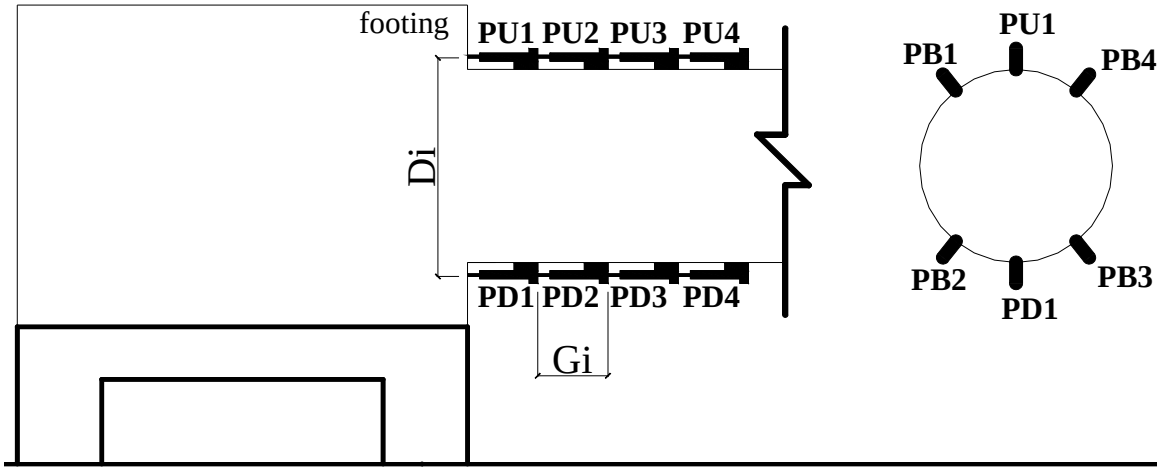

Figure 3.7. Linear potentiometers set up to measure flexural deflection

3.6.3.2 Obtaining shear deformation from LPOT data

Shear deformation was only measured in the short columns. Figure 3.8 shows the LPOT's configuration used to measure the shear induced deformations. The procedure used for obtaining shear deformation as well as vertical and horizontal extension from the LPOT's data is discussed in Kowalsky, Priestley and Seible (1995). This procedure is briefly described next.

The average change in longitudinal is calculated for cell *i* using equation 3.3, where XPU_i and XPD_i are the readings of the linear potentiometers in top and bottom of the column at the level *i*.

$$FL_i = \frac{XPU_i - XPD_i}{2} \tag{3.3}$$

The diagonal component of this deformation is then calculated using Equation 3.4 where λ is the angle the diagonal makes with the vertical LPOT.

$$\delta FL_i = FL_i \sin(\lambda) \tag{3.4}$$

Equations 3.5 and 3.6 are used to calculate the change in transverse displacement for the left, EXL_i, and right face, EXR_i, respectively, where $XPTL_i$ and $XPTR_i$ are the readings of the transverse LPOT's. The diagonal component of this deformation is calculated with Equation 3.7, where EX_i is the average of the values obtained for both faces of the column.

$$EXL_i = \frac{XPTL_i - XPTL_{i+1}}{2} \tag{3.5}$$

$$EXR_i = \frac{XPTR_i - XPTR_{i+1}}{2} \tag{3.6}$$

$$\delta EX_i = EX_i \cos(\lambda) \tag{3.7}$$

The diagonal displacement due only to shear deformation (δSi) will then be the displacement measured by the diagonal LPOT's (δMSi) minus the deformations found from Equations 3.4 and 3.7 as shown in Equation 3.8

$$\delta S_i = \delta MS_i - \delta FL_i - \delta EX_i \tag{3.8}$$

Shear induced displacement in each cell is calculated with Equation 3.9 and the overall shear displacement is the summation of the displacements on each cell, Equation 3.10.

$$\Delta S_i = \frac{\delta S_i}{\cos(\lambda)} \tag{3.9}$$

$$\Delta S = \sum_i \Delta S_i \tag{3.10}$$

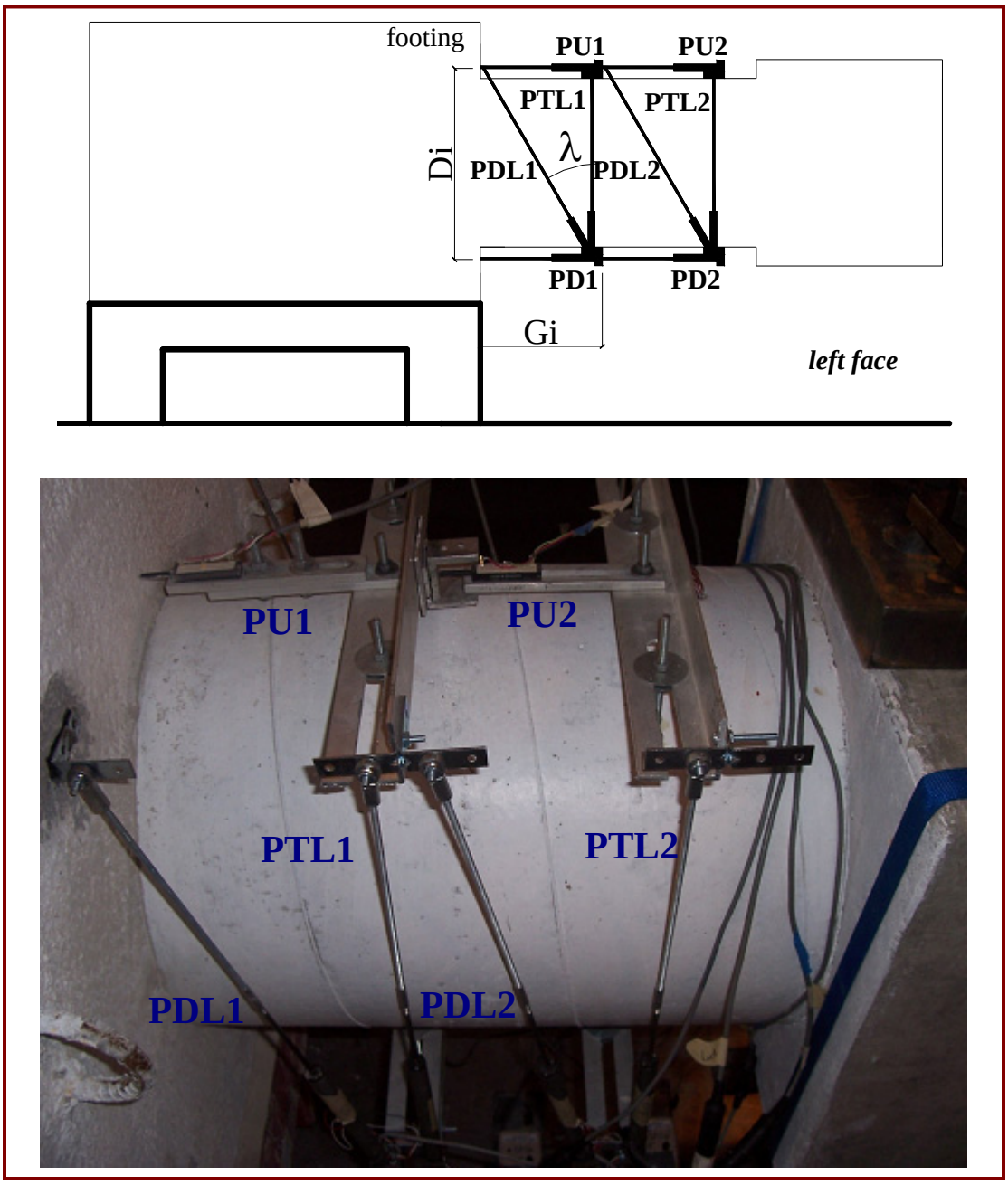

Figure 3.8. Linear potentiometers set up to measure shear deflection

3.6.4 Strain gages

Strain gages were used to measure strain in the longitudinal and transverse steel. Each specimen was instrumented with twenty-four strain gauges; half of them were placed on the spiral to measure shear and confinement strain profiles and the other half on the longitudinal reinforcement to obtain longitudinal strain profiles. The strain gauges

were labeled according to the type of bar they were placed on (longitudinal or transverse), the location with respect to the longitudinal axis of the column (up, down, left or right) and their relative position to the base of the column. For instance, SgTU-2 denotes a strain gage that was placed in the transverse steel in the "up" direction and is the second from the base of the column. Figure 3.9 shows the strain gages distribution. In addition to the twenty-four internal strain gages, the "steel tubed" specimens were instrumented with an additional twelve strain gages with the same distribution as in the transverse reinforcement to measure shear and confinement strain in the steel tube.

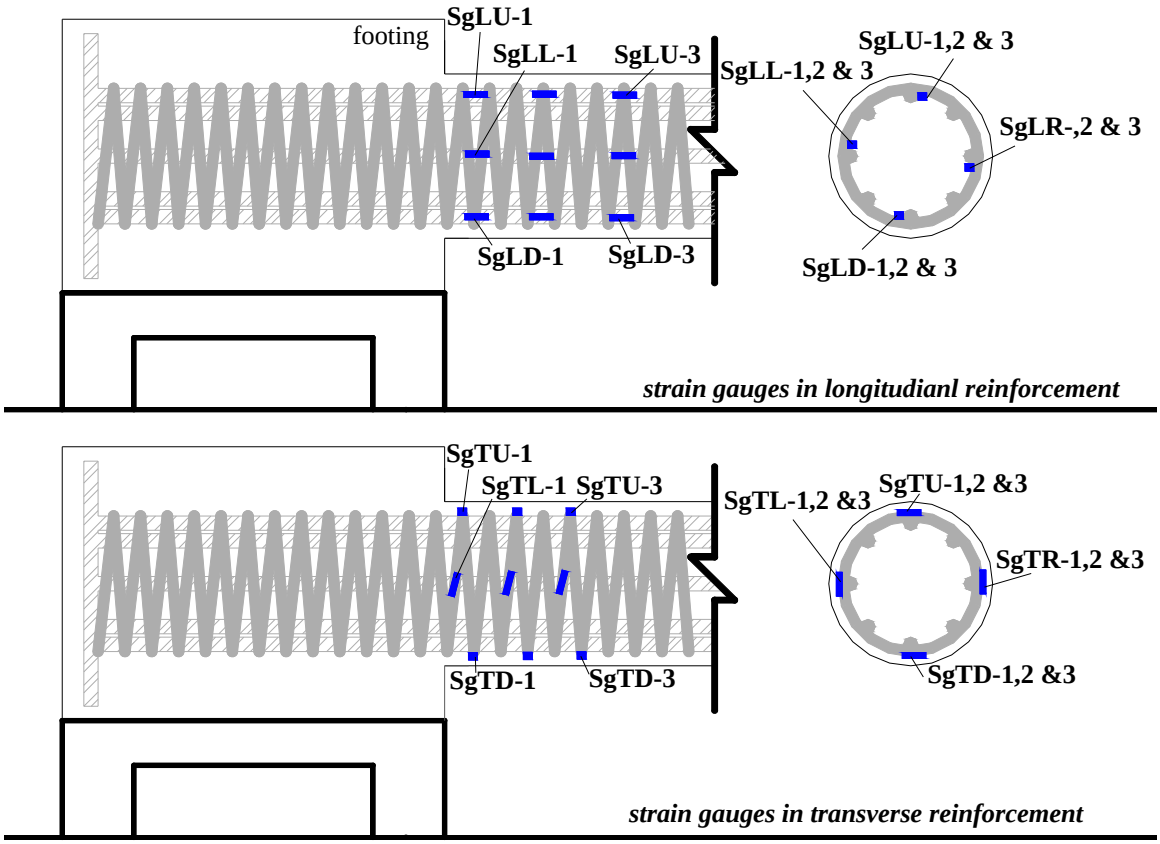

Figure 3.9 Strain gauges distribution

3.7 Testing procedure

The columns were tested quasi-statically. The procedure consisted of pushing and pulling the specimen in force control until first yield of the longitudinal reinforcement, and subsequently cycling in displacement control to prescribed ductility levels. A typical

loading pattern is shown Figure 3.9. The lateral force at first yield $F_y^{'}$ of the longitudinal reinforcement and the lateral ideal force F_i were found from a section analysis. The lateral ideal force is defined as the force at which the cover concrete reaches a compression strain of 0.004 or the longitudinal steel a tension strain of 0.015. The displacement corresponding to first yield $\Delta_y^{'}$ is obtained from the reading of the string potentiometer in the top of the column and the equivalent yield displacement Δ_y is obtained by extrapolation to the ideal lateral forces as in Equation 3.11. Therefore, the displacements corresponding to the prescribed ductility levels are not determined until the column reaches first yield.

$$\Delta_y = \Delta_y^{'} \frac{F_i}{F_y^{'}} \tag{3.11}$$

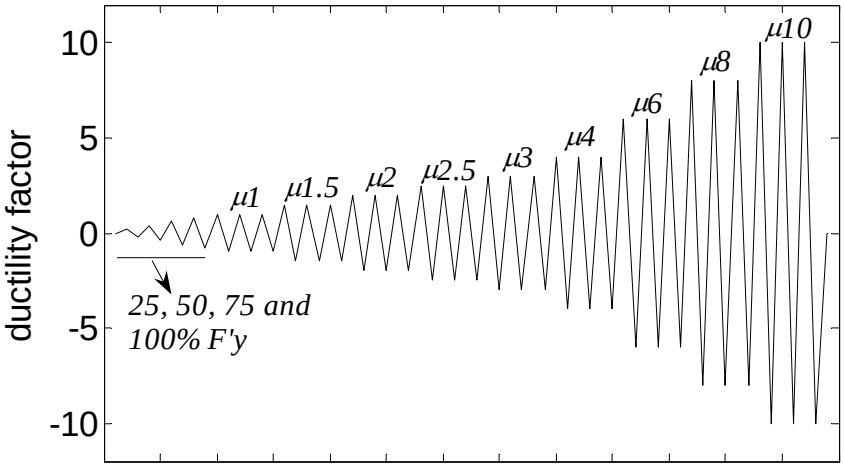

Figure 3.10 Load protocol

CHAPTER IV

SEISMIC BEHAVIOR OF FLEXURAL DOMINATED REINFORCED CONCRETE COLUMNS AT LOW TEMPERATURES

4.1 Introduction

In order to determine the effect of cold temperatures on the flexural behavior of reinforced concrete columns, two flexurally dominated columns were designed, built and tested. Both specimens were identical, one column was tested under ambient temperatures (23˚C, 74˚F) and the companion at cold temperatures (-40˚C, -40˚F). The information obtained by Sloan (2005) in a pilot study where four identical columns were tested at different temperatures is re-analyzed. This chapter presents the results obtained for all six flexural dominated reinforced concrete columns and compares it with the theoretical predictions obtained using the available analytical models. Finally, corrections to the available analytical models to predict the response of flexural dominated reinforced concrete members are introduced and discussed.

4.2 Lightly reinforced members without axial load

In a first attempt to estimate the effect of cold temperatures on the seismic behavior of reinforced concrete members, Sloan (2005) tested four identical columns at temperatures ranging from -40˚C (-40˚F) to 20˚C (68˚F). The columns were lightly reinforced (longitudinal steel ratio ~ 1%) and were tested without any axial load. The columns were tested following a load protocol of cyclic reversals similar to the one described in section 3.7, in

the displacement control regimen the columns were subjected to displacement ductilities of 1, 1.5, 2, 3, 4, 5, 6 and 8, the actual applied load protocol is presented in Figures 4.1 and 4.2. The test set up was similar to that presented in Chapter III and is displayed in Figure 4.3. Table 4.1 presents the test specimen matrix and Table 4.2 the results of the material tests. From the four specimens presented in Table 4.1 the results of three are discussed here, SL-3 is omitted because due to a malfunction in the environmental chamber it was not possible to keep the temperature constant during the test.

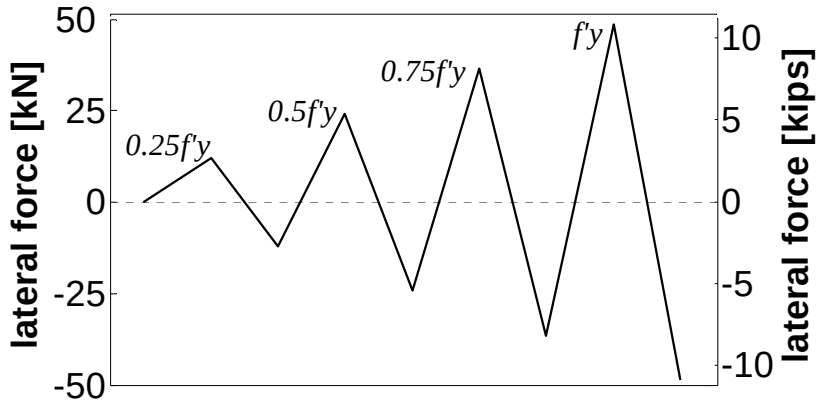

Figure 4.1 JS specimens load protocol: load control phase

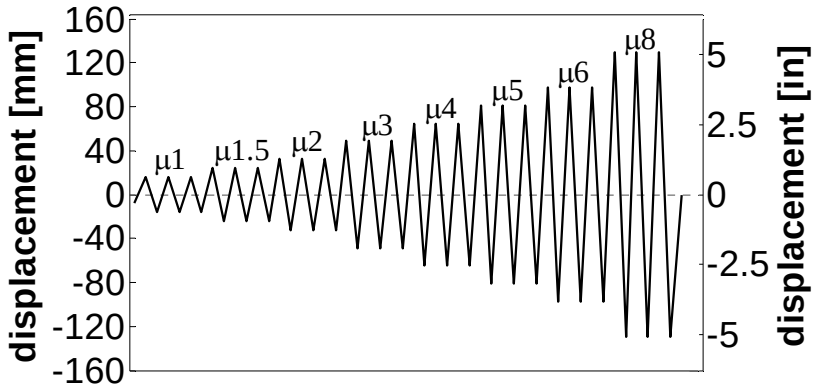

Figure 4.2 JS specimens load protocol: displacement control phase

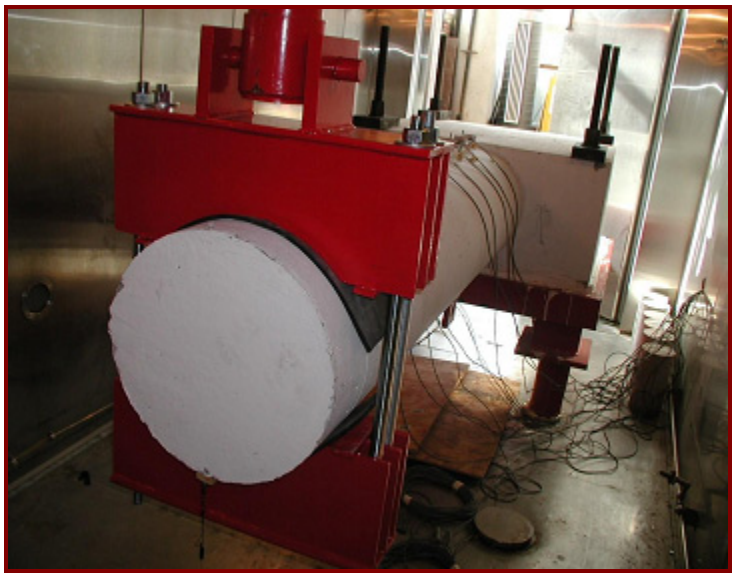

Figure 4.3 Sloan specimens set up

Table 4.1 Sloan test specimen matrix

UNIT	TEMP.	BEHAVIOR	DIMENSIONS	LONG. STEEL/ RATIO	TRANSVERSE STEEL/RATIO
SL-P20	74˚F/ 23˚C	Flexural	D. 457mm (18in) L. 1651mm (65in)	8#5 1.0%	#3@63.5mm (2.5in) 1.1%
SL-M20	-4˚F/ -20˚C	Flexural	D. 457mm (18in) L. 1651mm (65in)	8#5 1.0%	#3@63.5mm (2.5in) 1.1%
SL-M30	-22˚F/ -30˚C	Flexural	D. 457mm (18in) L. 1651mm (65in)	8#5 1.0%	#3@63.5mm (2.5in) 1.1%
SL-M40	-40˚F/ -40˚C	Flexural	D. 457mm (18in) L. 1651mm (65in)	8#5 1.0%	#3@63.5mm (2.5in) 1.1%

Table 4.2. Material properties values used for the response predictions

TEMP.	CONCRETE STRENGTH (f'_c)	STRAIN AT MAX. STRESS (ε_{co})	YIELDING STRESS (f_y) [LONG. BARS]	ULTIMATE STRESS (f_u) [LONG. BARS]	YIELDING STRESS (f_{yh}) [SPIRALS]
74˚F/ 23˚C	39.2MPa 5.7ksi	2E-3	503MPa 73ksi	689MPa 100ksi	469MPa 68ksi
-22˚F/ 30˚C	44.8MPa 6.5ksi	2.14E-3	538MPa 78ksi	730MPa 106ksi	503MPa 73ksi
-40˚F/ 40˚C	64.8MPa 9.4ksi	2.7e-3	565MPa 82MPa	772MPa 112ksi	531MPa 77ksi

Figures 4.4 to 4.6 show the hysteretic response obtained during the test of specimens SL-P20, SL-M20 and SL-M40, respectively. The predictions obtained with the models described in Chapter II are also presented in these figures. Horizontal dotted lines in those graphs correspond to the theoretical force for first yield and nominal moment. The predictions were obtained using the geometric characteristics and material properties displayed in Tables 4.1 and 4.2, respectively. The equivalent plastic hinge length and strain penetration are calculated with the material's room temperature properties. In general, the three specimens failed by buckling and then rupture of the bottom-most bar due to a combination of high axial strain and low cycle fatigue during the next half cycle in the pull direction of loading.

It should be noticed that when the columns are subjected to equal displacements in the two loading directions, the measured lateral force resistance in the push direction is lower than the measured in the pull direction, providing an unsymmetrical response. This difference is the result of three different phenomena:

- The steel cages in some of the columns may have been slightly off center.

- When testing the columns in a horizontal position the self weight of the column and the actuator chair start acting as an additional load in the push direction that is not being recorded.

- Once the concrete in the bottom face of the column crushes it fails from the column due to its own weight, however when the concrete in the top face of the column crushes it stays there providing some strength to the column when the force is applied in the pulling direction.

- The bottom side of the column footing was resting on a steel base plate while the top side has only the four Dywidag post-tensioning bars in the corners to anchor the specimen, this results in a footing that is stiffer in the bottom than in the top. This increase in stiffness provokes a reduction in the strain penetration in the bottom of the footing, more rotation is then required in the base of the column when pulling to reach a prescribed displacement. Larger rotations place larger strains in the steel and the required lateral force is increased. This hypothesis seems to be corroborated by the curvature profile displayed in Figure 4.12, where it can be noticed that the base curvature when pulling is about 20% larger than the curvature when pushing.

Nonetheless, the difference is minimal and an average of the measured responses in the two directions can be used to represent the response of the column. This approach is used to generate Figures 4.9 to 4.10 which display the first, second and third cycle peak envelopes of the hysteretic response, respectively. Horizontal lines in this figure correspond to the theoretical forces for first yield and nominal moment.

The data obtained from linear potentiometers is used to calculate average curvatures over the gage lengths. Figures 4.11 and 4.12 show the curvatures profiles of the column at the first cycle of ductilities 1 and 4 respectively. Dotted lines in these graphs correspond to the theoretical curvature distribution for first yield.

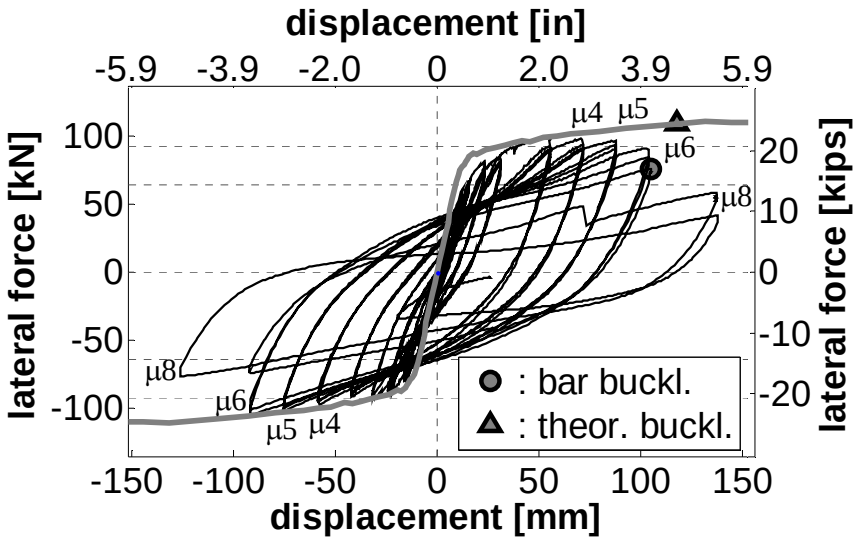

Figure 4.4 Hysteretic response and prediction for SL-P20

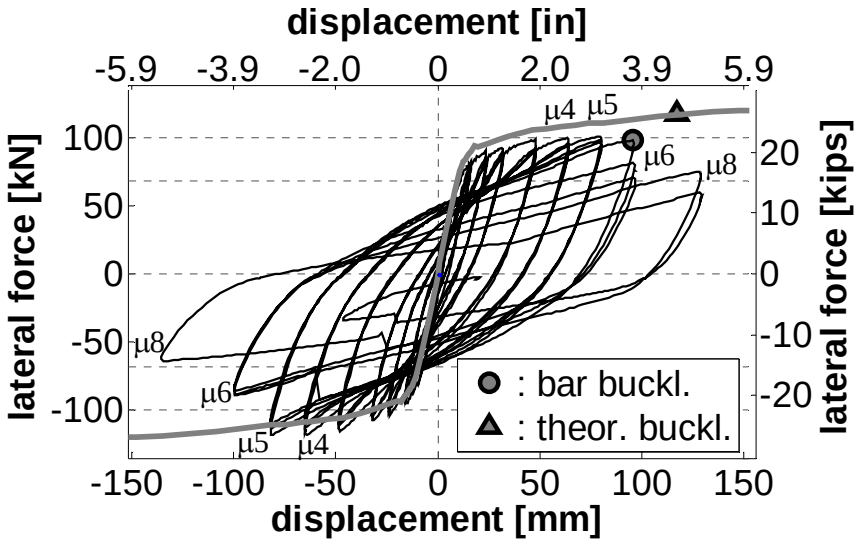

Figure 4.5 Hysteretic response and prediction for SLM20

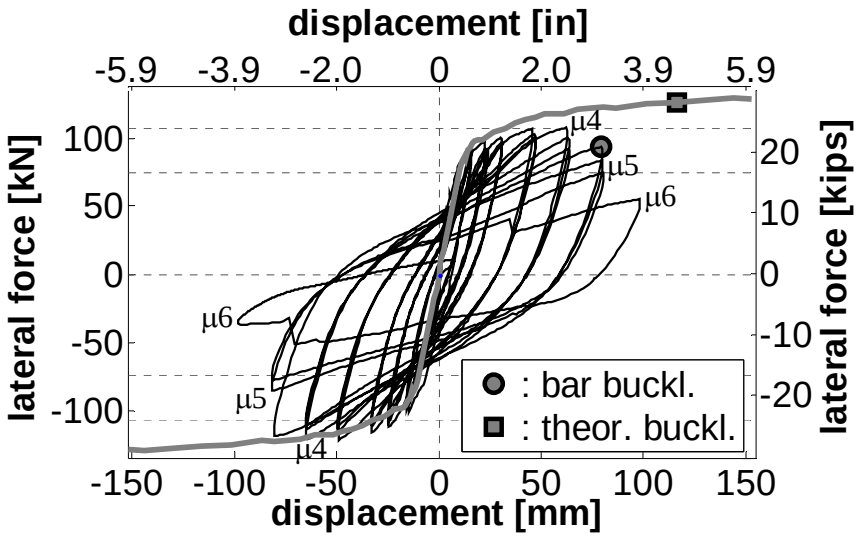

Figure 4.6 Hysteretic response and prediction for SLM40

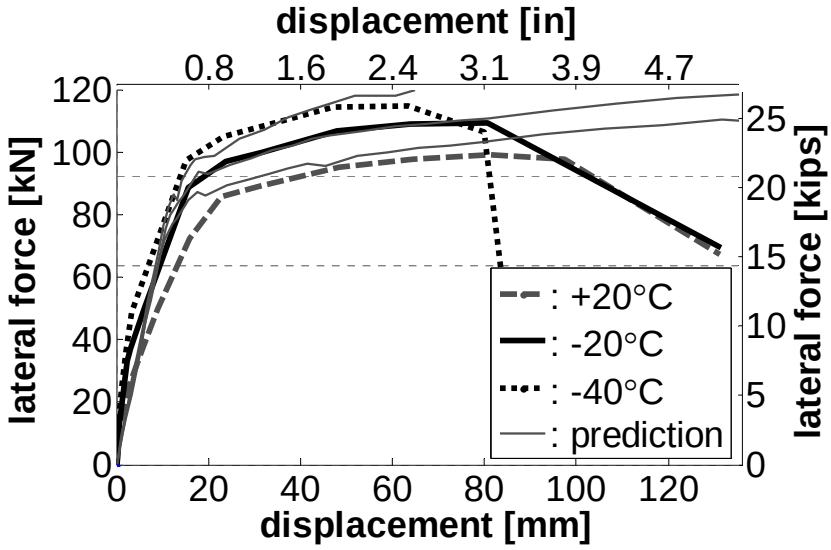

Figure 4.7 First cycle average peak envelope for SLP20, SLM20 and SLM40

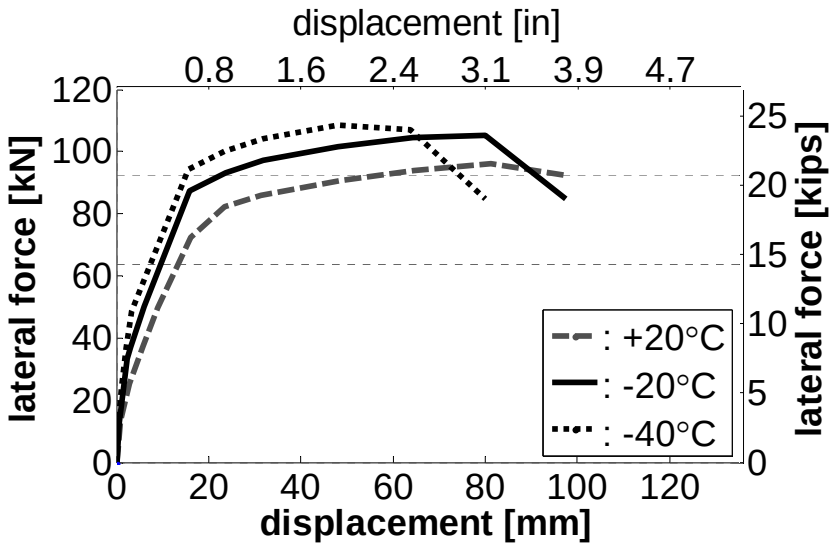

Figure 4.8 Second cycle average peak envelope for SLP20, SLM20 and SLM40

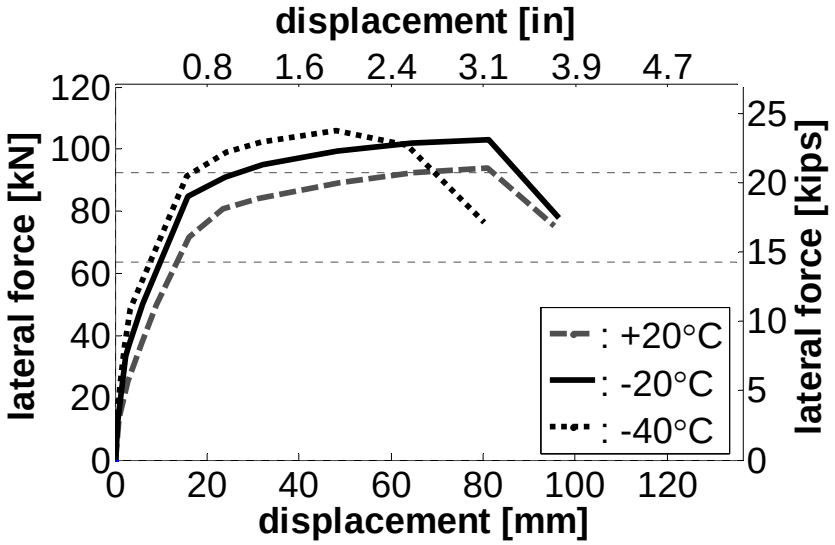

Figure 4.9 Third cycle average peak envelope for SLP20, SLM20 and SLM40

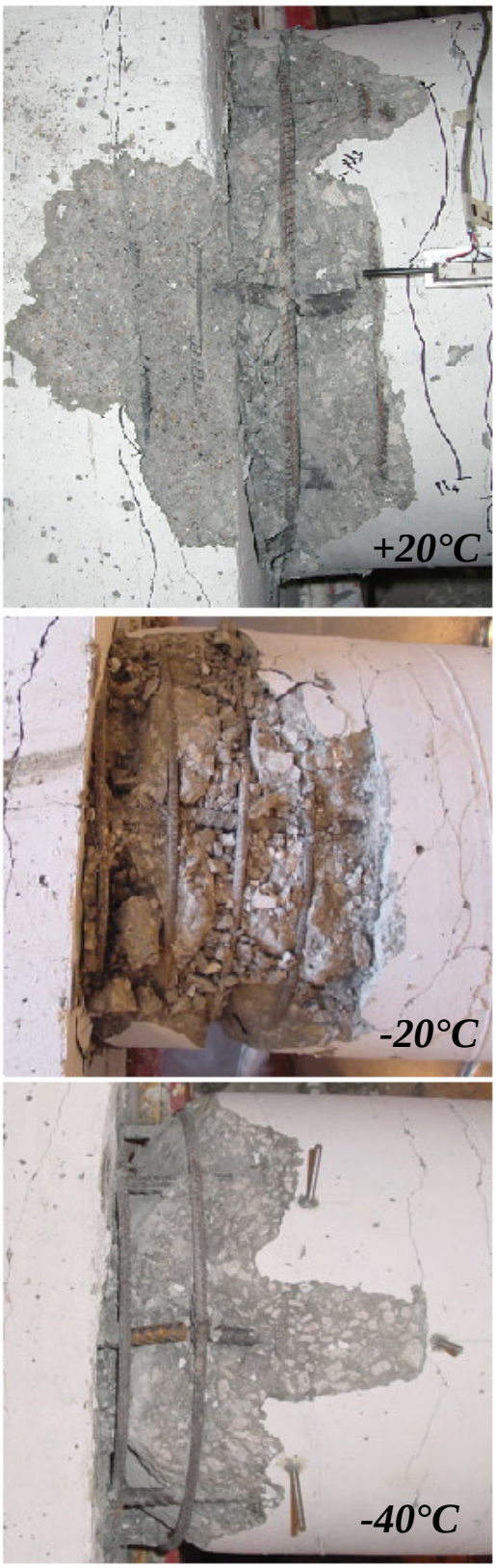

Figure 4.10 Specimens after test

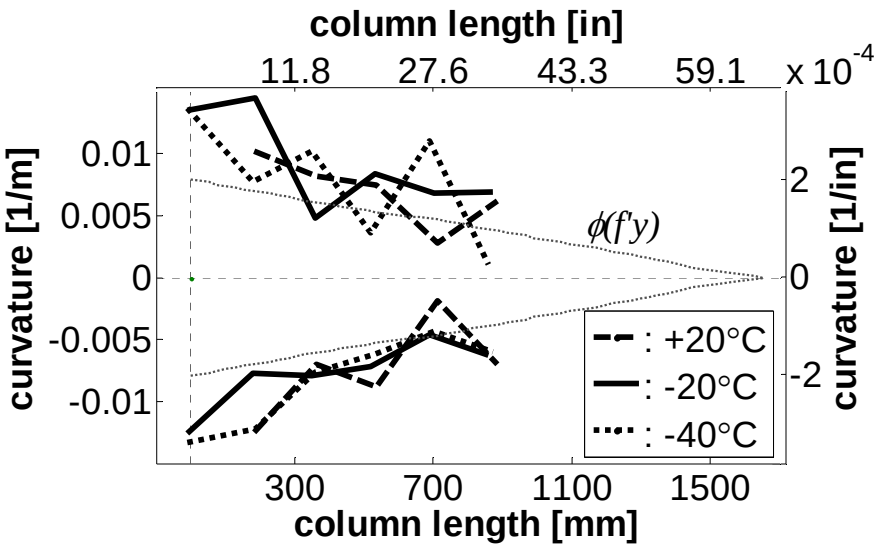

Figure 4.11 Curvature profile for the three specimens at ductility 1.

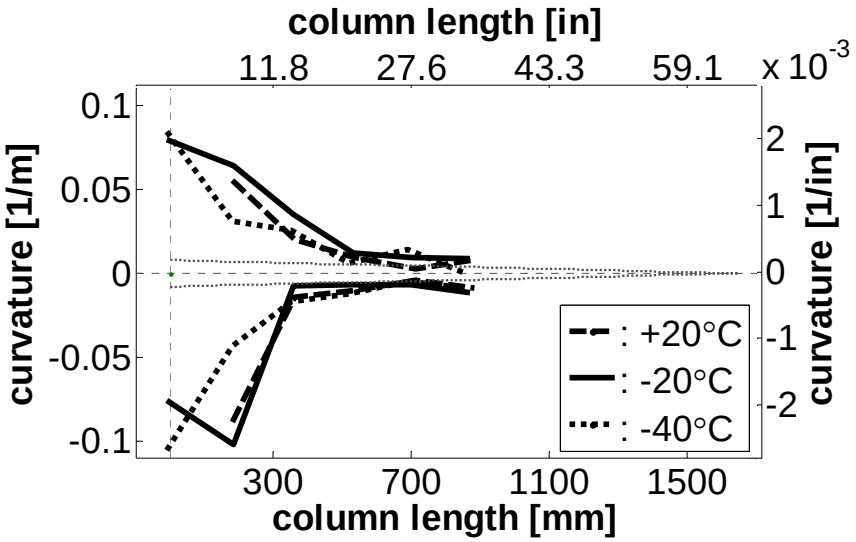

Figure 4.12 Curvature profile for the three specimens at ductility 4.

There are several observations that should be done from the results presented in Figures 4.4 to 4.12:

- The specimen tested at -40˚C developed the largest flexural strength. If the increase in strength is measured by the difference in the lateral force required to reach a target displacement (Table 4.4) before strength degradation starts, the average flexural strength when the temperature is -40˚C is found to be 20% larger

than the exhibited by the room temperature specimen. If we compare the maximum load reached by each specimen, then the increase is 16%.

- Nonetheless, the specimen tested at -40˚C also presents the smallest displacement capacity failing at a displacement ductility of 5, the other two specimens tested at -20˚C and 20˚C failed at a displacement ductility of 6.

- The theoretical models were able to predict the flexural strength and mode of failure of the specimens. Furthermore, the predicted on set of buckling for the specimen tested at 20˚C is very close to the actual point of failure. However, the available models were incapable to predict the effect of the cold temperature in the displacement capacity of the columns.

- The force-deformation responses for the three specimens show hysteretic loops with good damping characteristics. The hysteretic damping was calculated for each cycle using Jacobsen approach (1930) and no variation with temperature was found. For example, for the first cycle of ductility four, the hysteretic damping in the three specimens was 24%.

- The cold specimens exhibit an increase in the initial elastic stiffness of the specimen which is not captured by the prediction models. If the elastic stiffness is defined at the load level required for first yield of the room temperature specimen, then the elastic stiffness of the specimens tested at -40˚C and -20˚C are 270% and 180% larger than the elastic stiffness of the specimen tested at 20˚C, respectively. More often in design, an effective stiffness based upon the idealized yield conditions is required. The effective stiffness of the specimens tested at -40˚C and -20˚C are 35% and 23% larger than the effective stiffness of the specimen tested at 20˚C, respectively.

- From the curvature profile in Figure 4.12 note a significant reduction in the spread of plasticity of the specimen tested at -40˚C when compared with the other two specimens, this phenomenon is also observable in the conditions of the specimens after the test as shown in Figure 4.10. This reduction in the extent of plasticity and

a possible decrease of ductility in the steel caused by the low temperatures and the reversal of loads may explain the earlier bar fracture in the specimen tested at -40˚C. If the plastic hinge is reduced, larger rotations are needed in order to reach a given displacement and larger strains are then induced in the reinforcing bars.

Finally, Tables 4.3 and 4.4 summarize the results obtained during the tests. The initial study performed by Sloan (2005) demonstrated that reinforced concrete undergoes a gradual increase in strength and stiffness coupled with a reduction in displacement capacity as the temperature decreases. Remember that specimens tested by Sloan were flexurally dominated light reinforced concrete members without axial load. The next section will present the results obtained for heavier reinforced members with axial load.

Table 4.3. Summary of results obtained (Load control phase)

Cycle	Target Lat. Force (kN)	Average tip displacement [mm]			
		+20°C	-20°C	-40°C	-40°C / +20°C
0.25fy'	12.6	0.9	0.6	0.3	0.4
0.5fy'	27.7	2.9	2.4	1.1	0.4
0.75fy'	37.0	5.7	3.2	2.0	0.4
fy'	49.6	8.9	6.0	3.3	0.4

Table 4.4. Summary of results obtained (Displacement control phase)

Cycle	Target Displ. (mm)	First cycle average lateral force [kN]			
		+20°C	-20°C	-40°C	-40°C / +20°C
μ1	16	72.2	88.5	97.5	1.3
μ1.5	24	85.7	97.0	104.9	1.2
μ2	33	89.0	99.8	108.3	1.2
μ3	49	95.1	106.9	114.4	1.2
μ4	65	97.7	109.1	114.6	1.2
μ5	81	99.0	109.4	106.5	1.1
μ6	98	97.8	89.7	53.3	0.5
μ8	130	67.3	69.5	-	-

4.3 Heavy reinforced members with axial load

Two identical reinforced conventional circular concrete columns with a longitudinal steel ratio of 3% were designed and built. The columns were detailed to ensure a flexural failure. One of the columns was tested at room temperature while the other one was tested at -40˚C. The columns and its properties are presented in Figure 4.11 and Table 4.5. The temperature values in Table 4.5 are the average of the readings of the three thermocouple wires imbedded in the columns (see section 3.6.1). In the same way the axial load is defined by the average of the readings of the two load cells placed in the cross beams (see Figure 3.1).

Both columns were tested following the same load protocol. Target forces and displacements were obtained from the theoretical prediction using room temperature material properties, as explained in 3.7 the target displacement for ductility one is only obtained once the specimen is subjected to *f'y*. Room temperature specimen FL-89A was tested first and the resulting target displacements were applied to the cold specimen FL-89C for comparison purposes. The applied load protocol is displayed in Figures 4.14 and 4.15.

Table 4.5 Specimen matrix for the conventional heavy reinforced concrete columns

UNIT	TEMP.	DIMENSIONS	LONG. STEEL/ RATIO	TRANSV. STEEL/ RATIO	CONCRETE STRENGTH	AXIAL LOAD/ RATIO
FL-89A	72˚F 22˚C	D. 18 in 458 mm L. 65 in 1651 mm	8#9 3.1%	#3@2.35” 1.2%	3.1 ksi 21.4 MPa	49.4 kips 220 kN 6.2%
FL-89C	-33˚F -36˚C	D. 18 in 458 mm L. 65 in 1651 mm	8#9 3.1%	#3@2.35” 1.2%	4 ksi 27.6 MPa	49 kips 218 MPa 4.8%

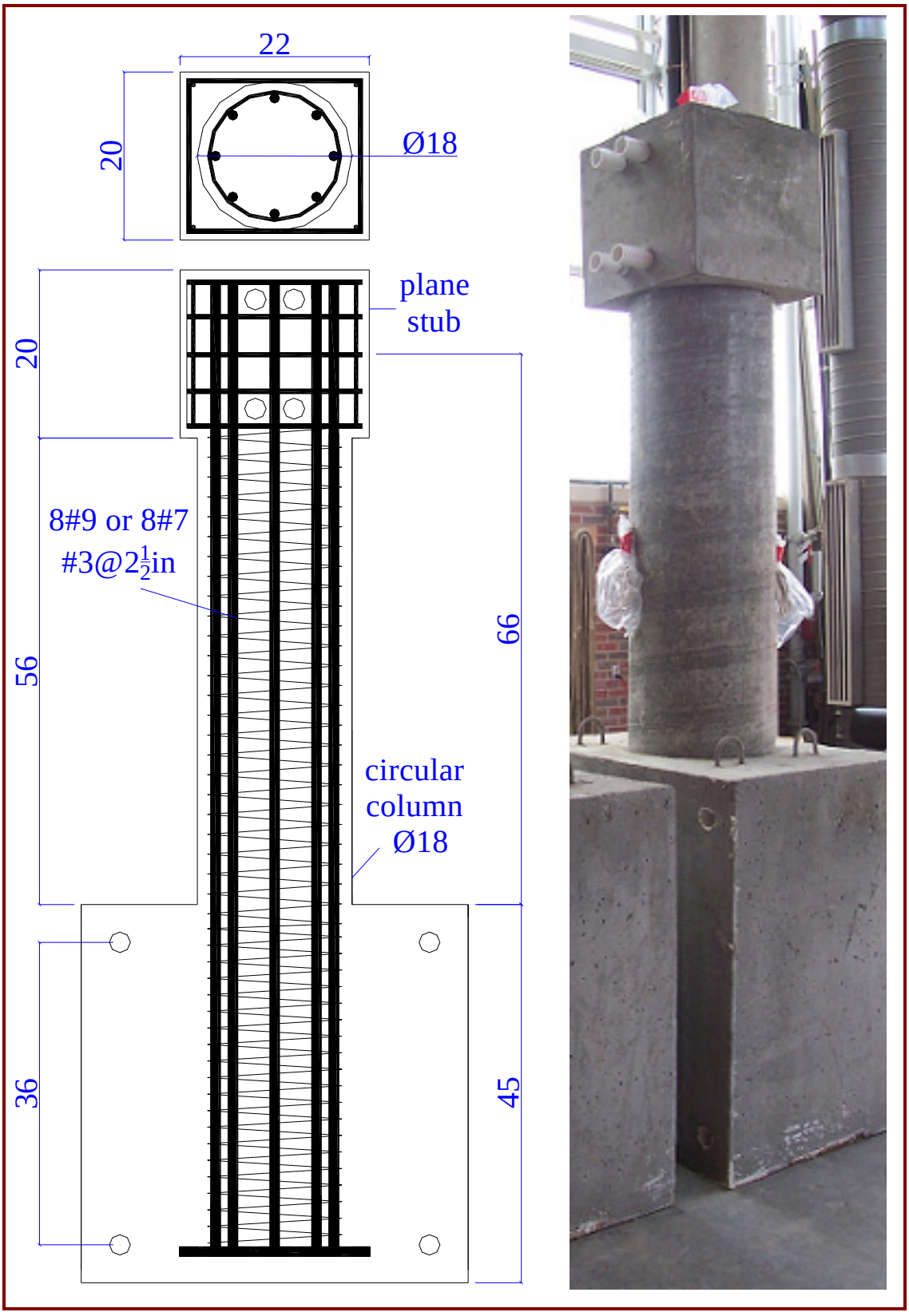

Figure 4.13 Heavy reinforced flexural dominated specimens.

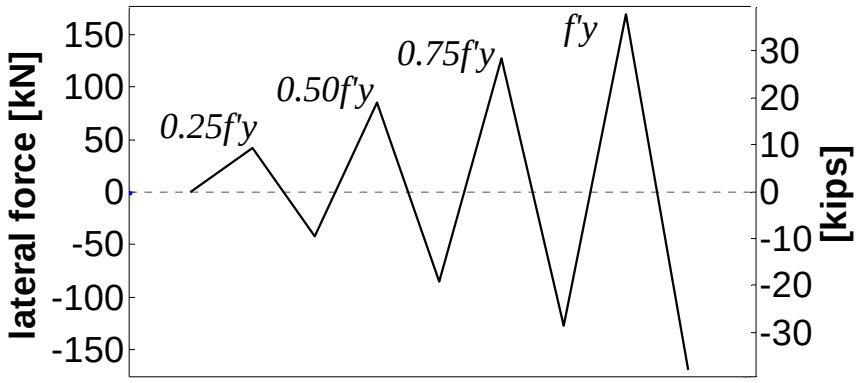

Figure 4.14 Load protocol: load control phase

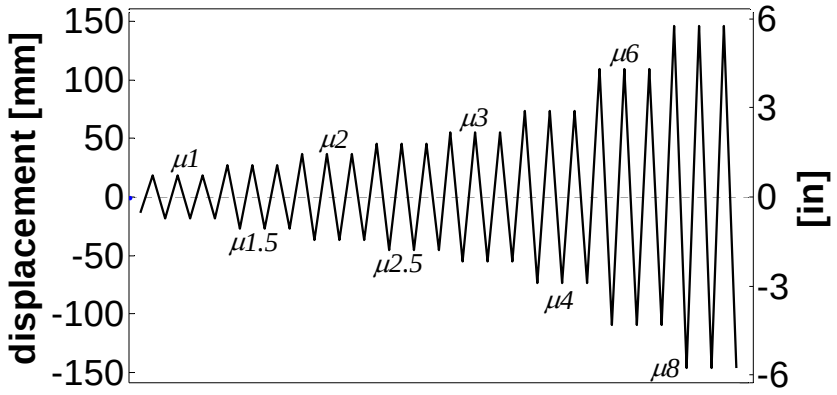

Figure 4.15 Load protocol: displacement control phase

4.3.1 Room temperature specimen FL-89A

Unit FL-89A was tested at room temperature on October 31/2006. Figures 4.14 and 4.15 show the applied load protocol. The loading history in force control consists of one cycle at 9.5, 19, 28.5 and 38 kips. Figure 4.16 shows the temperatures registered by the thermocouples imbedded in the specimen as a function of the column tip displacement. Figure 4.17 displays the variation of axial load during the test. Horizontal lines in this figure denote the average and ±10% average of the applied axial load. Even though the axial load is not completely constant as it tends to increase with the tip displacement, the constant pressure valve installed allows us to keep it with in ±10% of the applied load.

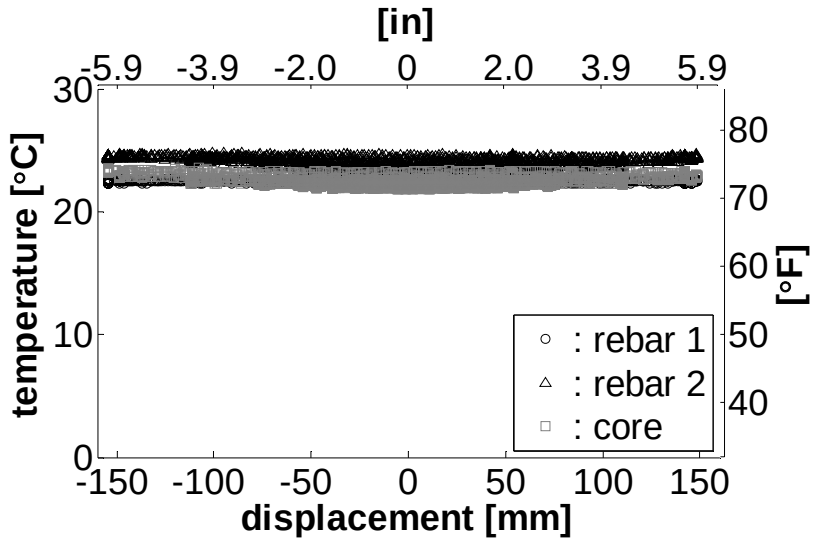

Figure 4.16 Temperature variations during testing of FL-89A.

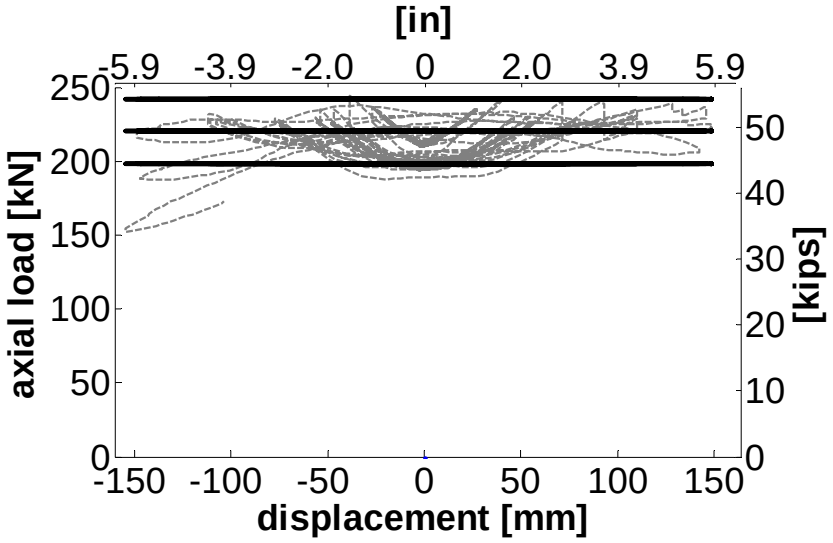

Figure 4.17 Axial load variations during testing of FL-89A.

4.3.1.1 FL-89A Test observations

First hairline cracks were noted at the top and bottom of the specimen after the second cycle of load control (19 kips), the cracks were located between 7 and 19 in from the base of the column and spaced 6 in between them. After the 28.5 kips cycle existing cracks extended in length and new hairline cracks appeared at 25 in from the base. With

the last cycle of load control (38 kips) the existing cracks keep increasing in length and new ones appeared at 31 in from the base, the first crack at the base of the column appear also at this point. Figure 4.18 shows the specimen just before the start of the test. Figure 4.19 is a photo of the specimen after the last cycle of load control loading.

The average displacement corresponding to first yield of the longitudinal reinforcement was 0.56 in that when extrapolated to ductility 1 (using Equation 3.11) gives a displacement of 0.72 in. After the three cycles of ductility 1 the hairline cracks extended over the whole length of the specimen, it was noticed that it takes approximately 8% more force to reach the target displacements in the pulling direction.

After the first cycle of ductility 2 concrete cover crushing was observed and the cracks up to 15 in from the base are now wider. After the final cycle of ductility 2 concrete crushing in the top and bottom are evident accompanied by some minor spalling. Figure 4.20 shows the specimen after the last cycle of ductility 2. With the cycles at ductility 2.5 and 3 the cracks kept becoming wider and the spalling kept increasing. As shown in Figure 4.21 at the final cycle of ductility 3 the spalling in the concrete extended 6 in from the base.

After the ductility 4 cycles the cover concrete is completely lost over the first 7 in from the base and the transverse steel is exposed (Figure 4.22). At the first cycle of ductility 6 crushing of the core concrete started and at the last cycle of this ductility some longitudinal reinforcement was exposed (Figure 4.23).

The first push cycle of ductility 8 saw an increase of 7% in strength over the last push cycle at ductility 6; however the initial maximum force at ductility 6 was not reached. Some spalling of the concrete in the footing was observed in this cycle as it is displayed in Figure 4.24. By the last push of ductility 8 the cover concrete is completely lost and the transverse and longitudinal steel are completely exposed over an area up to 12 in from the base of the column (Figure 4.25). During the last pull cycle of ductility 8 two of the top most bars buckled over the third visible layer of transverse reinforcement (Figure 4.26) at approximately 5 in from the base of the column, the test was finished at this point.

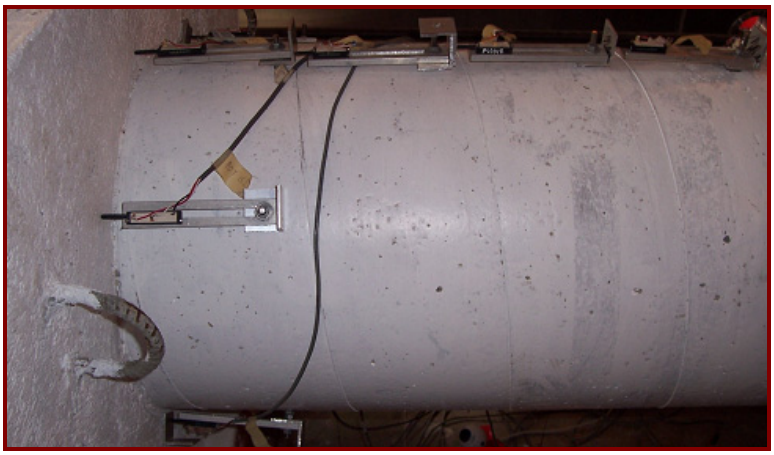

Figure 4.18 Specimen FL-89A before the test.

Figure 4.19 Specimen FL-89A after the last cycle of load control.

Figure 4.20 Specimen FL-89A (bottom) after the last cycle of ductility 2.

Figure 4.21 Specimen FL-89A (top) after the last cycle of ductility 3.

Figure 4.22 Specimen FL-89A (bottom) after the last cycle of ductility 4.

Figure 4.23 Specimen FL-89A (bottom) after the last cycle of ductility 6.

Figure 4.24 Specimen FL-89A (top) after the first cycle of ductility 8.

Figure 4.25 Specimen FL-89A (top) after the final push of ductility 8.

Figure 4.26 Specimen FL-89A (top) after the final pull of ductility 8.

4.3.1.2 FL-89A Force-displacement response

Figure 4.27 shows the measured force-deformation response along with the theoretical prediction. The theoretical envelope was obtained with an equivalent plastic hinge length 59% of the value $Lp = 0.044 f_y d_{bl}$ recommended in Priestley et al. (2007), the following section will explain why and how the new value was obtained. It can be seen from this graph that just as in Sloan's tests the response is not symmetric along the x axis; it is taking about 15% more lateral force to reach a target displacement in the pull direction that in the push direction. Again, an average of the measured responses in the two directions is used to represent the response of the column; the results obtained are displayed in Figure 4.28 along with the theoretical envelopes and the two different Lp values above mentioned. From this figure is seen that the match between the theoretical envelope and the actual member response is improved when Lp is reduced. However, the theoretical models were unable to predict the buckling of the longitudinal bars. Remember that the assessment of reinforcement buckling limit state is determined following two different methodologies, one is the proposed by Moyer and Kowalsky (2003) and the other is the proposed by Berry and Eberhard (2005). The problem seems to be that those models only account for buckling between two consecutive spirals, as in

the case of the Sloan columns. However, in this case buckling occurs over a layer of transverse reinforcement (see Figure 4.26).

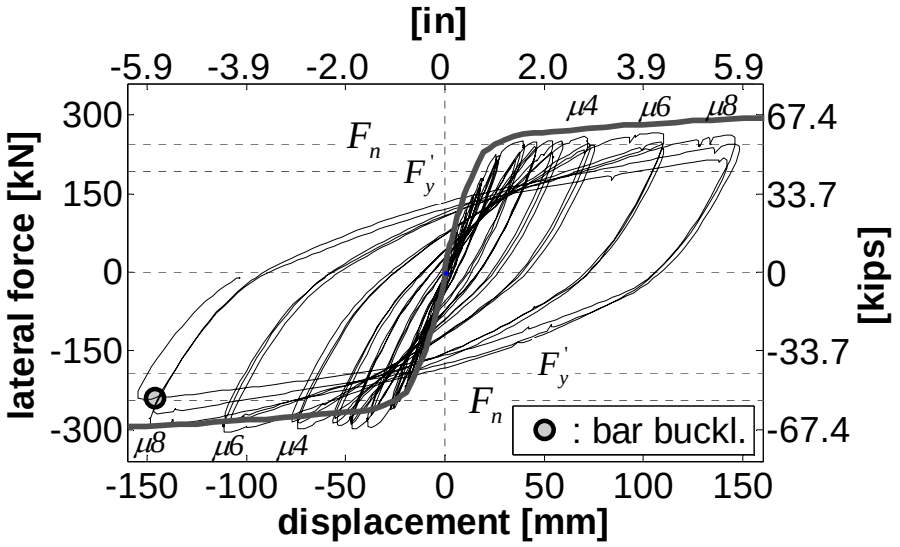

Figure 4.27 Hysteretic response and prediction for FL-89A.

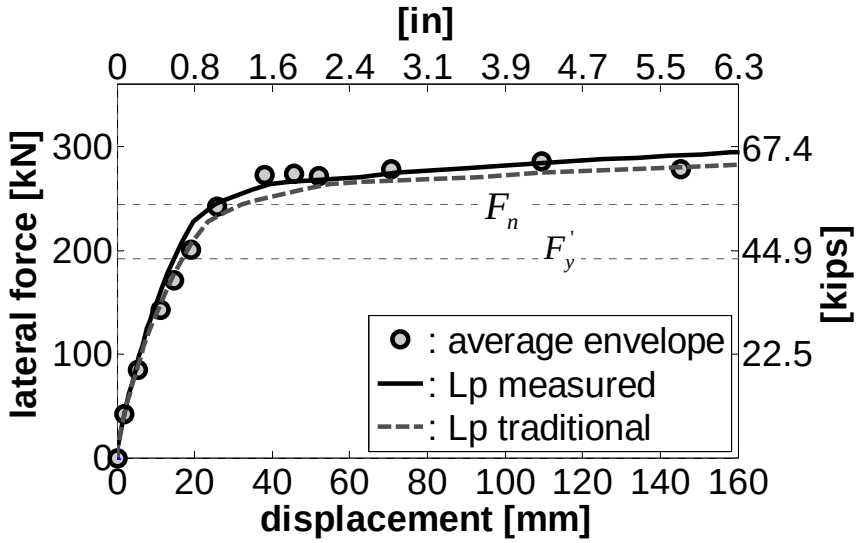

Figure 4.28 First cycle average peak envelop for FL-89A.

4.3.1.3 FL-89A Curvature profiles

Curvature profiles are plotted for four sections of the column. In each section the curvature is reported at the center of the cell and is the average curvature over the cell

height. The gauge length for the bottom cell includes a component due to strain penetration as it can be argued that the rotation evaluated in this cell is distributed into the footing, this will have the effect of reducing the curvature as plotted for the base cell. The magnitude of this addition, obtained by optimization of the match between the experimental and theoretical moment-curvature relation, was found to be 152 mm. Figure 4.29 shows the resulting match for the average first peak values of moment and curvature.

Figure 4.30 shows the curvature profiles at *f'y, μ1, μ2, μ3* and *μ4;* negative curvatures correspond to the pull direction. As in the Sloan specimens, due to the stiffness asymmetry of the footing, the base curvature when pulling is slightly larger than the curvature when pushing. It can be seen that all the plasticity is concentrated in the 2 first cells (approximately 330mm from the base of the column), after this point the column shows negligible curvature.

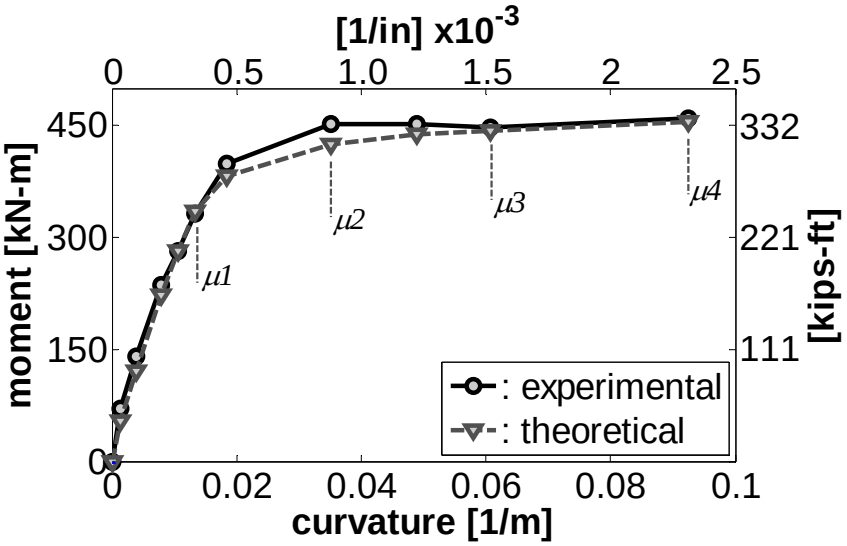

Figure 4.29 FL-89A Moment-curvature at column base.

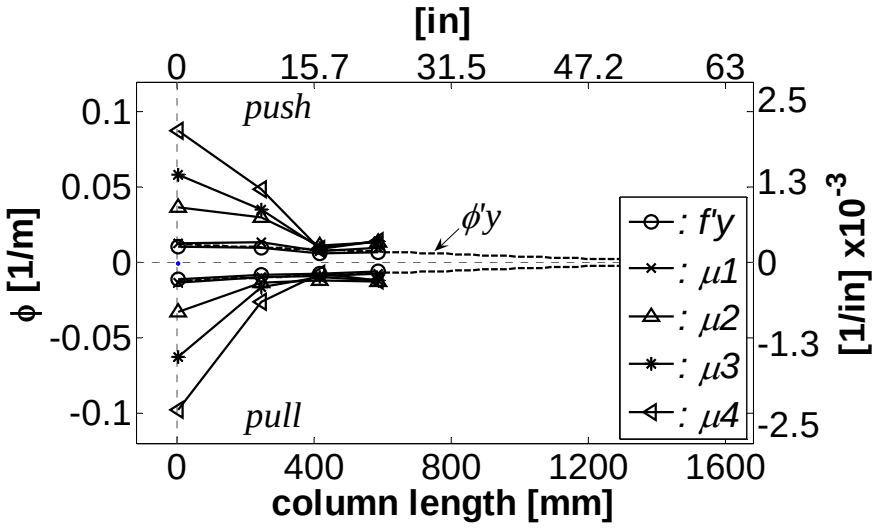

Figure 4.30 FL-89A Curvature profiles.

4.3.1.4 FL-89A Equivalent plastic hinge length

The curvatures calculated using the data recorded by the linear potentiometers can be used along with the measured tip displacement to define an equivalent plastic hinge length. Assuming that the deflection of the column after yield is attained by the formation of a plastic hinge of length L_p, within which curvatures are equal to the base curvatures, the tip displacement Δ can be expressed as:

$$\Delta = \Delta_y + \phi_p L_p L \tag{4.1}$$

where L_p is the equivalent plastic hinge length, ϕ_p is the plastic curvature, and L is the length from the face of the footing to the location of the applied load. The equivalent plastic hinge length is then obtained using Equation 4.2.

$$L_p \sim \frac{\Delta_p}{\phi_p L} \tag{4.2}$$

where Δ_p is the plastic displacement at a given displacement ductility. The value for Δ_p was determined by subtracting the equivalent yield displacement from the displacement at the given displacement ductility, while ϕ_p was calculated by subtracting the equivalent

yield curvature from the curvature in the base of the column at the given ductility. Plastic hinge lengths are calculated independently for the pull and push directions, Figure 4.31 shows the results obtained. It is seen that the value of $L_p = 411mm$ obtained from the experimental data is 59% of the values recommended in Priestly et al. (2007) $L_p = 0.044 f_y d_{bl} = 704mm$. This decrease in L_p may be explained from the way the specimen is fixed to the strong floor of the lab. As shown in Figure 4.32a the postensioned forces used to fix the footing of the specimen are developing "clamping" forces in the longitudinal bars. These forces increase the bonding stresses and reduce the strain penetration length, notice from Figure 4.32b that this phenomenon does not occur in conventional cyclic reversals test setups as the used to develop the current expression for L_p (Priestley and Park 1987).

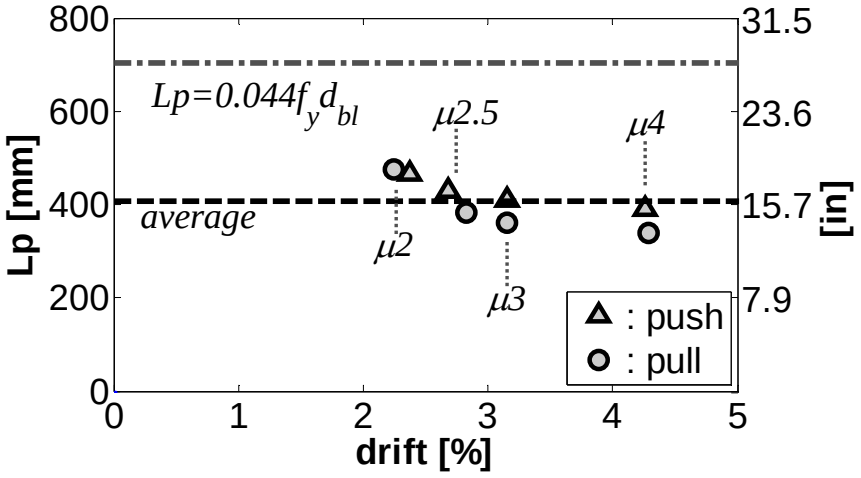

Figure 4.31 FL-89A Equivalent plastic hinge length.

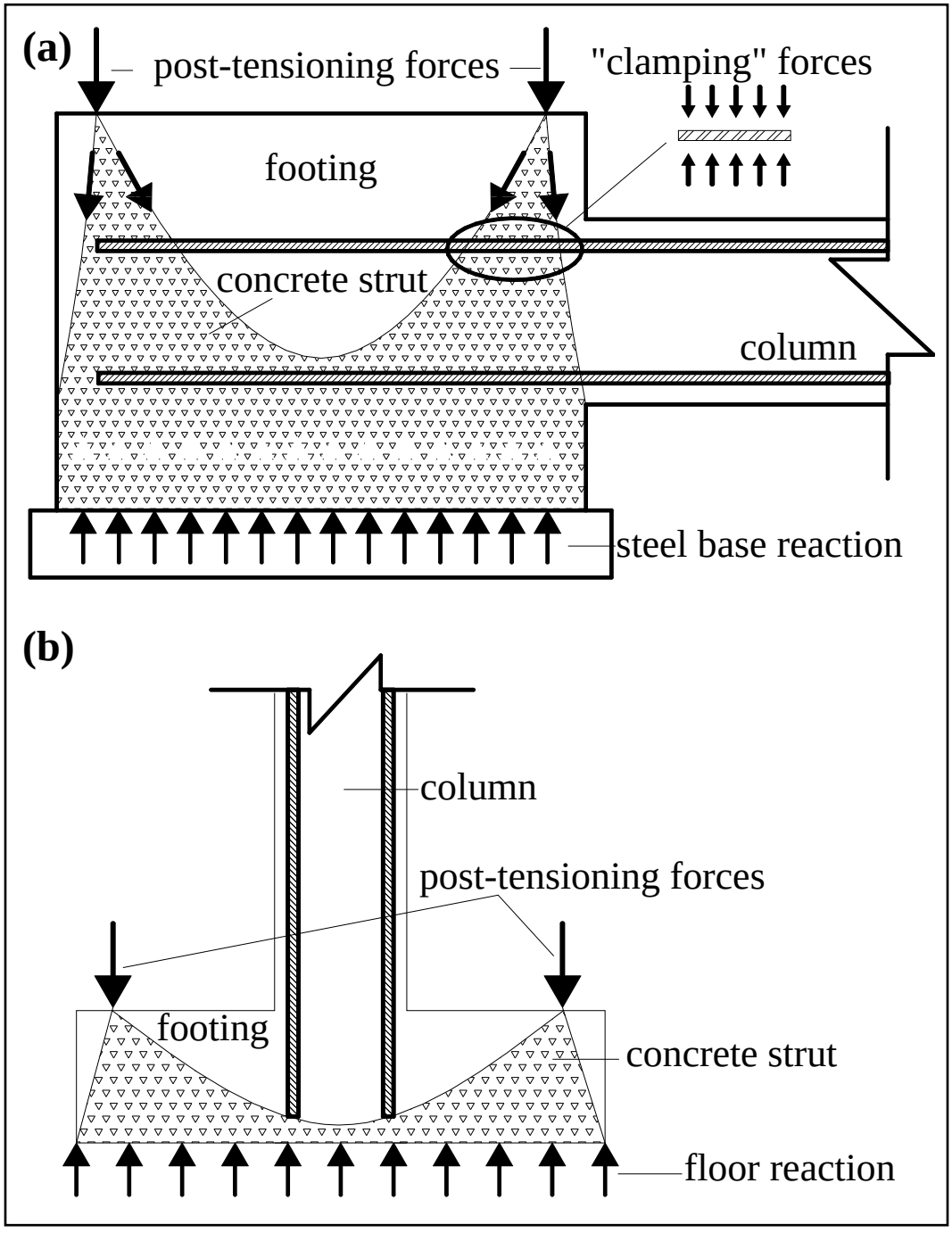

Figure 4.32 (a) Test setup inside environmental chamber (b) Conventional test setup.

4.3.1.5 FL-89A Strains on longitudinal reinforcement

Strain gage data from longitudinal bars is presented in the form of strain profiles and strain histories. Figures 4.33 and 4.34 present the longitudinal strain profile for the top most and bottom most bars, respectively. A positive measurement indicates elongation of the bar. Strain profiles are presented at *f'y, μ1, μ1.5* and *μ2*, after this point the data becomes very erratic. For the strain profile in the top bar (Figure 4.33) only the data from the three strain gages in the column are presented, the strain gage placed in the footing was lost during casting of the concrete. As expected, the strain demand is larger when the bars are in tension, increase in the vicinity of the base and then decrease inside the footing. Figure 4.35 displays the strain history recorded (up to ductility 4) by the strain gage placed in the bottom bar 216mm inside the footing. It is noticed that this spot of the bar didn't yield, which corroborates the hypothesis of a reduced plastic hinge length.

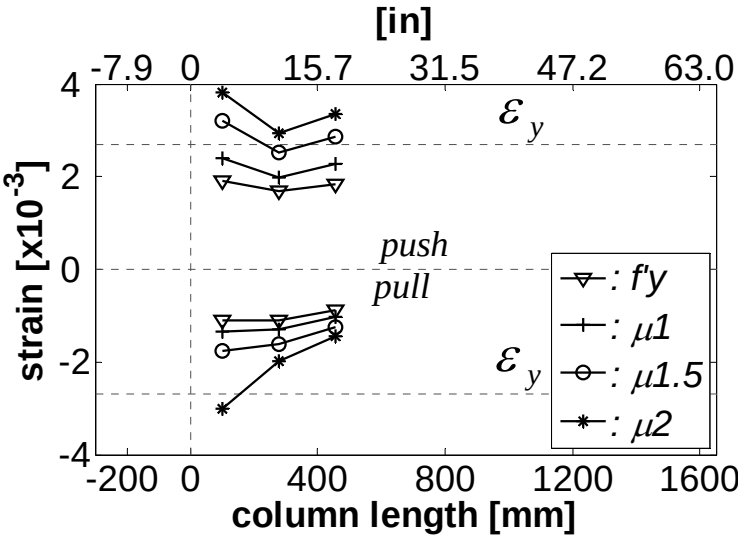

Figure 4.33 FL-89A top most bar strain profile.

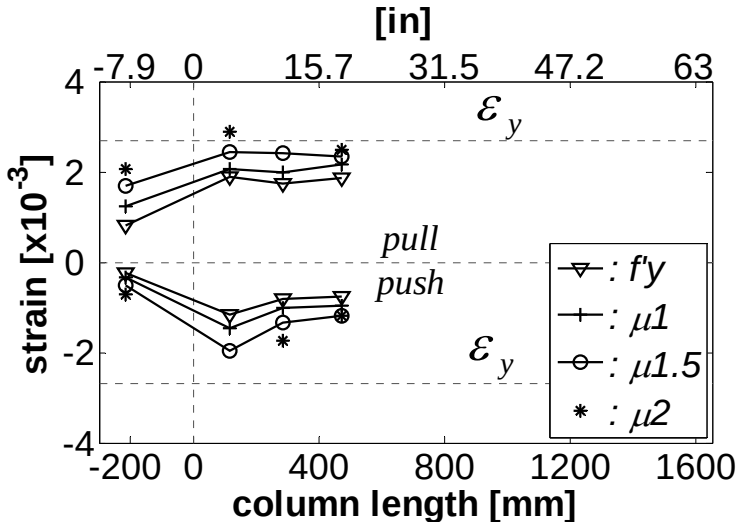

Figure 4.34 FL-89A bottom most bar strain profile.

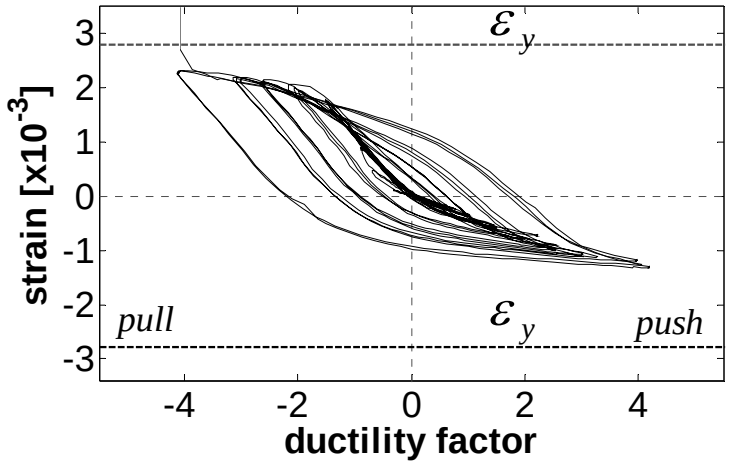

Figure 4.35 FL-89A Bottom bar strain history 216mm inside footing.

4.3.1.6 FL-89A Strains on transverse reinforcement

Strain gage data from transverse reinforcement is presented in the form of strain profiles and strain histories. As is often the case, several strain gages were damaged during the poring of the concrete and some profiles are incomplete. The strain gages in the spirals were distributed at three different levels and placed so that confinement and shear induced strains can be measured (section 3.6.8). Top and bottom faces of the column should not contain any shear induced strains, while the left and right faces should

predominantly contain shear induced strains. Figures 4.36 and 4.37 present the strain profiles on the top and bottom side of the spiral, respectively. In the pull direction, the top face of the column is in compression at the column base and confinement is provided by the spirals. Therefore, the strain on the top side of the spiral is larger in the pull direction and increases as it gets close to the base of the column. In the same way, strain on the bottom side of the spiral is larger in the push direction. It may be noticed from the confinement strain profiles and also from the strain history in Figure 4.40 that, for low levels of loading, the confinement strain is small and slowly increases until ductility 2. After ductility 2, the confinement strain in the base increases more quickly and reaches yield at ductility 4. This behavior is in agreement with the observations during the test, since spalling of the cover concrete took place between ductility 2 and 4.

Figures 4.38 and 4.39 present the strain profiles on the left and right side of the spiral, respectively. Unlike the confinement induced strains, shear strains are expected to be symmetric about the column center on each of the left and right faces and to be identical in the push and pulling direction. However, due to the reality of slight asymmetries, there is usually some variation in the data. It may be noticed from the shear strain profiles and also from the strain history in Figure 4.41 that, as for the confinement strain, yielding is reached at ductility 4. However the distribution of shear strains along the column is different than the distribution of confinement strain. In this case the maximum is reached at some distance from the base and not in the immediate vicinity of the base was the case for the confinement strain. This is due to additional shear strength provided by the footing to the adjacent part of the column.

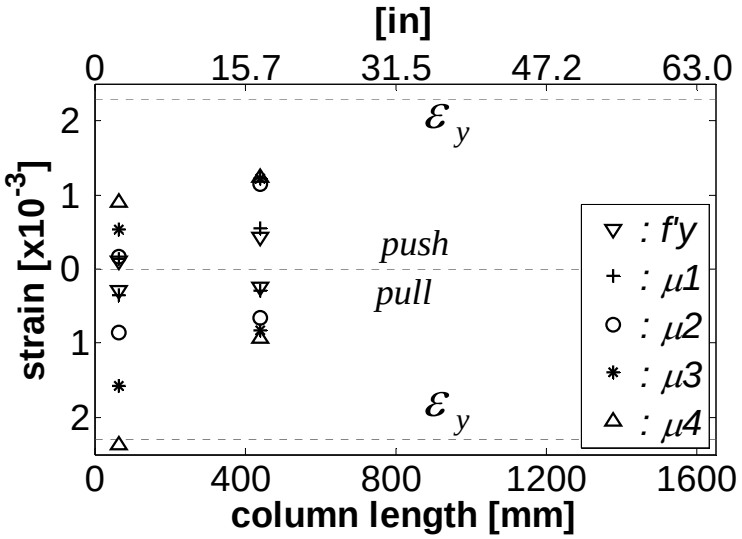

Figure 4.36 FL-89A strains on the top side of the spirals.

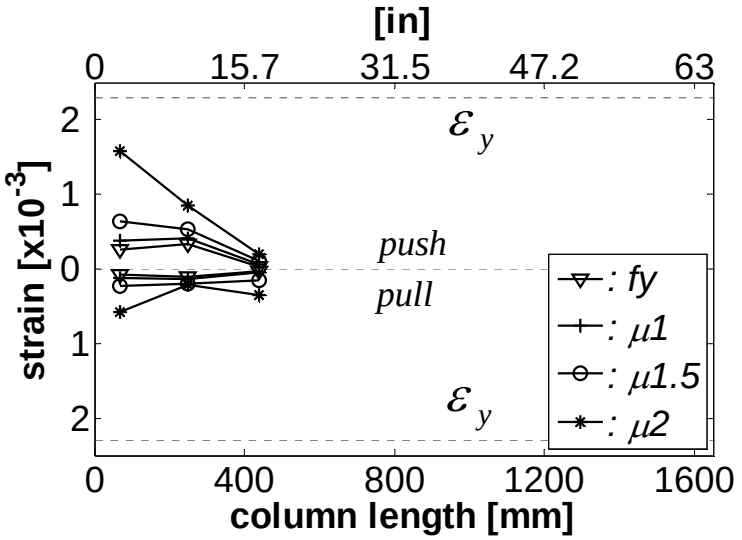

Figure 4.37 FL-89A strains on the bottom side of the spirals.

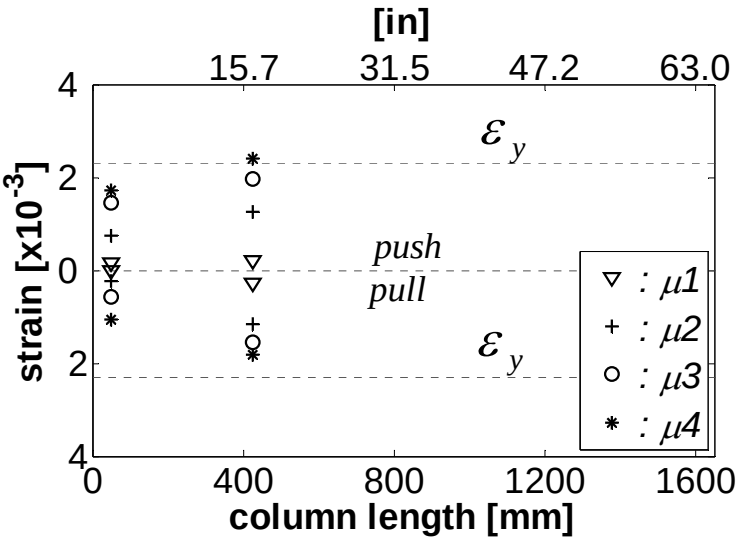

Figure 4.38 FL-89A strains on the right side of the spirals.

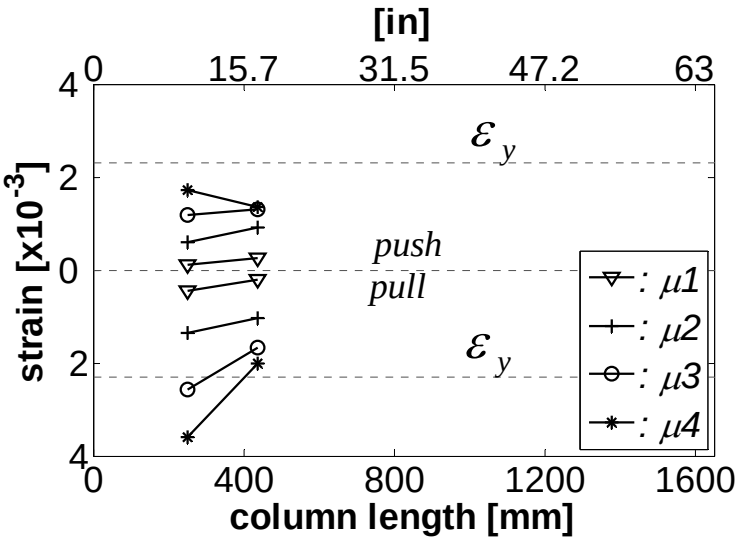

Figure 4.39 FL-89A strains on the left side of the spirals.

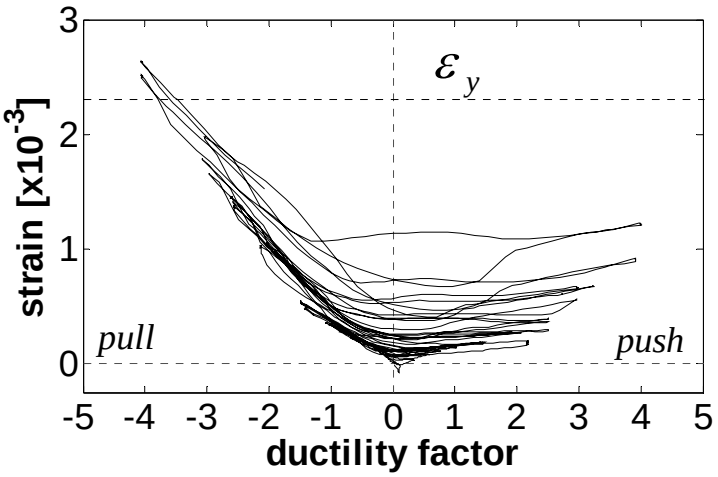

Figure 4.40 FL-89A Strain history: Top spiral #1 (105mm from the base).

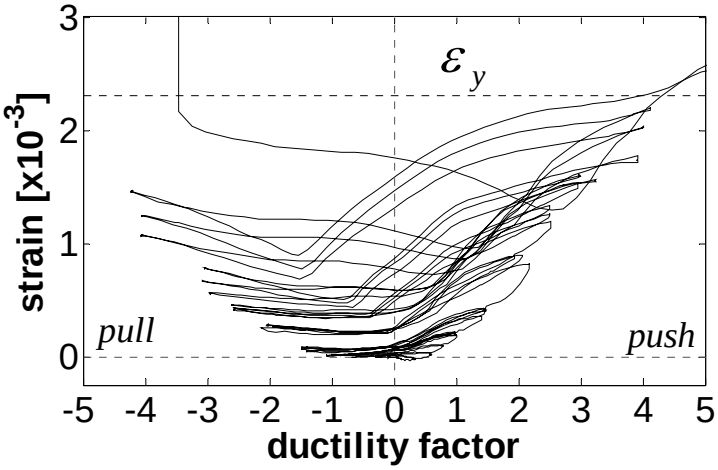

Figure 4.41 FL-89A Strain history: Left spiral #2 (285 mm from the base).

4.3.1.7 FL-89A Validity of the test data

In order to validate the data that has been recorded the following procedure is utilized. With the information collected from the linear potentiometers curvatures at different levels of the column is calculated, then the displacement at the top of the column is obtained by taking the first moment of the area of the curvature profile about the location of the applied load. This displacement is then compared to the one measured by the string pot placed at the top of the column. Figure 4.42 shows the results obtained,

again only the results up to ductility 4 are shown since after this point the linear potentiometers at the base of the column were removed. It should be noticed that, even though the match is very close, the calculated displacements from the lpot data is always below the measured displacement. The difference increases with the displacement and seems to become stable after the section has yielded. This apparent discrepancy is due to the fact that the methodology used to calculate the displacements only accounts for flexural deformations (shear deformations are ignored). If we add the theoretical shear component to the calculated flexural component (dotted line in Figure 4.42), then the match is improves.

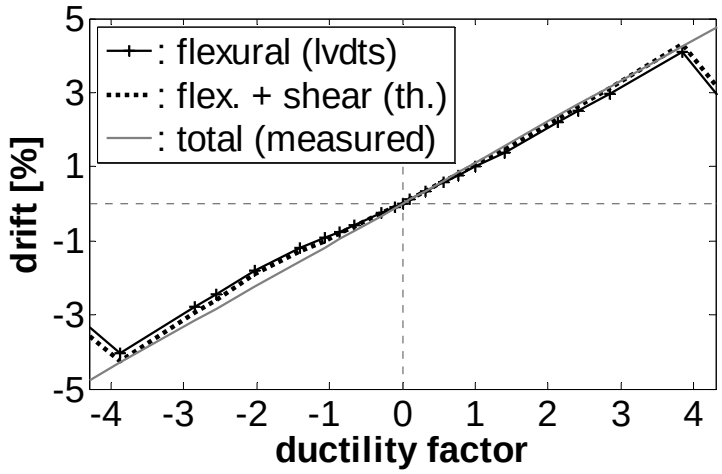

Figure 4.42 FL-89A Validity of test data.

4.3.2 Cold temperature specimen FL-89C

Unit FL-89C was tested on February 211/2007. The column was subjected to the same load history of cyclic reversals applied to the companion warm specimen (FL-89A). The cooling process started ~26 hours before the test, during all this time and all through the test, the specimen was exposed to a constant temperature of -40°C (-40°F). Figure 4.43 shows the temperatures registered by the thermocouples imbedded in the specimen as a function of the column tip displacement. Even though the temperature in the core of the column was ~4°C warmer than at the level of the longitudinal bars, it can be seen from this figure that temperature was constant through the entire test. Figure 4.44

displays the variation of axial load during the test. Horizontal lines in this figure denote the average and ±10% average of the applied axial load. It was more difficult to keep the axial load constant in the cold test that in the room temperature test, presumably because the hydraulic fluid feeding the jacks started losing its ability to flow at low temperatures.

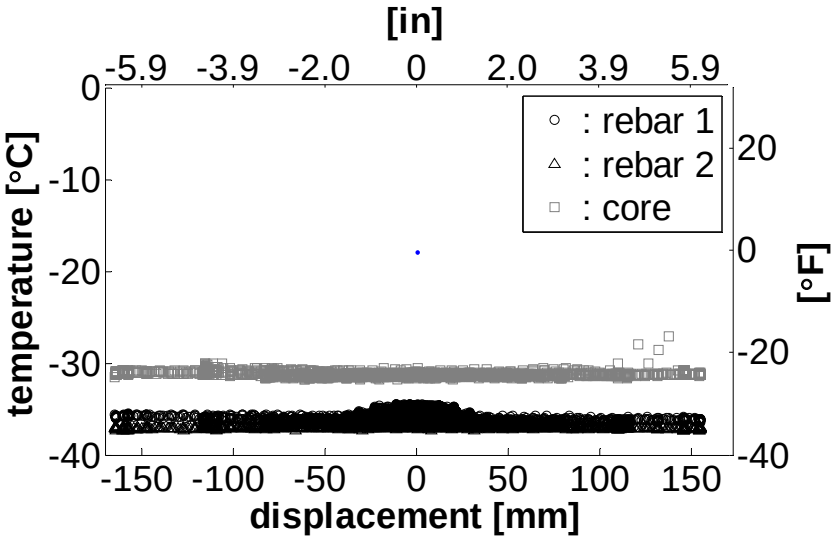

Figure 4.43 Temperature variations during testing of FL-89C.

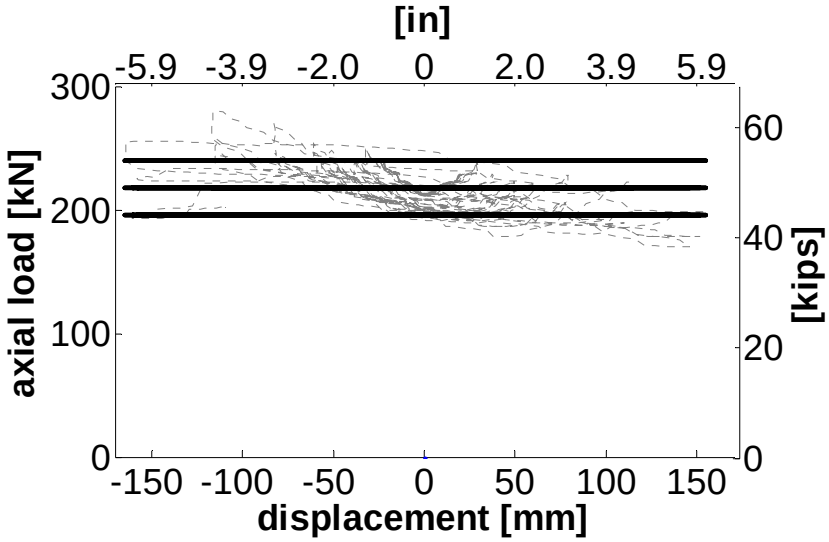

Figure 4.44 Axial load variations during testing of FL-89C.

4.3.2.1 FL-89C Test observations

In order to monitor the condition of the specimen during the test webcams were installed inside the environmental chamber. However, the webcams froze and did not work properly during the test. Conventional digital pictures were then taken by going inside the environmental chamber at key points during the test. All the pictures shown were taken from the top of the column.

First hairline cracks appear after the third cycle of load control (28.8 kips) at 9 in from the base of the column and at the base of the column, one cycle after the room temperature specimen. The lateral force required to reach the target displacement at ductility one was 55.5 kips in the push direction and 60.5 kips in the pull direction, with an average of 58 kips, i.e. 20% more than the average force required at room temperature (45.5 kips). At the first cycle of ductility 1 a new hairline crack become visible at 4 in from the base of the column and the existing cracks become wider, as shown in Figure 4.45. At ductility 2 the three existing cracks are now well defined and ran around the circumference of the column. A new crack just becomes visible at 13in from the base (Figure 4.46).

As shown in Figure 4.47 initial concrete cover crushing was noticed at the first cycle of ductility 2.5 (compared to first cycle of ductility 2 in the room temperature specimen). At ductility 3 (Figure 4.48) the plastic hinge is clearly defined by three wide flexural cracks ~equally spaced from the base to a distance of 9in. The fourth crack that appeared at ductility two was still a hairline crack. During the last cycle of ductility 3 concrete spalling is noted in the base of the column and also in the footing (Figure 4.49).

After the ductility 4 cycles (Figure 4.50) the crushing of the cover concrete extends over 4 in from the base. Note that at this same point the room temperature specimen has already lost all the cover concrete over a distance 7 in from the base and the transverse steel was exposed. During the ductility 6 cycles (Figure 4.51) cover concrete is lost in the base of the column at the interface with the footing, transverse reinforcement is exposed.

In the same way as the room temperature specimen, the first push cycle of ductility 8 saw an increase of 9% in strength over the last push cycle at ductility 6; however the initial maximum force at ductility 6 was not reached. In Figure 4.52 can be appreciated that the column was trying to dig into the footing, this phenomenon was not visible at room temperature. In the last pull of ductility 8 buckling of the top most bar was observed accompanied of rupture of the spiral that was restraining it (Figure 4.53), the test was finished at this point. Buckling at room temperature was observed at this same cycle, though without spiral rupture.

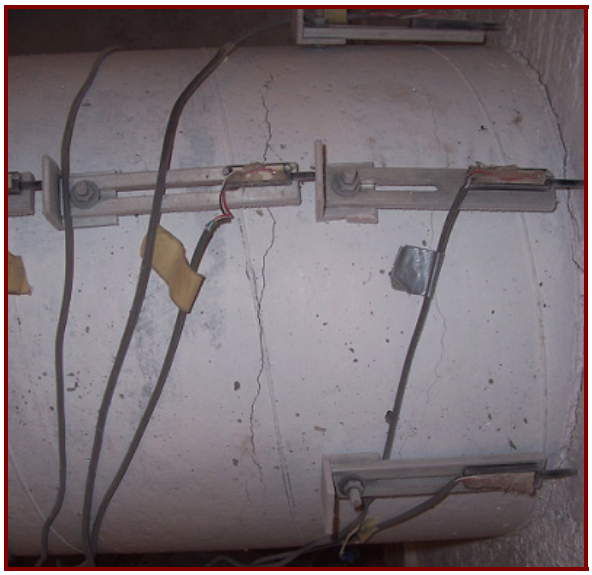

Figure 4.45 Specimen FL-89C after the first cycle of ductility 1.

Figure 4.46 Specimen FL-89C after the first cycle of ductility 2.

Figure 4.47 Specimen FL-89C after the first cycle of ductility 2.5.

Figure 4.48 Specimen FL-89C after the first cycle of ductility 3.

Figure 4.49 Specimen FL-89C after the last cycle of ductility 3.

Figure 4.50 Specimen FL-89C after the last cycle of ductility 4.

Figure 4.51 Specimen FL-89C after the last cycle of ductility 6.

Figure 4.52 Specimen FL-89C after the first cycle of ductility 8.

Figure 4.53 Specimen FL-89C after the last cycle of ductility 8.

4.3.2.2 FL-89C Force-displacement response

Figure 4.54 shows the measured force-deformation response along with the theoretical envelope. The theoretical envelope shown was obtained for an equivalent plastic hinge length of 264 mm, i.e. 64% of the value used for the room temperature

specimen (411 mm) more will be said about this reduction in the next sections. In this case the response of the specimen is more symmetric than for the room temperature test. The average of the measured responses in the two directions is displayed in Figure 4.55 along with theoretical envelopes using two different L_p values; one is the obtained value using the traditional equation for L_p, with the correction factor of 0.59 obtained from the room temperature specimen for the current setup, i.e. $L_p = 0.59(0.044 f_y d_{bl}) = 472mm$ (evaluated with the cold temperature material properties) and the other one is the calculated from the experimental data $L_p = 264mm$. It is seen that the match between theoretical and actual response is improved by reducing the equivalent plastic hinge length. However, as for the room temperature specimen, the onset of buckling is not predicted.

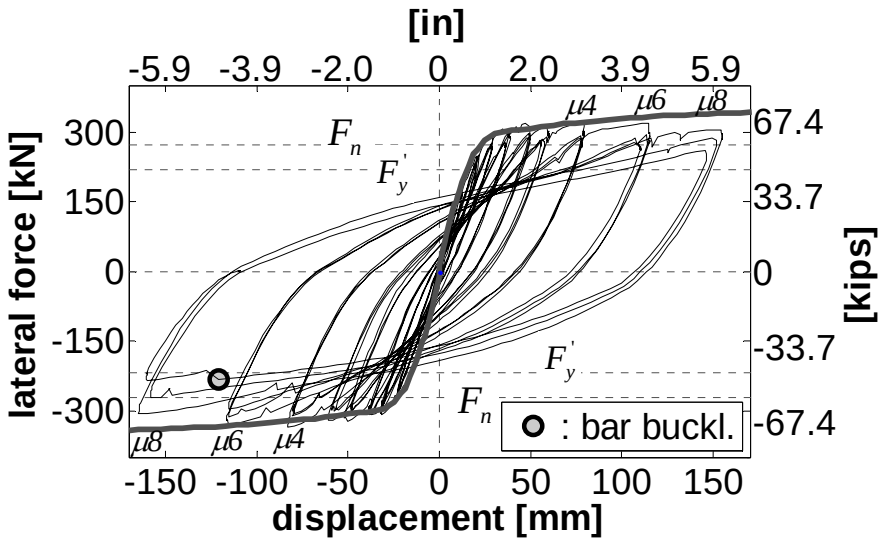

Figure 4.54 Hysteretic response and prediction for FL-89C.

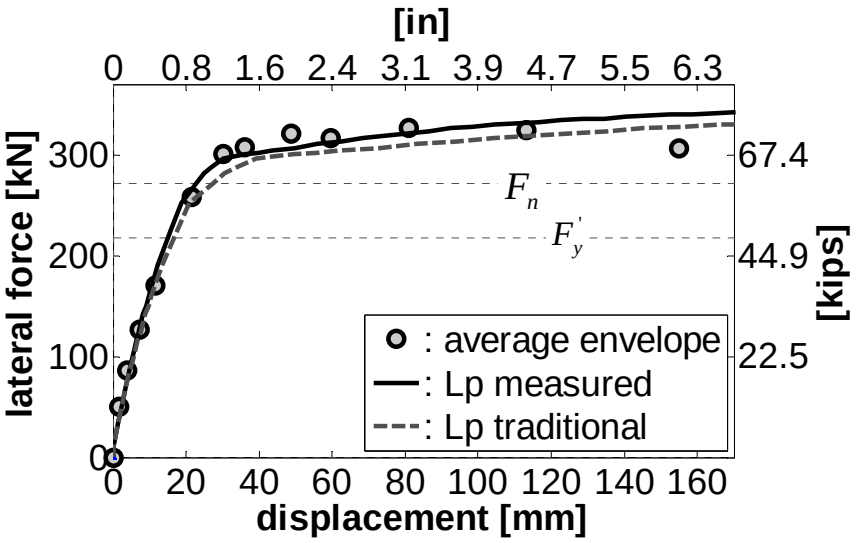

Figure 4.55 First cycle average peak envelop for FL-89C.

4.3.2.3 FL-89C Curvature profiles

As was the case for the warm specimen, the gauge length for the bottom cell includes a component due to strain penetration. The magnitude of this addition for the cold specimen was found to be 18 mm. Figure 4.56 shows the match between the theoretical and actual moment curvature response at the base of the column. Figure 4.57 shows the curvature profiles at *f'y, μ1, μ2, μ3* and *μ4* calculated with the data recorded by the lpot's, it can be noticed that curvatures measured in the two first cells increased with each increasing ductility level. However, in cells 3 and 4, the curvature remains almost constant in the push direction while varying slightly in the pull direction. It should also be noticed that after ductility 2 the rate of increase in curvature is larger in the first cell that in the second. As a result we can conclude that the inelastic deformation was concentrated over the first two cells, and for elevated levels of ductility mostly in the first one, i.e. ~ 200 mm from the base of the column.

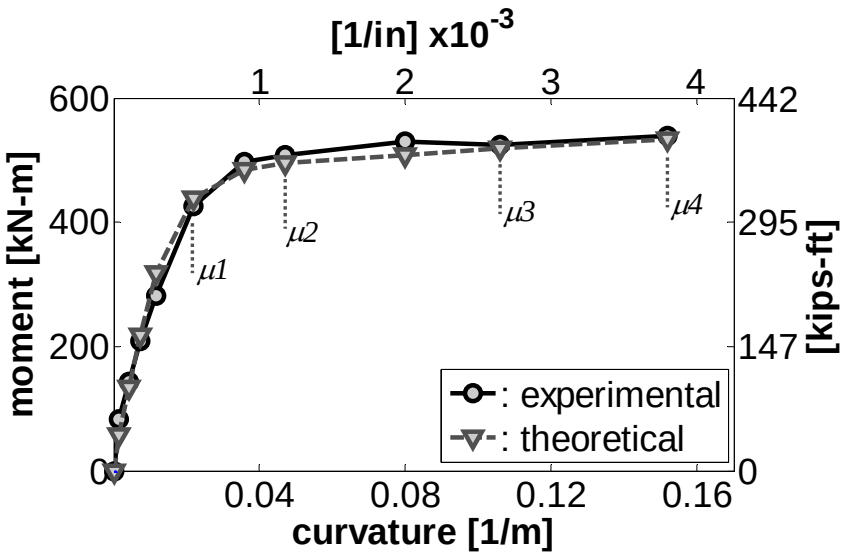

Figure 4.56 FL-89C Moment curvature at column base.

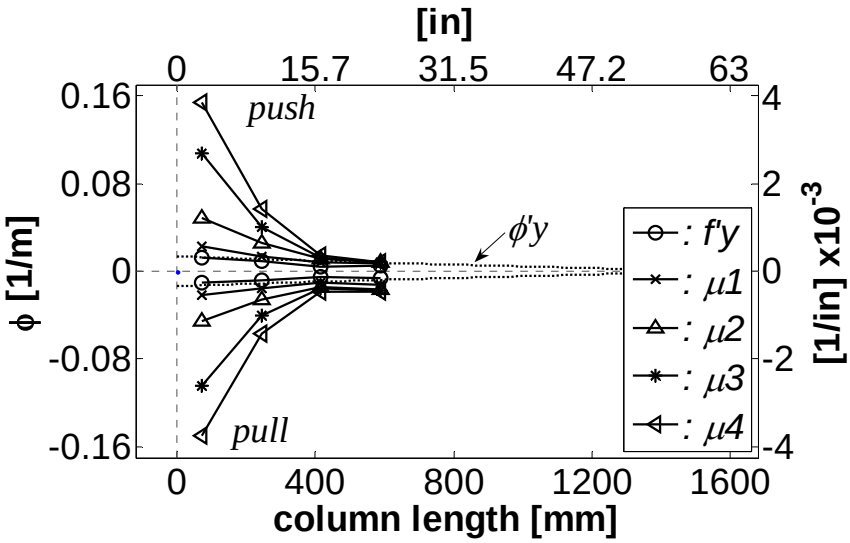

Figure 4.57 FL-89CCurvature profiles.

4.3.2.4 Equivalent plastic hinge length

The equivalent plastic hinge length for the cold specimen is obtained following the same procedure described for the room temperature specimen. Figure 4.58 shows the results obtained, it is seen that the equivalent plastic hinge length is substantially reduced when compared with the expected value. For the geometric properties and reinforcement

of the column the length of the equivalent plastic hinge length is dominated by $L_p = 2L_{sp}$. If the expected value is calculated using cold material properties and a factor of 0.59 is inculed to account for the reduction in strain penetration due to the fixing conditions of the footing we get $L_p = 0.59(0.044 f_y d_{bl}) = 472mm$, then the experimental value obtained for the cold condition $L_p = 264mm$ is 57% of the expected value. Then, the equivalent plastic hinge length at low temperature (~-36°C) L_p is given by

$$L_p\left(-36^\circ C\right) = 0.57\left(kL + L_{sp} \geq 2L_{sp}\right) \tag{4.3}$$

This reduction in the plastic hinge is supported by the condition of the specimens after the test, where a reduction in the spread of plasticity is evident (Figure 4.59). Furthermore, past research have shown that bond strength increase with cold temperatures, Shih et al. 1988 reported an increase of 76% in bond strength of bars subjected to cyclic reversals when the temperature is reduced from 20°C to -40°C. This large increase in bond strength is expected to reduce the strain penetration length.

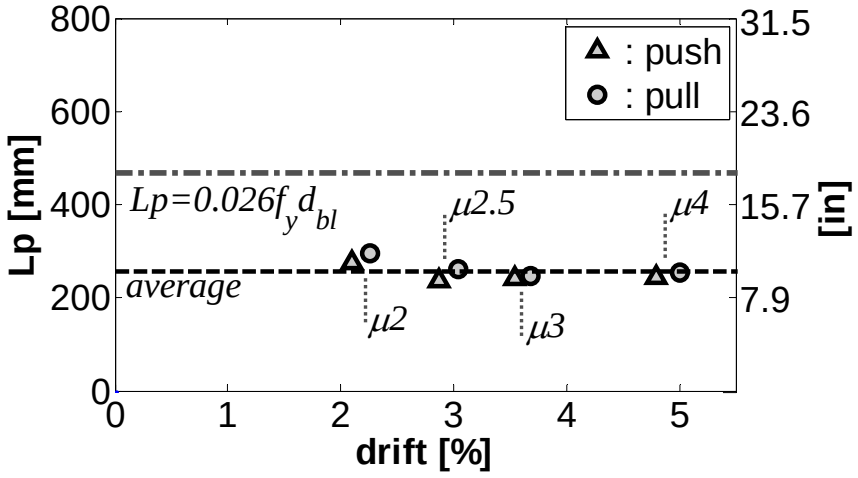

Figure 4.58 FL-89CEquivalent plastic hinge length.

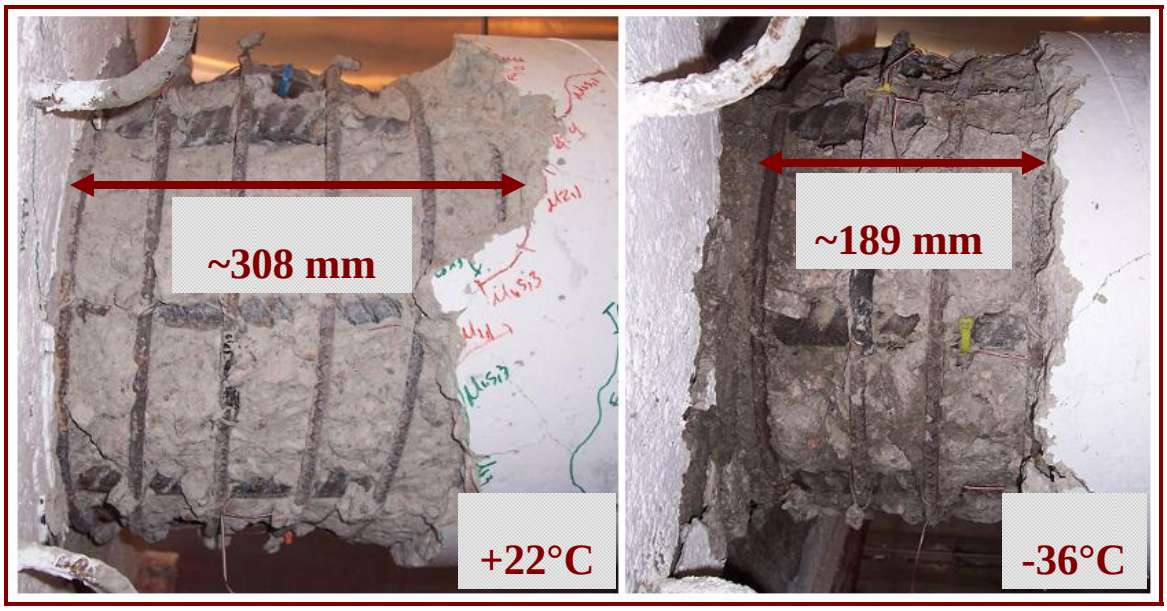

Figure 4.59 Condition of the flexural specimens after the test.

4.3.2.5 FL-89C Strains on longitudinal reinforcement

Strain gage data from longitudinal bars is presented in the form of strain profiles. Figures 4.60 and 4.61 present the longitudinal strain profile for the top most and bottom most bars, respectively. In general, the strain distribution presented in these figures is in agreement with the curvature profile displayed in Figure 4.57. For both bars a jump in the strain can be noticed when going from the last cycle of force control to ductility 1, at this same level the first well defined flexural cracks were first observed in the base of the column. According to the profiles both bars started yielding at ductility 1.

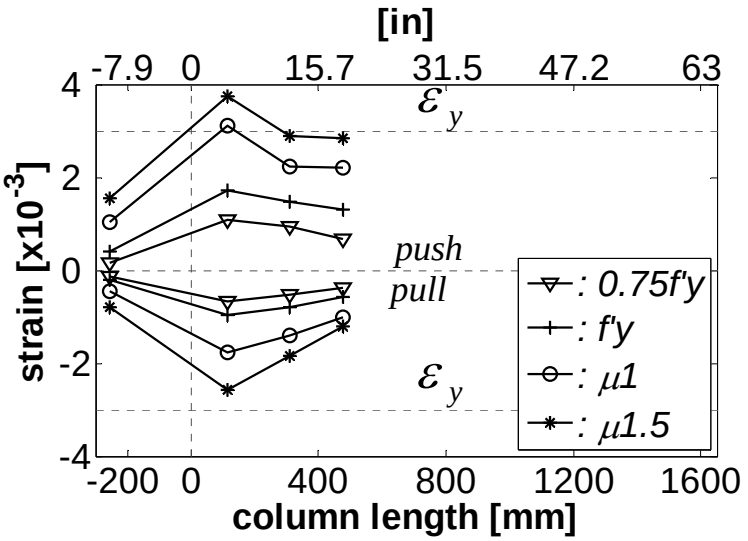

Figure 4.60 FL-89C top most bar strain profile.

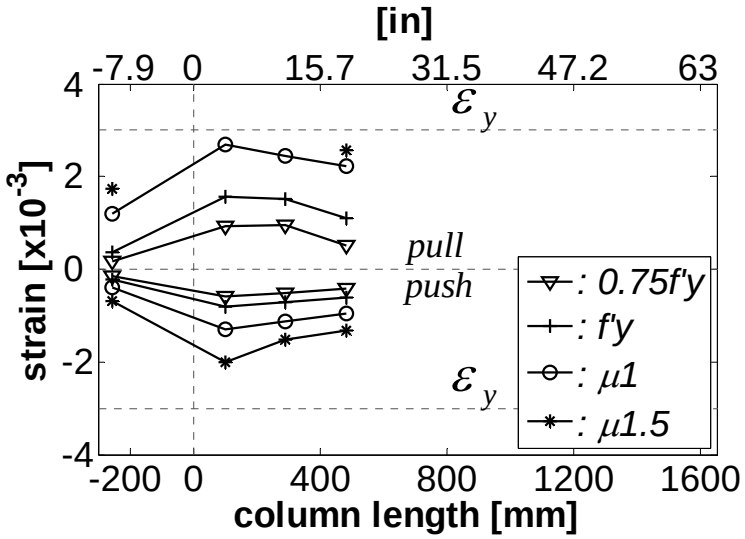

Figure 4.61 FL-89C bottom most bar strain profile.

4.3.2.6 FL-89C Strains on transverse reinforcement

Regrettably, the majority of the strain gages on the spiral did not work properly during the test; presumably due to the extreme temperature they were exposed. As a result, generation of strain profiles as those generated for the room temperature specimen are not possible. Nonetheless, information regarding the strain on transverse

reinforcement is presented in the form of strain history of two strain gages that worked properly at low levels of ductility. Figure 4.62 shows the strain history of the strain gage placed on the bottom face of the spiral at a distance of 114 mm from the base, as expected strains are larger in the push direction because the concrete on the bottom face at the base of the column is in compression and is trying to expand due to the Poisson effect. Figure 4.63 shows the strain history of the strain gage placed on the left face of the spiral at a distance of 476 mm from the base. The strain recorded was very low which means that up to ductility 1.5 shear strength in the column is mainly provided by the concrete mechanism.

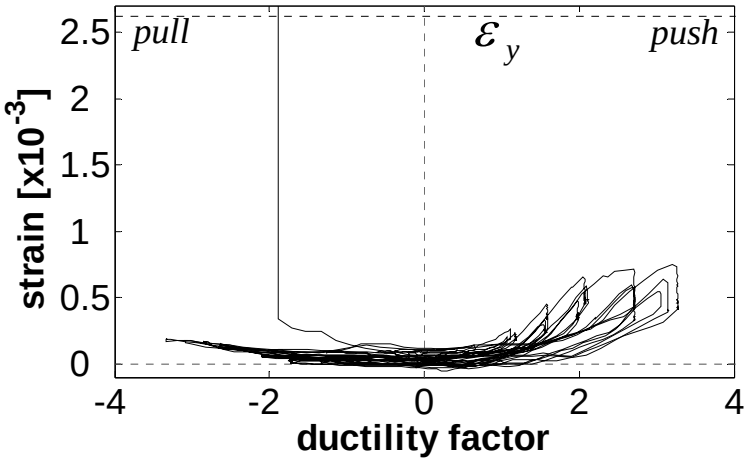

Figure 4.62 FL-89C Strain history: Bottom spiral #1 (114mm from the base).

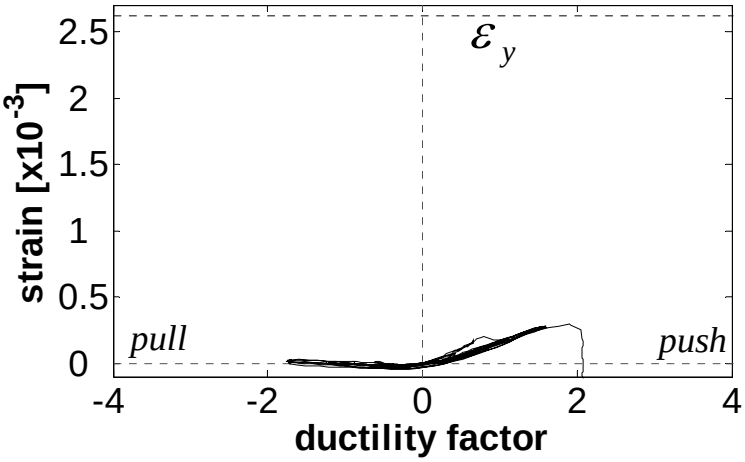

Figure 4.63 FL-89C Strain history: Left spiral #3 (476 mm from the base).

4.3.2.7 FL-89C Validity of the test data

Data recorded during the test is validated as explained in section 4.3.1.7. Figure 4.61 shows the results obtained. The match between measured displacement and the calculated from the lpot's is very close, though not as good as in the room temperature test.

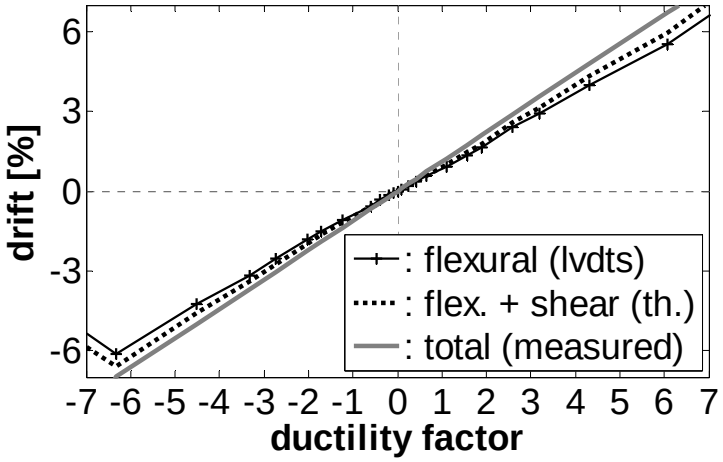

Figure 4.64 FL-89C Validity of test data.

4.3.3 FL -89A and FL-89C results comparison

Figure 4.65 shows the hysteretic responses and Figure 4.66 shows the average first peak envelopes, F_{nr} and F'_{yr} represent the nominal and first yield force, respectively. From these figures note that the effect of freezing temperatures was to increase the strength and initial stiffness of the column. If the elastic stiffness is defined at the load level required for first yield of the room temperature specimen, then the elastic stiffness of the specimen tested at -36˚C is 27% larger than the elastic stiffness of the specimen tested at 22˚C. The largest lateral forces reached were 326.4 kN (at the first cycle of ductility 4) for the cold specimen and 285.7 kN (at the first cycle of ductility 6) for the room temperature unit, i.e. the cold specimen exhibited 14% larger flexural strength than the ambient temperature test. If the increase in flexural strength is calculated from the average of the differences between the lateral force required to reach

the given target displacements, the increase in flexural strength is of 16%. Displacement capacity was not affected by the low temperature since both specimens failed by buckling of the top most bar at the same cycle and level of displacement demand. Nonetheless, the cold failure also included spiral fracture in addition to bar buckling.

Figure 4.67 shows the average peak envelopes for the three cycles per ductility the columns were subjected to. It can be noted from this figure that the strength degradation with increasing ductility demand started earlier in the cold specimen, after ductility 4, while in the ambient temperature test it started only after ductility 6. The strength degradation associated with cycling at the same level of ductility demand is also larger in the cold specimen.

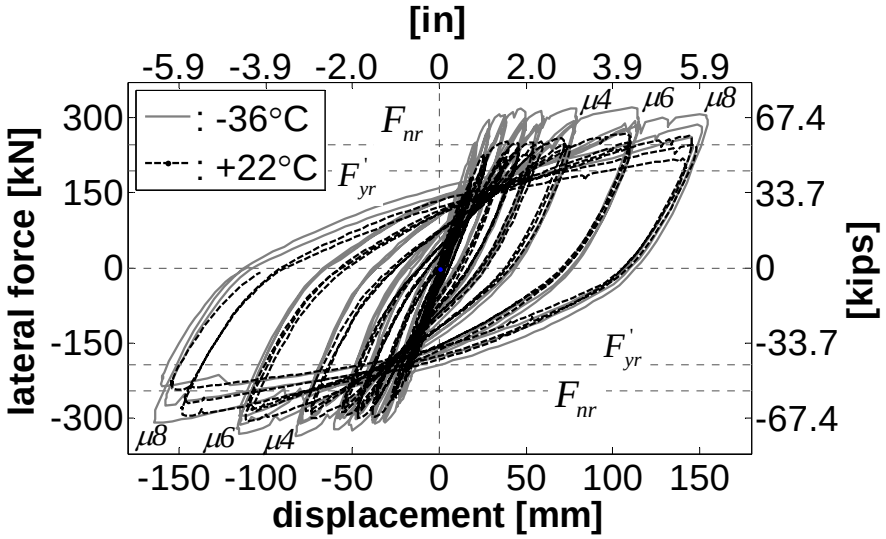

Figure 4.65 Hysteretic responses of FL-89C and FL-89A.

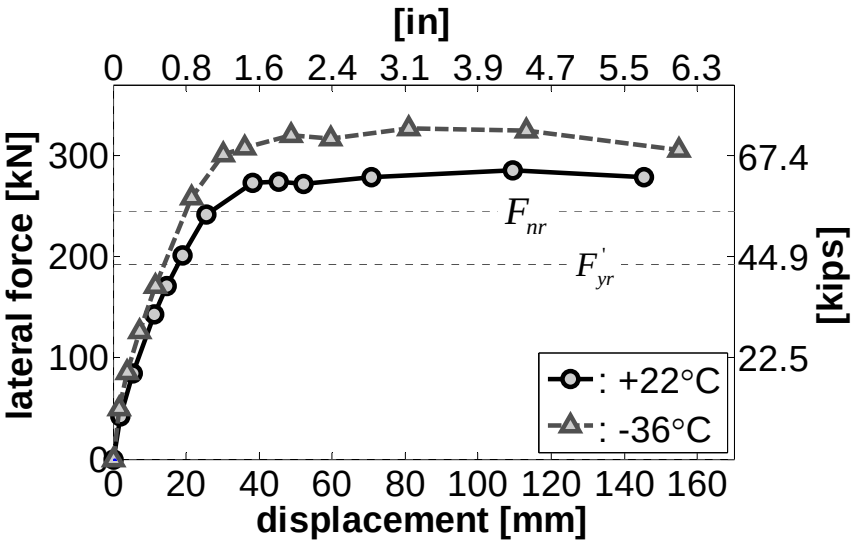

Figure 4.66 Average first cycle envelopes of FL-89C and FL-89A.

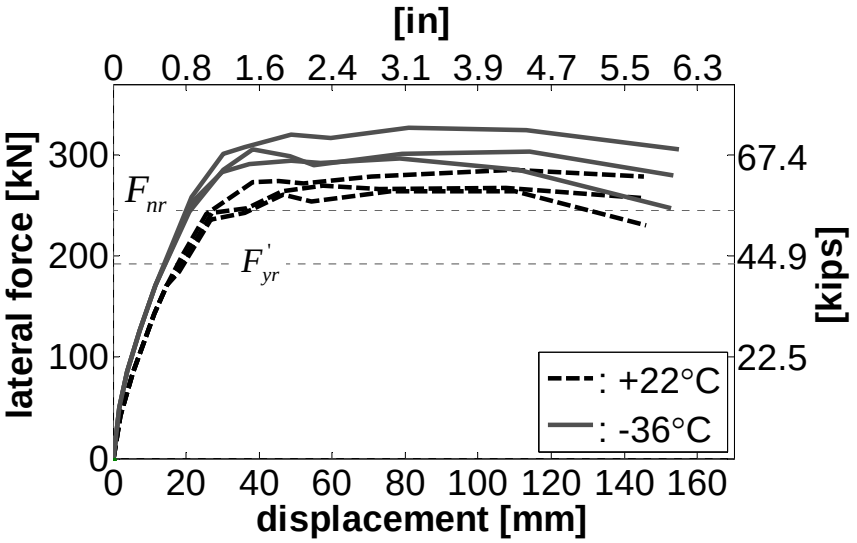

Figure 4.67 Average cycle envelopes of FL-89C and FL-89A.

The energy dissipated was calculated by determining the area inside each loop. After determining the area inside each loop (*A1*), the hysteretic damping was calculated using Equation 4.4 (Jacobsen, 1930)

$$\xi = \frac{2}{\pi}\frac{A1}{A2} \tag{4.4}$$

where *A2* is the area of a rigid, perfectly-plastic member with the same maximum strength and the same maximum displacement in each direction as the actual member (Figure 4.68). Figures 4.69 and 4.70 show the energy dissipated and hysteretic damping for both specimens. From Figure 4.69 can be noticed that energy dissipation capacity of the cold specimen is slightly larger than for the room temperature one, mainly because of the larger strength of the section. However, the values of area based equivalent viscous damping AB-EVD (Equation 4.1) in Figure 4.70 are practically the same for both temperatures. It must be noticed that the EVD calculated with Equation 4.4 are not the values to use for displacement based design as they may largely overestimate the effective equivalent viscous damping for systems with high energy absorption (Chopra and Goel, 2001). Appropriate levels of EVD have been calibrated for different hysteretic rules to give the same peak displacements as the hysteretic response using ITHA (Dwairi et al. 2007, Grant et al. 2005). Correction factors to be applied to area based equivalent viscous damping AB-EVD are displayed in Figure 4.71 (Priestley et al. 2007), trend lines in this figure correspond to Equation 4.5. Figure 4.72 presents the corrected equivalent viscous damping. Note that the values obtained are in agreement with the equation proposed in Dwairi et al. (2007) for bridge column (Equation 4.6).

$$(ITHA/AB)\ EVD\,ratio = (0.53\mu + 0.8)\xi^{-(\mu/40+0.4)} \tag{4.5}$$

$$\xi_{eq} = 50\left(\frac{\mu - 1}{\pi\mu}\right) \tag{4.6}$$

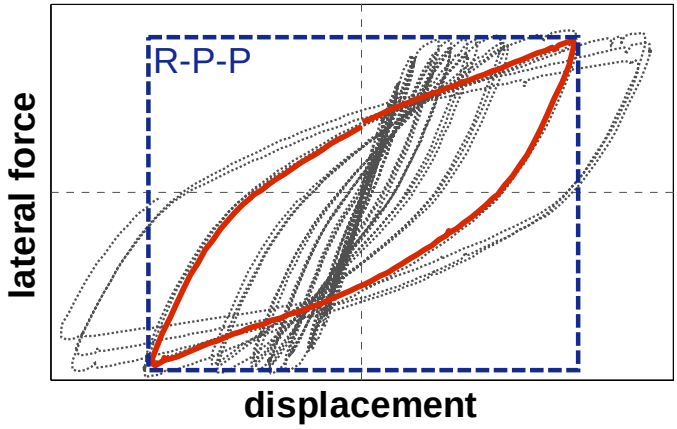

Figure 4.68 Equivalent damping.

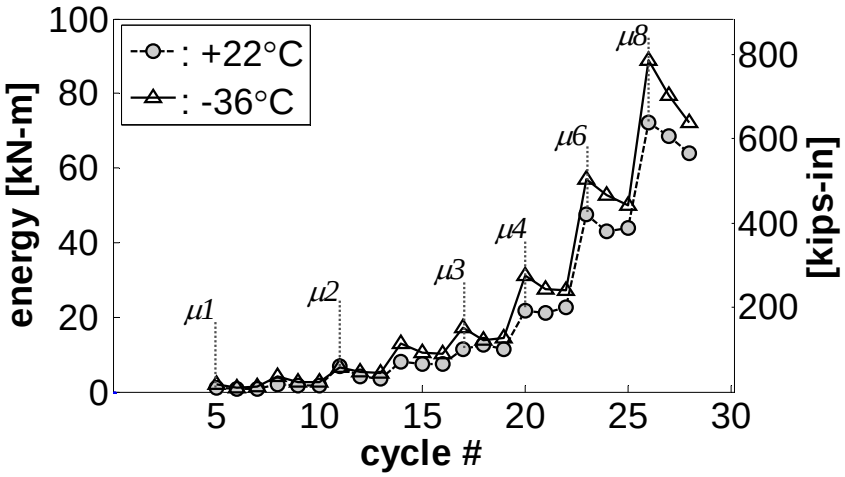

Figure 4.69 Energy released for FL-89C and FL-89A.

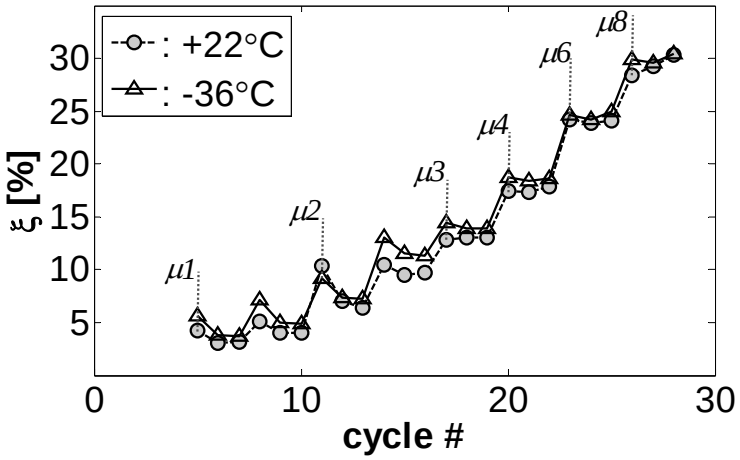

Figure 4.70 Hysteretic damping for FL-89C and FL-89A.

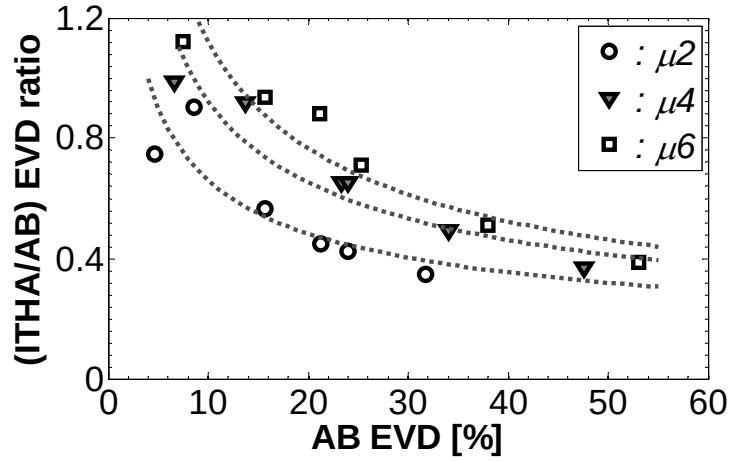

Figure 4.71 Correction factors to be applied to AB-EVD.

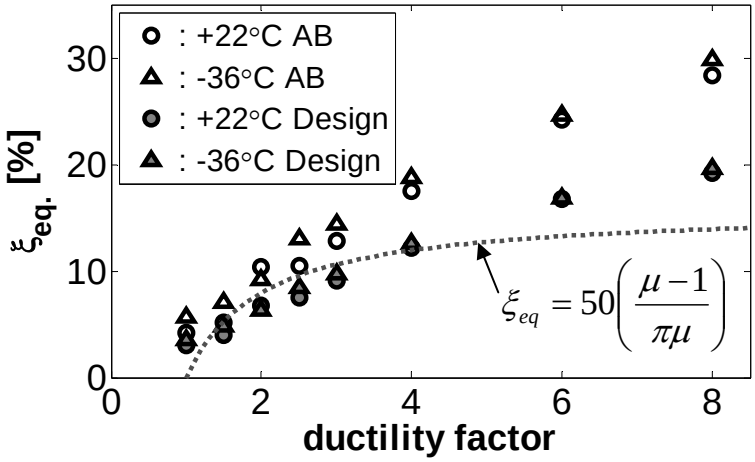

Figure 4.72 Corrected values of equivalent damping.

Curvature profiles are presented in Figure 4.73. From this figure, it can be noticed that plastic curvatures in the base on the column of the cold specimen are larger when compared with the room temperatures profiles. This implies that plastic curvatures in the room temperature unit should be distributed over a larger length in order to reach a specified displacement when compared with the cold unit. This phenomenon can be also noticed in Figure 4.74, which presents the equivalent plastic hinge lengths obtained from the experimental results. Plastic hinge lengths are calculated independently for the pull and push directions, Figure 4.74 show the averages of the values obtained in both directions. Finally, Tables 4.6 and 4.7 summarizes the results obtained during the tests.

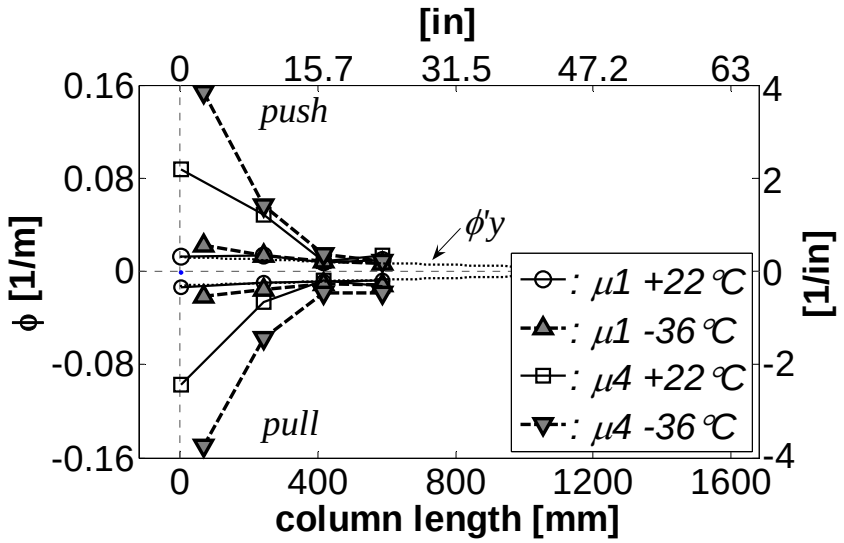

Figure 4.73 Curvature profiles for FL-89C and FL-89A.

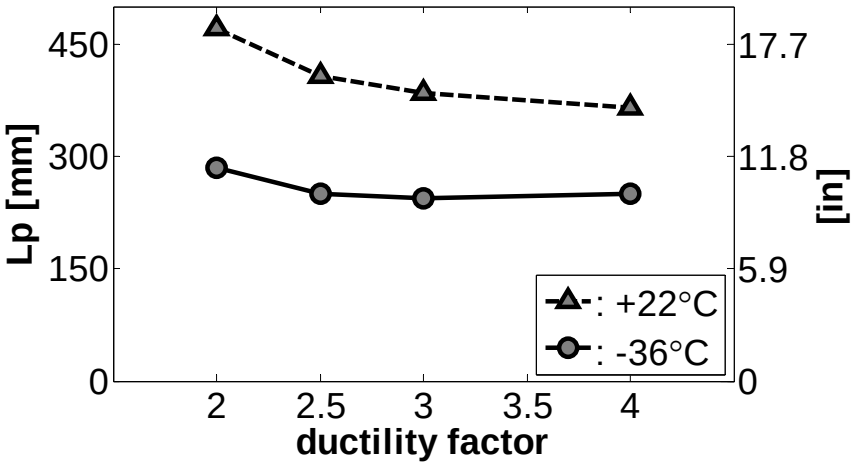

Figure 4.74 Plastic hinge lengths for FL-89C and FL-89A.

Table 4.6 Summary of results obtained (Load control phase)

Cycle	Average Lat. Force [kN]	Average tip displacement [mm]		
		+22°C	-36°C	-36°C / +22°C
0.25fy'	46.2	2.2	1.7	0.73
0.5fy'	85.7	5.6	3.9	0.70
0.75fy'	134.7	10.4	8.1	0.78
fy'	170.8	14.8	11.6	0.79

Table 4.7 Summary of results obtained (Displacement control phase)

Cycle	Average Displacement [mm]	First cycle average lateral force [kN]		
		+22°C	-36°C	-36°C / +22°C
μ1	20.2	208.9	247.1	1.18
μ1.5	27.9	247.8	289.7	1.17
μ2	37.0	270.7	308.6	1.14
μ2.5	47.1	273.1	318.9	1.17
μ3	55.9	272.9	318.3	1.17
μ4	75.8	279.3	324.1	1.16
μ6	111.4	285.3	324.9	1.14
μ8	150.2	278.0	308.2	1.11

4.4 Revised predictive models

Through all the results presented in this chapter it was shown that the available predictive models for the assessment of the seismic response of RC members at ambient temperatures can be used to determine the increase in flexural strength of members exposed to freezing temperatures if the appropriate material properties are used. Nonetheless, the reduction in displacement capacity in the cold specimens was not captured by these theoretical models. During the analysis of the results obtained for the heavy reinforced specimen tested at cold temperature FL-89C, a considerable mismatch between the theoretical and experimental force-displacement envelopes was noted. Basically, the theoretical envelope was under predicting the strength of the member at each displacement. Nevertheless, the theoretical nominal force was in agreement with the experimental results. Based on physical observations, it was suspected that these changes may be attributed to a reduction of the equivalent plastic hinge length L_p. The equivalent plastic hinge length was that calculated from the base curvatures and tip displacement recorded during the test. It was found that the equivalent plastic hinge was 57% of the predicted value. Figure 4.75 show the results obtained when this variation in the equivalent plastic hinge method is applied to predict the response of the light reinforced member at -40°C (unit JS-M40). This figure presents:

- The actual average first peak envelope force displacement response.

- The theoretical envelope obtained using the conventional expression the equivalent plastic hinge $L_{pr} = 2L_{sp} = 2(0.022 f_y d_{bl}) = 395mm$.

- The theoretical envelope obtained using the L_p value recommended for freezing conditions $L_{pc} = 0.57(2L_{sp}) = 225mm$.

It should be noticed from Figure 4.75 that a change in the plastic hinge length does not affect the strength of the member, i.e. the first yield and nominal forces (dotted horizontal lines) are the same for both predictions. By simple inspection of Equation 4.7, it may be said that reducing the plastic hinge length L_p will increase the curvature ϕ required at the base of the column to reach a given displacement. An increase in the curvature implies an increase in the strains on the longitudinal bars and in the lateral force required to reach a particular displacement. It should also be noted from Figure 4.75 that the predicted onset of buckling using the model proposed by Moyer and Kowalsky (2003) is drastically improved when L_p is reduced. This due mainly to the fact that this model directly consider the influence of tension strain on the on-set of buckling, which as mention before increase when the plastic hinge length is reduced.

$$\Delta = \Delta_y + (\phi - \phi_y) L_p L \tag{4.7}$$

Now, the buckling of the longitudinal bars in the heavily reinforced specimens was not predicted by either of the two buckling models employed (Moyer and Kowalsky 2003, and Berry and Eberhard 2005), not even for the ambient temperature conditions. As mentioned by the authors the Moyer-Kowalsky model (as presented) only accounts for buckling between two consecutive spirals, as in the case of the Sloan columns. However, in this case buckling occurs over a layer of transverse reinforcement (see Figures 4.26 and 4.50). In the case of the Berry-Eberhard the problems seems to be that the model attempt to capture two different phenomenon, buckling between two consecutive spirals and buckling over a layer of spirals, with a single expression.

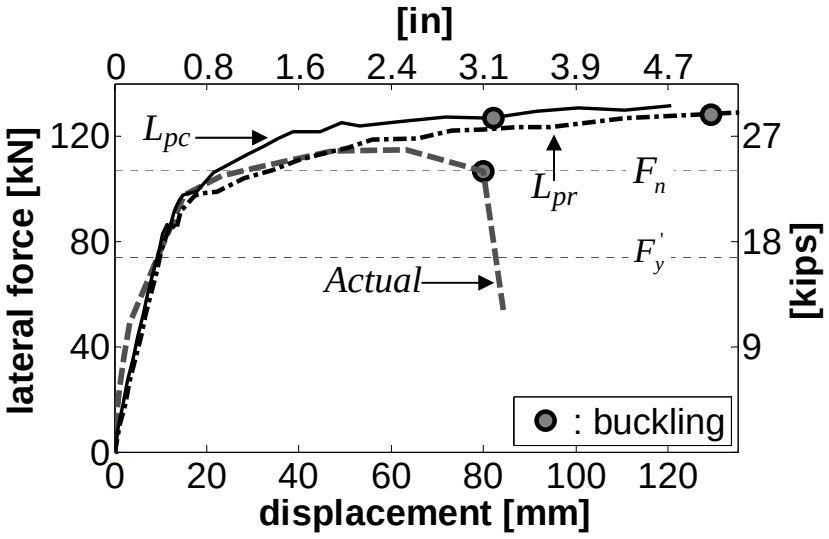

Figure 4.75 Theoretical and experimental F-D responses for JS-M40.

4.5 Final discussion and concluding remarks

From the results presented in this Chapter, the effects of freezing temperatures on the seismic behavior of flexural dominated RC member can be summarized as follows:

- Flexural strength increases with low temperatures. Both types of specimens tested, lightly and heavy reinforced, saw an increase of ~15% in the peak flexural strength when the temperature was reduced to ~-40˚C. This increase was expected since both, concrete and steel rebars; increase its strength when the temperature drops below freezing.

- The elastic stiffness also increases with low temperatures. This increase is more evident in members lightly reinforced (ρ~1%) tested without axial load (270% when the temperature drops to -40˚C) than in heavy reinforced members (ρ~3%) tested with ~6% axial load ratio (27% when the temperature drops to -36˚C). This increase in stiffness can be attributed in part to the increase in the modulus of elasticity of concrete at low temperatures but mostly to the reduction of the plastic hinge length.

- Member ductility decrease when it is exposed to freezing temperatures. As with the elastic stiffness this effect was more evident in the lightly reinforced members which exhibited a reduction of 20% in the displacement capacity when the temperature was reduced to -40°C. In the case of the heavy reinforced members, the cold and room temperature specimens failed by buckling at the same displacement. However it can be said that the failure of the cold specimen was more brittle in nature because the spiral restraining the longitudinal bar broke when the bar buckled.

- A reduction in the spread of plasticity was detected in all the specimens tested at freezing conditions. Based on physical observations (Figures 4.10 and 4.59) and calculation of equivalent plastic hinges from the data collected, a reduction in the equivalent plastic hinge length of 43% is proposed when the temperature in the specimen is dropped to -40°C. More tests are required to determine the variation of L_p at other temperatures. However, the proposed values can be conservatively used to estimate the displacement capacity of RC columns exposed freezing temperatures above -40°C.

- Notice that in all the specimens tested the length of the equivalent plastic hinge was controlled by $2L_{sp}$. Larger specimens need to be tested at freezing conditions to determine if the same reduction applies in members which equivalent plastic hinge length is controlled by $kL + L_{sp}$.

CHAPTER V

SEISMIC BEHAVIOR OF REINFORCED CONCRETE FILLED STEEL TUBE COLUMNS AT LOW TEMPERATURES

5.1 Introduction

In order to determine the effect of cold temperatures on the behavior of reinforced concrete filled steel tube RCFST columns, four of these types of columns were designed, built and tested. In RCFST columns a steel tube is used as formwork during casting of the concrete. In the majority of the cases a gap is left between the steel tube and the beam – column joint or foundation, so that the steel tube is only providing shear and confinement strength to the column, and not (in a direct way) flexural or axial strength (which are provided by the concrete and the longitudinal bars). Some of the advantages of RCFST are that (1) no formwork is required, (2) the whole concrete section is very well confined which, in theory, will increase the ductility capacity of the section and (3) since the steel tube provides shear and confinement strength a minimum number of conventional ties is required.

Several researchers have investigated the seismic behavior of steel-tubed and steel-jacket retrofitted RC columns. Aboutaha and Machado (1998, 1999) found that, even though the increase in flexural strength is insignificant, rectangular RCFST columns exhibit a larger displacement capacity than ordinary reinforced concrete columns when subjected to cyclic reversals and high axial loads ALR>10% (condition proper of tall buildings in active seismic zones). However, when the level of axial load in the column is

low, no difference was found between the seismic behavior of RCFST and ordinary columns.

Chai et al. (1991) and Priestley et al. (1994a, 1994b) investigated the use of steel jackets for seismic retrofit of non-ductile reinforced concrete columns. The results obtained show that the columns retrofitted with steel jackets exhibited extremely stable lateral force-displacement hysteretic response. The pattern of inelastic deformation was changed from predominantly shear deformation for the as-built columns to predominately flexural deformation for the retrofitted columns. An increase in the elastic stiffness and a reduction in the spread of plasticity were also noticed in the retrofitted columns. A reduction in the spread of plasticity was also noticed on the ordinary columns tested at freezing temperatures in Chapter IV, this was identified as the main cause for the reduced displacement capacity of cold specimens when compared to the room temperature specimens.

This Chapter explores the combined effect of low temperatures and the extreme confinement provided by the steel tube in the seismic behavior of RCFST columns. In order to accomplish this objective two pairs of RCFST columns were tested at room (23˚C, 74˚F) and freezing temperatures (-40˚C, -40˚F). The results obtained are compared with the theoretical predictions obtained using the available analytical models. Finally, corrections to the available analytical models to predict the response of RCFST columns at room and freezing temperatures are introduced and discussed.

5.2 Details of tests columns

The RCFST columns tested in this research were designed to emulate typical bent columns of Alaska DOT bridges. As shown in Figure 5.1, the tests simulate the part of the column from the cap beam to the inflection point. The behavior of in-ground hinges, which develop in multiple column bents with continuous pile/shaft column system, was not experimentally investigated in this project (an ongoing research at NCSU is dealing with this topic). Geometric properties and test set up of the units are displayed in Figure 5.2. Table 5.1 presents the test matrix. In order to accommodate the range of

temperatures desired, the columns were tested inside an environmental chamber. Due to the space limitations for testing inside the chamber, the columns were tested in a horizontal position and designed at half the scale of the actual bridge column/pile. The thickness of the pipe was selected so that the Diameter-Thickness ratio represents that of actual practice in the pile/column design of the Alaska DOT (D/t~48). In the same way, the gap between the steel tube and the cap beam was reduced to 25 mm (1 in) as typical gaps in Alaska's DOT bridges is 50 mm (2 in). The column diameter of all the specimens was 457 mm (18in), cantilever length was 1651mm (65in), and transverse reinforcement was in the form of spirals spaced at 60mm (2.4in) and a steel pipe API-5L X52 of thickness 9.5mm (3/8in). The only variable between pairs of columns was the amount of longitudinal reinforcement; one pair was reinforced with 8#9 bars while the other pair was reinforced with 8#7 bars.

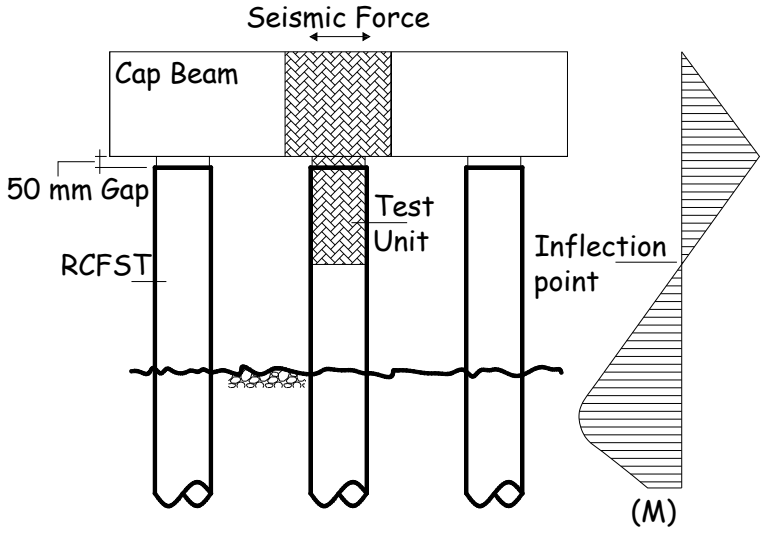

Figure 5.1 Prototype structure and its representative test model.

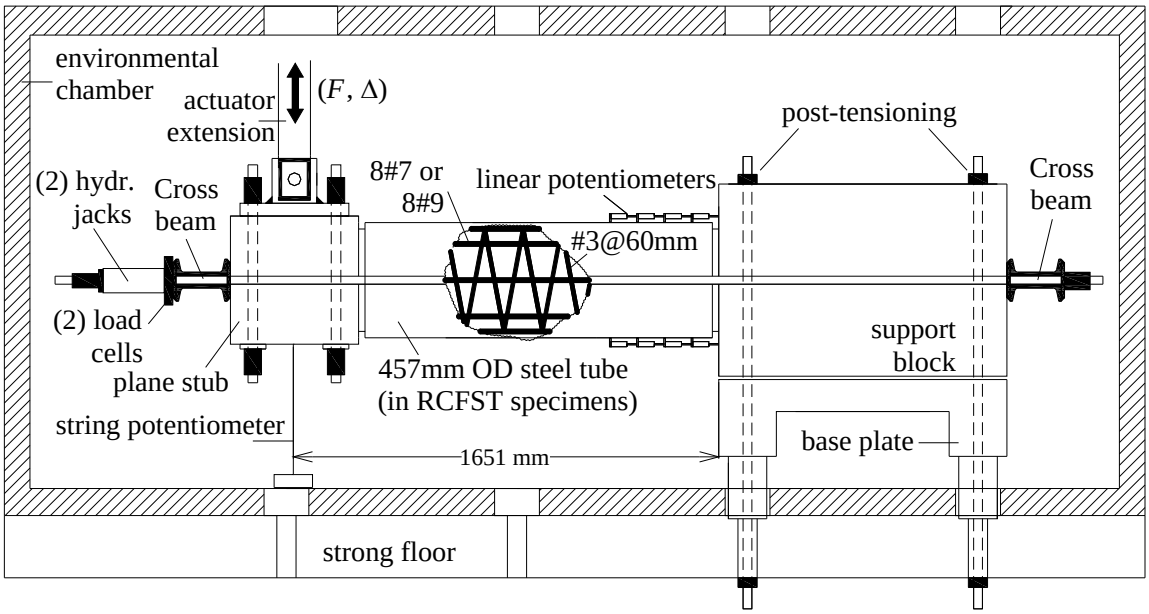

Figure 5.2 Reinforced concrete filled steel tube RCFST columns.

Table 5.1 Specimen matrix for the RCFST columns

UNIT	TEMP.	LONG. STEEL/ RATIO	TRANSV. STEEL/ RATIO	CONCRETE STRENGTH	AXIAL LOAD/ RATIO
RCFST 89A	22˚C 72˚F	8#9 3.1%	#3@60mm (2.4in) 9.5mm (3/8in) th. steel tube (1.2+8.5)%	26.2 MPa 3.8 ksi	231 kN 51.9 kips 5.9%
RCFST 89C	-36˚C -33˚F	8#9 3.1%	#3@60mm (2.4in) 9.5mm (3/8in) th. steel tube (1.2+8.5)%	44 MPa 6.4 ksi	219 kN 49.2 kips 3.3%
RCFST 87A	22˚C 72˚F	8#7 2.1%	#3@60mm (2.4in) 9.5mm (3/8in) th. steel tube (1.2+8.5)%	26.2 MPa 3.8 ksi	226 kN 50.8 kips 5.7%
RCFST 87C	-36˚C -33˚F	8#7 2.1%	#3@60mm (2.4in) 9.5mm (3/8in) th. steel tube (1.2+8.5)%	44 MPa 6.4 ksi	231 kN 51.9 kips 3.5%

5.3 Room temperature specimen RCFST-89A

This was the first specimen tested using the setup designed for cyclic reversal tests inside the environmental chamber. The test was started on August 25/2006 but it was stopped at ductility 1 because a piece of the actuator extension buckled. The extension was redesigned and the test was resumed on September 11/2006, unfortunately the test has to be stopped again at ductility 3 because the actuator extension started touching the hole in the roof of the environmental chamber. The extension was then redesigned and the test was resumed on October 4/2006, and it was possible to take the specimen up to ductility 6 where one of the longitudinal bars buckled. Figures 5.3 and 5.4 show the variation of temperature and axial load during the test, respectively.

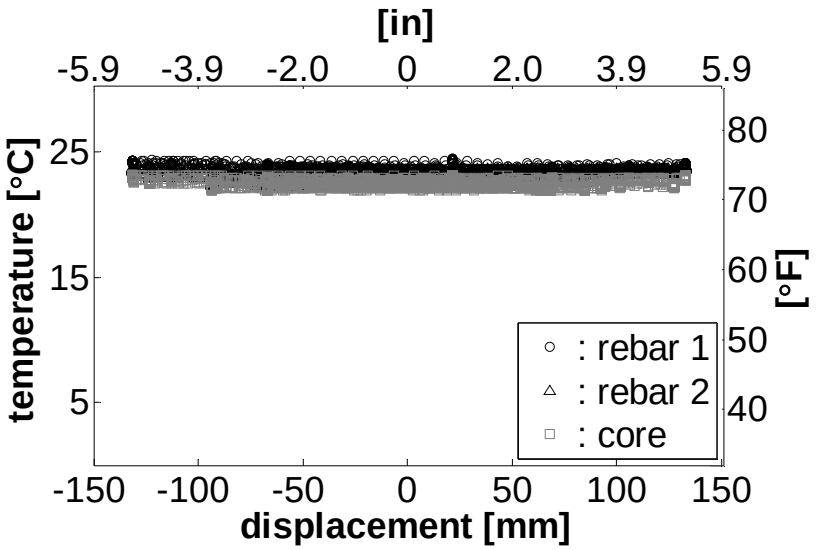

Figure 5.3 Temperature variations during the test of RCFST-89A.

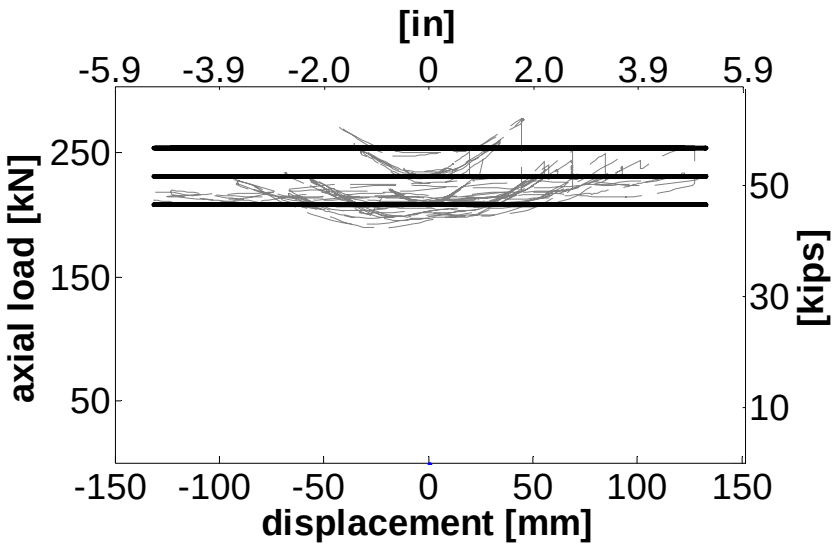

Figure 5.3 Axial load variations during the test of RCFST-89A.

5.3.1 RCFST-89A Test observations

The first hairline cracks become visible at the interface of the column with the footing during the third cycle of load control (127kN, 28.5kips). At the last cycle of force control (169kN 38kips) a hairline crack appeared in the top of the footing running parallel to the column. At ductility 1 the crack in the base of the column is well defined and run around the entire circumference of the column, the crack running parallel to the column in the top of the footing extended ~300mm (12in) from the base of the column (Figure 5.4).

After the last cycle of ductility 1.5 the crack at the interface of the column and the footing became wider at the top and bottom of the column. The first signs of concrete crushing were also noticed at this point. During the ductility 2 cycles (Figure 5.5) it was noticed that: (1) the crack around the base of the column was becoming deeper in the top and bottom faces, as if the column was trying to separate from the footing at the interface; (2) diagonal cracks appeared in the column-footing, extending from the column to the points where the footing is clamped to the floor and (3) the steel tube slipped about 5mm (0.2in) from the concrete in the column (Figure 5.6).

At ductility 2.5 concrete crushing is evident and a new wide crack appeared in the top of the footing running perpendicular to the column at about 70mm (2.75in) from the interface as shown in Figure 5.7. Cover concrete spalling was noticed during the cycles at ductility 3, damage to the concrete footing surrounding the base of the column was also observed at this level (Figure 5.8).

At the first cycle of ductility 4 the column reached the maximum lateral force during the test 311kN (70kips), cover concrete in the top and bottom face of the column is completely lost and some transverse steel is exposed. The level of damage of the footing at this point is significant and unexpected; it is clear at this point of the test that the steel tube has strengthened the column so significantly that most of the plasticity has moved into the footing (Figure 5.9). With the ductility 6 cycles the top part of the footing adjacent to the column started falling apart (Figure 5.10). During the last pull cycle of ductility 6 the top most bar buckled and the test was stopped at this point due to the severe footing damage. Figure 5.11 shows the specimen after removal of the instrumentation. It can be appreciated from this picture that the bar buckled at the column-footing interface and that damage to the core concrete was minimal due to the large confinement provided by the steel tube. However, this also provoked a migration of the spread of plasticity to the footing which is by no means desired in the capacity design approach.

Figure 5.4 Specimen RCFST-89A (top) after the first cycle of ductility 1.

Figure 5.5 Specimen RCFST-89A (top) after the first cycle of ductility 2.

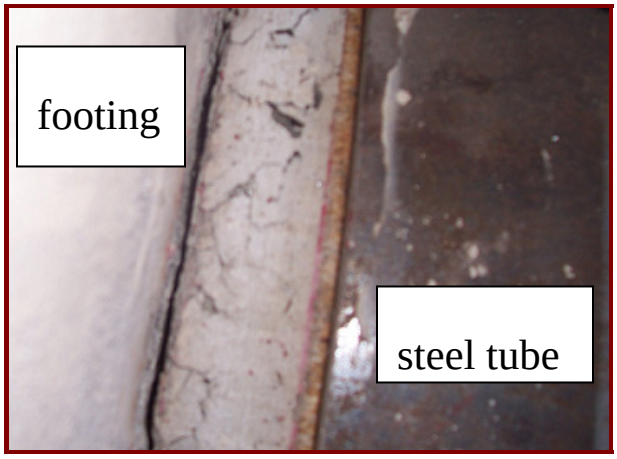

Figure 5.6 Specimen RCFST-89A (top) after the last cycle of ductility 2.

Figure 5.7 Specimen RCFST-89A (top) after the last cycle of ductility 2.5.

Figure 5.8 Specimen RCFST-89A (bottom) after the last cycle of ductility 3

Figure 5.9 Specimen RCFST-89A (top) after the last cycle of ductility 4

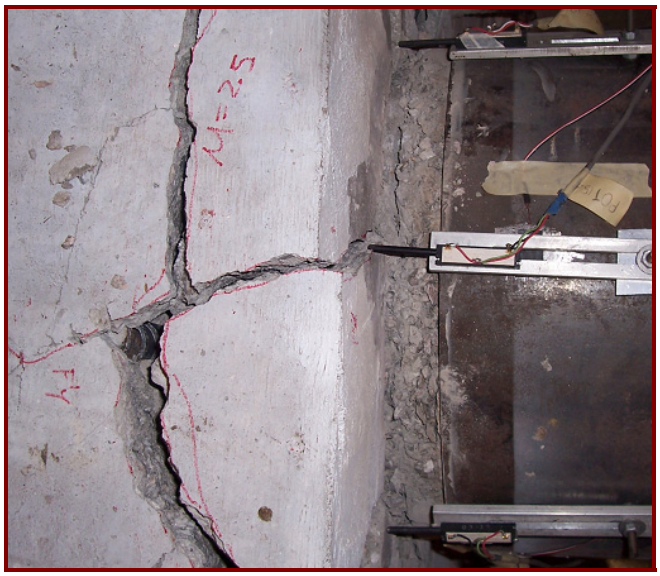

Figure 5.10 Specimen RCFST-89A (top) after the last cycle of ductility 6

Figure 5.11 Specimen RCFST-89A (top) after test

5.3.2 RCFST-89A Force displacement response.

The hysteretic force-displacement response obtained during the test is presented in Figure 5.12 along with the theoretical prediction obtained with a reduced equivalent plastic hinge length as will be discussed in the next section. Figure 5.13 shows the

average first peak force-displacement envelope next to the theoretical envelopes obtained using: (1) The equivalent plastic hinge length recommended for steel jacketed columns (Chai et al. 1991) including the correction factor of 0.59 for the current test set up $L_p = 0.59\left(2L_{sp} + g\right) = 435mm$ and (2) The equivalent length obtained in this specimen from the experimental results $L_p = 225mm$. It is seen from Figure 5.13 that a closer match is obtained using the reduced plastic hinge length. In the case of the RCFST specimens transverse steel is present in the form of circular spirals and steel tubes. However, as shown in Figure 5.22, the confinement induced strain in the steel tube reached only half the yield strain. Therefore, in the theoretical predictions the confined concrete was modeled considering all the confinement provided by the spirals and only half the confinement provided by the steel tube.

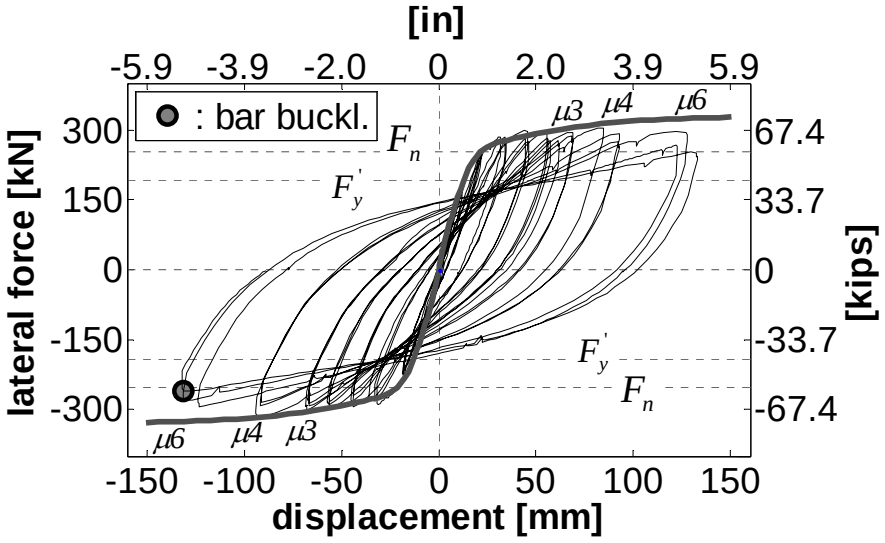

Figure 5.12 RCFST-89A Hysteretic response and theoretical envelope

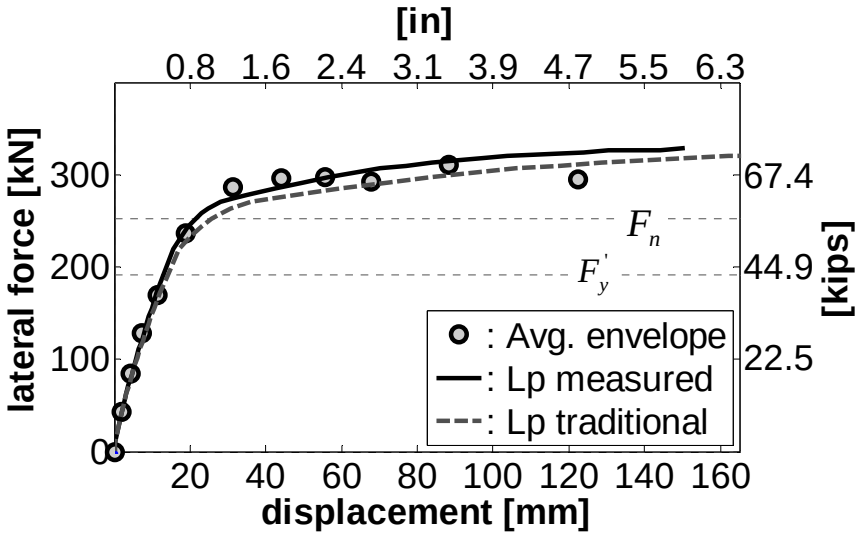

Figure 5.13 RCFST-89A First cycle envelope and theoretical envelopes

5.3.3 RCFST-89A Curvature profiles.

As was the case for the conventional columns (specimens FL-89A and F-89C), the gauge length for the bottom cell includes a component due to strain penetration. The magnitude of this addition for unit RCFST-89A was found to be 150 mm. Figure 5.14 shows the match between the theoretical and actual moment curvature response at the base of the column. Figure 5.15 shows the curvature profiles at *f'y, μ1, μ2, μ3* and *μ4* calculated with the data recorded by the lpot's. These profiles show that all the curvature is concentrated in the first cell; readings in all the other cells were negligible. It is important to note that the base curvature values are not reliable since the threaded studs connecting the lpot's to the column were drilled only into the steel tube which slipped from the concrete in the column during the test (Figure 5.6). Furthermore, curvatures at the base of the column presented in Figure 5.15 may be even larger as the gage and location of the first cell, 160 mm (6.3 in) from the base of the column, was certainly not the most appropriate for the behavior exhibited by this column. It can be observed from the condition of the specimen after the test (Figure 5.16) that all the plasticity was concentrated in the 25 mm (1 in) gap and 100 mm (4 in) inside the footing. Nevertheless, Figure 5.15 provides us with key qualitative information regarding the behavior of RCFST columns.

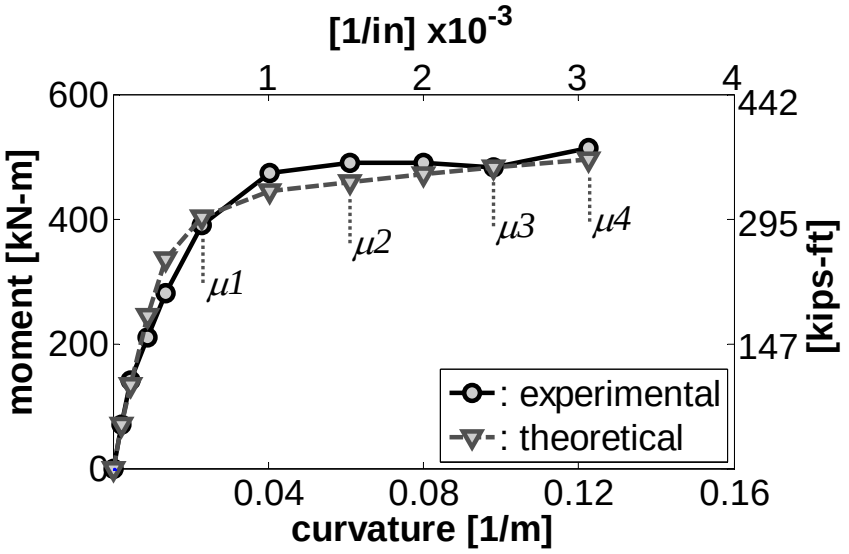

Figure 5.14 RCFST-89A Moment curvature at column base.

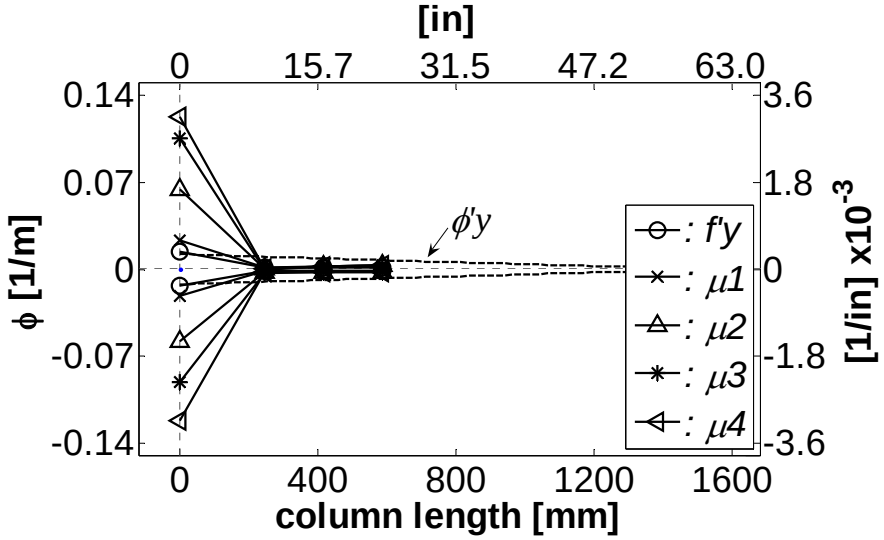

Figure 5.15 RCFST-89A Curvature profile

Figure 5.16 RCFST-89A Condition of the specimen after test

5.3.4 RCFST-89A Equivalent plastic hinge length.

It is evident from the condition of the specimen during the test (Figure 5.16) and from the shape of the curvature profiles (Figure 5.15) that the spread of plasticity in the column was minimal when compared to ordinary RC columns (e.g. FL-89A). For reasons mentioned before, the readings of the linear potentiometers in the base of the column are not reliable for calculating curvature values, therefore the methodology used in the ordinary RC columns (FL-89A and FL-89C) to calculate the equivalent plastic hinge length from the experimental data can not be applied in this case. In order to estimate a value for the equivalent plastic hinge length we use the theoretical moment-curvature relation at the base of the column along with the lateral force and tip displacement measured during the test. As it has been shown that all the plasticity in this specimen is concentrated in the base of the column, the results obtained should be very close to the proper value. Figure 5.17 shows the results obtained, different values are obtained for the pull and push directions. An average value of 225 mm (8.9 in) is adopted. This implies a reduction of 52% over the value recommended by Chai et al. (1991) and Priestley et al. (1996) for steel jacket retrofitted columns once the correction factor of 0.59 for the

current setup is applied $L_p = 0.59\left(2L_{sp} + g\right) = 435mm$. This difference can be attributed to 2 different facts:

- As the steel tube is present in the RCFST columns since the casting of the concrete, it is expected to provide better confinement than the steel jacket of a retrofitted column, which in theory should increase the bond strength between the longitudinal bars and the core concrete and reduce the strain penetration length.

- The ratio Diameter/thickness of the steel jacketed columns tested by Priestley et al. was D/t = 122 providing a transverse steel ratio of 3.1%, which is less than half the transverse steel ratio provided by the steel pipe in RCFST columns of 8.5% with D/t = 48. The presence of such a stiff pipe cause the column to deflect almost as a rigid body with a reduced plastic hinge centered at the base of the column.

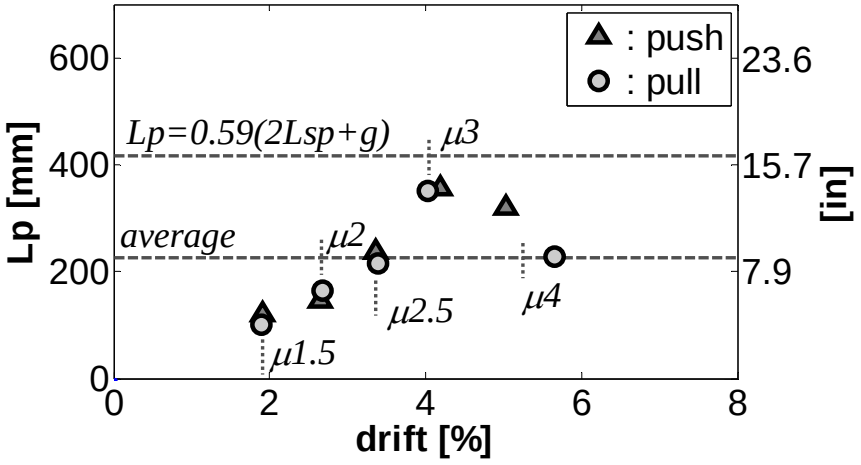

Figure 5.17 RCFST-89A Equivalent plastic hinge length

5.3.5 Strains on longitudinal reinforcement

Strain profiles of the bottom most bar are not shown for this specimen because only one of the strain gages in this bar worked properly. Figure 5.18 presents the strain profiles of the top most bar at different levels of ductility. It is seen from this figure that up to the last cycle of force control (when the extreme bar is at first yield) the distribution

of strain is linear along the bar. However, with the displacement control cycles (when the bar has reached yield and the plastic hinge is defined), the strains are concentrated in the base of the column and the increase in strain at other locations is minimal. Figure 5.19 shows the strain history of the second strain gage in the top bar placed 240 mm (9.5 in) from the base of the column. It is noted that this location on the bar did not yield during the test. If we assume that the strain in the bar increases linearly from this point to the base of the column and then decreases inside the footing at the same rate, then the length of the equivalent plastic hinge length should be a little less than 240 mm. This corroborates the reduction of the equivalent plastic length found using the moment-area method.

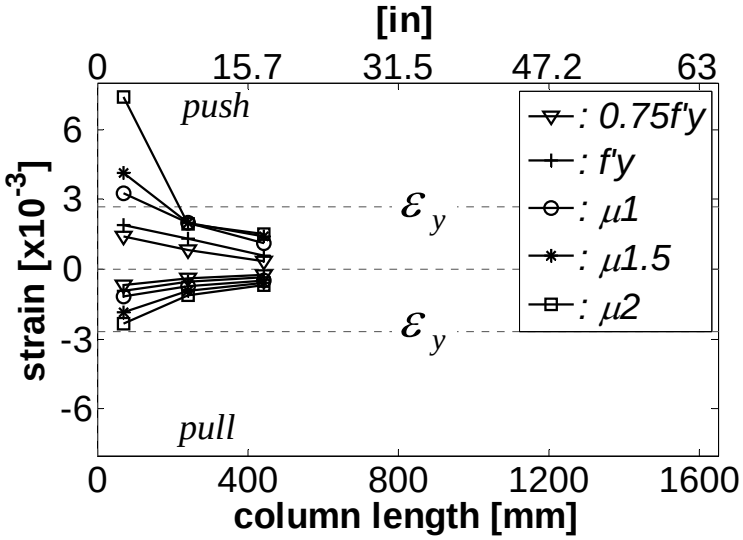

Figure 5.18 RCFST-89A Top most bar strain profiles

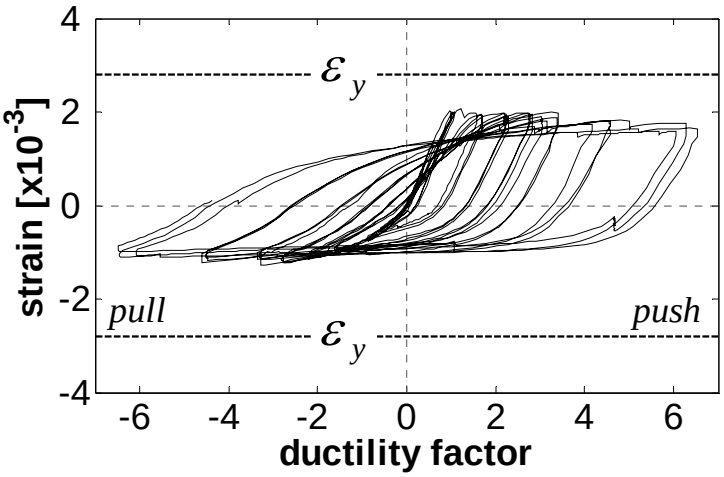

Figure 5.19 RCFST-89A Top bar strain history 240mm from the base.

5.3.6 Strains on transverse reinforcement

Figure 5.20 shows the confinement strains in the bottom side of the spirals. Notice that the values of strain are very small, e.g. at ductility 4 the strain does not reach even half of the yield strain. This was expected due to the effect of the thick pipe surrounding the column and providing extreme confinement and shear strength. Despite the smaller of the strains recorded, the shape of the profile corroborates once again the reduction of the plastic hinge length as a direct effect of the disproportionate stiffness provided by the steel pipe to the column. Figure 5.21 shows the shear strains in the spiral, just as in the confinement strains and due also to the effect of the steel pipe, the shear strains in the spiral are very small.

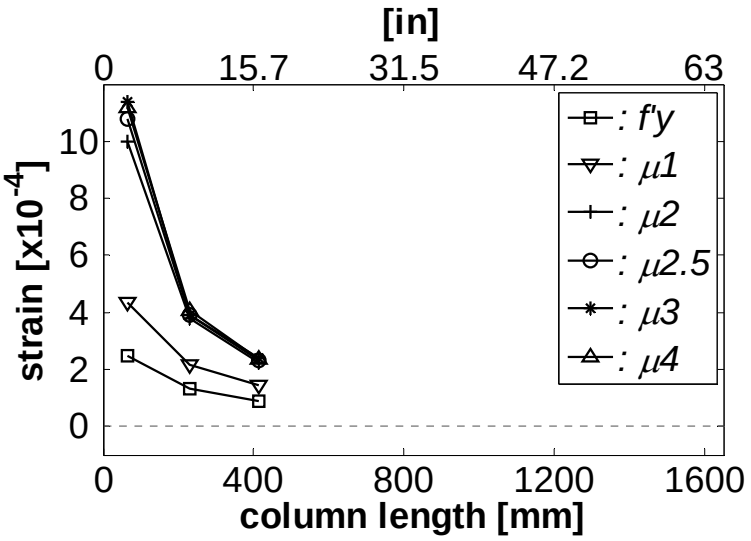

Figure 5.20 RCFST-89A Bottom side of spiral (confinement) strain profiles

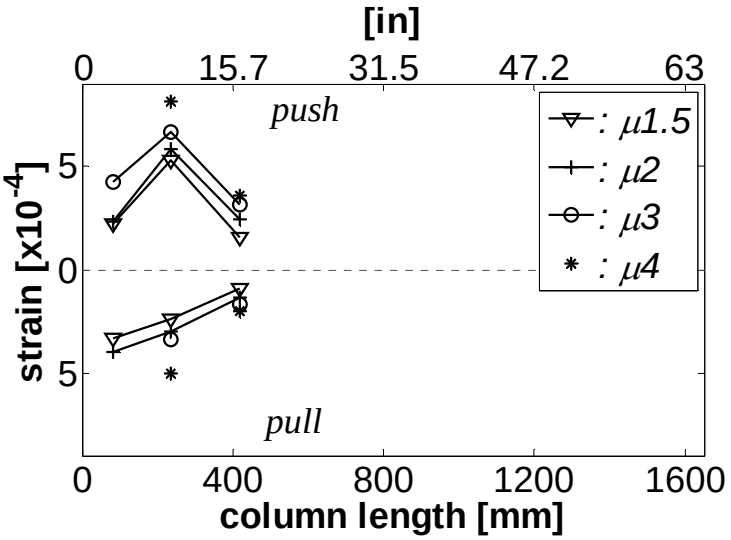

Figure 5.21 RCFST-89A Right side of spiral (shear) strain profiles

5.3.7 Strains on steel tube

Information collected from the strain gages placed on the external surface of the steel pipe is also presented in the form of strain profiles. Figures 5.22 and 5.23 show the steel tube confinement induced strain profiles while Figures 5.24 and 5.25 show the steel tube shear induced strains profiles. As with the spiral strains, the strains recorded are very

small which implies that the thickness of the pipe is larger than needed from a structural behavior point of view. It is important to mention here that the thickness of the steel tube pipe is commonly determined from geotechnical considerations. Very thin-wall pipe piles may be difficult to drive in some cases and a thicker wall may be required (PDCA, 2007).

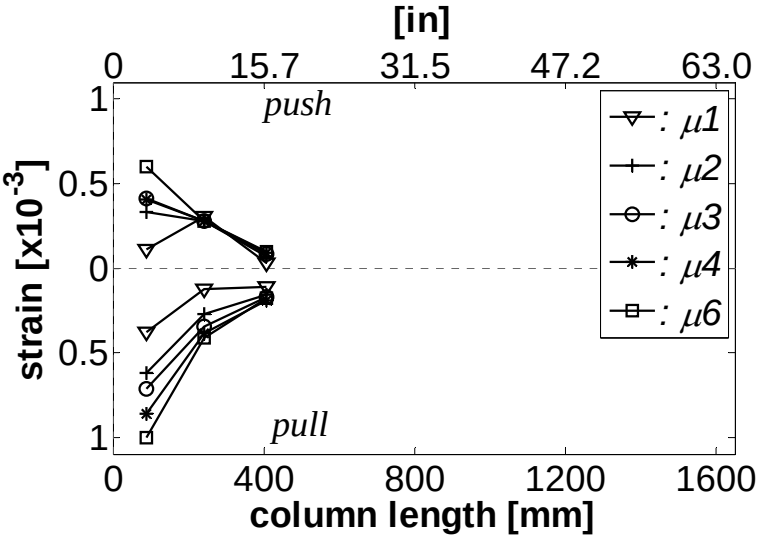

Figure 5.22 RCFST-89A Top side of pipe confinement strain profiles

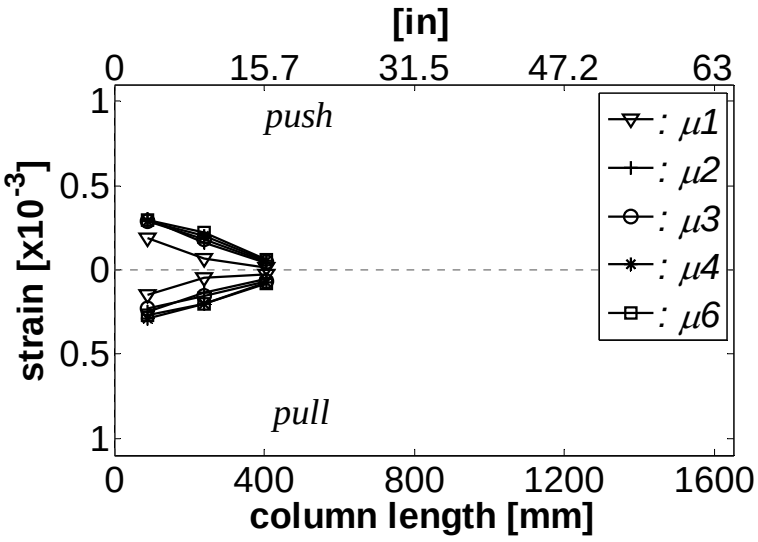

Figure 5.23 RCFST-89A Bottom side of pipe confinement strain profiles

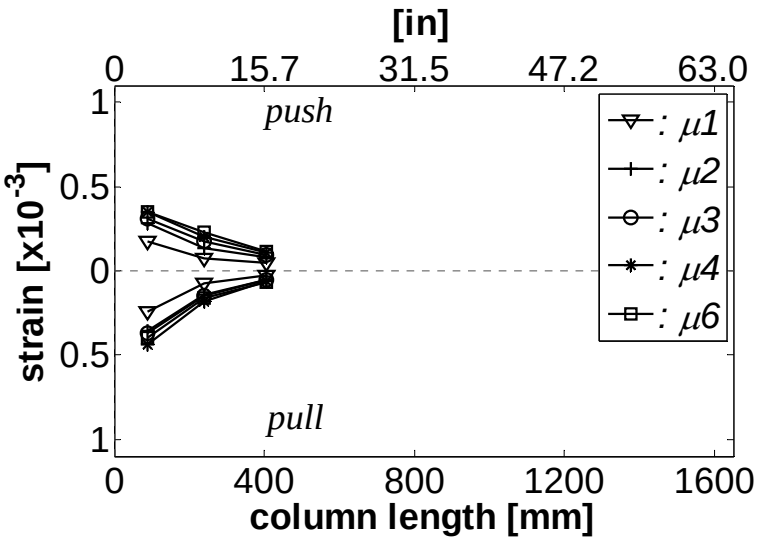

Figure 5.24 RCFST-89A Right side of pipe shear strain profiles

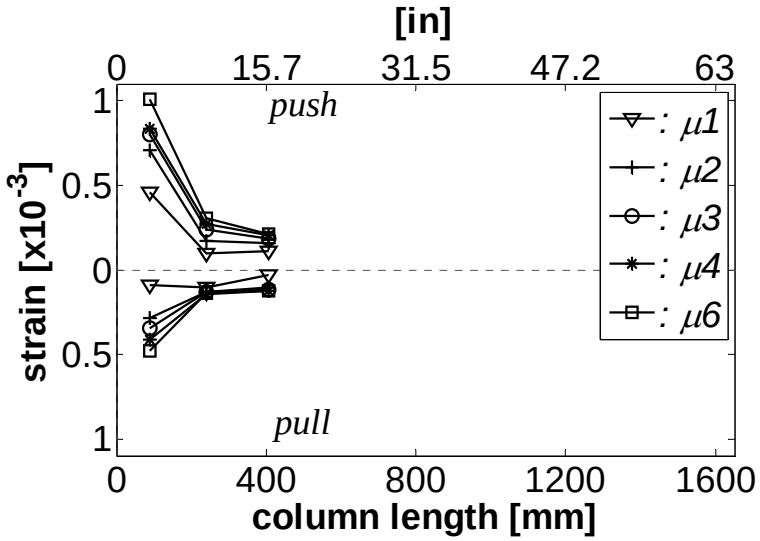

Figure 5.25 RCFST-89A Left side of pipe shear strain profiles

5.3.8 Validity of test data

Data recorded during the test is validated as explained in section 4.3.1.6. Figure 5.26 shows the results obtained. The match between measured displacement and the calculated from the lpot's is very close up to ductility 4.

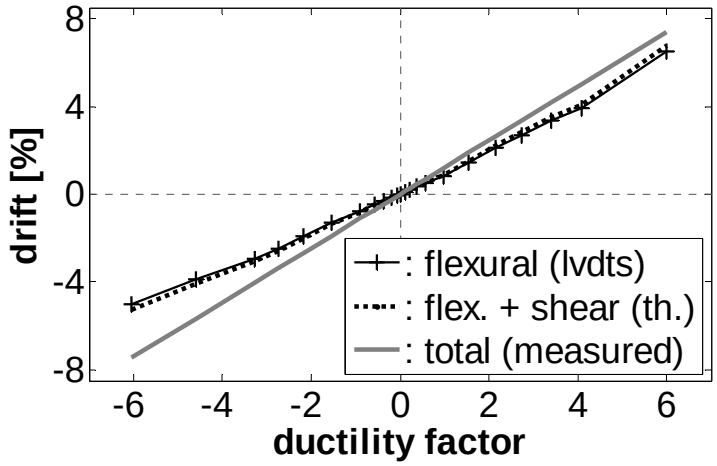

Figure 5.26 RCFST-89A Validity of test data

5.3.9 Comparison with FL-89A

This section compares the results obtained from the tests of units FL-89A and RCFST-89 with the aim of evaluating the advantages and disadvantages of using RCFST columns over ordinary reinforced concrete ORC columns. Notice that the only differences between both columns is the presence of the steel tube in RCFST-89A and the compressive strength of the concrete. Day of test compressive strength for RCFST-89A was 24.6 MPa (3.8 ksi) and 21.4 MPa (3.1 ksi) for FL-89A.

A number of observations can be made form the average first peak envelopes displayed in Figure 5.27:

(1) The RCFST column exhibits an average increase of 8% in the flexural strength when compared to the ordinary column. As mentioned before the concrete strength of the RCFST column was 22% larger than the strength of the ORC column. However from section analyses this increase in the concrete compressive strength will represent an increase of just 2% in the section flexural strength, leaving a 6% increase on flexural strength due mainly to the confinement provided by the steel tube.

(2) Strength degradation associated with the increasing ductility demand started earlier in the RCFST specimen, at a displacement 20% smaller than the exhibited by the ORC column.

(3) Lateral displacement at which buckling was first observed was 17% shorter in the RCFST column than in the ORC column.

(4) Initial stiffness, calculated at the theoretical force level for first yield in the ORC column, is 28% larger in the RCFST column.

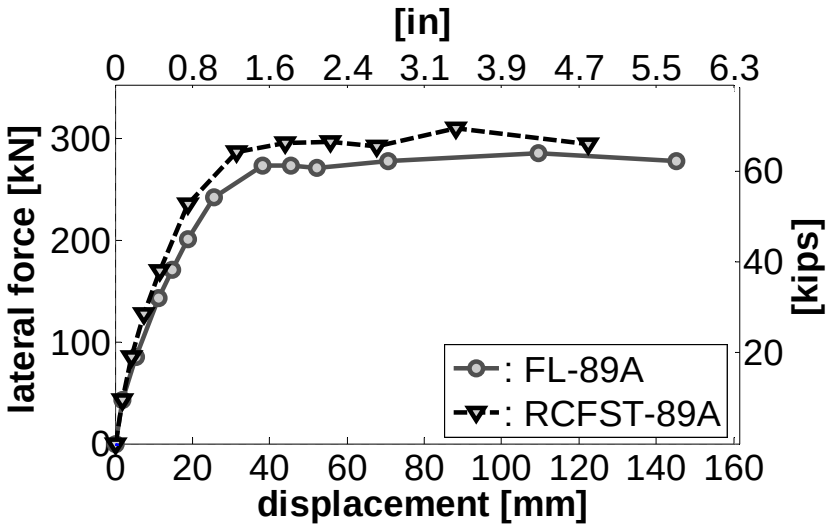

Figure 5.27 RCFST-89A and FL-89A first peak envelope

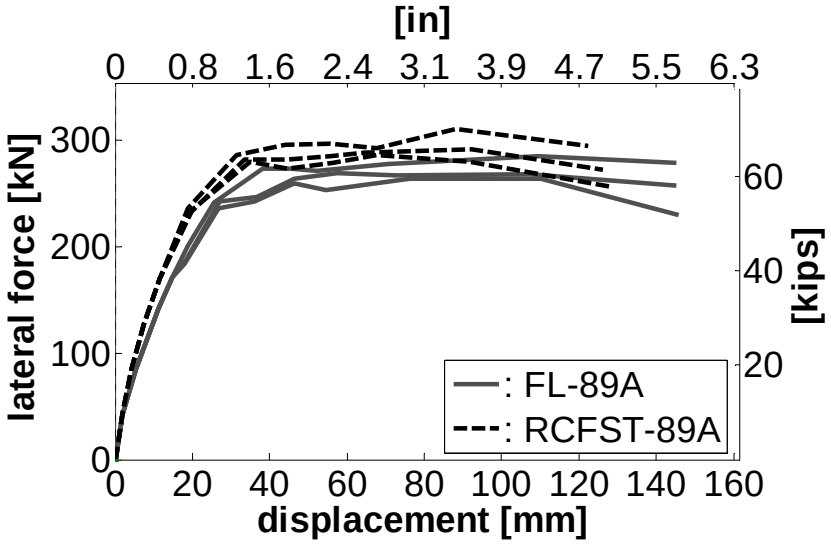

Figure 5.28 RCFST-89A and FL-89A three cycles envelope

Figure 5.28 shows the average envelopes for the three cycles, it is noticed that the strength degradation associated with increasing number of cycles at the same ductility demand is basically the same for both specimens.

Figures 5.29 and 5.30 compare the energy dissipation and hysteretic damping properties, respectively. It is noticed that for a given drift level, the RCFST exhibited larger energy dissipation and hysteretic damping than the ORC column.

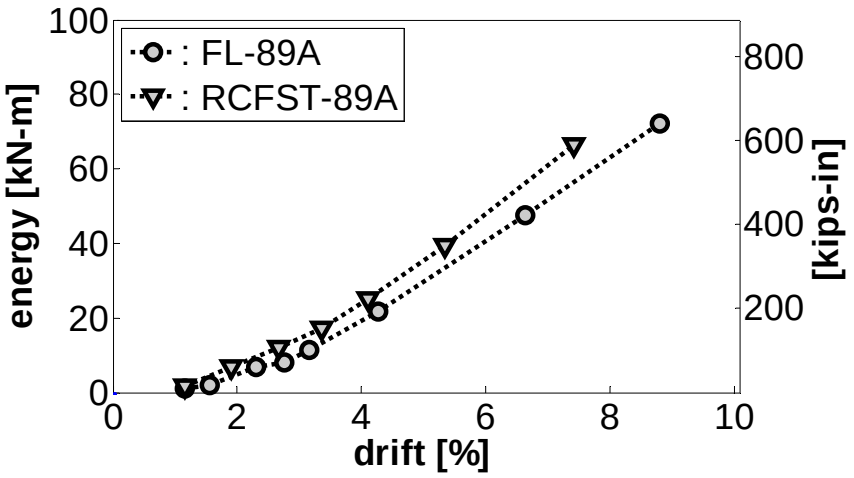

Figure 5.29 RCFST-89A and FL-89A energy dissipation

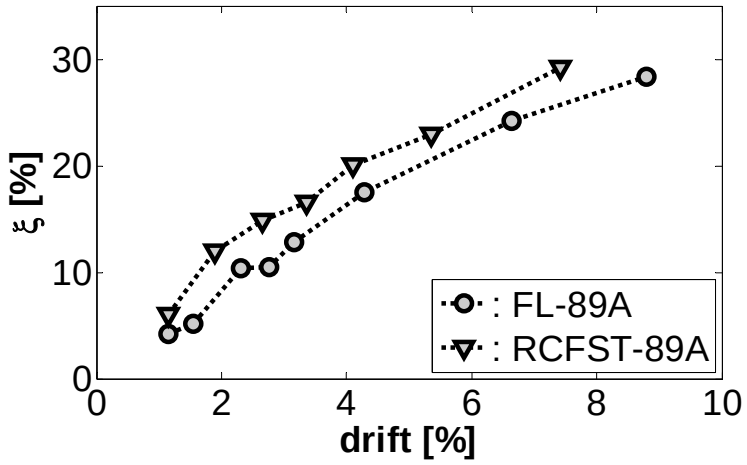

Figure 5.30 RCFST-89A and FL-89A hysteric damping

Figure 5.31 compares the curvature profiles at ductility 4 of both units. For the ORC columns, curvature profiles indicated significant contribution of flexural deformations over a length 500mm (20in) from the base of the column. On the other hand, RCFST columns concentrate practically all the rotation in the base of the column, with no contribution from gage lengths away from the base. This phenomenon is also observable from the equivalent plastic hinge lengths displayed in Figure 5.32, it is seen that the equivalent plastic hinge length on RCFST columns is almost half the obtained for ORC columns. Finally, Figure 5.33 compares the final condition of both specimens, notice from this figure that large rotations concentrated in the base of the RCFST columns caused the inelastic action to propagate inside the footing (cap beam in the real structure) and provoke severe damage to it.

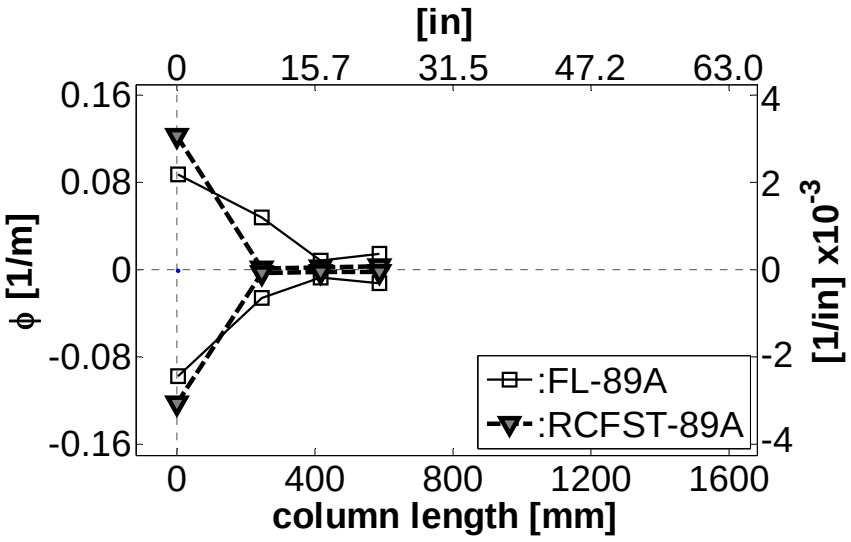

Figure 5.31 RCFST-89A and FL-89A curvature profiles at ductility 4

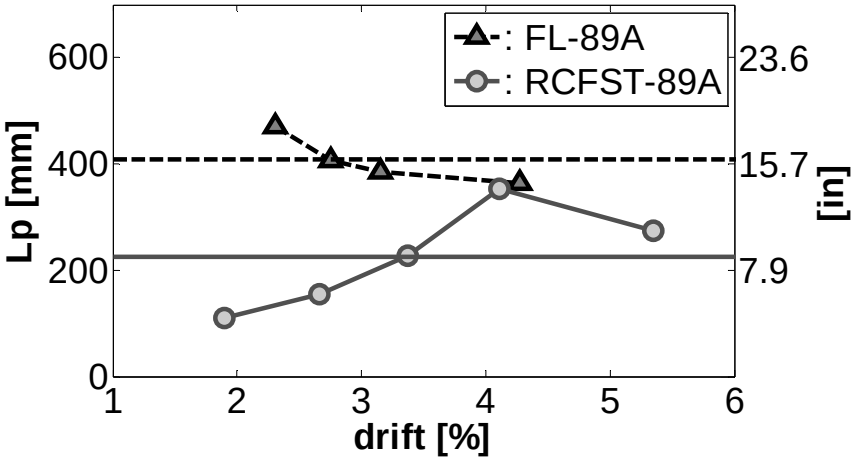

Figure 5.32 RCFST-89A and FL-89A equivalent plastic hinge length

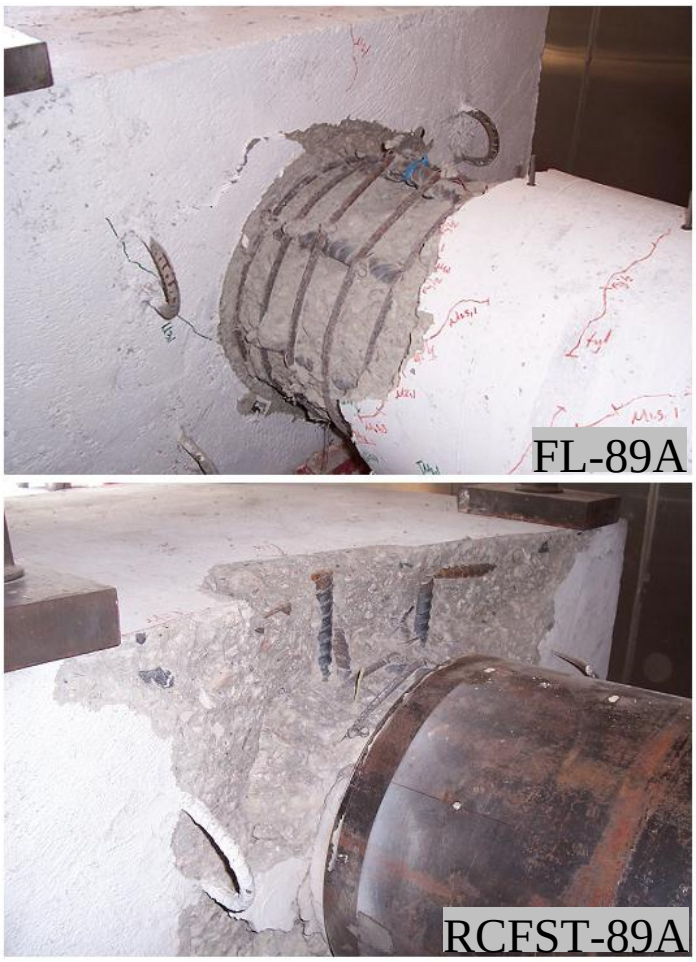

Figure 5.33 RCFST-89A and FL-89A conditions of the specimen after test

5.4 Cold temperature specimen RCFST-89C

Unit RCFST-89C was tested on February 9/2007. The column was subjected to the same load history of cyclic reversals applied to the companion room temperature specimen (RCFST-89A). The cooling process started ~26 hours before the test, during all this time and all through the test, the specimen was exposed to a constant temperature of -40°C (-40°F). Figure 5.34 shows the temperatures registered by the thermocouples imbedded in the specimen as a function of the column tip displacement. As in the conventional columns, the temperature in the core of the column was ~5°C warmer than at the level of the longitudinal bars. However, it is seen from this figure that the temperature was constant throughout the entire test. Figure 5.35 displays the variation of axial load during the test. Horizontal lines in this figure denote the average and ±10% deviations from average of the applied axial load.

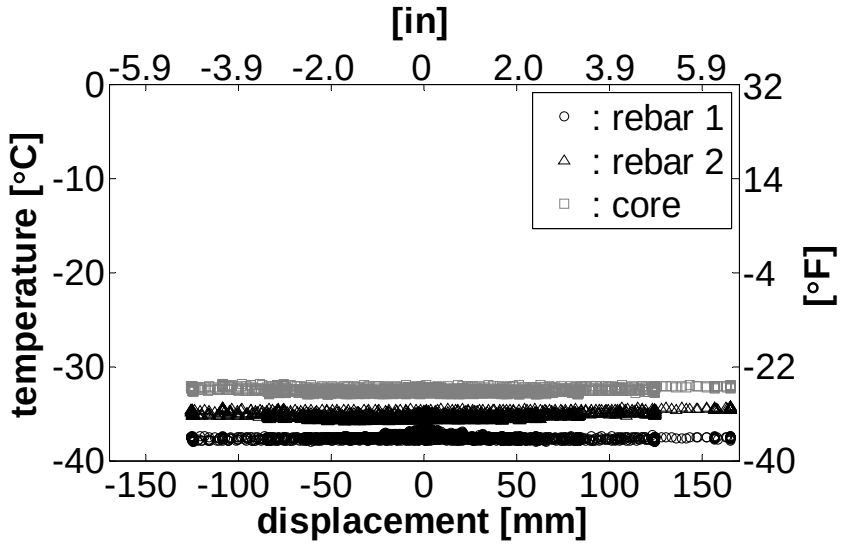

Figure 5.34 Temperature variations during testing of RCFST-89C.

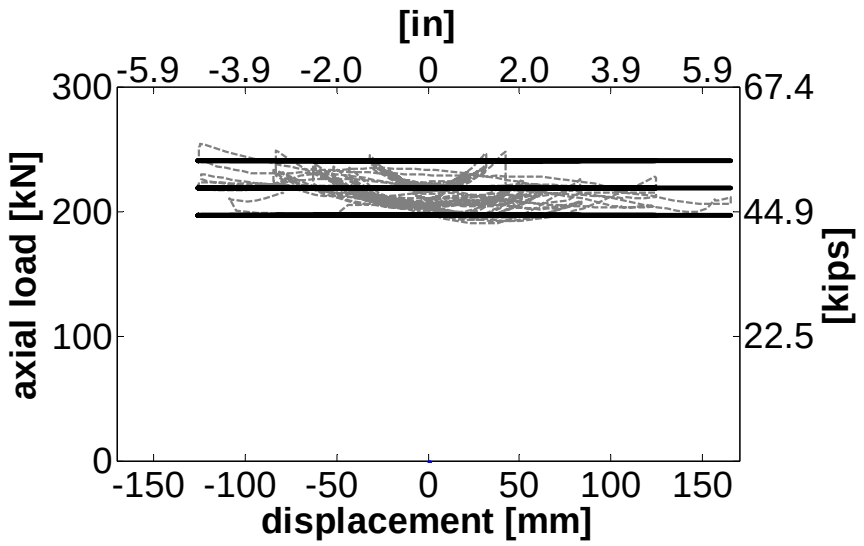

Figure 5.35 Axial load variations during testing of RCFST-89C.

5.4.1 RCFST-89C Test observations

First cracks were noticed at the base of the column during the first push of ductility 1, after three cycles at this level of ductility a well defined flexural crack is observed running all around the base of the column (Figure 5.36). After the cycles at ductility 1.5 (Figure 5.37) the crack in the base has become wider and deeper, it is also noticed that the steel tube slipped from the concrete ~2 mm.

Crushing of the cover concrete is first noticed at ductility 2 along with some spalling of the concrete at the interface between the column and footing (Figure 5.38). At ductility 2.5 (Figure 5.39) crushing and spalling of the cover concrete is evident. After the cycles at ductility 3 (Figure 5.40) it was noticed that the column was digging inside the footing.

During the ductility 4 cycles (Figure 5.41) it was noticed that the damage is concentrated not only in the gap between the steel pipe and the footing, but also at the part of the footing surrounding the base of the column. After the first cycle at ductility 6 (Figure 5.42), concrete damage is more severe in the part of the column imbedded in the footing, to the point that part of the spiral inside the footing is now exposed. As confinement is not a localized action, the large confinement provided by the pipe also

effects the surrounding concrete, which explains why concrete in the vicinity of the steel tube looks to be in better condition. When going to the last push cycle of ductility 6 the top most bar fractured before reaching the target displacement of 122 mm (4.8 in). The fracture occurred at a tip displacement of 81 mm (3.2 in).

At the first push of ductility 8 (Figure 5.43) another of the top bars fractured just before the target displacement of 163 mm (6.4 in) was reached. Finally, during the first pull cycle of ductility 8 the bottom most bar fractured when the tip displacement in the pull direction was only 50 mm (2 in). The test was stopped at this point. Inspection of the specimen after the test in Figure 5.44 shows that the bottom-most bar did not completely fracture, but rather cracked in three different spots along the bottom face of the bar. It was also noticed that the bottom face of the column presented more severe damage in the core concrete than the top face.

Figure 5.36 RCFST-89C (top) after the last push of ductility 1.

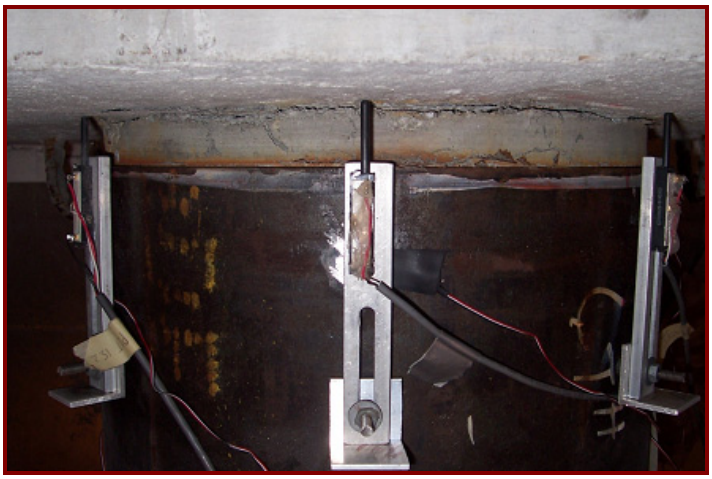

Figure 5.37 RCFST-89C (top) after the last push of ductility 1.5.

Figure 5.38 RCFST-89C (top) after the last push of ductility 2.

Figure 5.39 RCFST-89C (top) after the last push of ductility 2.5.

Figure 5.40 RCFST-89C (top) after the last push of ductility 3.

Figure 5.41 RCFST-89C (top) after the last push of ductility 4.

Figure 5.42 RCFST-89C (top) after the first push of ductility 6.

Figure 5.43 RCFST-89C (top) after the first push of ductility 8.

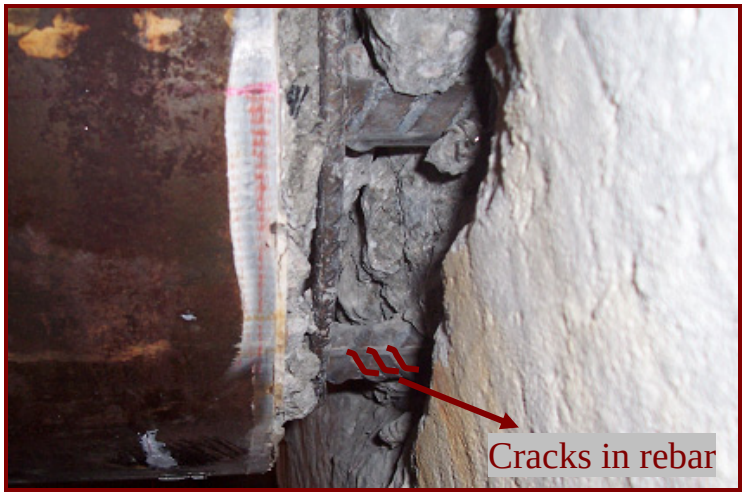

Figure 5.44 RCFST-89C (bottom) after test.

5.4.2 RCFST-89C Force displacement response.

Figure 5.45 shows the hysteretic force-displacement response recorded during the test along with the theoretical envelope obtained using the equivalent plastic hinge length calculated from the results obtained during the test. The rupture of three longitudinal bars can be clearly identified in this graph. Figure 5.46 shows the average first peak envelope next to the theoretical envelopes. As was the case for the room temperature specimen, the predictions presented were obtained using (1) the equivalent plastic hinge length recommended for steel jacketed columns (Priestley et al. 1996) including the correction

factor for the current test set up $L_p = 0.59\left(2L_{sp} + g\right) = 487mm$ and (2) the equivalent length obtained from the experimental results $L_p = 226mm$. It is noticed from Figure 5.46 that the reduction of the plastic hinge length does not improve the matching with the experimental results by much. However, the prediction of the displacement capacity do is improved when the plastic hinge is reduced. Note that the match between the predicted envelopes and the actual results is very good up to ductility 2. After this point some increase in the strength of the specimen, which is expected due to the strain hardening of the longitudinal steel (as it is reveal in the theoretical predictions), was not observed during the test. Based on this we can say that strength degradation started prematurely in this unit.

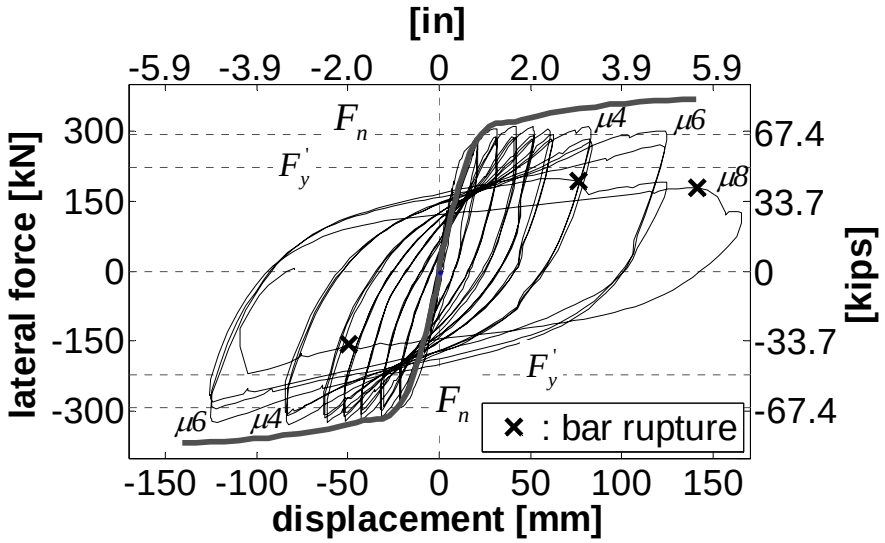

Figure 5.45 RCFST-89C Hysteretic response and theoretical envelope

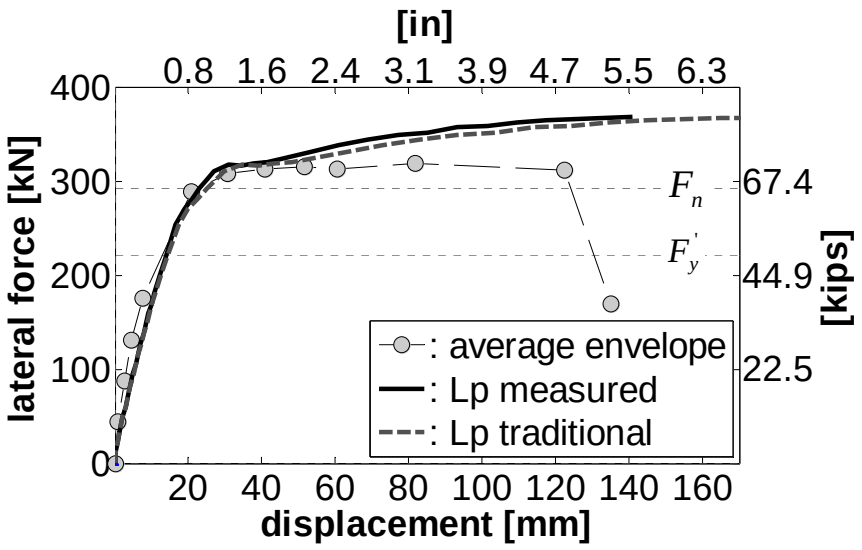

Figure 5.46 RCFST-89C First cycle envelope and theoretical envelopes

5.4.3 RCFST-89C Curvature profiles.

As for all previously discussed specimens, the gauge length for the bottom cell includes a component due to strain penetration. The magnitude of this addition for unit RCFST-89C was found to be 56 mm. Figure 5.47 shows the match between the theoretical and actual moment curvature response at the base of the column. Figure 5.48 shows the curvature profiles at *f'y, μ1, μ1.5, μ2* and *μ2.5* after this point lpot's data was not consistent. For example, the room temperature specimen profiles show that all the curvature is concentrated in the first cell with the readings in all the other cells being negligible. The curvature values calculated at the base of the column are more reliable than that calculated for the room temperature unit because the slip between the steel pipe and the concrete was minimal. This reduction in the amount of pipe slip can be attributed to the high adhesive force associated to the ice surface (Frankenstein and Tuthill, 2002).

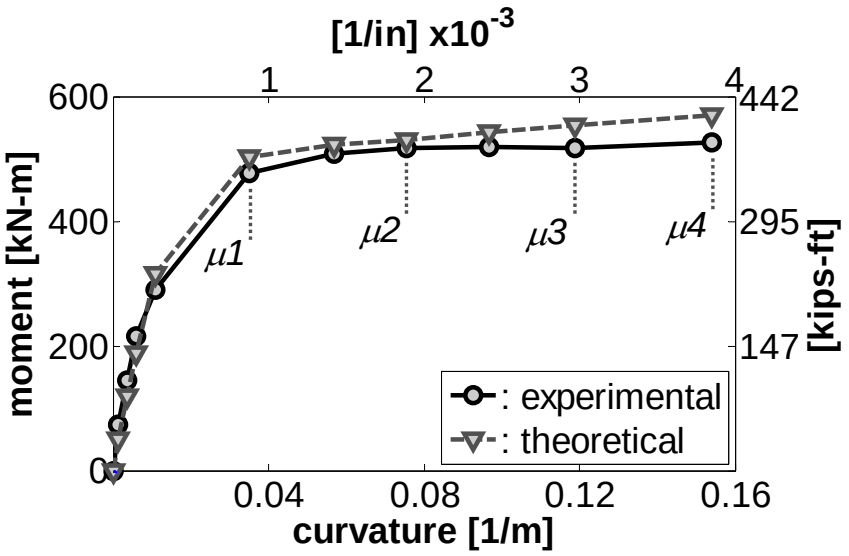

Figure 5.47 RCFST-89C Moment curvature at column base.

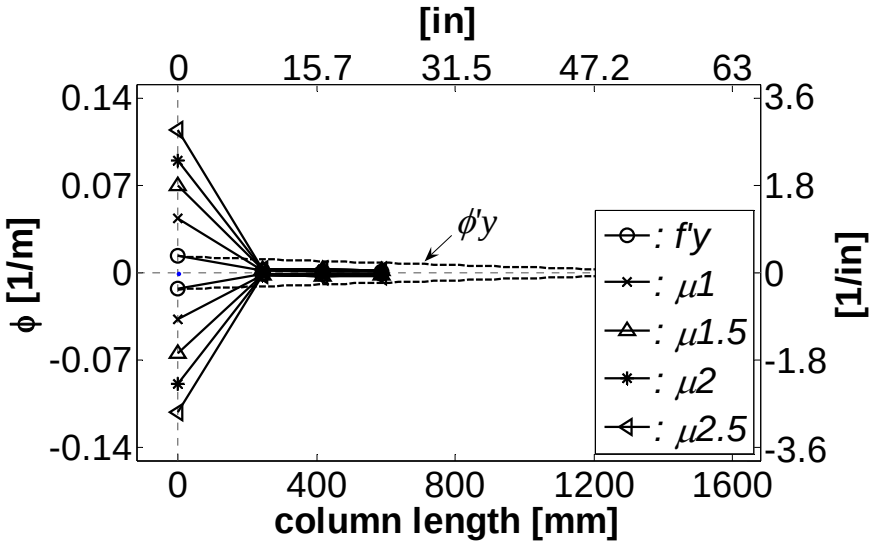

Figure 5.48 RCFST-89C Curvature profile

5.4.4 RCFST-89C Equivalent plastic hinge length.

Figure 5.49 shows the equivalent plastic hinge lengths obtained using the peak base curvatures, tip displacements and lateral forces for different levels of displacement demand. It is seen that the average value obtained is 226 mm which is practically the same length obtained as for the room temperature specimen (RCFST-89A). This implies

a reduction of the plastic hinge length in the cold specimen for the reason that L_p increases with the yielding stress of the steel, which has been shown to be larger at low temperatures. A reduction of 46% over the value recommended by Chai et al. (1991) for steel jacket retrofitted columns once the correction factor of 0.59 for the current setup is applied $L_p = 0.59\left(2L_{sp} + g\right) = 487mm$ is identified.

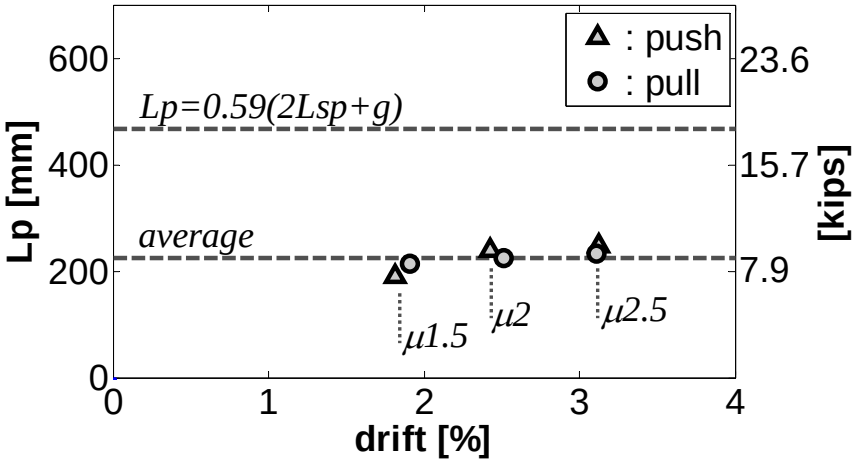

Figure 5.49 RCFST-89C Equivalent plastic hinge length

5.4.5 Strains on longitudinal reinforcement

Most of the strain gages placed on the main longitudinal bars did not work properly due presumably to the extreme environment they were exposed to. Therefore, information regarding strains on the longitudinal reinforcement is limited for this specimen. Strain profiles were only generated for the top bar and only for low levels of lateral demand. Figure 5.50 shows the results obtained, as expected the strain distribution follows the same pattern as the curvature profiles with most of the deformation in the longitudinal bar concentrated near the column base.

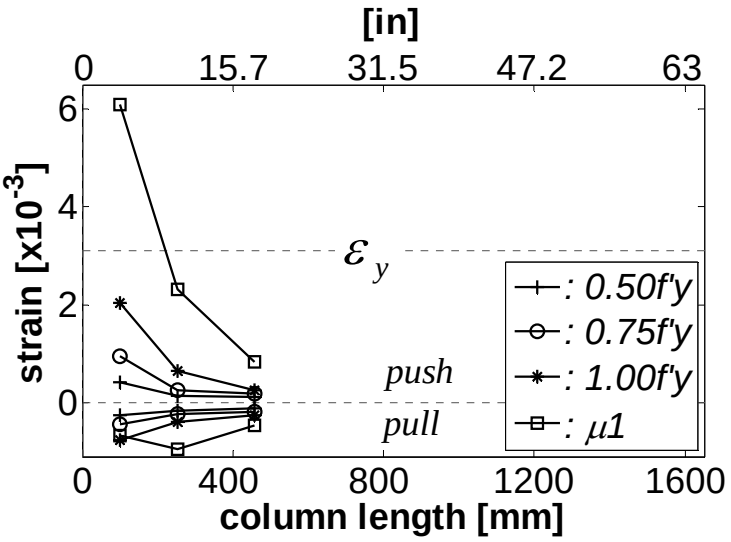

Figure 5.50 RCFST-89C Top most bar strain profiles

5.4.6 Strains on transverse reinforcement

Figure 5.51 shows the induced shear strains recorded by a strain gage placed on the right side of the spiral a distance 270 mm from the base of the column. This was the only strain gage in the transverse reinforcement that worked properly during a significant period of time during the test. It is seen that strains recorded are small even for a large level of ductility demand, which implies that most of the shear strength is provided by the steel tube.

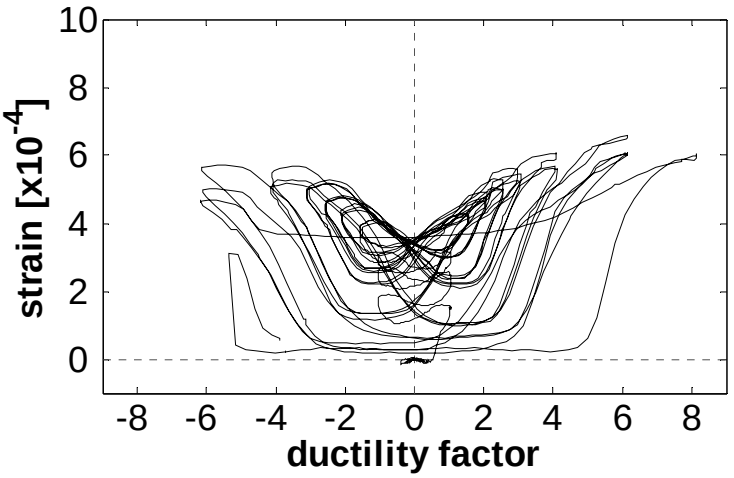

Figure 5.51 RCFST-89C Shear induced strain in spiral

5.4.7 Strains on steel tube

Figures 5.52 and 5.53 show the confinement induced strain profiles in the top and bottom face of the steel tube, respectively. As expected, in the top face larger strains are recorded in the pull direction when the concrete in the top of the column is in compression and tries to expand due to the Poisson effect. However, in the bottom face the strains recorded are similar in both directions and smaller than the strains recorded in the top face. This is due to the strength provided by the large metallic plate in which the footing of the column rests.

Figures 5.54 and 5.55 show the shear induced strain profiles in the right and left faces of the pipe, respectively. As for the confinement induced profiles the strains recorded are small, not even reaching half the yield strain of the pipe.

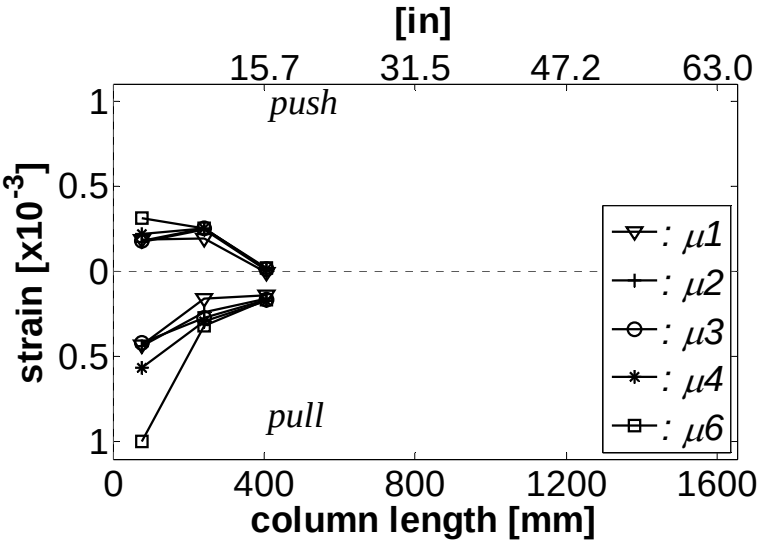

Figure 5.52 RCFST-89C Top side of pipe confinement strain profiles

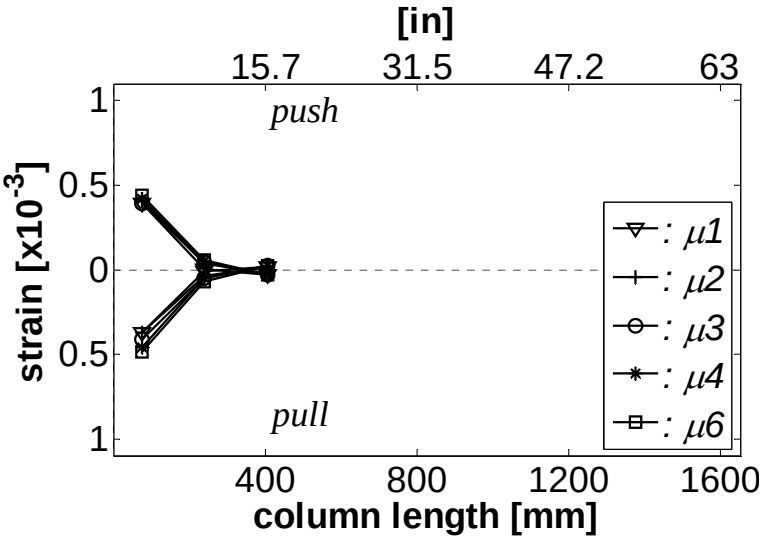

Figure 5.53 RCFST-89C Bottom side of pipe confinement strain profiles

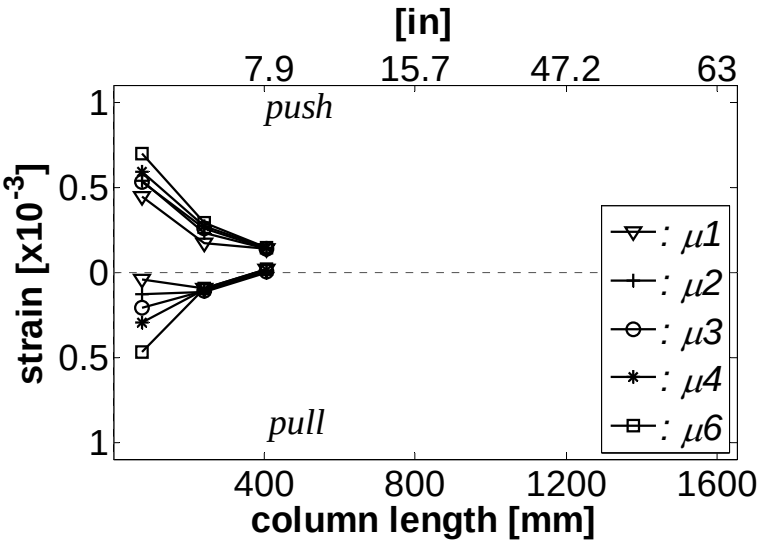

Figure 5.54 RCFST-89C Right side of pipe shear strain profiles

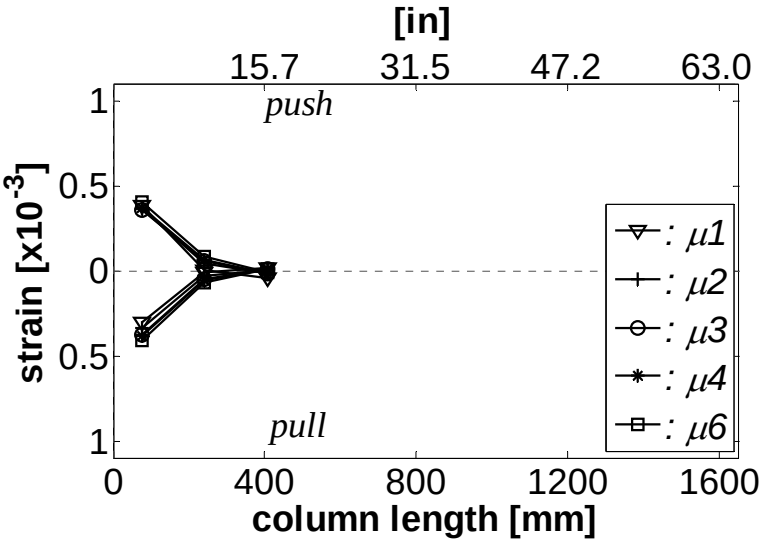

Figure 5.55 RCFST-89C Left side of pipe shear strain profiles

5.4.8 Validity of test data

The match between measured displacement and that calculated from the lpot's is displayed in Figure 5.56. It is seen that linear potentiometer data is valid only up to ductility 2.5.

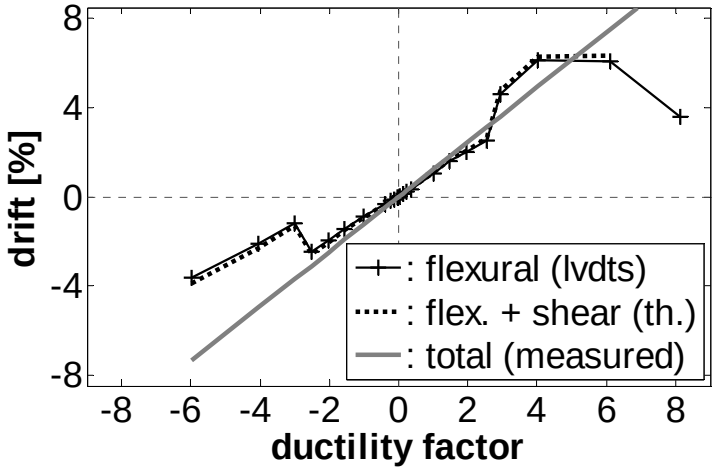

Figure 5.56 RCFST-89C Validity of test data

5.4.9 Comparison with FL-89C

This section compares the results obtained from the tests of units FL-89C and RCFST-89C in order to evaluate the advantages and disadvantages of using RCFST columns over ordinary reinforced concrete ORC columns in freezing conditions. The only differences between both columns are the presence of the steel tube in RCFST-89C and the compressive strength of the concrete. The estimated concrete compressive strength at -36°C for RCFST-89C was 44 MPa (6.4 ksi) compared with 27.6 MPa (4 ksi) for FL-89C.

Figure 5.57 compares the first peak envelopes for both specimens, from this graph it is noticed that:

(1) Though the concrete compressive strength of the RCFST specimen was larger, the flexural strength of both specimens was practically the same.

(2) Strength degradation associated with the increasing ductility demand started earlier in the RCFST specimen, at a displacement 35% smaller than that exhibited by the ORC column.

(3) Displacement capacity of the RCFST specimen was 25% less than that exhibited by the ORC column. Also, the mode of failure of the RCFST, rupture of the longitudinal rebar, was more brittle in nature than the failure of the ORC columns, where buckling of the longitudinal bar occurred.

(4) Initial stiffness, calculated at the theoretical force level for first yield in the ORC column, is 50% larger in the RCFST column.

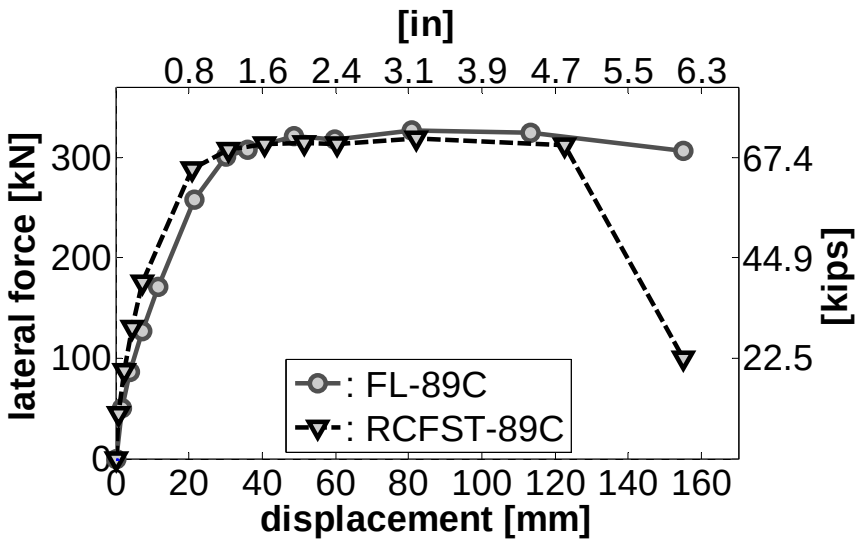

Figure 5.57 RCFST-89C and FL-89C first peak envelope

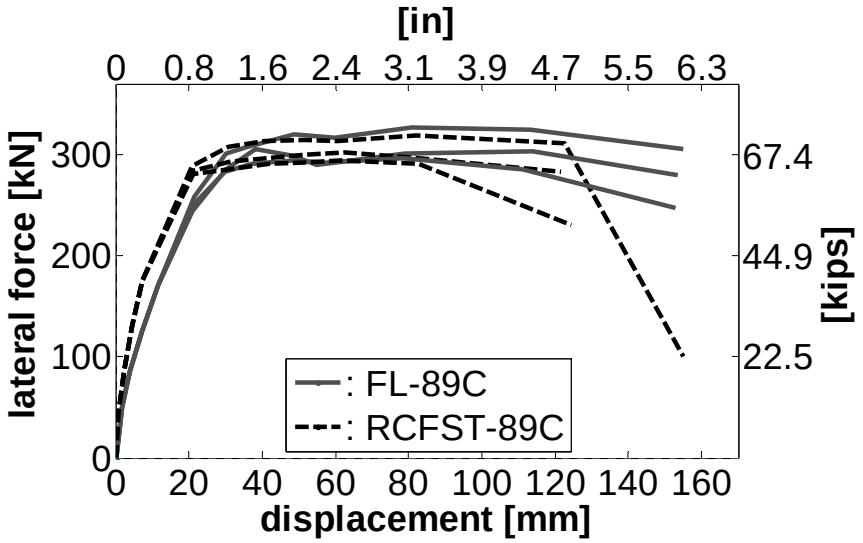

Figure 5.58 RCFST-8CA and FL-89C three cycles envelope

Figure 5.58 shows the average envelopes for the three cycles, it is noticed that the strength degradation associated with increasing number of cycles at the same ductility demand is larger for the RCFST column.

Figures 5.59 and 5.60 compare the energy dissipation and hysteretic damping properties, respectively. It is noticed that for a given drift level, the RCFST exhibit larger energy dissipation and hysteretic damping than the ORC column.

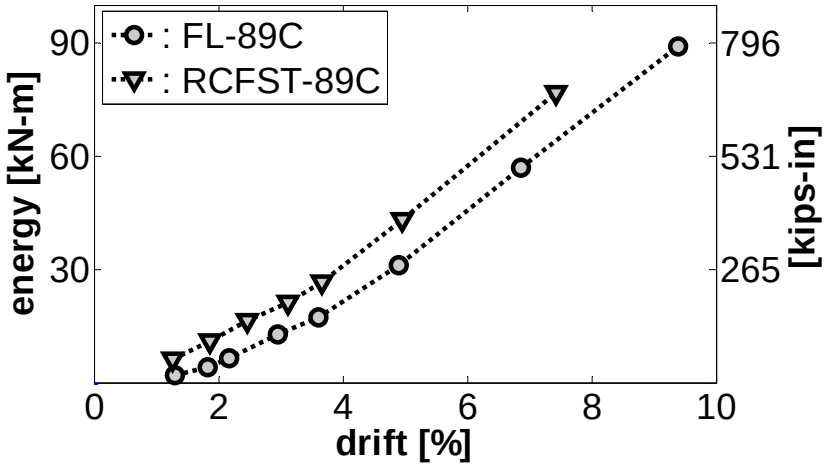

Figure 5.59 RCFST-89C and FL-89C energy dissipation

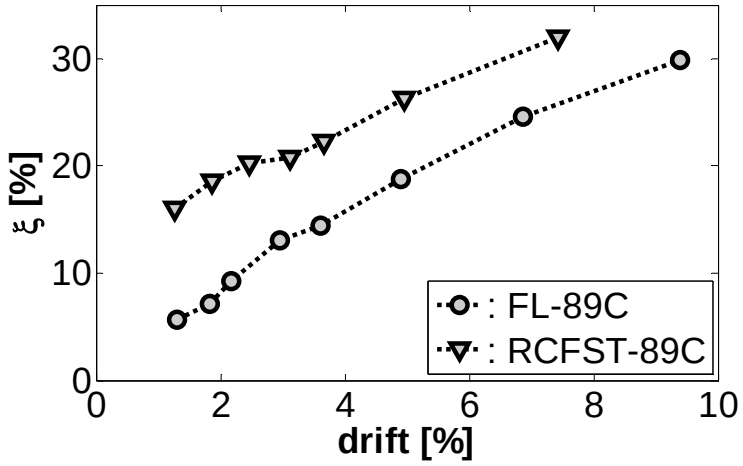

Figure 5.60 RCFST-89C and FL-89C hysteric damping

Figure 5.61 compares the curvature profiles at ductility 2 for both units. As for the room temperature specimens, it is seen that the RCFST columns concentrate most of the curvature in the base, provoking a larger rotation demand when compared with the ORC column, which distributes the curvature over a larger length of the column. This phenomenon can also be appreciated from the condition of the specimens after the test. In Figure 5.62, it is seen from this figure that damage in the RCFST columns was concentrated in only 76 mm (3 in) compared with 229 mm (9 in) in the ORC column. Despite the large difference in the extent of damage of the specimens, the difference in the equivalent plastic hinge length (Figure 5.63) was small, average values of L_p were

226 mm for the RCFST column and 264 mm for the ORC column. Note that even though the plastic hinge length is loosely related to the spread of plasticity observed in the column, the equivalent plastic hinge length is not intended to be a direct measure of the spread of plasticity but rather, an artifice to simplify the calculation of the force-displacement response of a column from its theoretical section moment-curvature relation.

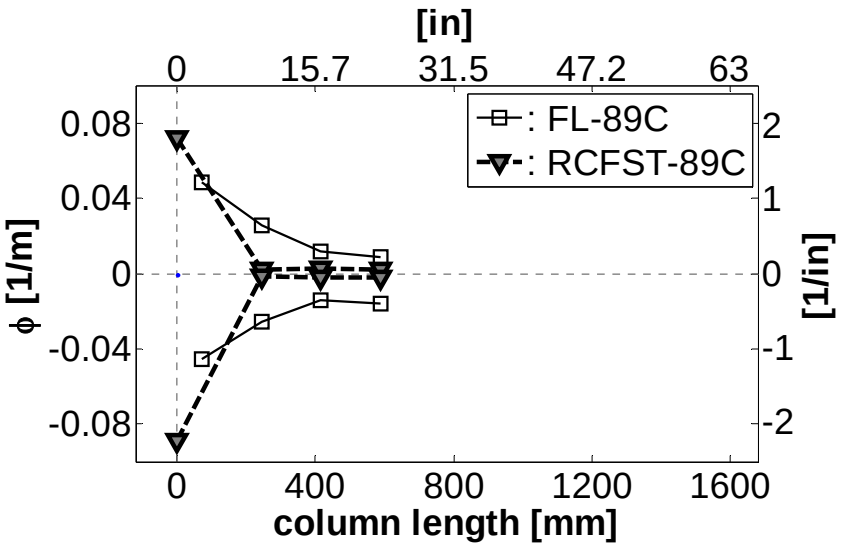

Figure 5.61 RCFST-89C and FL-89C curvature profiles at ductility 2

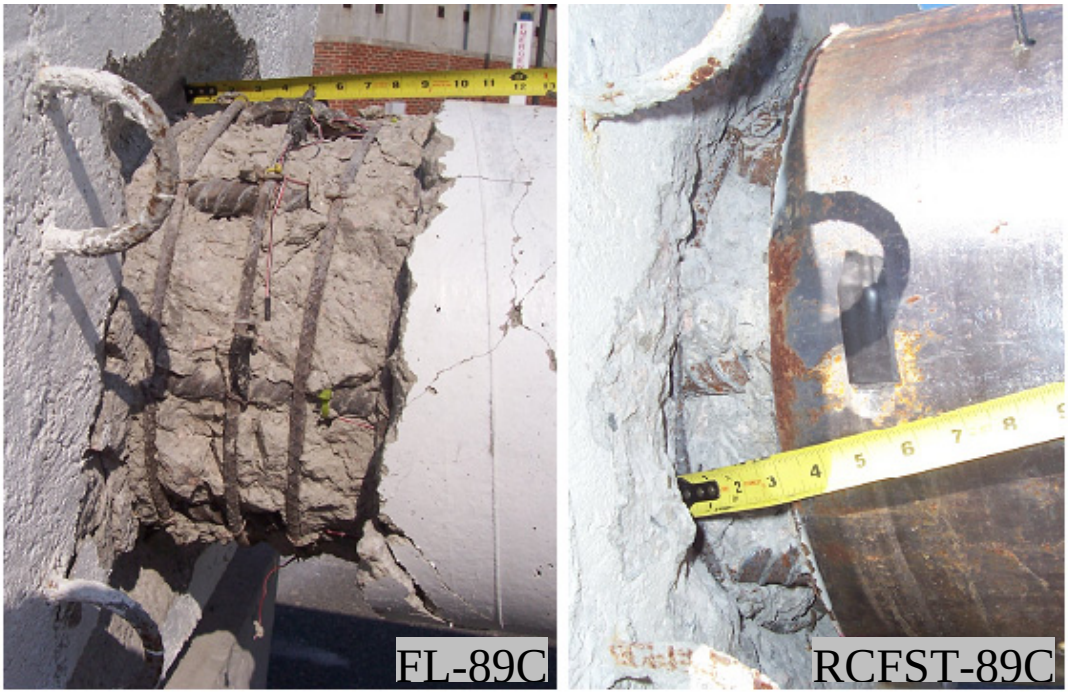

Figure 5.62 RCFST-89C and FL-89C conditions of the specimen after test

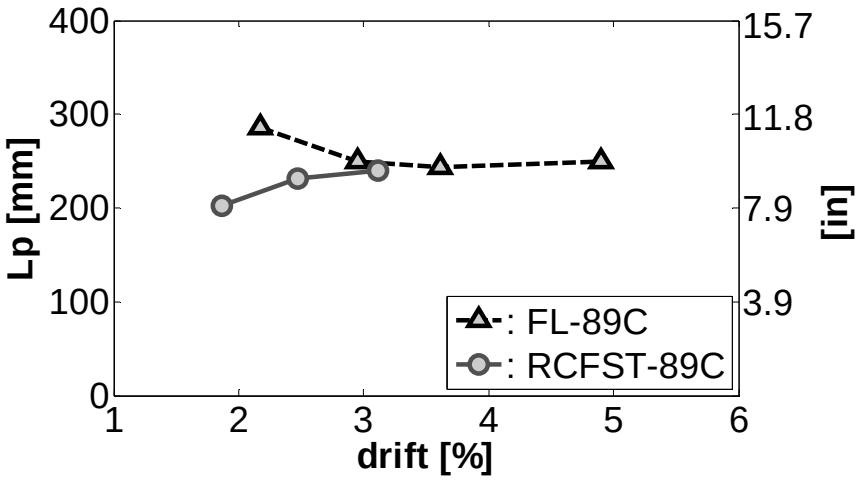

Figure 5.63 RCFST-89C and FL-89C equivalent plastic hinge length

5.5 Comparison of RCFST-89A and RCFST-89C units

Figure 5.64 shows the hysteretic responses and Figure 5.65 shows the average first peak envelopes, F_{nr} and F_{yr} represent the room temperature nominal and first yield force, respectively. It is seen that the increase in flexural strength at low temperatures for RCFST columns is about 7%, i.e. half the increase observed in ORC columns. However, the increase in the initial stiffness at low temperatures (60%) is more than twice the observed in ORC columns (27%). Even though both specimens failed at the third cycle of ductility 6, failure of the cold specimen was more brittle as it involves rebar rupture while the room temperature unit only exhibited buckling of the rebar. It was also noticed that strength degradation started earlier in the cold specimen.

Figure 5.66 shows the three cycle's force-displacement envelopes for both specimens. It is seen that strength degradation over cycles at the same displacement demand is larger in the cold specimen.

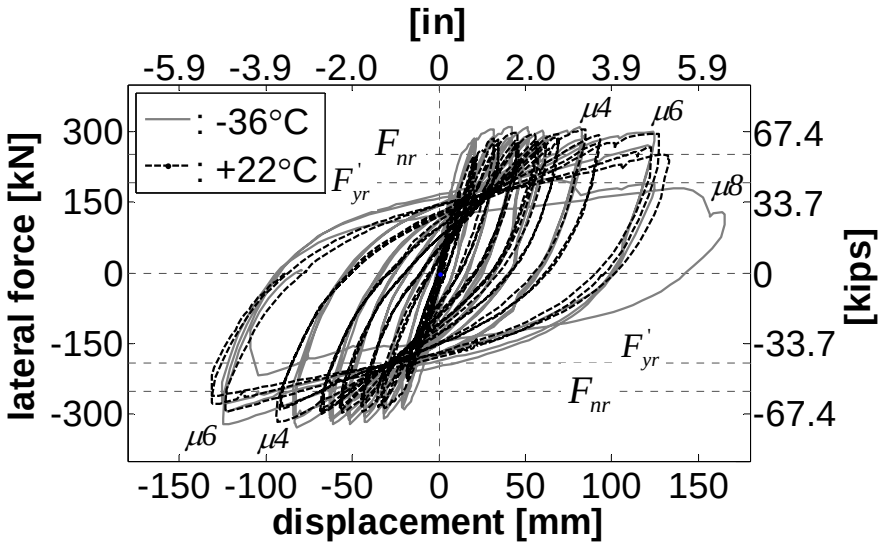

Figure 5.64 Hysteretic responses of RFCST-89C and RCFST-89A.

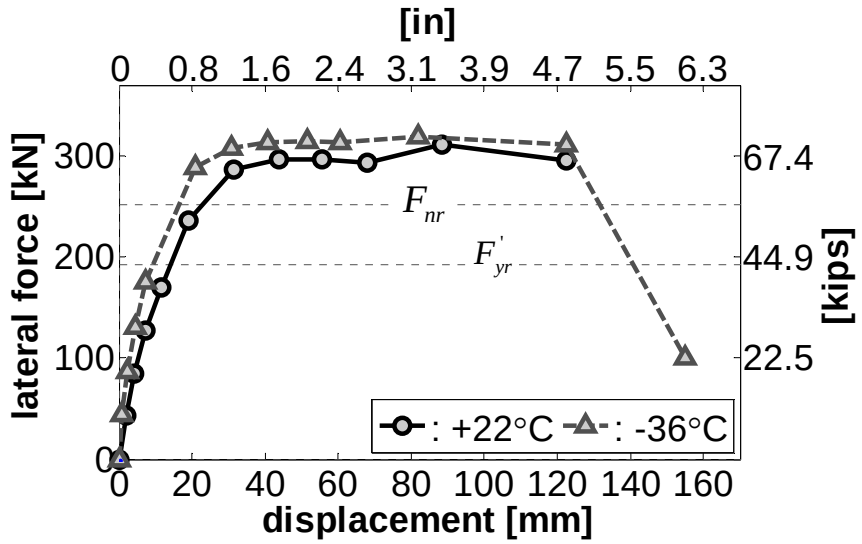

Figure 5.65 Average first cycle envelopes of RCFST-89C and RCFST-89A.

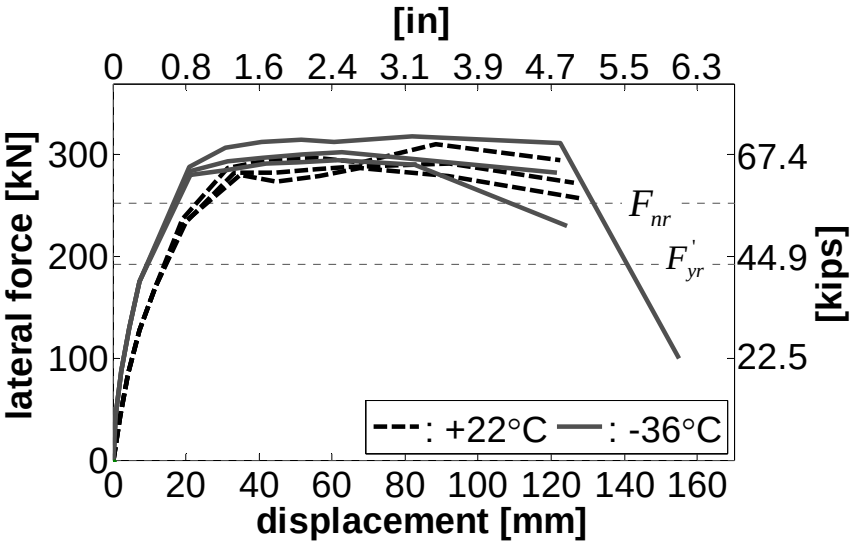

Figure 5.66 Average cycle envelopes of RCFST-89C and RCFST-89A.

Low temperatures seem to have no effect on the energy dissipation properties of RCFST columns as shown in Figure 5.67. Hysteretic damping is investigated in Figure 5.68, it is seen that area based damping of the cold specimen is slightly larger than for the room temperature unit. However, when the damping values are corrected, so they can be used in direct-displacement based design (Figure 5.69), the difference becomes negligible.

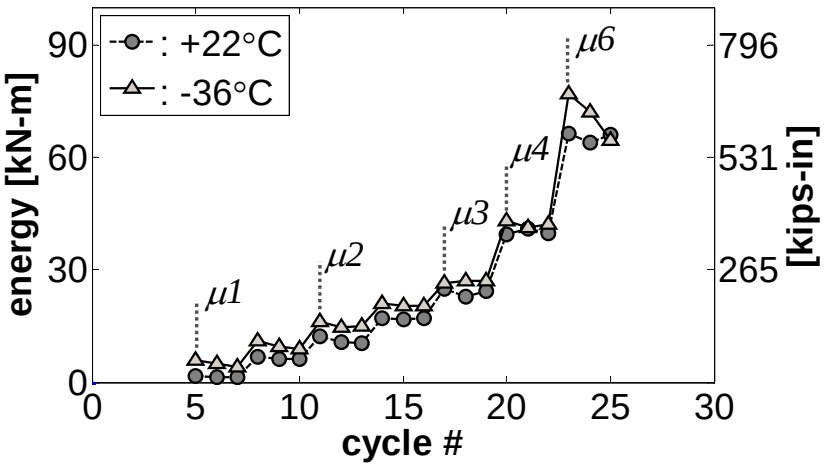

Figure 5.67 Energy released for RCFST-89C and RCFST-89A.

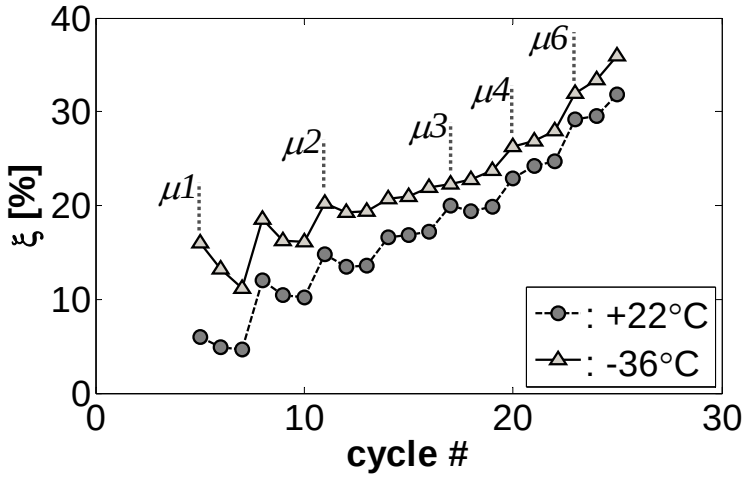

Figure 5.68 Hysteretic damping for RCFST-89C and RCFST-89A.

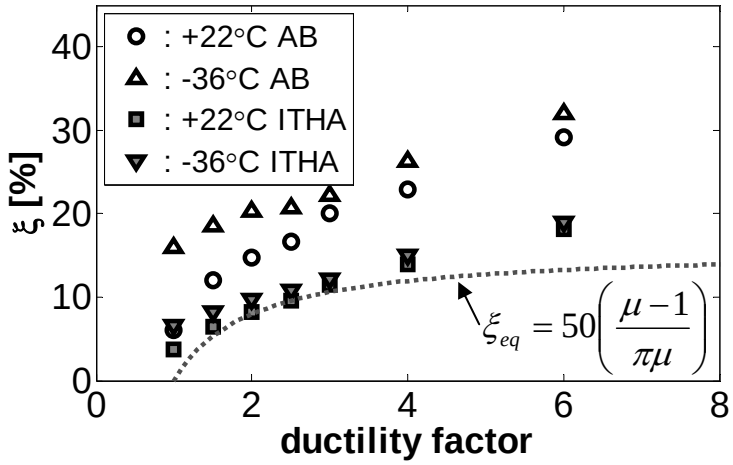

Figure 5.69 Corrected values of equivalent damping for RCFST-89C and RCFST-89A.

Curvature profiles of both specimens are displayed in Figure 5.70. Both profiles have the same shape and similar curvature values, therefore the calculated equivalent plastic hinge length (Figure 5.71) resulted to be practically the same for both specimens. Figure 5.72 compares the condition of both units after the test, it is noticed that damage in the footing was reduced in the cold specimen, most likely due to an enhancement in the mechanical properties of the footing concrete at low temperatures. Finally, Tables 5.2 and 5.3 summarize the results obtained during these two tests.

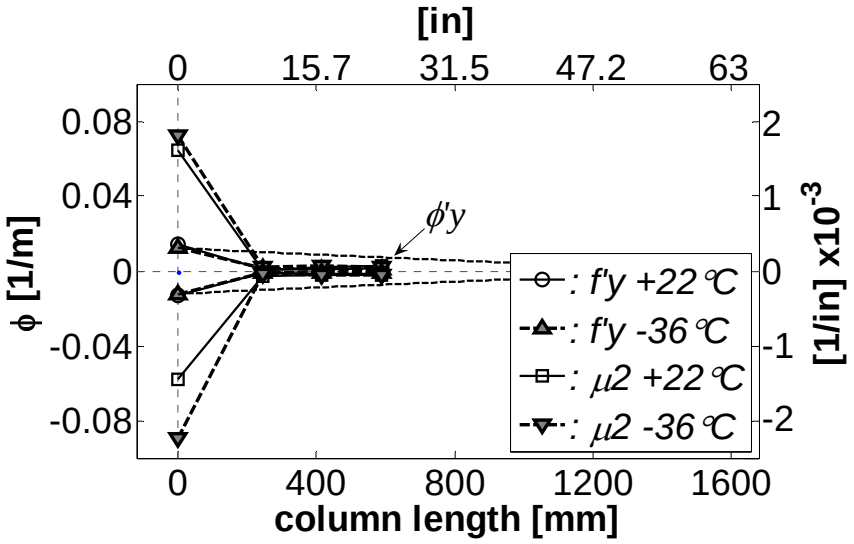

Figure 5.70 Curvature profiles for RCFST-89C and RCFST-89A.

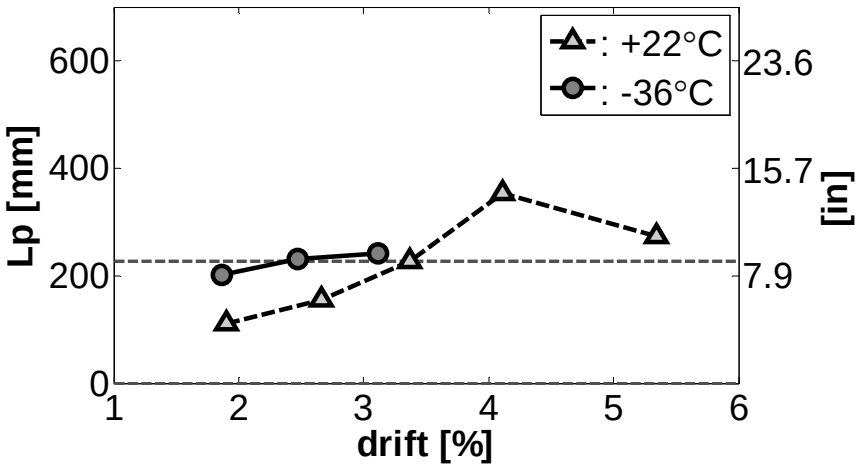

Figure 5.71 Plastic hinge lengths for RCFST-89C and RCFST-89A.

Figure 5.72 RCFST-89C and RCFST-89A after the test.

Table 5.2 Summary of results obtained (Load control phase)

Cycle	Average Lat. Force [kN]	Average tip displacement [mm]		
		+22°C	-36°C	-36°C / +22°C
0.25fy'	43.7	1.9	0.7	0.38
0.5fy'	86.2	4.4	2.4	0.55
0.75fy'	128.9	7.5	4.6	0.61
fy'	172.7	11.8	7.2	0.61

Table 5.3 Summary of results obtained (Displacement control phase)

	Average	First cycle average lateral force [kN]		
Cycle	Displacement [mm]	+22°C	-36°C	-36°C / +22°C
μ1	19.9	240.0	280.9	1.17
μ1.5	31.1	285.5	307.7	1.08
μ2	42.4	295.2	313.3	1.06
μ2.5	53.5	296.7	314.2	1.06
μ3	64.1	294.0	313.8	1.07
μ4	85.1	307.8	318.1	1.03
μ6	122.5	295.4	311.5	1.05
μ8	155.0	-	100.0	-

5.6 Room temperature specimen RCFST-87A

This specimen was tested on October 16/2006 at room temperature (~23°C/73°F). Figure 5.73 shows the variation of the temperature inside the specimen and Figure 5.74 the axial load history during the test. Horizontal lines in this figure denote the average and ±10% deviations from average of the applied axial load.

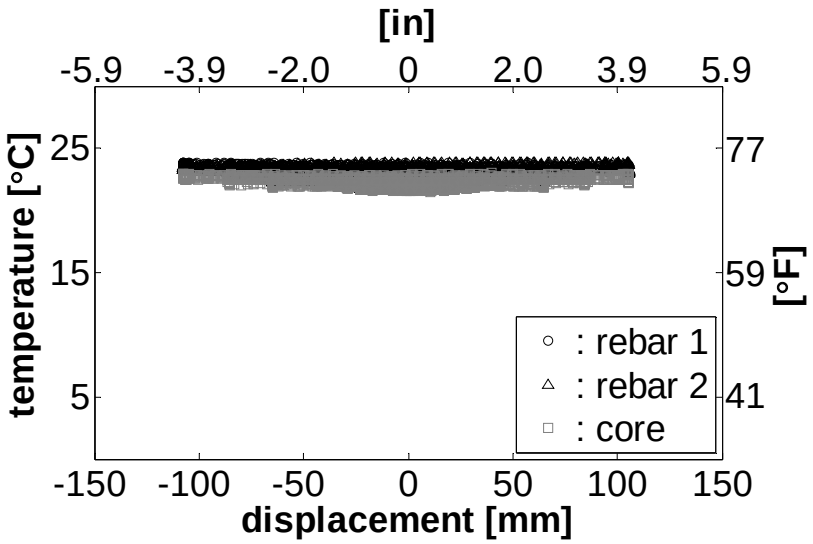

Figure 5.73 RCFST-87A Temperature variations.

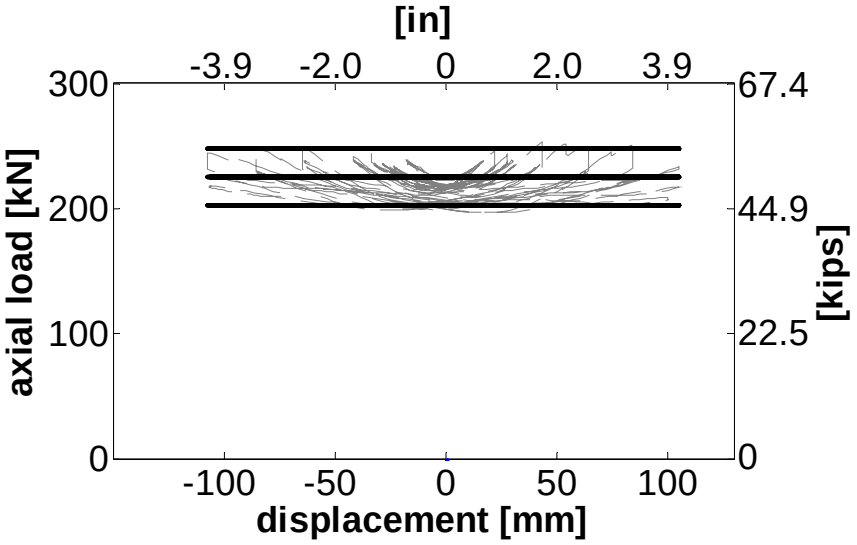

Figure 5.74 RCFST-87A Axial load variations.

5.6.1 RCFST-87A Test observations

First hairline cracks appear at the top and bottom faces in the base of the column during the last cycle of force control (116 kN). With the three cycles at ductility 1 the initial hairline cracks extended all around the circumference of the column (Figure 5.75), from this point and up to the last cycle of ductility 2 the only change observed in the specimen was a small increase in the width of the existing crack.

Slip of the steel tube from the concrete was noticed during the first push at ductility 2.5 (Figure 5.76). First signs of cover concrete crushing were noticed at ductility 2.5 (Figure 5.77). At this level of demand all the damage is concentrated in the base of the column with the existing crack becoming deeper. With the three cycles at ductility 3 the only observable augment on damage was an increase in the cover concrete crushing and in the width of the initial and secluded crack (Figure 5.78).

Crushing of the of the core concrete is observed with the cycles at ductility 4, part of the spiral on the top face of the column is exposed and spalling of the surrounding concrete in the footing is also noticed (Figure 5.79). At the first cycle of ductility 6 a flexural crack appeared in the footing (Figure 5.80), also in this cycle the specimen reached its peak load (190 kN). After the last cycle at ductility 8 (Figure 5.81), it is seen

that the inelastic action is extended into the footing causing considerable damage on it. Finally, at ductility 10 the damage in the footing was quite large (Figure 5.82) and the test was stopped after completing the three cycles at this ductility.

Figure 5.83 is a picture of the specimen after the instruments have been removed, it is seen that the damage was concentrated in the gap between the steel tube and the footing and also transmitted inside the footing. Substantial damage is observed in this zone including the core concrete.

Figure 5.75 RCFST-87A (bottom) after the tree cycles at ductility 1.

Figure 5.76 RCFST-87A (top) after the first push at ductility 2.5.

Figure 5.77 RCFST-87A (bottom) after the tree cycles at ductility 2.5.

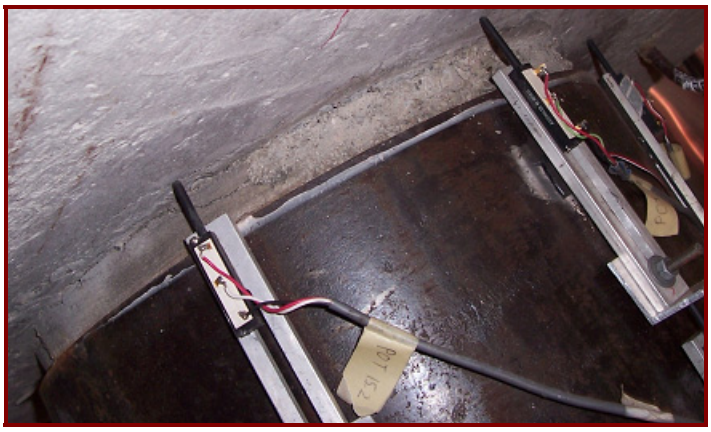

Figure 5.78 RCFST-87A (top) after the tree cycles at ductility 3.

Figure 5.79 RCFST-87A (top) after the tree cycles at ductility 4.

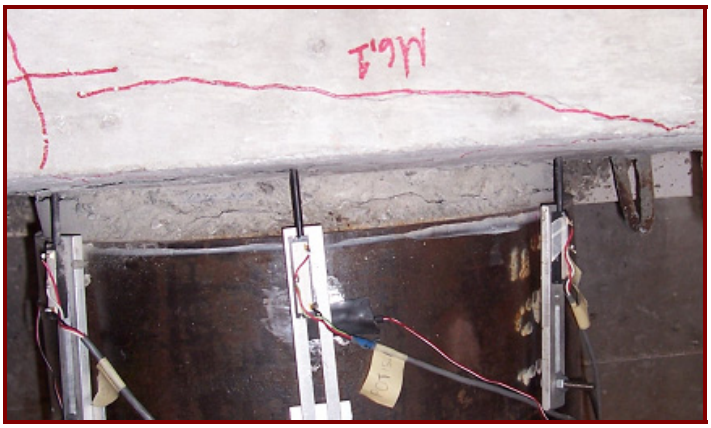

Figure 5.80 RCFST-87A (top) after the first cycle at ductility 6.

Figure 5.81 RCFST-87A (bottom) after the last cycle at ductility 8.

Figure 5.82 RCFST-87A (top) after the last cycle at ductility 10.

Figure 5.83 RCFST-87A (bottom) after instrumentation removal.

5.6.2 RCFST-87A Force displacement response.

Figure 5.84 displays the force-displacement hysteretic response recorded during the test. This figure also shows the theoretical force-displacement envelope obtained using the equivalent plastic hinge length calculated from the experimental results $L_p = 190mm$. Figure 5.85 shows the average first peak force-displacement response along with the theoretical envelopes calculated using the conventional equivalent plastic

hinge length (including the set-up correction factor of 0.59) $L_p = 0.59\left(2L_{sp} + g\right) = 268mm$ and the prediction using the measured $L_p = 190mm$. It is seen that the match between theoretical and actual response is slightly improved using the reduced equivalent plastic hinge length.

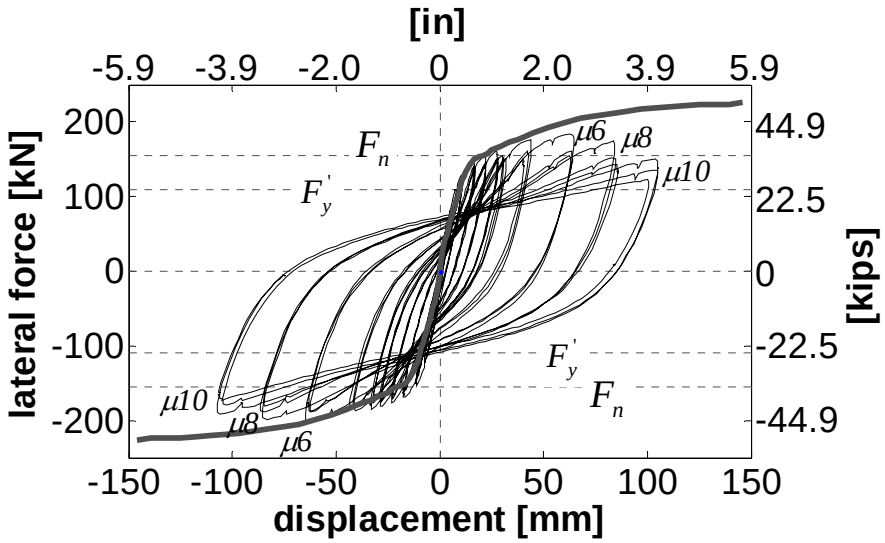

Figure 5.84 RCFST-87A Hysteretic force displacement response.

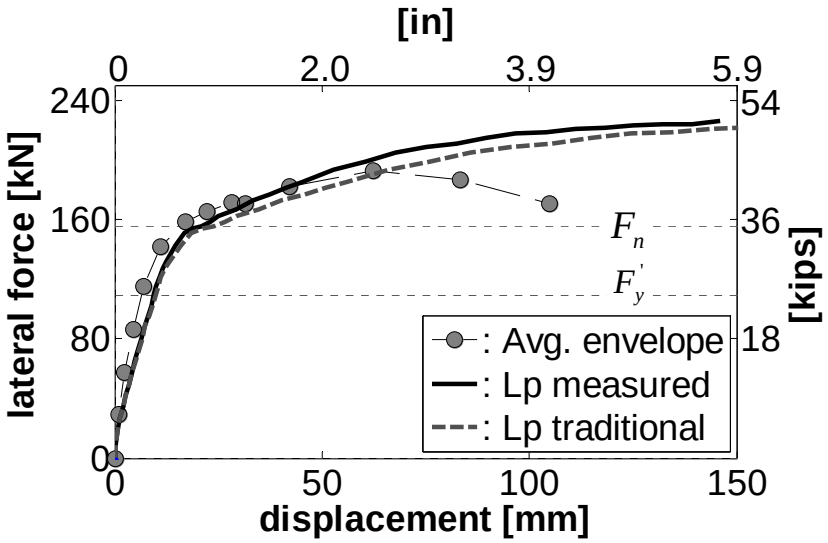

Figure 5.85 RCFST-87A First peak average response and theoretical envelopes.

5.6.3 RCFST-87A Curvature profiles.

As mentioned before, the gauge length for the bottom cell of lpot's should include a component due to strain penetration. The magnitude of this addition for RCFST-87A was found to be 25 mm. Figure 5.86 shows the match between the theoretical and actual moment curvature response at the base of the column. Figure 5.87 shows the curvature profiles at *μ1, μ2, μ3, μ4* and *μ6*. From these profiles it can be seen how all the curvature is concentrated in the first cell. This limited extend of plasticity generated very large rotation demands in the base of the column that induced severe damage in the footing and the core concrete in the base of the column as shown in Figure 5.83.

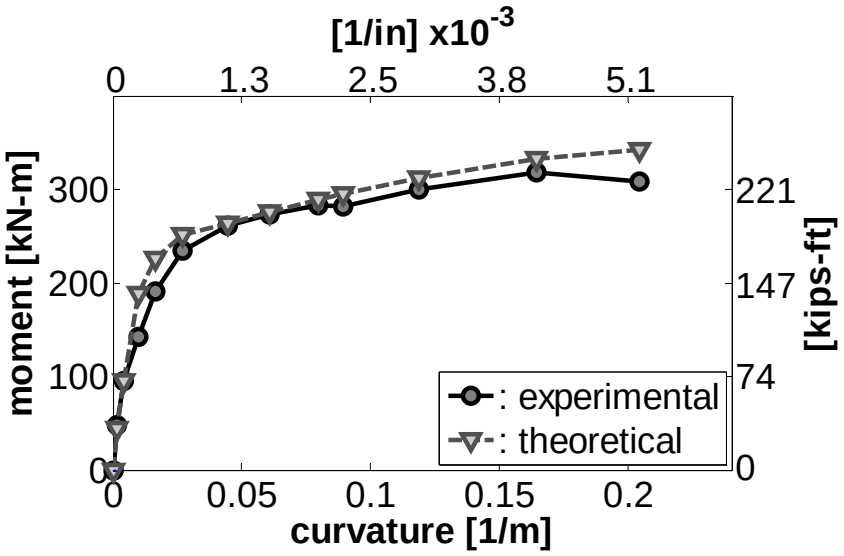

Figure 5.86 RCFST-87A Moment curvature at column base.

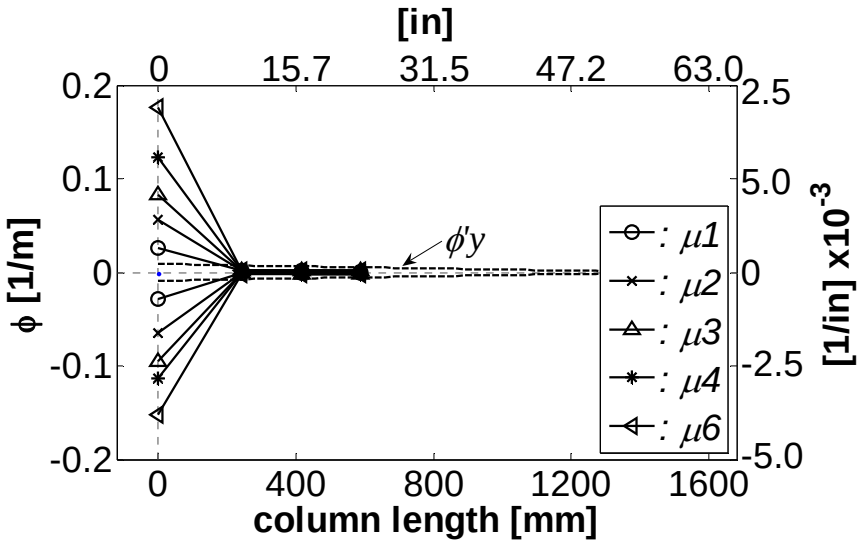

Figure 5.87 RCFST-87A Curvature profiles.

5.6.4 RCFST-87A Equivalent plastic hinge length.

Figure 5.88 shows the results obtained for the equivalent plastic hinge length, note that the value obtained of 190mm (7.5in) is 71% of the commonly used value for L_p in steel jacketed columns once the correction factor obtained for the actual set up is applied, i.e. $L_p = 0.59\left(2L_{sp} + g\right) = 268mm$.

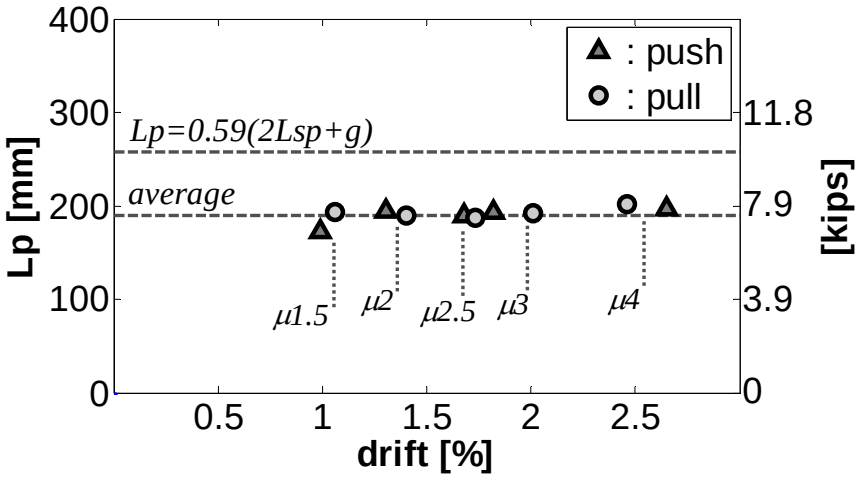

Figure 5.88 RCFST-87A Equivalent plastic hinge length

5.6.5 Strains on longitudinal reinforcement

Figure 5.89 shows the longitudinal strain profiles on the bottom most bar. Profiles are generated only up to ductility 1.5 because after this point the readings of the first strain gage were not reliable. It is noticed that up to ductility 1 the increase in strain is linear, as expected for the elastic range. However, for larger demands all the plasticity seems to be concentrated in the base of the column. This is corroborated by the strain history recorded by a strain gauge located at 270mm from the base in Figure 5.90. It is seen that this spot of the bar barely reach yield at the largest levels of ductility demand.

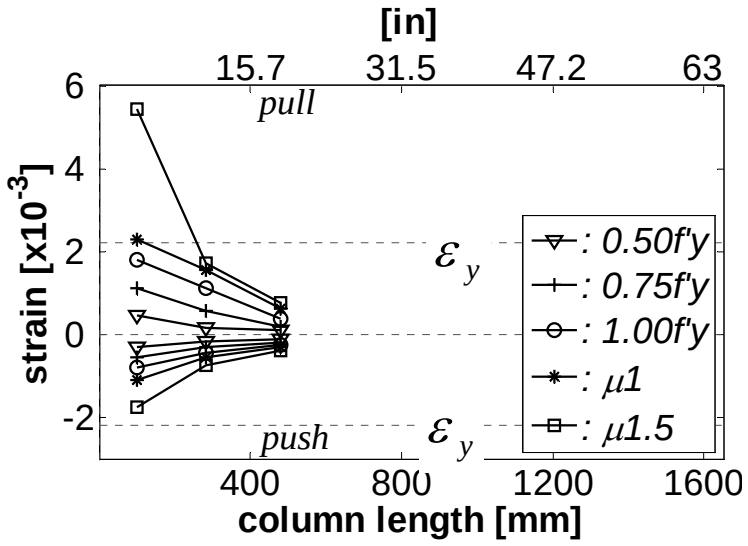

Figure 5.89 RCFST-87A Strain profile on Bottom most longitudinal bar

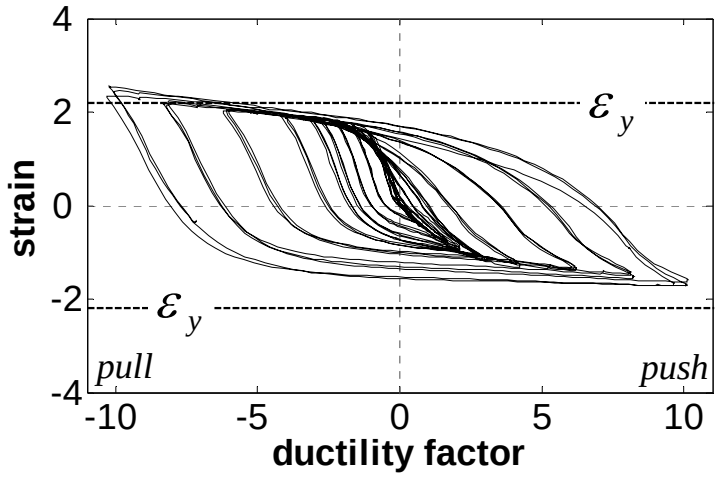

Figure 5.90 RCFST-87A Bottom bar strain history at 270 mm form the base

5.6.6 Strains on transverse reinforcement

Figure 5.91 shows the confinement strains in the bottom side of the spirals and Figure 5.92 shows the shear induced strain profiles in right side of the spiral. It is noticed that both type of strains are very low (not even reaching half the yield strain) as most of the confinement and shear strength is provided by the steel tube.

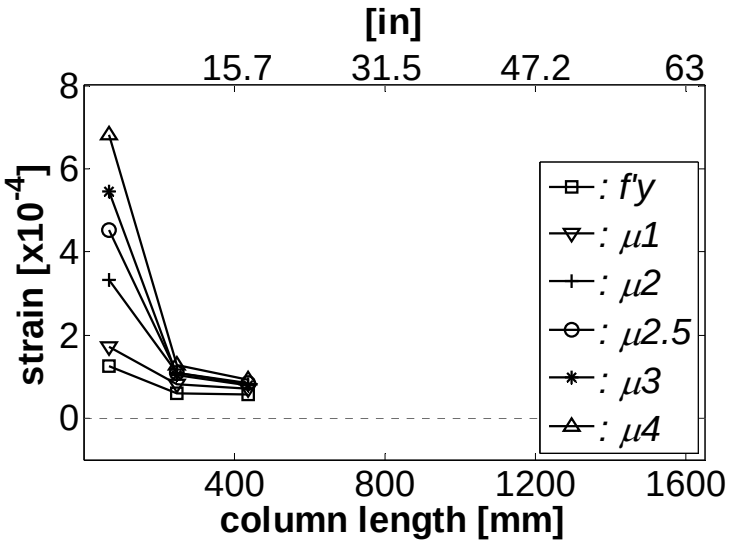

Figure 5.91 RCFST-87A Bottom side of spiral (confinement) strain profiles

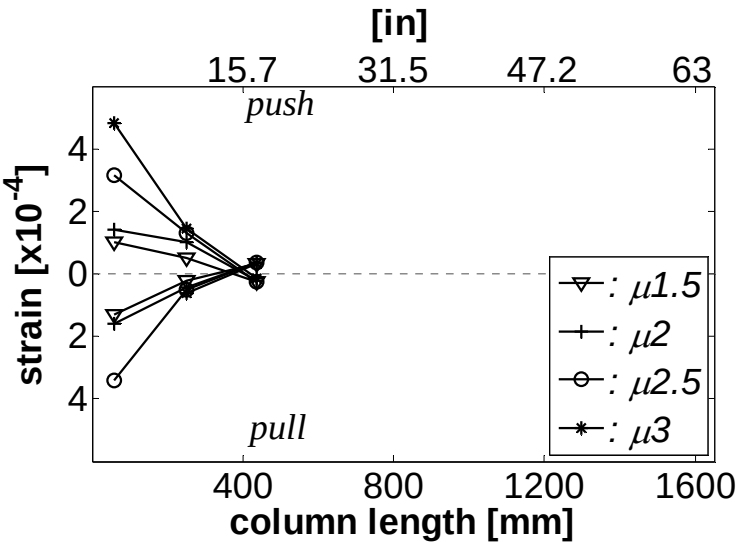

Figure 5.92 RCFST-87A Right side of spiral (shear) strain profiles

5.6.7 Strains on steel tube

Information collected from the strain gages placed in the external surface of the steel pipes is presented in the form of strain profiles. Figures 5.93 and 5.94 show the steel tube confinement induced strains profiles and, Figures 5.95 and 5.96 the steel tube shear induced strains profiles. As for the previous analyzed RCFST specimens strains recorded in the steel pipe are very low.

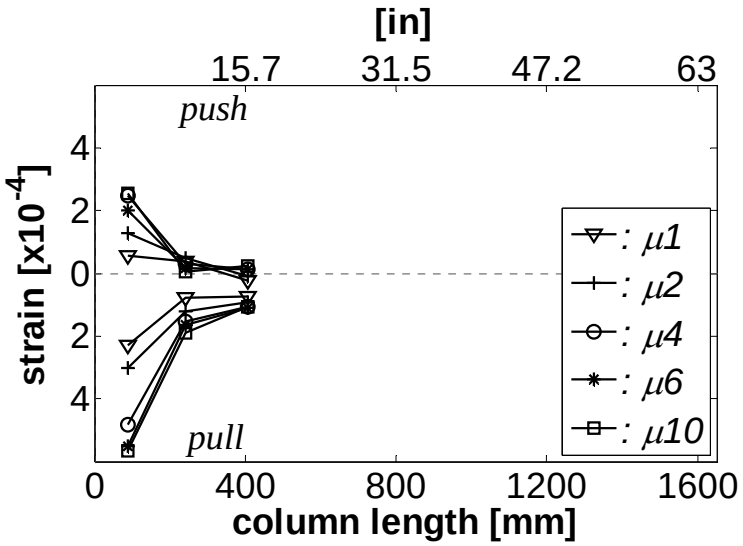

Figure 5.93 RCFST-87A Top side of pipe confinement strain profiles

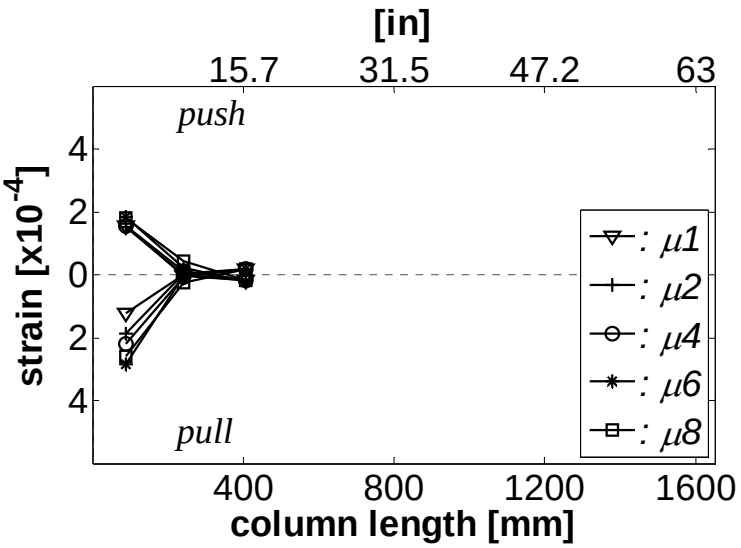

Figure 5.94 RCFST-87A Bottom side of pipe confinement strain profiles

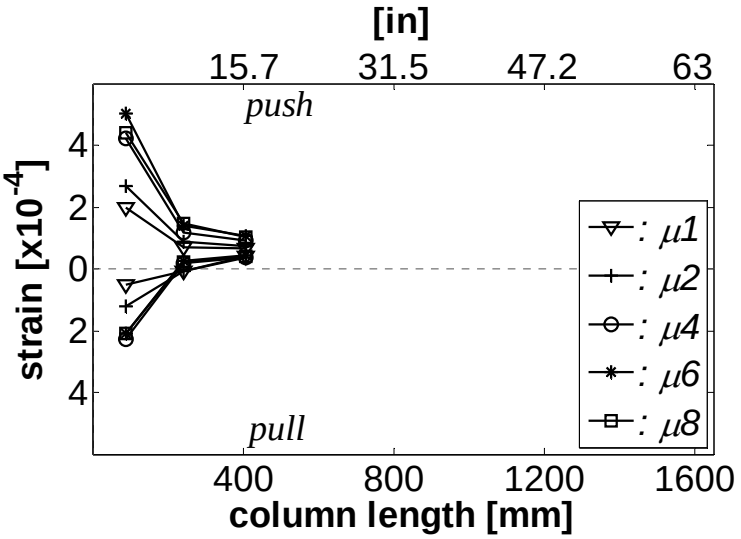

Figure 5.95 RCFST-87A Right side of pipe shear strain profiles

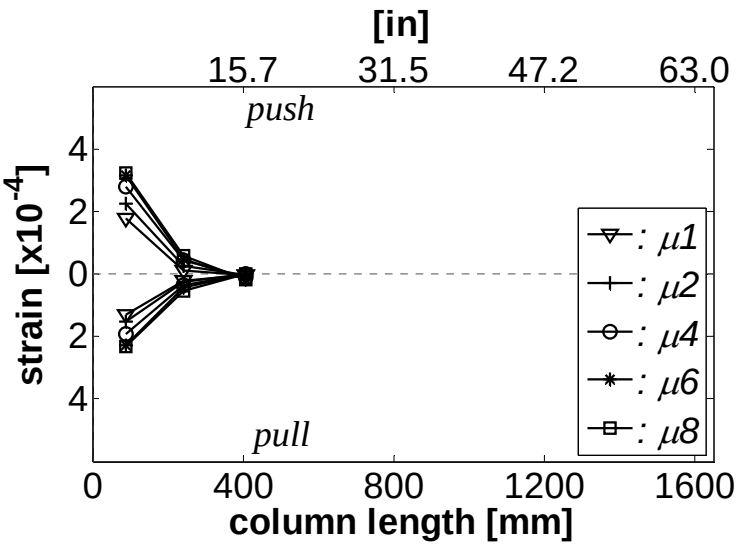

Figure 5.96 RCFST-87A Left side of pipe shear strain profiles

5.6.8 Validity of test data

Figure 5.97 compares the tip displacements calculated using the data recorded with the linear potentiometers with the displacement measured with the string potentiometer placed at the top of the column. It is seen that data recorded from the linear potentiometers is reliable up to ductility 6.

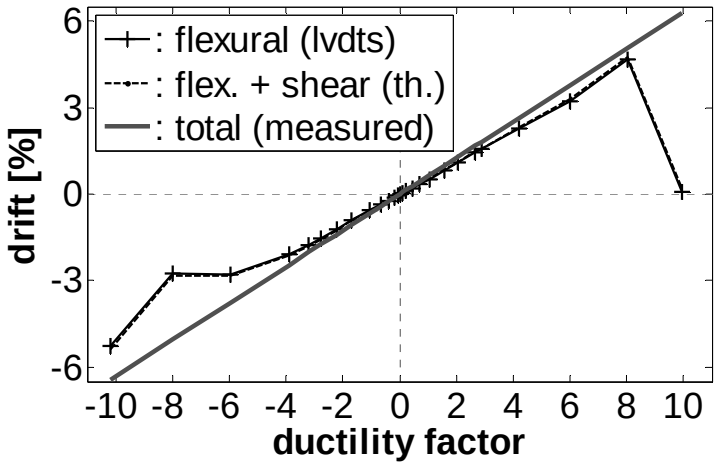

Figure 5.97 RCFST-87A Validity of test data

5.7 Low temperature specimen RCFST-87C

This specimen was tested on December 01/2006. Cooling process started 26 hours before the test, ambient temperature during this time and the duration of the test was kept constant at -40°C (-40°F). Figure 5.98 shows the temperature variation inside the specimen during the test and Figure 5.99 shows the variation of the applied axial load.

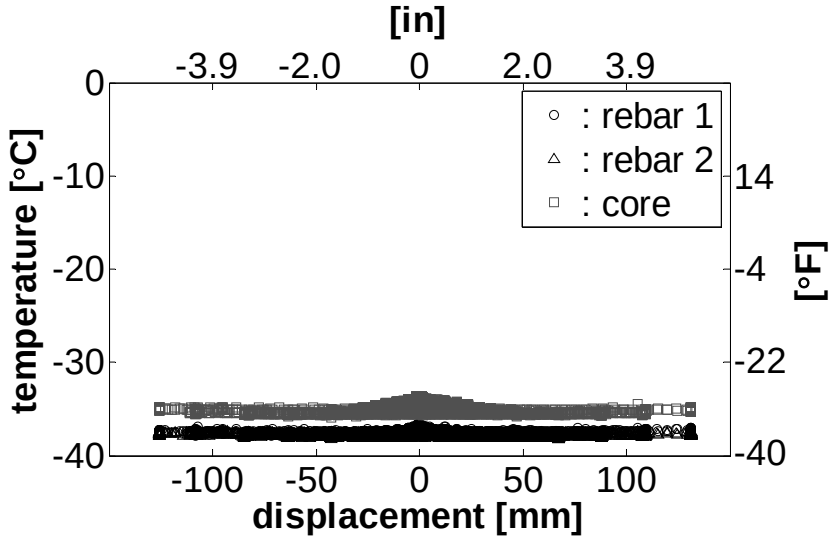

Figure 5.98 RCFST-87C Temperature variations

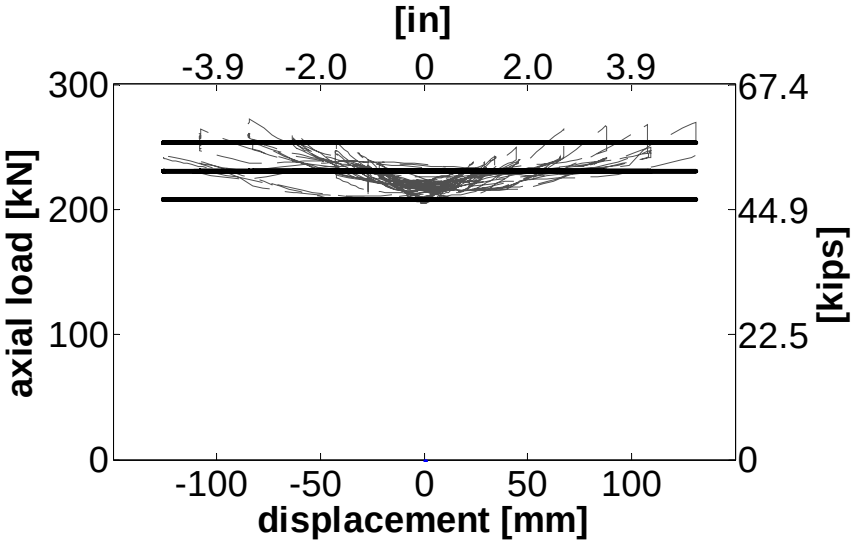

Figure 5.99 RCFST-87C Axial load variations

5.7.1 RCFST-87C Test observations

This was the first specimen being tested at freezing conditions. Initially, two webcams were placed above and below the base of the column to monitor the level of damage on the specimen. Later on it was noticed that the webcams were not working properly, it was then decided to get inside the environmental chamber at key points during the test and take pictures with a conventional digital camera. That's why observations are not made since the beginning of the test but rather from ductility 2.5 and up. Figure 5.100 shows the condition of the specimen after the first push at ductility 2.5, it is noticed that the condition of the concrete in the gap between the steel tube and the footing is still good with exception of a flexural crack located at the base of the column that runs all around its circumference. Some spalling of the footing concrete surrounding the column is also noticed. No significant increment in the level of damage is noticed when the column is taken up to ductilities 3 and 4, Figures 5.101 and 5.102, respectively.

During the first cycle of ductility 6 the specimen reached the maximum lateral load during the test. Extensive crushing and spalling of the concrete in the gap was noticed at this level of demand (Figure 5.103). Crushing of the core concrete is noticed during the cycles at ductility 8 (Figure 5.104).

Rupture of the top most bar occurred during the first push at ductility 10 (Figure 5.105), it is also noticed that damage has extended to the footing. After the three cycles at ductility 10 the transverse reinforcement is exposed (Figure 5.106). Rupture of a second top bar was noticed during the first push at ductility 12, rupture of one of the bottom bars occurred during the corresponding pull, the test was stopped at this point. Figure 5.107 is a picture of the bottom face of the specimen after removal of the instrumentation. It is seen that the extension of damage is limited to a very short length; the mechanism of failure was basically a single crack in the base of the column that penetrated very deep into the core concrete.

Figure 5.100 RCFST-87C (top) after the first push at ductility 2.5

Figure 5.101 RCFST-87C (top) after the first push at ductility 3

Figure 5.102 RCFST-87C (top) after the first push at ductility 4

Figure 5.103 RCFST-87C (top) after the first push at ductility 6

Figure 5.104 RCFST-87C (top) after the first push at ductility 8

Figure 5.105 RCFST-87C (top) after the first push at ductility 10

Figure 5.106 RCFST-87C (top) after the last push at ductility 10

Figure 5.107 RCFST-87C (bottom) after instrumentation removal

5.7.2 RCFST-87C Force displacement response.

Figure 5.108 displays the force-displacement hysteretic response recorded during the test. Figure 5.109 shows the average first peak envelope along with the theoretical prediction obtained two different equivalent plastic hinge lengths: (1) the conventional value with the correction factor for the actual set-up and (2) the equivalent length obtained from the analysis of the data collected during the test. It is seen that the match between theoretical and actual response is slightly improved using the measured L_p .

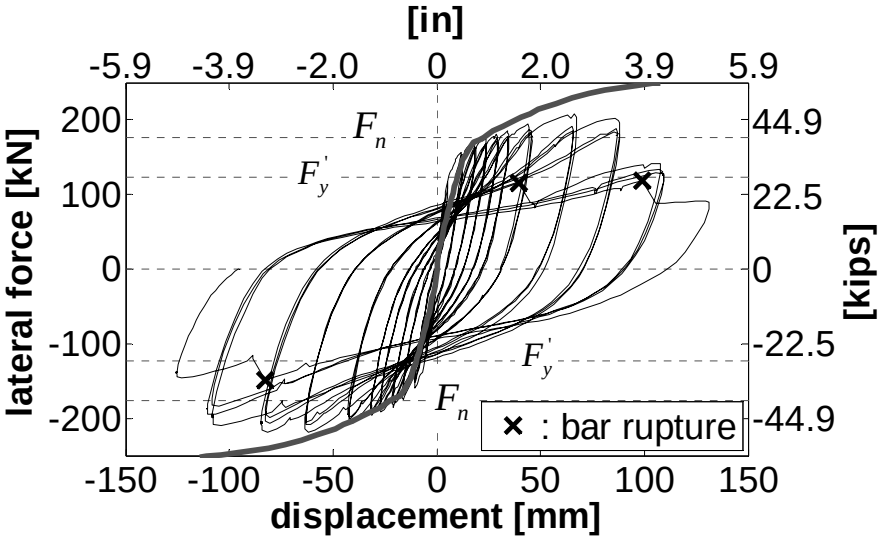

Figure 5.108 RCFST-87C Hysteretic force displacement response.

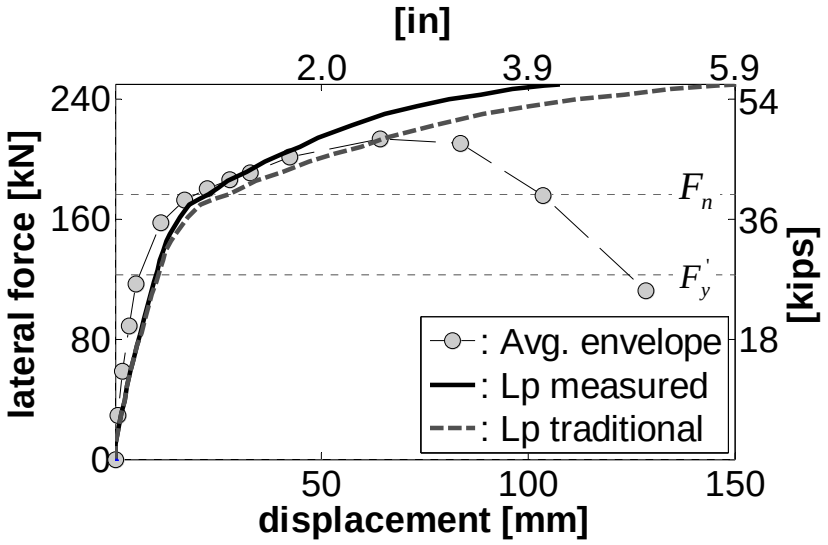

Figure 5.109 RCFST-87C First peak average response and theoretical envelopes.

5.7.3 RCFST-87C Curvature profiles.

The magnitude of the addition for the gauge length of the first cell of this unit was found to be 38 mm. Figure 5.110 shows the match between the theoretical and actual moment curvature response at the base of the column. Figure 5.111 shows the curvature

profiles at selected ductility demands. As noticed for the RCFST specimens analyzed before, the majority of the inelastic action is concentrated in the base of the column.

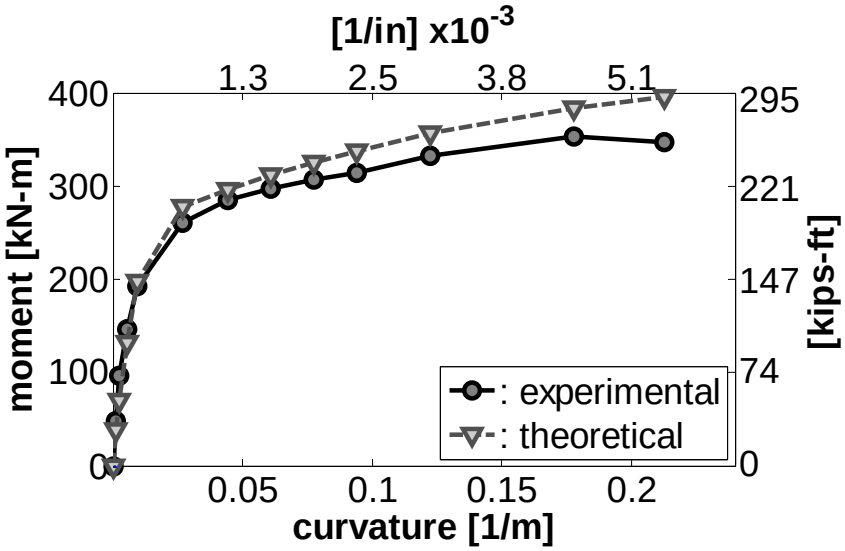

Figure 5.110 RCFST-87C Moment curvature at column base.

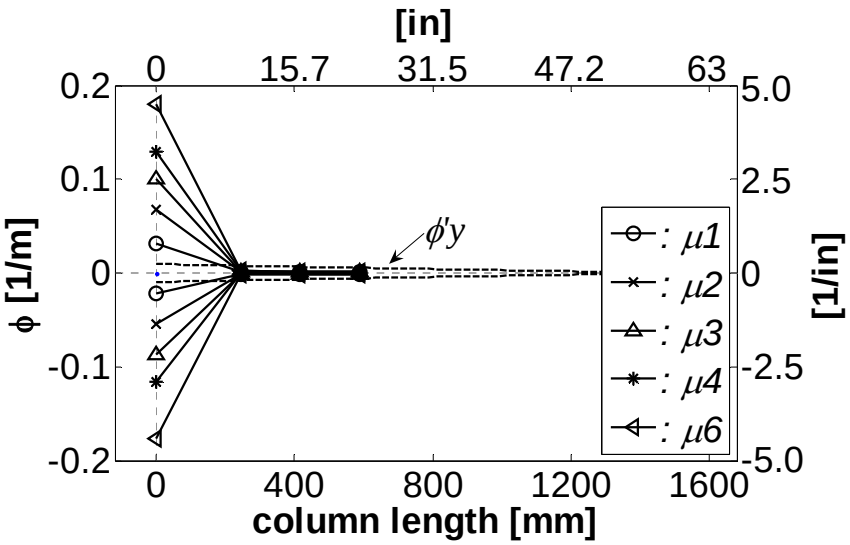

Figure 5.111 RCFST-87C Curvature profiles.

5.7.4 RCFST-87A Equivalent plastic hinge length.

Figure 5.112 shows the results obtained for the equivalent plastic hinge length, note that the value obtained of 190 mm (7.5in) is the same value obtained for the room

temperature specimen RCFST-87A. Nonetheless, as the equivalent plastic hinge length is directly related to the yield strength of the longitudinal rebar (which has been show to increase at low temperatures) this apparently equality in the equivalent plastic hinge length obtained for the room and low temperatures conditions actually implies a reduction on L_p due to the freezing conditions. A reduction of 64% over the value recommended by Chai et al. (1991) for steel jacket retrofitted columns (once the correction factor of 0.59 for the current setup is applied) $L_p = 0.59\left(2L_{sp} + g\right) = 295mm$ is identified.

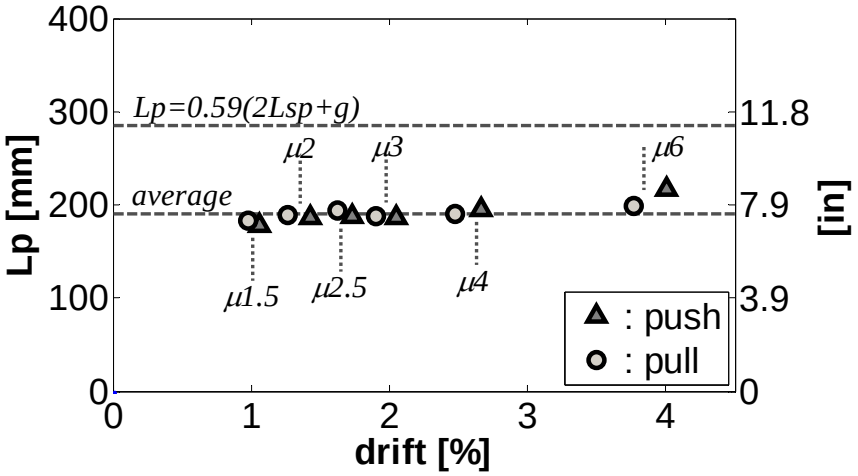

Figure 5.112 RCFST-87C Equivalent plastic hinge length

5.7.5 Strains on longitudinal reinforcement

There was not enough reliable data from the strain gages placed at the longitudinal bars in this specimen as to generate strain profiles. Nonetheless, this information is presented in the form of stain histories recorded by selected strain gages that worked properly during most of the test. Figures 5.113 and 5.114 show the strains recorded by strain gages placed at the top and bottom bar, respectively, at 304 mm (12 in) from the base of the column. It is seen that both bars exhibited the same behavior and that this spot of the bars did not reach yield during the test. This implies that all the inelastic action was concerted in a very limited length in the base of the column, this phenomena was also noticed from the curvature profiles on Figure 5.111.

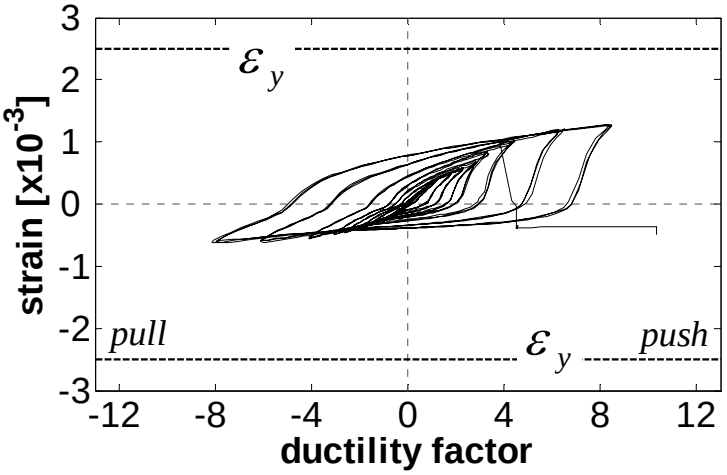

Figure 5.113 RCFST-87C Top bar strain history at 304mm from the base

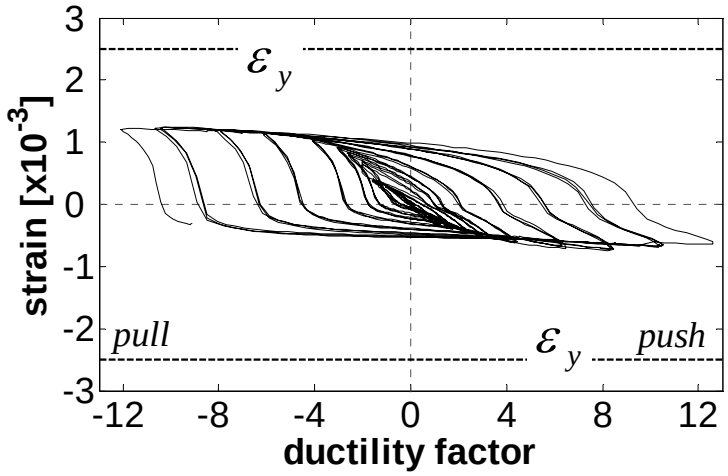

Figure 5.114 RCFST-87C Bottom bar strain history at 304mm from the base

5.7.6 Strains on transverse reinforcement

Figures 5.115 displays the confinement induced strain recorded by a strain gage placed in the bottom side of the spiral at 273 mm (10.8 in) from the base of the column. Figure 5.116 presents the shear induced strain recorded by a strain gage located in the right side of the spiral at 82 mm (3.2 in) from the base of the column. It is seen from these figures that the strains induced in the spiral are very low (maximum strains were about 10% of the yield strain), similar observations were done for the others RCFST specimens.

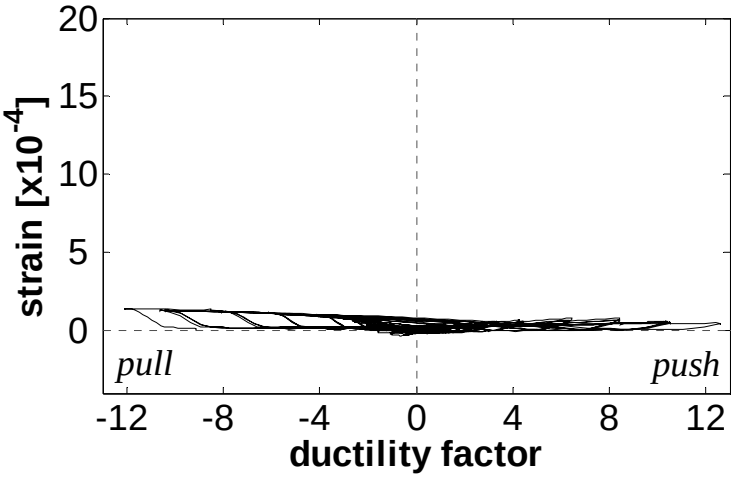

Figure 5.115 RCFST-87C Confinement strain on spiral bottom side at 273mm from the base

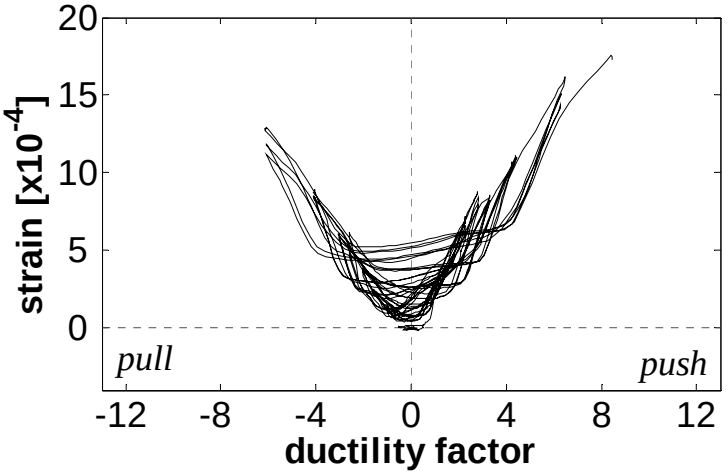

Figure 5.116 RCFST-87C Shear strain on spiral right side at 82mm from the base

5.7.7 Strains on steel tube

Confinement induced strain profiles in the steel tube are presented in Figures 5.117 and 5.118, and shear induced strain profiles in Figures 5.119 and 5.120. As noticed for the RCFST specimens examined before, strains induced in the steel tube are very low as result of the relatively large thickness of the steel pipe.

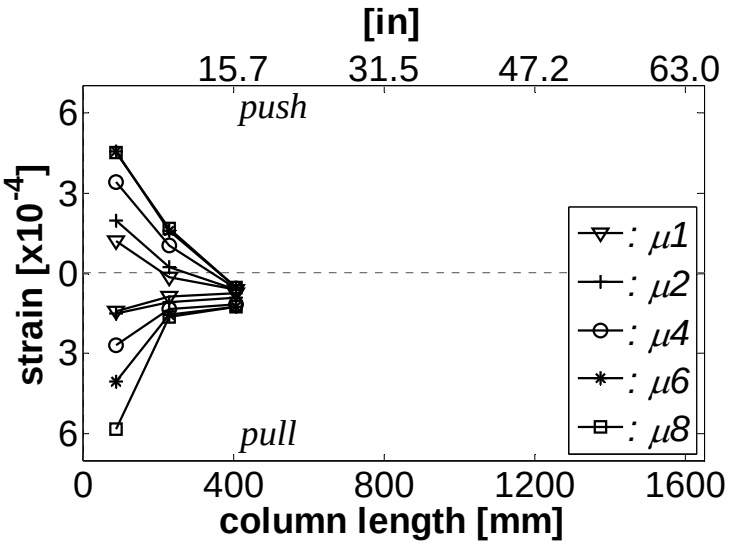

Figure 5.117 RCFST-87C Confinement strain profiles on top side of pipe

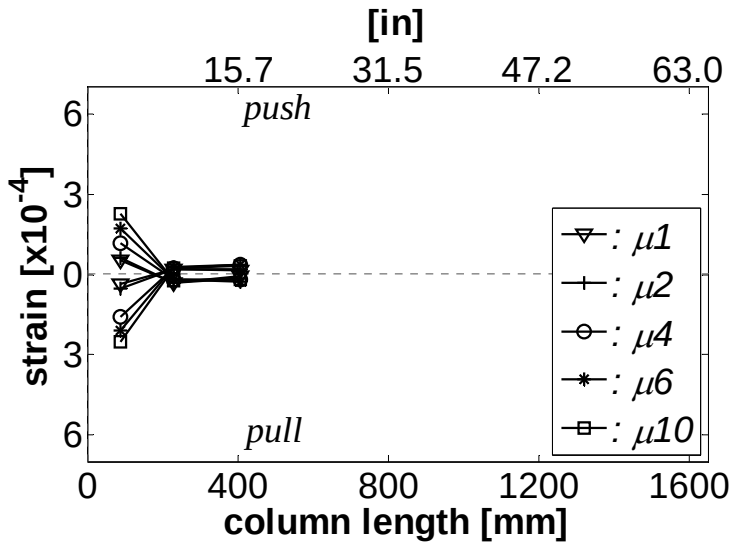

Figure 5.118 RCFST-87C Confinement strain profiles on bottom side of pipe

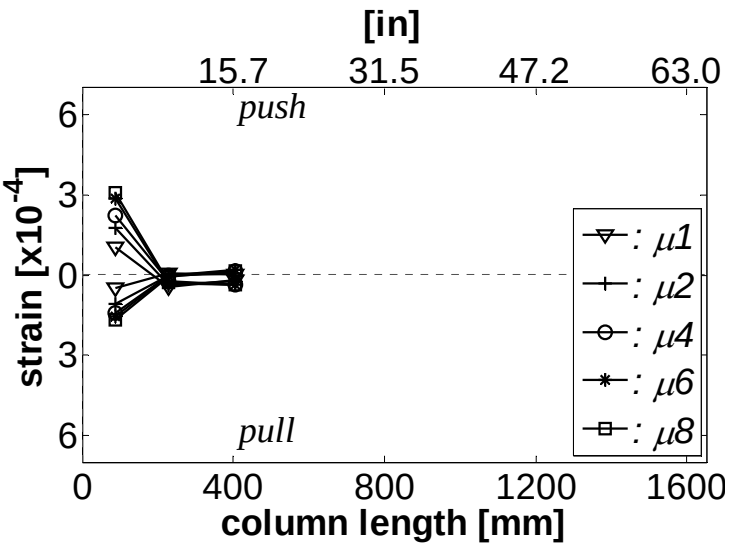

Figure 5.119 RCFST-87C Shear strain profiles on left side of pipe

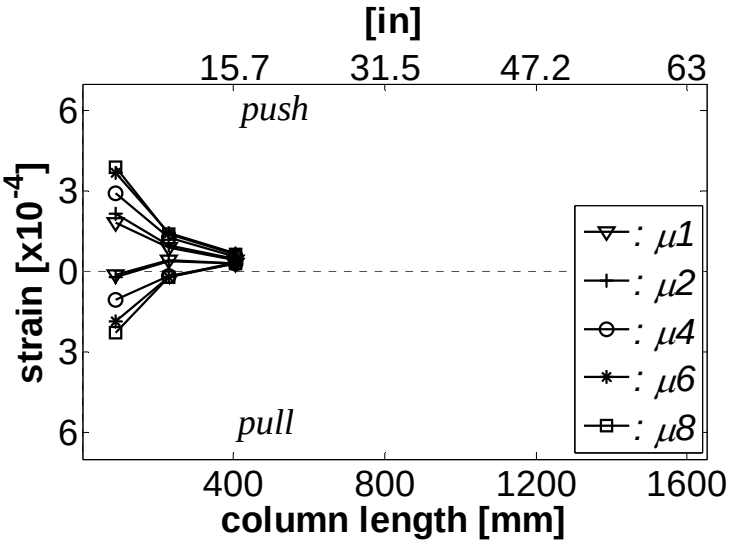

Figure 5.120 RCFST-87C Shear strain profiles on right side of pipe

5.7.8 Validity of test data

The procedure used for validation of the linear potentiometers data has been already explained for the other flexural specimens. From Figure 5.121 it can be noticed that data recorded by the linear potentiometers is reliable up to ductility 8.

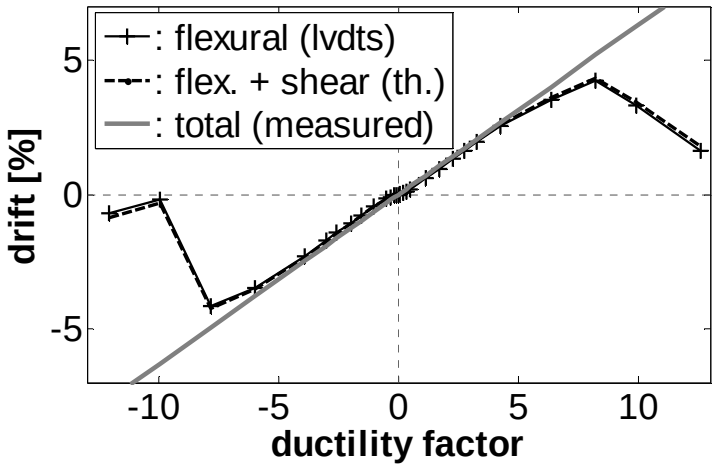

Figure 5.121 RCFST-87C Validity of test data

5.8 Comparison of RCFST-87A and RCFST-87C units

In order to identity the effect of low temperatures in the seismic behavior of reinforced concrete steel tube RCFST columns. This section compares the results obtained from the tests of the cold and room temperature specimens RCFST-87C and RCFST-87A. Figure 5.122 compares the hysteretic force displacement response for both specimens and Figure 5.123 compares its average first peak envelope. It is noticed from these graphs that: (1) The cold specimen exhibited an average increase of 10% in the flexural strength and 40% in the initial stiffness. (2) Strength degradation associated with the increasing lateral demand started at the same point for both specimens, at a lateral displacement of 64 mm (2.5 in). (3) Although both specimens failed at the same lateral displacement 104 mm (4.1 in), failure of the cold specimen involved rupture of longitudinal bar while failure of the room temperature specimen was controlled by strength degradation due to excessive damage in the core concrete. Figure 5.124 shows the three cycle envelopes for both specimens, it is seen that there is practically no difference in the strength degradation associated with repetitive cycles at the same level of demand for both units.

Energy dissipation properties are analyzed by means of (1) the energy absorbed in each cycle calculated as the area of each loop in the force-displacement hysteretic response of the specimen (Figure 5.125), (2) the hysteretic damping displayed in Figure

5.126 and (3) the equivalent damping to use in direct-displacement design in Figure 5.127. From these figures can be concluded that low temperatures did not have any effect on the energy dissipation capabilities.

Curvature distribution along the column is basically the same for both specimens (Figure 5.128) as a consequence the equivalent plastic hinge length is also very similar (Figure 5.129). Figure 5.130 is a picture of the specimens after the test and instrumentation removal, note that the level of damage in the footing is larger in the room temperature specimen than in the cold specimen, presumably due to the improvement of the mechanical properties of concrete at low temperatures. Finally, Tables 5.4 and 5.5 summarize the results obtained from the tests.

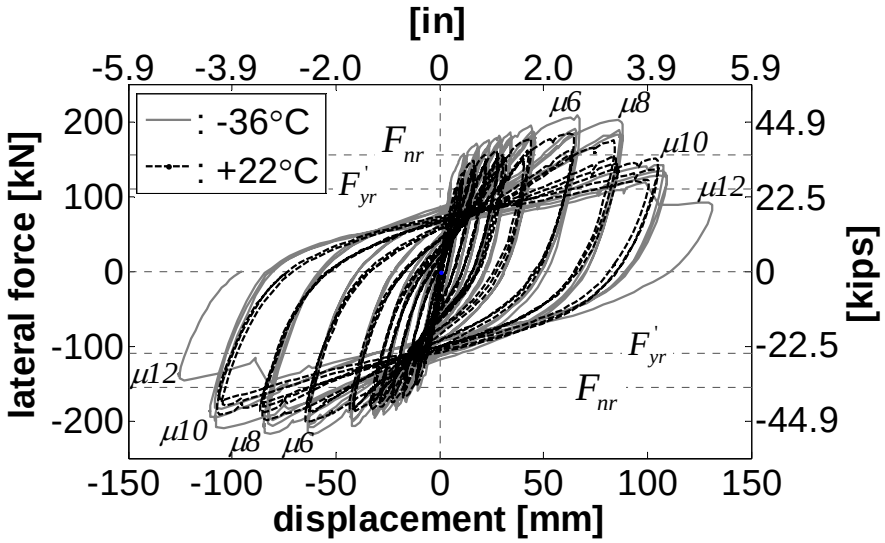

Figure 5.122 Hysteretic responses of RCFST-87A and RCFST-87C

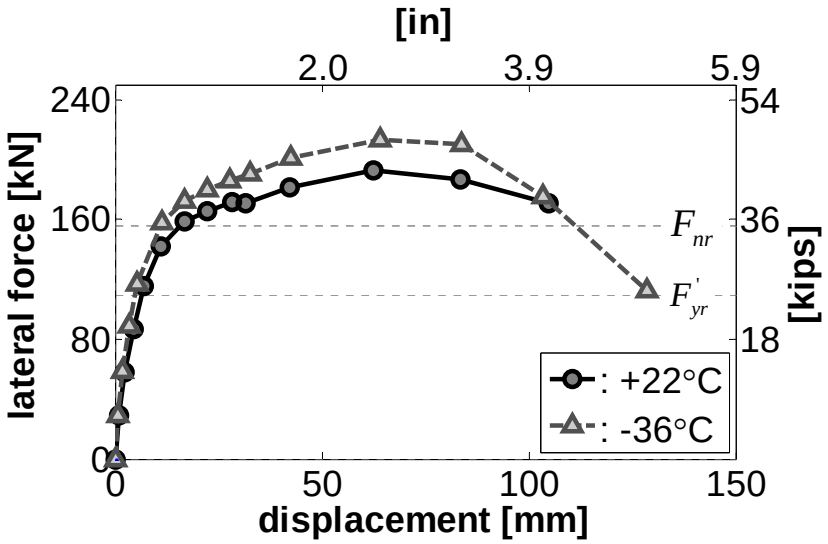

Figure 5.123 First cycle average envelope of RCFST-87A and RCFST-87C

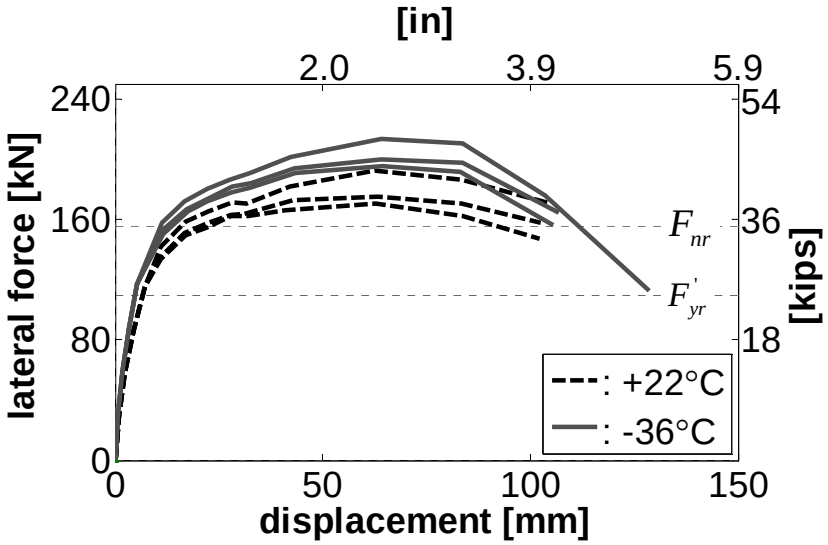

Figure 5.124 Average cycles envelopes of RCFST-87A and RCFST-87C

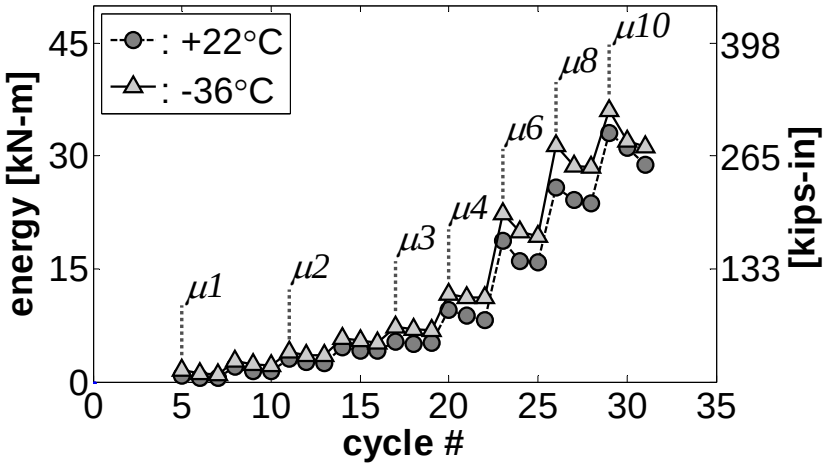

Figure 5.125 Energy released for RCFST-87C and RCFST-87A.

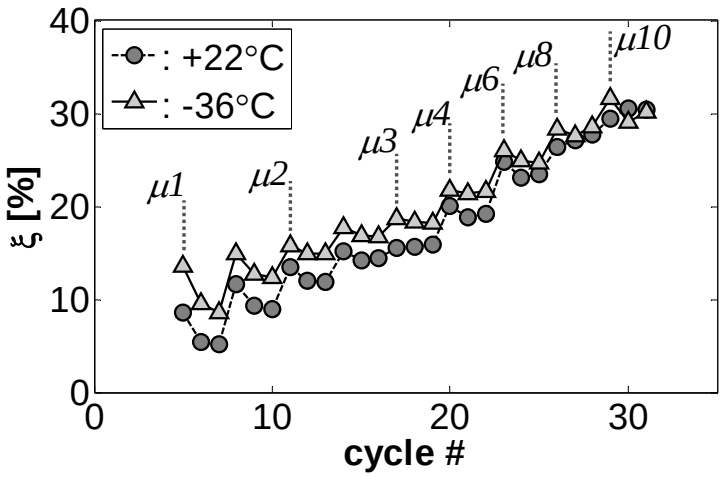

Figure 5.126 Hysteretic damping for RCFST-87C and RCFST-87A.

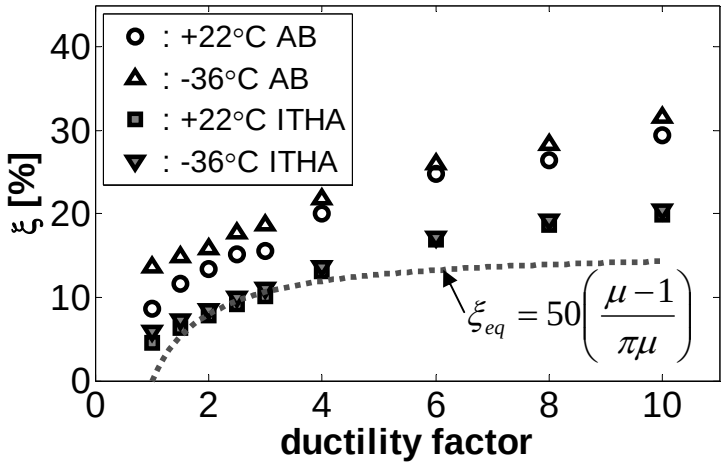

Figure 5.127 Corrected values of equivalent damping for RCFST-87C and RCFST-87A.

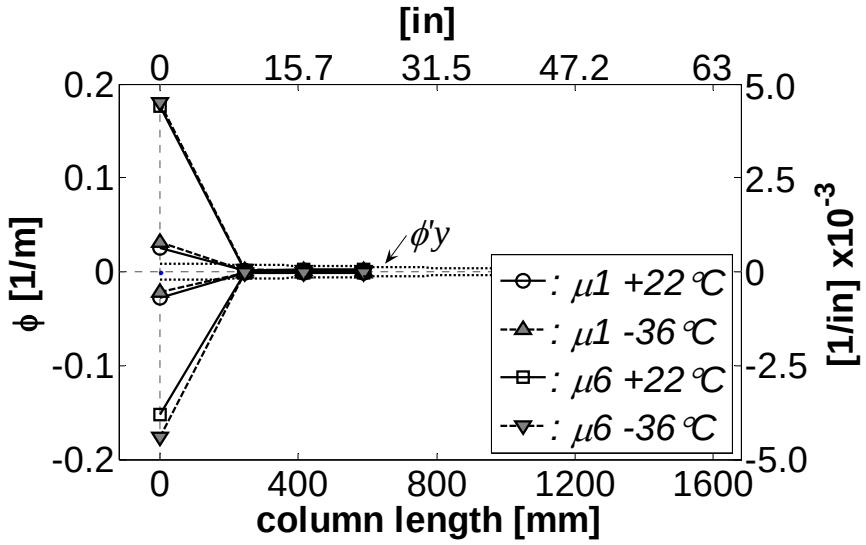

Figure 5.128 Curvature profiles for RCFST-87C and RCFST-87A.

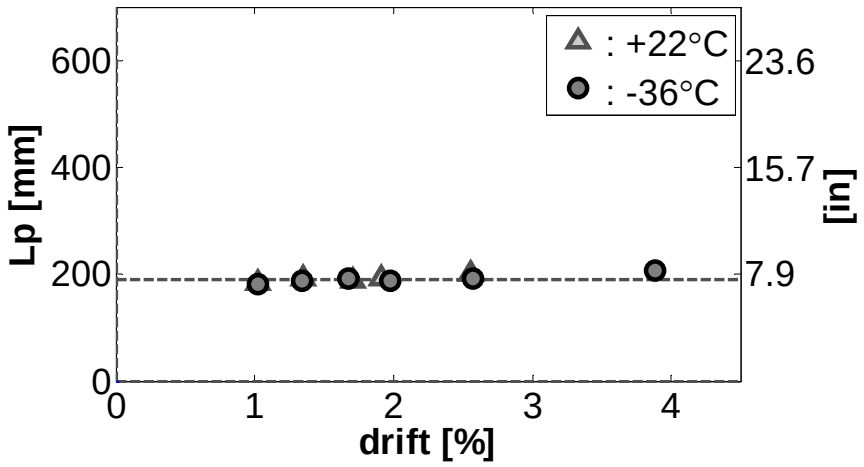

Figure 5.129 Plastic hinge lengths for RCFST-87C and RCFST-87A.

Figure 5.130 RCFST-87C and RCFST-87A after the test.

Table 5.4 Summary of results obtained (Load control phase)

Cycle	Average Lat. Force [kN]	Average tip displacement [mm]		
		+22°C	-36°C	-36°C / +22°C
0.25fy'	29.0	0.9	0.7	0.80
0.5fy'	58.2	2.2	1.8	0.80
0.75fy'	87.7	4.5	3.4	0.74
fy'	116.3	7.2	5.1	0.71

Table 5.5 Summary of results obtained (Displacement control phase)

Cycle	Average Displacement [mm]	First cycle average lateral force [kN]		
		+22°C	-36°C	-36°C / +22°C
μ1	11.2	142.0	157.5	1.11
μ1.5	16.9	158.3	172.5	1.09
μ2	22.3	165.4	180.3	1.09
μ2.5	27.9	171.1	186.5	1.09
μ3	32.1	171.2	190.2	1.11
μ4	42.3	181.8	201.0	1.11
μ6	63.2	192.2	213.1	1.11
μ8	83.6	186.6	210.5	1.13
μ10	104.2	171.2	173.8	1.02
μ12	128.5	-	112.0	-

5.9 Revised predictive models

Analysis of the results obtained during testing of the RCFST specimens reveals a significant reduction of the equivalent plastic hinge length when compared to ORC columns. Same observations have been made by past researchers when testing steel jacket retrofitted columns (Chai et al. 1991, Priestley et al. 1994a, b) and Equation 5.1 have been proposed for the estimation of L_p in the retrofitted columns. However, it was shown that values of L_p obtained for the RCFST specimens using Equation 5.1 are still larger than the actual values.

$$L_p = 2L_{sp} + g = 0.044 d_{bl} f_y + g \tag{5.1}$$

where d_{bl}, f_u, and f_y are the diameter, ultimate stress and yield stress of the longitudinal rebar, and g is the gap between the steel tube and the adjacent member.

The plastic hinge length plays a key role in the inelastic response of a column as it is where the inelastic rotation required to reach a target displacement (beyond yield) is accommodated. Thus, a short hinge length will imply larger inelastic demands in the

hinge region that may compromise the displacement capacity of the column. Based on the experimental results obtained in this investigation, the following equation is proposed to determine the equivalent plastic hinge length in reinforced concrete filled steel tube columns:

$$L_p = 9.3 d_{bl} \frac{f_u}{f_y} + g \tag{5.2}$$

where f_u is the ultimate stress of the longitudinal bar. As no change in L_p was detected during the cold tests of the RCFST specimens compared to the room temperature tests, assessment of the behavior of this type of columns at low temperatures can be performed using the equivalent plastic hinge length predicted by Eq. 12 without any correction for reduced temperatures. Figure 5.131 compares the results predicted by Equation 5.2 with the experimental results obtained in this research.

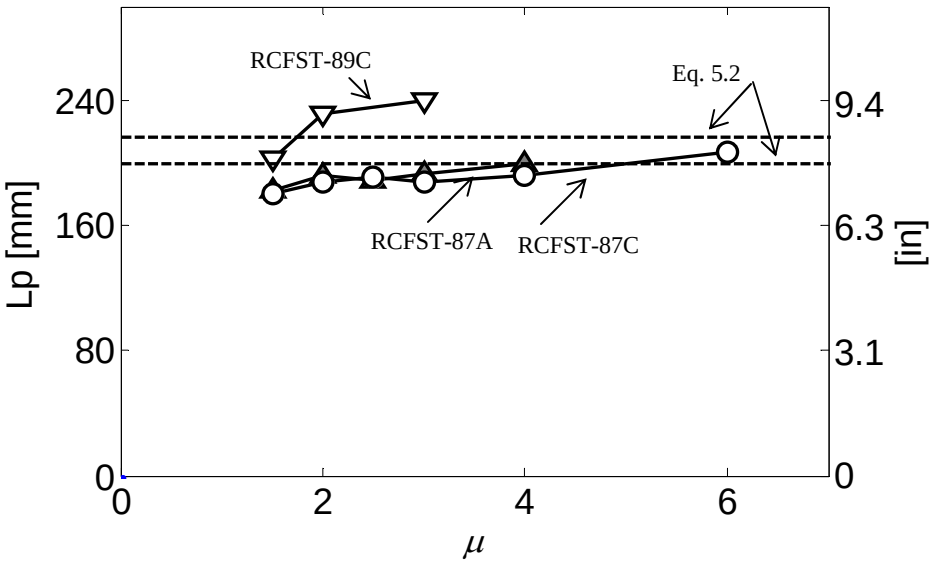

Figure 5.131 Equivalent plastic hinge lengths for the RCFST units

5.10 Final discussion and concluding remarks

This chapter presented the results obtained from the testing of two pairs of RCFST columns subjected to increasing cyclic reversals and constant axial load. One of

the columns of each pair was tested at room temperatures while the other one was tested at an average internal temperature of -36°C (-33°F). Differences between pairs of columns were the amount and properties of longitudinal reinforcement. Units RCFST-89A and RCFST-89C were reinforced with 8#9 bars ($\rho = 3\%$) with a yield stress of 558 MPa (81 ksi); units RCFST-87A and RCFST-87C were reinforced with 8#7 bars ($\rho = 2.1\%$) with a yield stress of 442 MPa (64 ksi). The results obtained were used to determine the effect of very low temperatures in the seismic behavior of RCFST columns. Additionally, the seismic behavior of the RCFST columns was weighted against the behavior of well detailed ordinary reinforced concrete columns by direct comparison with specimens FL-89A and FL-89C presented in Chapter IV. Main findings related to the effect of low temperatures in the seismic behavior of RCFST columns are summarized next:

- Specimens tested at low temperatures exhibited an increase in peak flexural strength. The amount of this increase was of 7% for the units with $\rho = 3\%$ and 10% for the units with $\rho = 2.1\%$. Note that this increase is calculated from the average differences between the lateral loads required to reach the target displacements before strength degradation starts. If the maximum loads reached by the specimens through all the tests are compared, then the increments are 3% for the units with $\rho = 3\%$ and 10% for the units with $\rho = 2.1\%$. This increase is below the increase of 15% noticed for the ordinary reinforced concrete columns (FL-89A and FL-89C) analyzed in Chapter IV.

- Cold specimens also show an increase in the initial elastic stiffness. The amount of this increase was of 60% for the units with $\rho = 3\%$ and 40% for the units with $\rho = 2.1\%$. Where the elastic stiffness is defined at the theoretical force level required for first yield of the room temperature specimen. This increase is larger than the increase of 27% noticed for the ordinary reinforced concrete columns (FL-89A and FL-89C) analyzed in Chapter IV.

- No major difference was noticed in the displacement capacity of the cold and room temperature specimens. Nonetheless, it can be said that failure of the

cold specimens was more brittle than the failure of the room specimens as it involves rupture of the longitudinal bars. Failure of the room temperature specimens was controlled by strength degradation of the columns due to excessive damage in the core concrete and footing, and also -in the case of RCFST-89A- buckling of the longitudinal bar.

- Strength degradation linked with increasing levels of lateral demand started earlier in the cold specimens, also strength degradation related to cyclic load at the same level of demand was found to be slightly larger for the cold specimens.

- Energy dissipation and hysteretic damping increased at low temperatures. However, when hysteretic damping values are converted to equivalent viscous damping so they can be used in direct-displacement design, the difference become negligible.

- Equivalent plastic hinge length was found to be the same for cold and room temperature specimens. Note that his implies a reduction in the plastic hinge length of the cold specimen as L_p is directly proportional to the rebar yield stress which increases at low temperatures.

- The available predictive models were able to capture the increase in strength in RCFST columns due to the low temperature effect.

- Earlier rebar rupture in the cold specimens implies a reduction in the deformation capacity of steel rebars subjected to reversals of loads and low temperatures. Furthermore, an unusual phenomenon was noticed during the testing of RCFST-89C where one of the main longitudinal bars cracked in three different spots along its surface.

Regarding the behavior of RCFST columns over well detailed ORC columns with low levels of axial load (ALR<10%), the only improvements observed during the tests were a slight increase in the flexural strength and energy dissipation properties. An

increase in flexural strength is generally not advantageous for seismic design as it then requires that capacity protected members such as footing and cap-beams must be designed for higher force levels. Furthermore, RCFST columns concentrate large rotations in the base of the column which may cause a significant reduction in the displacement capacity of the column and also, an extension of the plastic action into the adjacent member. It must be said at this point that these observations are valid only for the hinge developing adjacent to the cap beam and that other aspects such as soil-structure interaction, P-delta effects and residual drift are not addressed in this research.

CHAPTER VI

SEISMIC BEHAVIOR OF SHEAR DOMINATED REINFORCED CONCRETE COLUMNS AT LOW TEMPERATURES

6.1 Introduction

In order to determine the effect of cold temperatures on the behavior of shear dominated reinforced concrete columns two pairs of squat columns were tested. The only variable between columns of the same pair is the temperature of the specimen during testing: one of the columns was tested at room temperature ~22°C (72°F) while the other one was tested at ~-40°C (-40°F). Differences between each pair of identical columns were the ratios of transverse and longitudinal reinforcement that were designed with the aim of achieving shear failures at low levels of ductility (brittle shear failure) and high levels of ductility (ductile shear failure). The columns were designed using the equivalent plastic hinge method as described in Priestley et al. (2007) along with the "revised UCSD model" (Kowalsky and Priestley, 2000) for the assessment of shear strength.

The test set up and instrumentation are displayed in Figure 6.1. Table 6.1 presents the test matrix. For the four short columns cantilever length was 762 mm (30 in) and the diameter was 419 mm (16.5 in), i.e. all the columns have a moment to shear ratio of 1.8. Average concrete compressive strength at room temperature was 27.6 MPa (4 ksi) and 37.2 MPa (5.4 ksi) was the estimated compressive strength at -36°C (-32°F). More

detailed information regarding concrete compressive strength is presented in Table 2.6 on Chapter II.

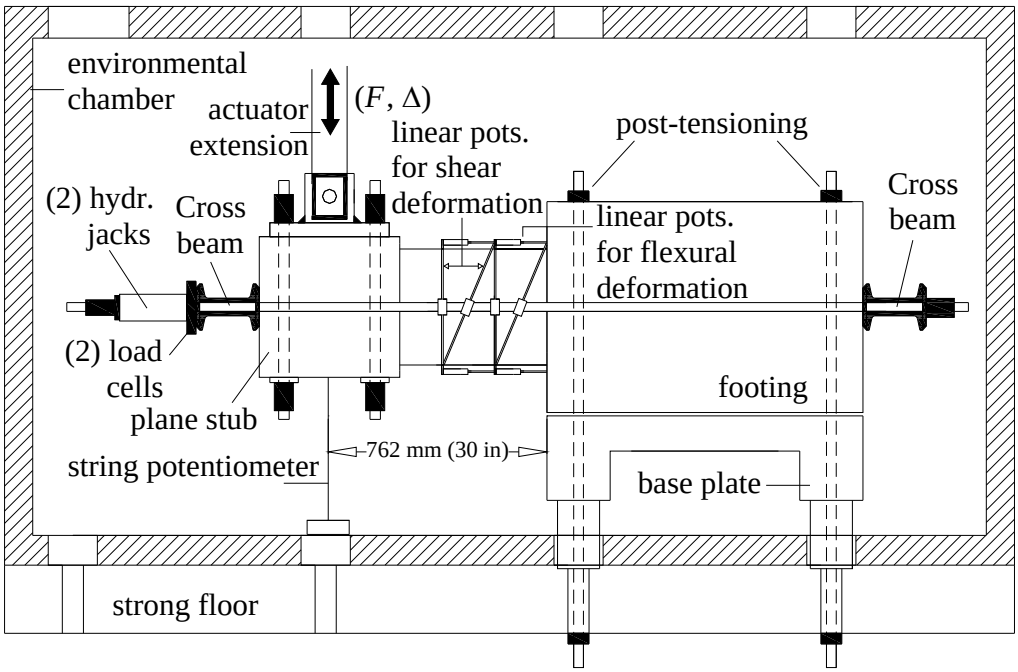

Figure 6.1 Short columns test setup and instrumentation

Table 6.1 Specimen matrix for the short columns

UNIT	TEMP.	BEHAVIOR	LONG. STEEL/ RATIO	TRANSVERSE STEEL/RATIO	AXIAL LOAD/ RATIO
DSH 87A	22˚C 72˚F	Ductile shear	8#7 2.2%	#3@102mm (4in) 0.8%	142 kN (3.7%) 32 kips
DSH 87C	-36˚C -32˚F	Ductile shear	8#7 2.2%	#3@102mm (4in) 0.8%	130 kN (2.5%) 29 kips
BSH 89A	22˚C 72˚F	Brittle shear	8#9 3.8%	#3@145mm (5.7in) 0.6%	135 kN (3.5%) 30 kips
BSH 89C	-36˚C -32˚F	Brittle shear	8#9 3.8%	#3@145mm (5.7in) 0.6%	135 kN (2.6%) 30 kips

6.2 Room temperature specimen DSH-87A

This specimen was tested on March 15/2007. Figures 6.2 and 6.3 show the variations of temperature and axial load during the test. Horizontal lines in Figure 6.3 denote the average applied axial load and the ±10% deviation.

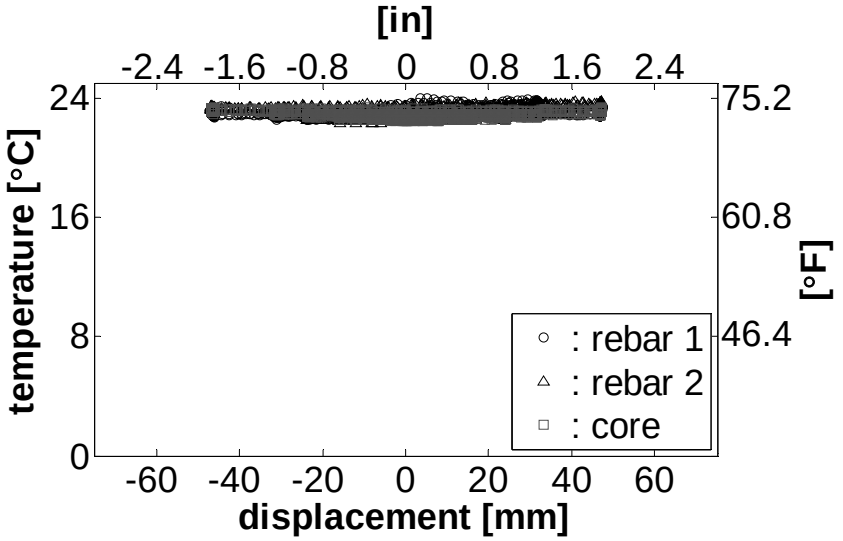

Figure 6.2 Temperature variations during the test of DSH-87A

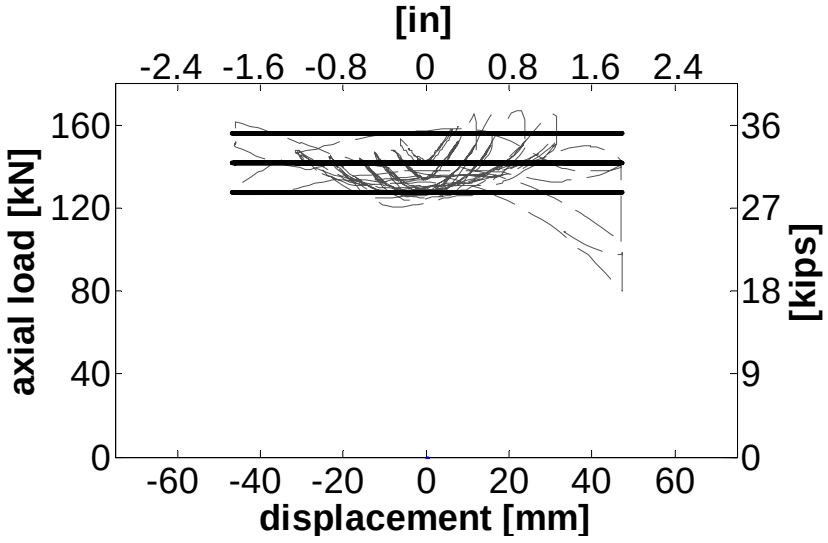

Figure 6.3 Axial load variations during the test of DSH-87A

6.2.1 DSH-87A Test observations

Figure 6.4 is a picture of the specimen before the tests. At the third cycle of the load control phase 170 kN (38.5 kips), two hairline flexural cracks were noted in the top and bottom faces of the columns and spaced 190 mm (7.5 in) from the column base and between them. During the last cycle of force control 229 kN (51.4 kips) the initial cracks that were primarily flexural in nature continued to extend and incline to ~70° with the columns axis. The first "shear only" crack developed also at this level inclined at ~45°. The width of the cracks is still very small (Figure 6.5). No major changes were noticed during the cycles at ductility 1 (Figure 6.6).

During the cycles at ductility 1.5 the existing cracks kept extending and a new flexural crack appeared at ~50 mm (2 in) from the base of the column (Figure 6.7). After the cycles at ductility 2 (Figure 6.8) a new flexural crack and a new shear crack appeared at mid height of the column, existing shear cracks have extended and are now inclined at 35°. Also at this point the first signs of concrete crushing were noticed in the base of the column. At ductility 3 (Figure 6.9) cover concrete crushing is evident, flexural cracks close to the base of the column widened to 2 mm and shear cracks to 1 mm.

Spalling of the cover concrete along the 50 mm (2 in) adjacent to the base of the column was noticed at ductility 4 (Figure 6.10), cracks on both faces largely widen due to column dilatation. During the cycles at ductility 6 (Figure 6.11) the column exhibited very large dilation causing the spalling of all cover concrete over a distance 220 mm (8.6 in) from the base of the column. Severe strength degradation was noticed with cycling. At the last push of ductility 6 the column only reached 42% of the maximum load attained during the test and the test was stopped at this point.

Figure 6.12 is a picture of the specimen after instrumentation removal. It is seen that the large dilation that the column suffered during the test caused spalling of the cover concrete over a large area leaving all the transverse and longitudinal completely exposed.

Figure 6.4 DSH-87A before test

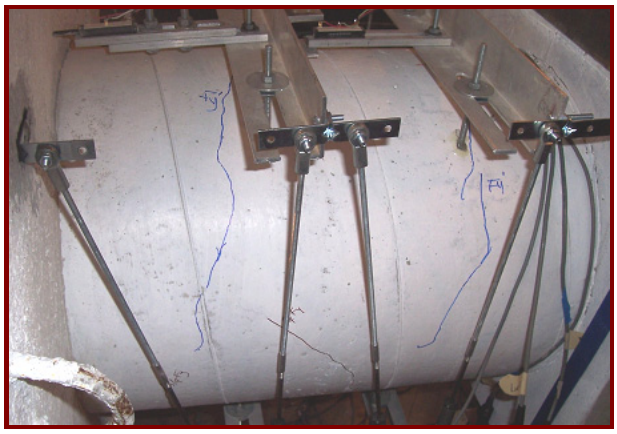

Figure 6.5 DSH-87A after the load control phase

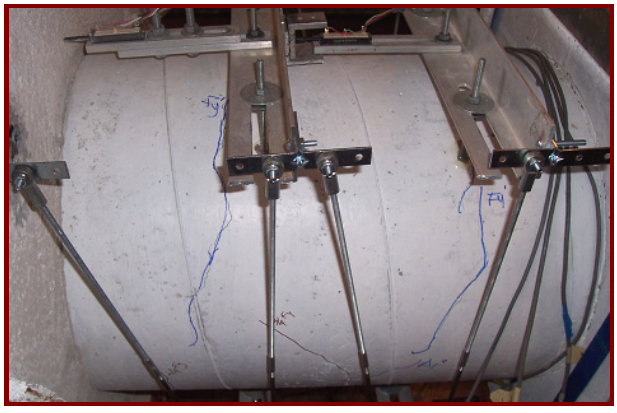

Figure 6.6 DSH-87A after the cycles at ductility 1

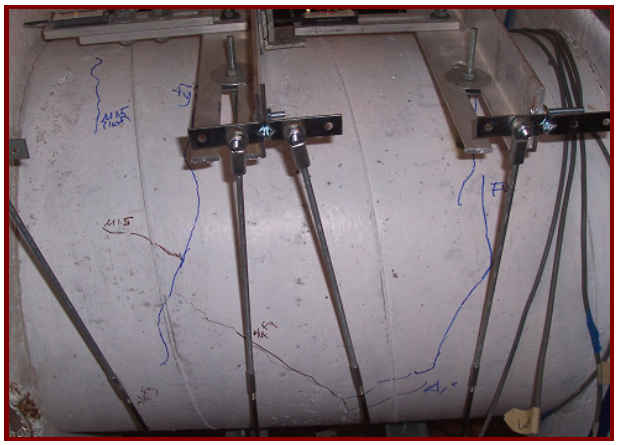

Figure 6.7 DSH-87A after the cycles at ductility 1.5

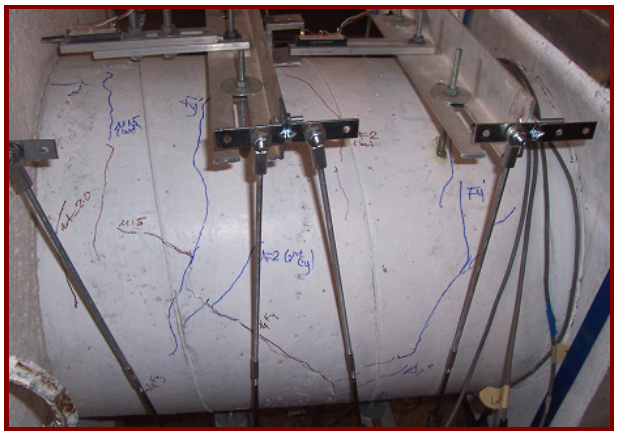

Figure 6.8 DSH-87A after the cycles at ductility 2

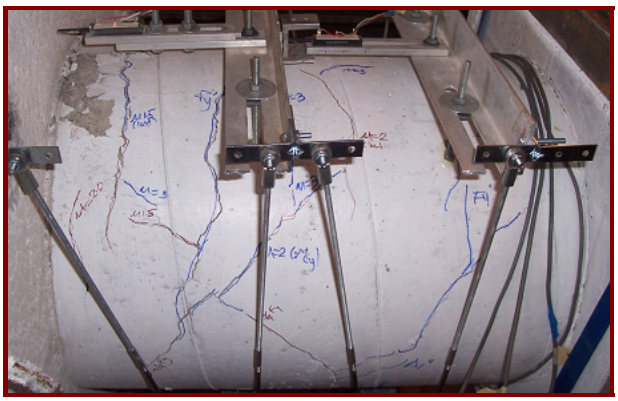

Figure 6.9 DSH-87A after the cycles at ductility 3

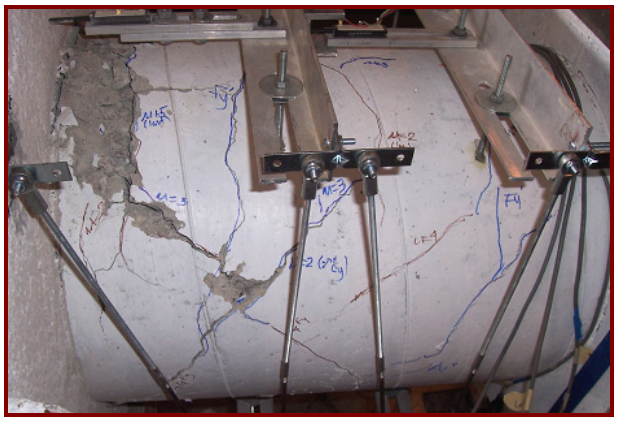

Figure 6.10 DSH-87A after the cycles at ductility 4

Figure 6.11 DSH-87A after the cycles at ductility 6

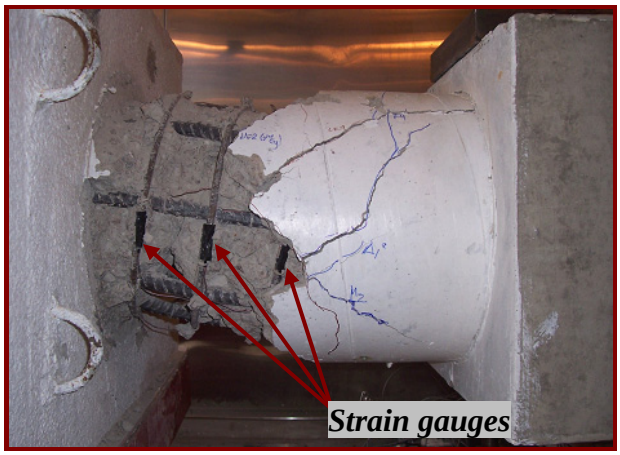

Figure 6.12 DSH-87A after instrumentation removal

6.2.2 DSH-87A Force displacement response

Figure 6.13 displays the hysteretic force-deformation response recorded during the test along with the theoretical force-deformation and shear strength envelopes. As mentioned earlier in Chapter II, in the revised UCSD model (Kowalsky and Priestley, 2000) the shear strength degradation with increasing cyclic inelastic demand is computed based on the displacements due to flexural deformations only. Ductility values displayed in Figure 6.13 correspond to total deflections. It is noticed from this figures that the hysteretic loops are stable up to the first cycle of ductility 6 when excessive dilation occurred in the concrete of the column, provoking serious damage in the concrete and severe strength degradation.

Figure 6.14 shows the average of both directions first peak force-displacement envelope along with the theoretical force-deformation and shear strength envelopes. It is seen that predicted flexural and shear strengths are very close to the actual results. In Figures 6.13 and 6.14 the ductility values for calculation of the shear strength envelope are obtained based on the results obtained during the test. When designing a new structure this information is not available and estimation of the shear strength envelope has to be done based on the theoretical force-displacement envelope. Results obtained using this approach are displayed on Figure 6.15 and 6.16, notice from these figures that the match between predicted and actual response is still acceptable.

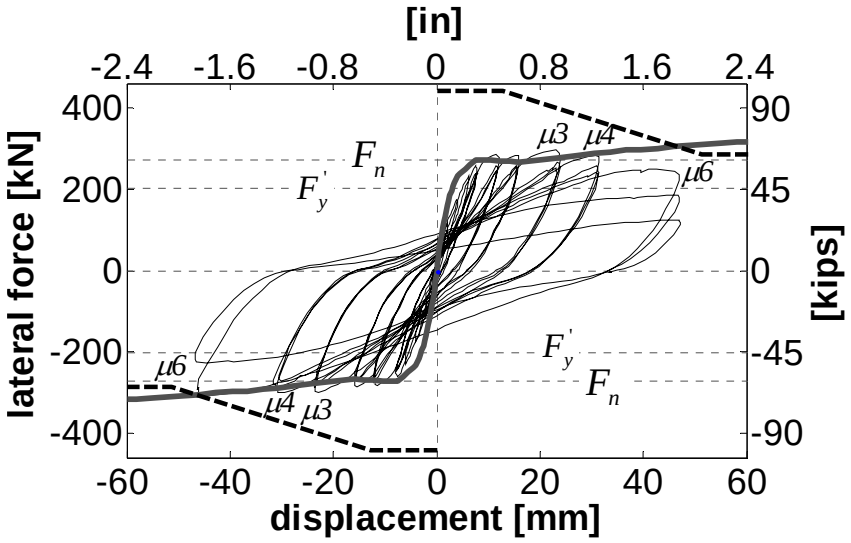

Figure 6.13 DSH-87A Force displacement response and theoretical shear strength envelope

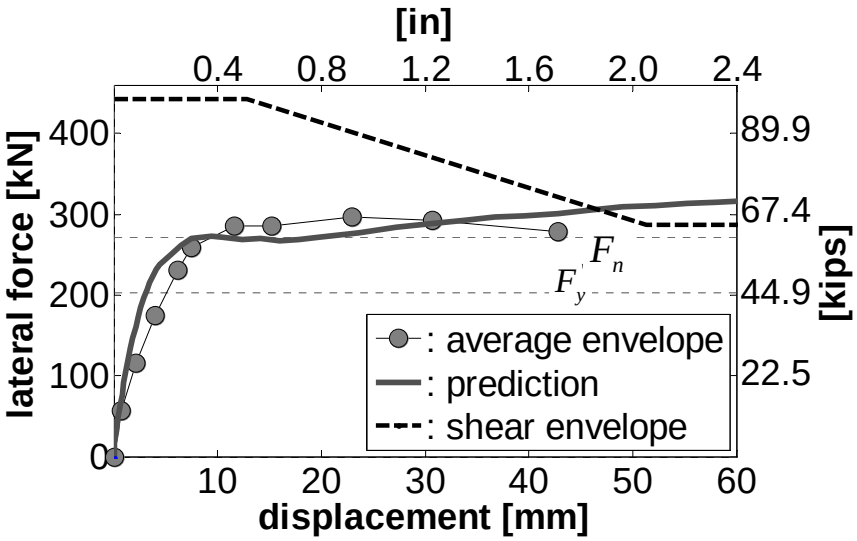

Figure 6.14 DSH-87A First peak envelope and theoretical shear strength envelope

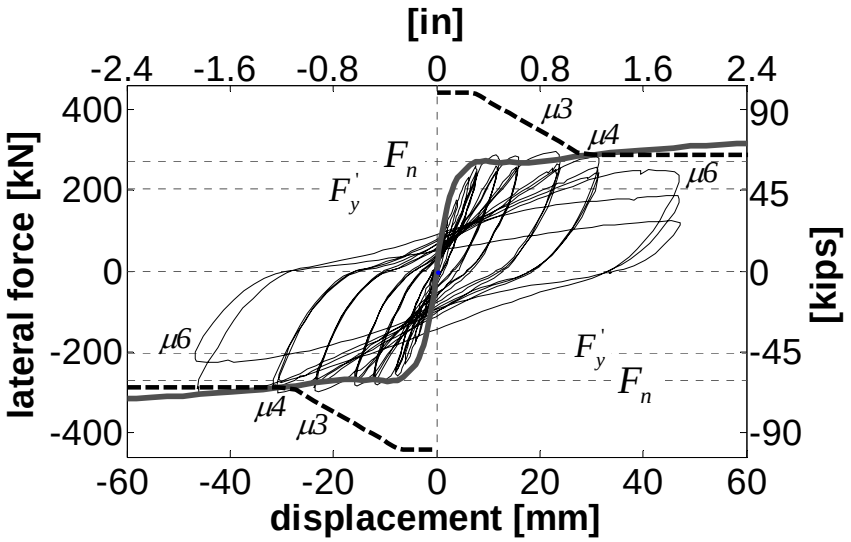

Figure 6.15 DSH-87A Force displacement response with shear strength envelope obtained using the theoretical force-displacement envelope

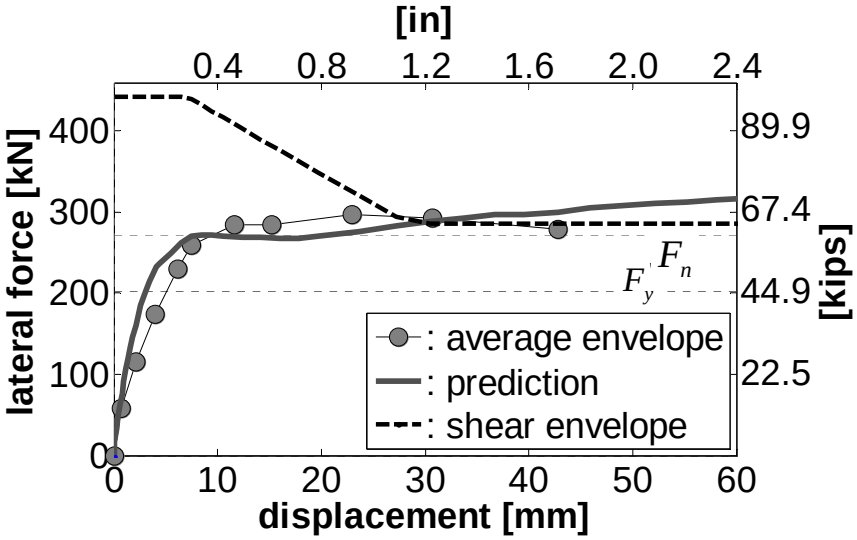

Figure 6.16 DSH-87A First peak envelope with shear strength envelope obtained using the theoretical force-displacement envelope

6.2.3 DSH-87A Curvature profiles

Using results from linear potentiometers mounted on the extreme tension/compression faces of the columns, average curvatures over the potentiometer gage lengths were obtained by dividing the rotation indicated by the potentiometers by

the gage length. The gage length of the potentiometer next to the base of the column includes a component due to strain penetration as it can be argued that the rotation evaluated in this cell is distributed into the footing, this will have the effect of reducing the curvature as plotted for the base cell. The magnitude of this addition (114 mm / 4.5 in) is obtained by optimization of the match between the experimental and theoretical moment-curvature relation. Figure 6.17 shows the moment-curvature response along with the theoretical moments associated with the experimental curvature recorded during the test. Figure 6.18 shows the curvature profiles for selected ductilities, also shown in this figure is the theoretical curvature profile for first yield of the longitudinal steel in the base of the column. From the curvature profiles in Figure 6.18 it is noticed that up to ductility 1 the curvature distribution is almost uniform along the column, at ductilities larger than 1 most of the curvature is concentrated in the first cell.

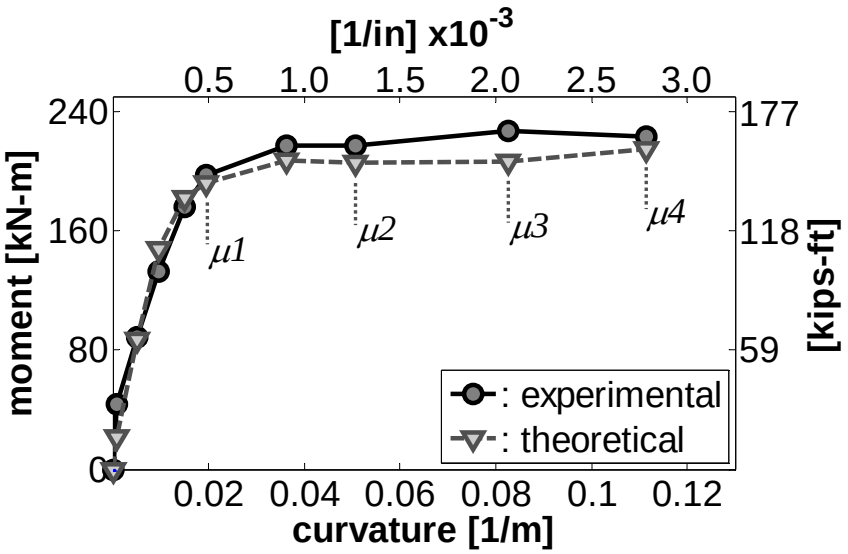

Figure 6.17 DSH-87A Moment curvature at column base.

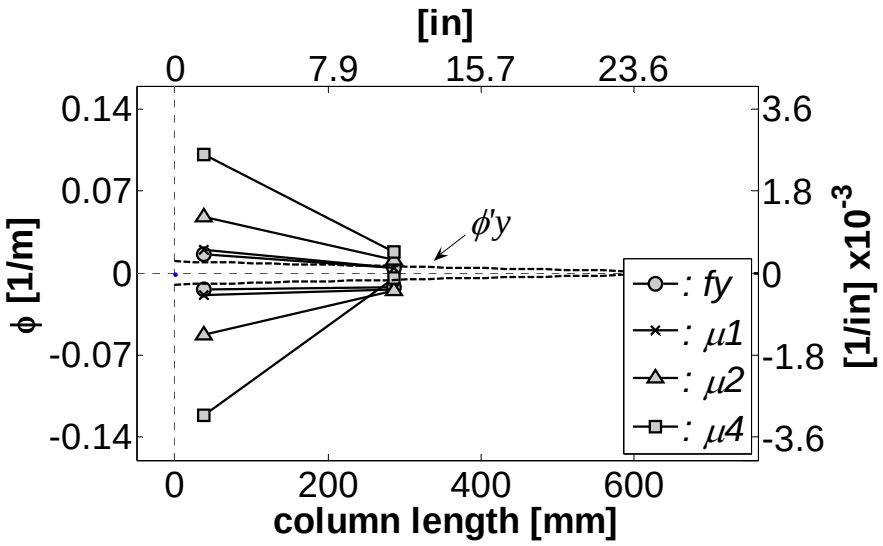

Figure 6.18 DSH-87A Curvature profile

6.2.4 DSH-87A Equivalent plastic hinge length

Curvatures calculated at the base of the column are used along with the recorded tip displacement of the column to determine an equivalent plastic hinge length over which the plastic curvatures are assumed to be constant. Figure 6.19 shows the results obtained. Note that the average value obtained 256 mm (10.1 in) is basically the same predicted by the traditional expression $L_p = 0.044 f_y d_{bl}$ once the hinge reduction factor of 0.59 obtained for the current test set up in Chapter IV is applied, $L_p = 0.59(0.044 * 442 * 22.2) = 254.7mm\ (10in)$.

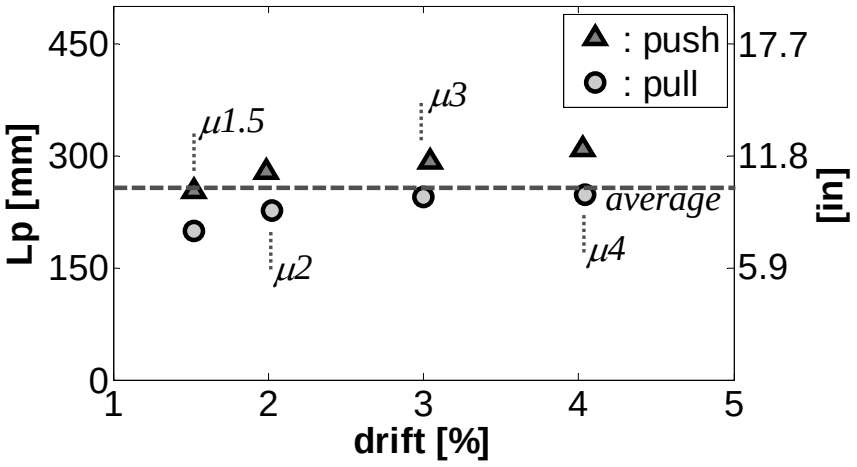

Figure 6.19 DSH-87A Equivalent plastic hinge length

6.2.5 DSH-87A Deformation components

Linear potentiometers were specially distributed in the short columns to allow the calculation of flexural and shear components of deformation following the procedure described in Chapter III. A measure of the accuracy of these deformation components may be found by using them to predict the total lateral displacement at the top of the column. Figure 6.20 shows the results obtained. It is seen that the sum of flexural and shear components of displacement is in reasonably close agreement with the measured displacement up to ductility 4, after this point the diagonal and vertical linear pots used to measured the shear were disconnected from the specimen because of the excessive damage in the column. As a result, data beyond this point is not longer reliable. With the increasing lateral demand both components increase linearly up to ductility 3, being the shear component ~11% of the total deformation. After this point the contribution of shear induced deformation to the total deflection starts increasing. At ductility 4 the shear component contribution is ~14% and at ductility 6 is expected to be ~19% of the total displacement.

Theoretical models used to estimate shear and flexural deformations are evaluated by direct comparison with the deformation components recorded during the test. The results obtained are displayed in Figures 6.21 to 6.24, comparisons are performed as

function of the total displacement and also as function of the applied lateral force. It is seen from these figures that actual and predicted values are in close agreement.

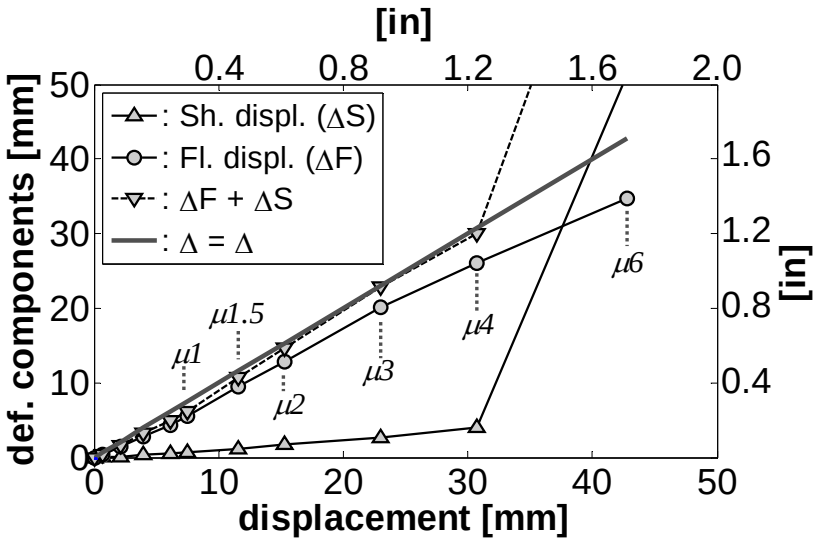

Figure 6.20 DSH-87A Deformation components

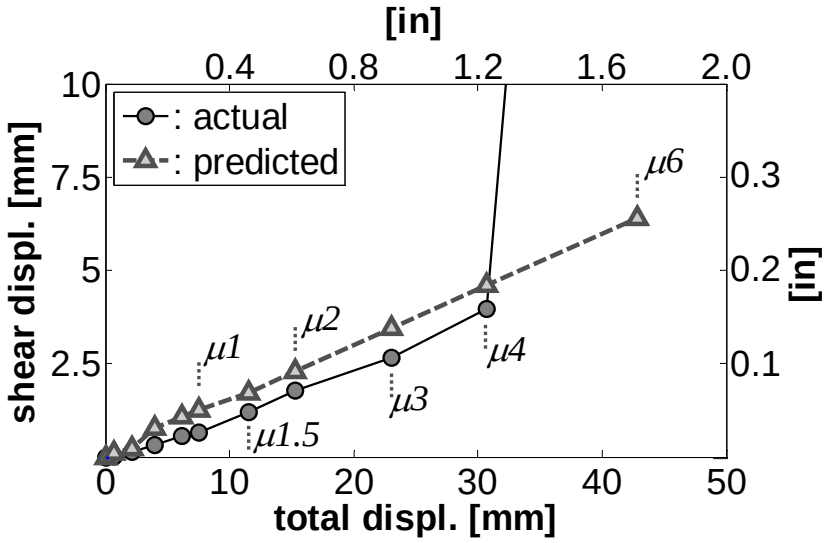

Figure 6.21 DSH-87A measured and predicted shear deformation components as function of the total displacement

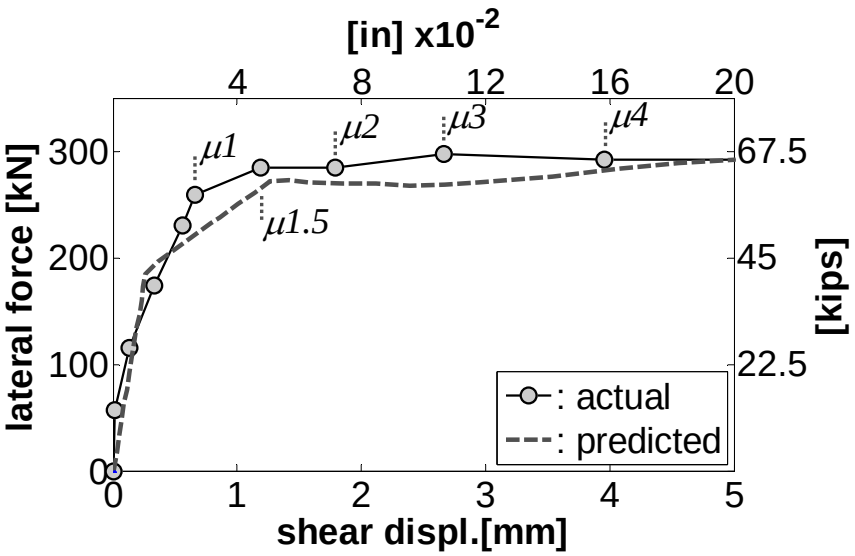

Figure 6.22 DSH-87A force vs. shear displacement envelope

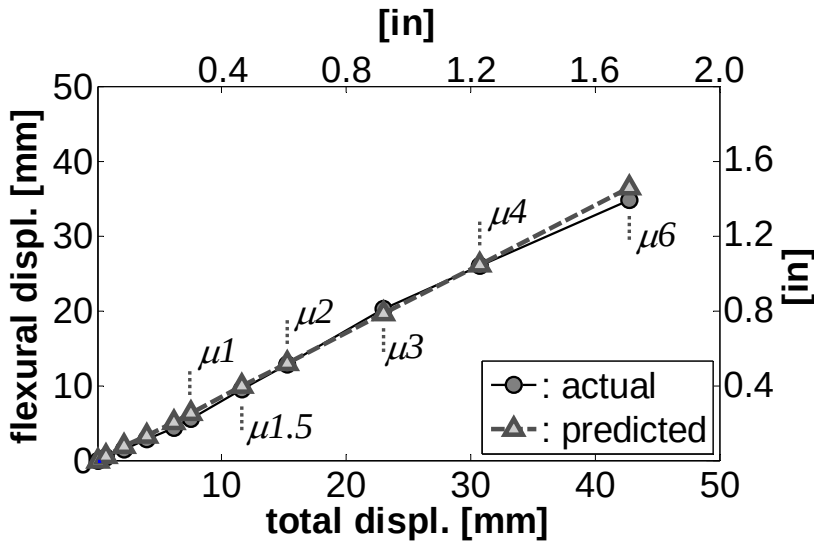

Figure 6.23 DSH-87A measured and predicted flexural deformation components as function of the total displacement

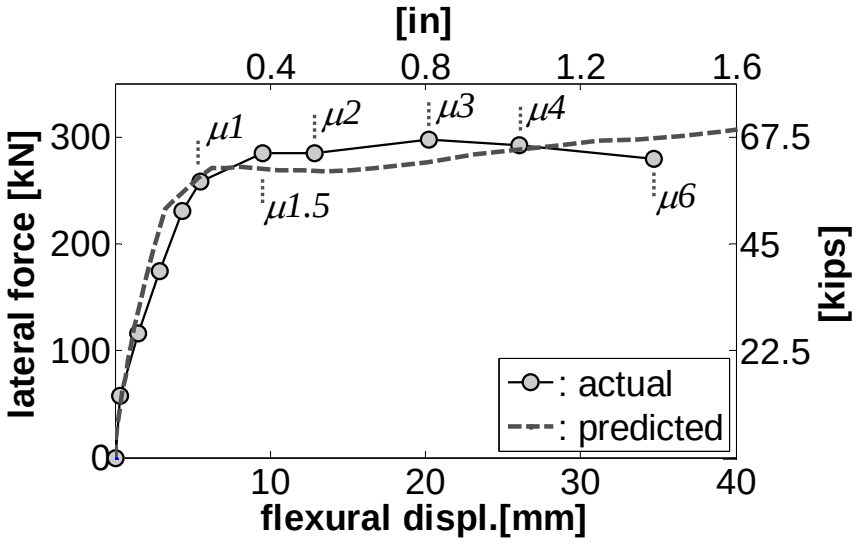

Figure 6.24 DSH-87A force vs. flexural displacement envelope

6.2.6 DSH-87A Strains on longitudinal steel

Data recorded by the strain gages placed on the longitudinal rebars are presented in the form of longitudinal strain profiles. Regrettably, the data collected was only reliable for low levels of lateral demand, which is not unusual for strain gauge data, highlighting the importance of developing alternative strain measuring systems. Figure 6.25 shows the strain profiles for the top most bar and Figure 6.26 for the bottom most bar. It is noted that maximum strains are reached not in base of the column (as for the flexural specimens presented in Chapters IV and V) but at a distance ~ 175 mm (6.9 in) from the base. This is in agreement with the location of the first flexural cracks developed during the test (Figure 6.5) and is also consistent with past test observations (Kowalsky et al. 1995).

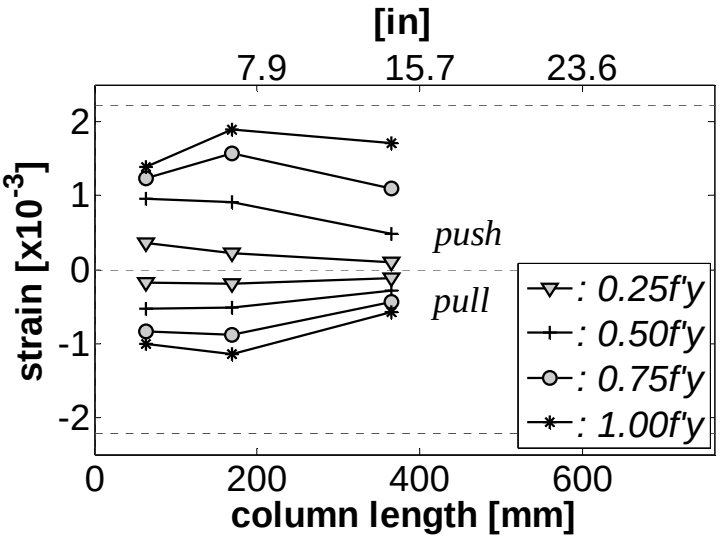

Figure 6.25 DSH-87A longitudinal strain profiles in top most bar

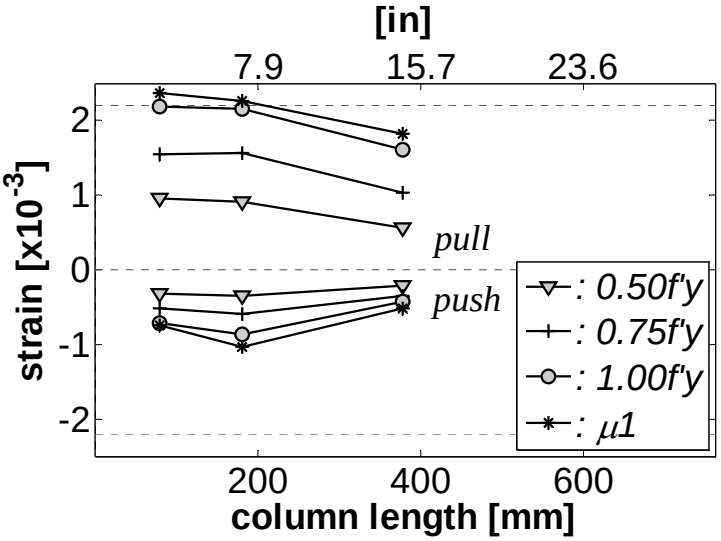

Figure 6.26 DSH-87A longitudinal strain profiles in bottom most bar

6.2.7 DSH-87A Strains on transverse steel

Data collected from the strain gages placed on the spiral is also presented in the form of strain profiles. According to the position of the gages, strains are classified as confinement or shear induced strains. Figure 6.27 show the strain profiles in the bottom face of the spiral, i.e. confinement induced. As expected larger strains are recorded in the push direction when the concrete in the bottom face is in compression and dilates due to

the Poisson effect. As for the longitudinal strain profiles, maximum strains are recorded not by the gauge closest to the column base but by one placed 254 mm (10 in) from the base. There was not enough reliable data to generate the top face profile or the right side shear induced profile.

Figure 6.28 shows the shear induced strain profile for the left side of the spiral. It is seen that the larger strains are recorded by a gage placed 292 mm (11.5 in) from the base. This is understandable as this gage was just in the middle of the main shear crack developed in the specimen during the test (Figure 6.12). Figure 6.29 show the strain history recorded by this gauge. Unfortunately, the strain gauge broke at ductility 3 registering a maximum strain of 0.0054. If it is assumed that the increase in strain will follow the same pattern for larger ductility demands, then the expected strain at ductility 4 is expected to be around 0.007 and 0.01 at ductility 6.

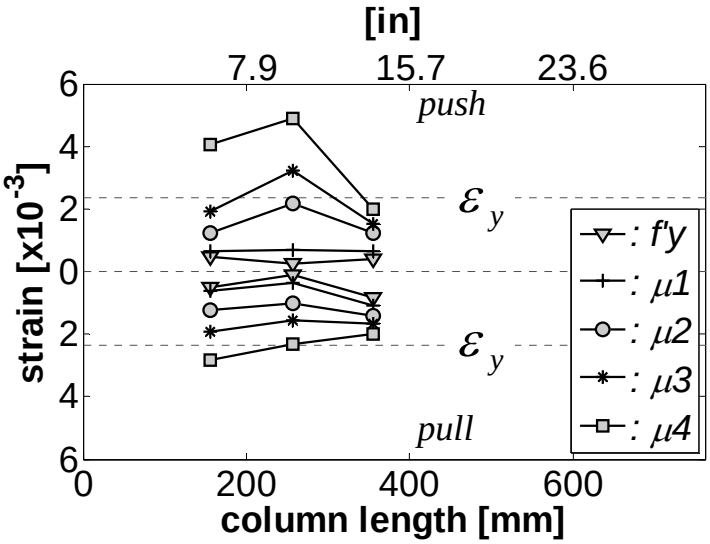

Figure 6.27 DSH-87A confinement induced strain profiles in bottom face of spiral

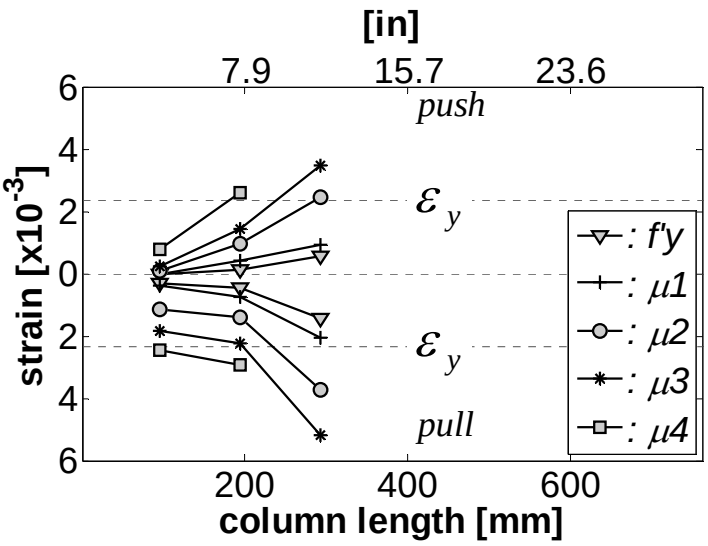

Figure 6.28 DSH-87A shear induced strain profiles in left face of spiral

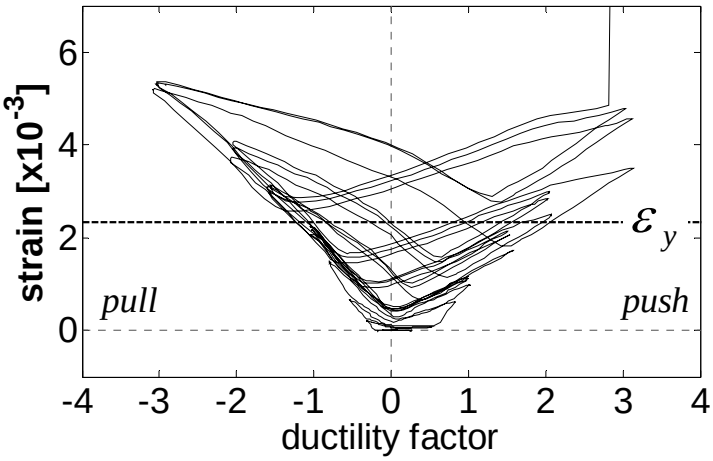

Figure 6.29 DSH-87A shear induced strain history 292 mm from base

6.3 Cold temperature specimen DSH-87C

This specimen was tested on April 4/2007. Like for the cold flexural units, cooling of the specimen started 26 hours before the test. Figures 6.30 and 6.31 show the variations of temperature and axial load during the test. As mentioned in earlier chapters for the flexural units, the axial load is more difficult to control in the cold condition because of the effect cold temperatures have in the viscosity of the hydraulic fluid running in the jacks.

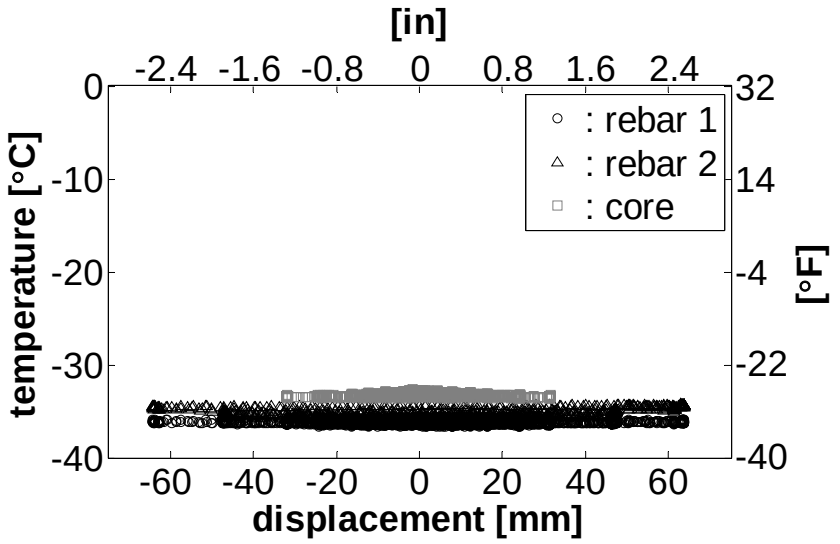

Figure 6.30 Temperature variations during the test of DSH-87C

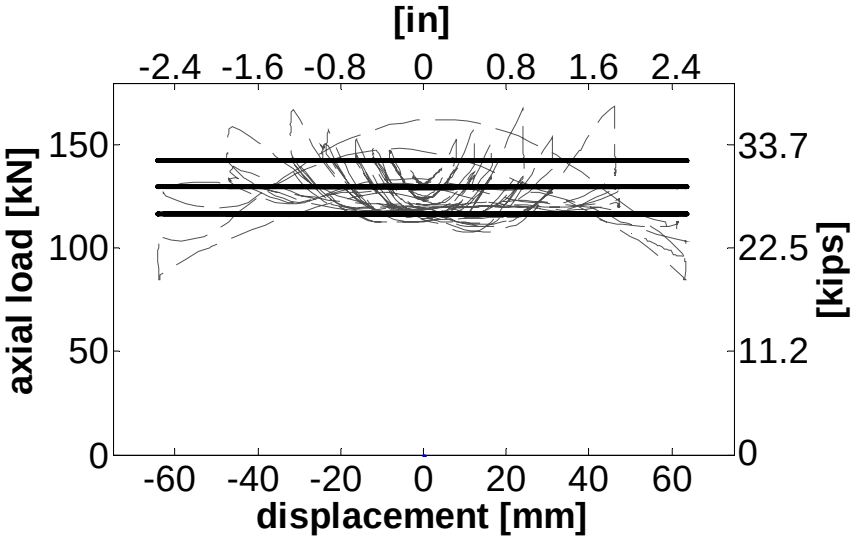

Figure 6.31 Axial load variations during the test of DSH-87C

6.3.1 DSH-87C Test observations

The first hairline cracks were noticed only up to the last cycle of load control 229 kN (51.5 kips) and were flexural in nature, the cracks were spaced ~190 mm (7.5 in) between them and from the base of the column as shown in Figure 6.32. With the cycles at ductility 1 the cracks extend and incline ~70° with the column axis (Figure 6.33). No

major changes were observed in the specimens during the ductility 1.5 cycles except by a widened of the existing cracks (Figure 6.34). At ductility 2 (Figure 6.35) the two original cracks keep extending and are incline now 45°, first signs of concrete crushing at the column base were noticed at this level of demand.

With the cycles at ductility 3 (Figure 6.36) existing cracks widened, shear cracks are inclined at ~30° and a new flexural crack appears at ~50 mm (2 in) from the base. During the cycles at ductility 4 (Figure 6.37) new minor shear cracks appeared in the specimen and the concrete crushing at the base of the column is now evident.

A number of new shear cracks appeared during the cycles at ductility 6 (Figure 6.38), all the cracks are now interconnected between them and cause large damage in the specimen. Severe crushing and spalling of the concrete close to the base of the column is also noticed during these cycles. The lateral load required to reach the target displacement for ductility 6 was 93% the required for ductility 4.

The lateral load required to reach the target displacement for ductility 8 was 83% the maximum load reached during the test. At this ductility (Figure 6.39) spalling of the concrete occurred over almost the whole circular part of the column due to the large dilation in the specimen. Severe strength degradation was noticed over the cycles at this demand. The maximum load reached during the last push at ductility 8 was only 65% the load reached during the first cycle at the same level of ductility. The test was stopped at this point. Figure 6.40 is a picture of the specimen after instrumentation removal, it seen that the longitudinal and transverse steel is exposed almost over the whole specimen.

Figure 6.32 DSH-87C after the last cycle of load control

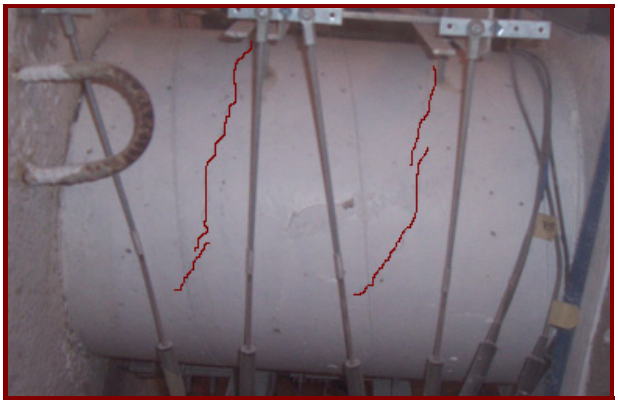

Figure 6.33 DSH-87C after the last push at ductility 1

Figure 6.34 DSH-87C after the last push at ductility 1.5

Figure 6.35 DSH-87C after the last push at ductility 2

Figure 6.36 DSH-87C after the last push at ductility 3

Figure 6.37 DSH-87C after the last push at ductility 4

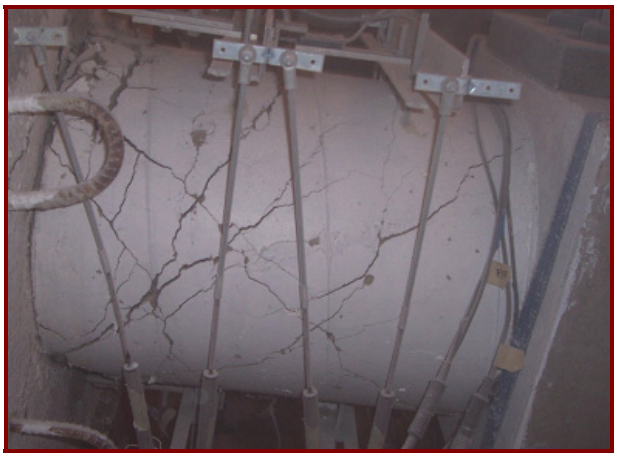

Figure 6.38 DSH-87C after the last push at ductility 6

Figure 6.39 DSH-87C after the last push at ductility 8

Figure 6.40 DSH-87C after instrumentation removal

6.3.2 DSH-87C Force displacement response

The hysteretic force displacement response recorded during the test is displayed in Figure 6.41, this figure also shows the theoretical force displacement envelope and shear strength envelope. It is seen that the hysteretic loops are stable up to ductility 8 where severe strength degradation is noticed due to the large damage induced in the column concrete. Figure 6.42 shows the first peak envelope along with the predicted response and shear strength envelope, it is seen that the theoretical models were able to predict the response of the column. In Figures 6.41 and 6.42 the shear strength envelope is calculated based on the actual flexural displacement ductilities observed during the test. Figures 6.43 and 6.44 are similar to Figures 6.41 and 6.42, but this time the shear strength envelope is calculated using the displacement ductilities from the theoretical prediction. Note that this will only affect the displacements at which shear strength degradation starts and ends, and not the shear strength values. It is noticed from Figures 6.43 and 6.44 that the match between predicted and actual response is still very acceptable when the complete “blind prediction” is performed, as will be the general case for the seismic assessment of an existing structure. Note that as used the model is for the assessment of shear strength and no for design purposes. Chapter III presented the modifications proposed by the authors (Kowalsky and Priestley, 2000) to utilize the model for design.

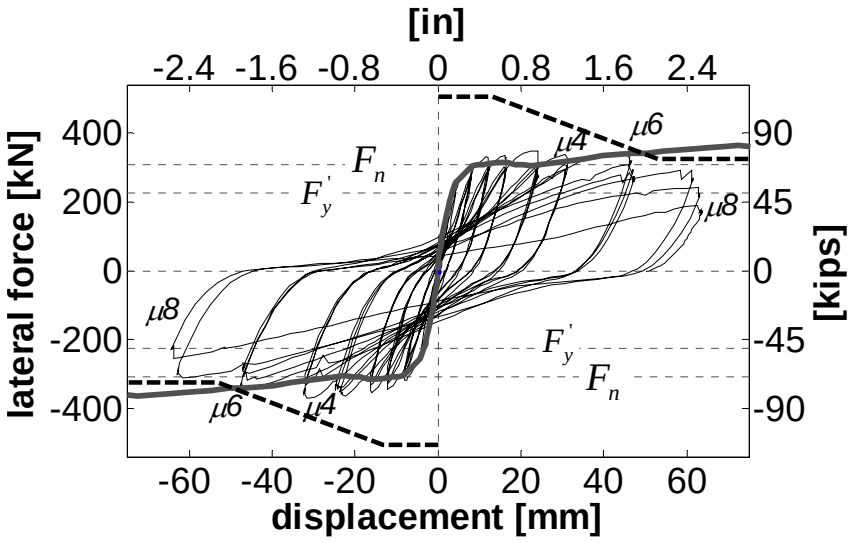

Figure 6.41 DSH-87C Force displacement response and theoretical shear strength envelope

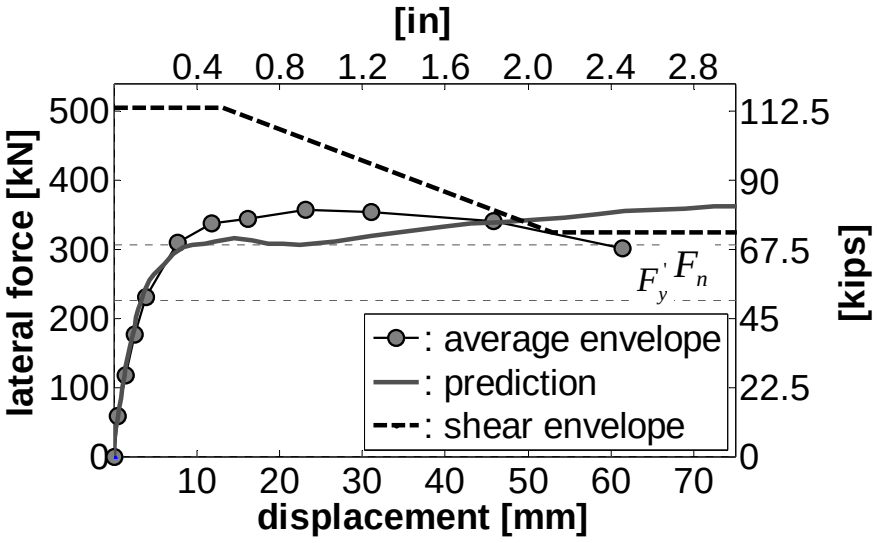

Figure 6.42 DSH-87C First peak envelope and theoretical shear strength envelope

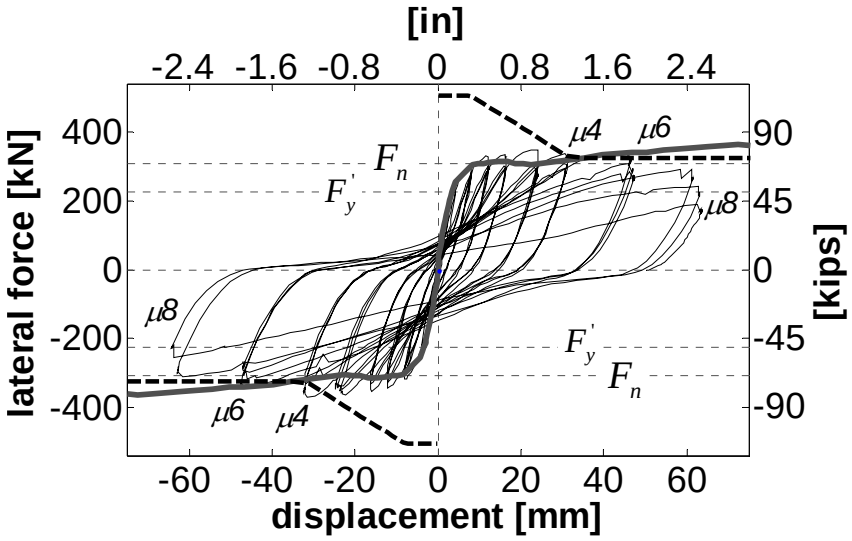

Figure 6.43 DSH-87C Force displacement response with shear strength envelope obtained using the theoretical force-displacement envelope

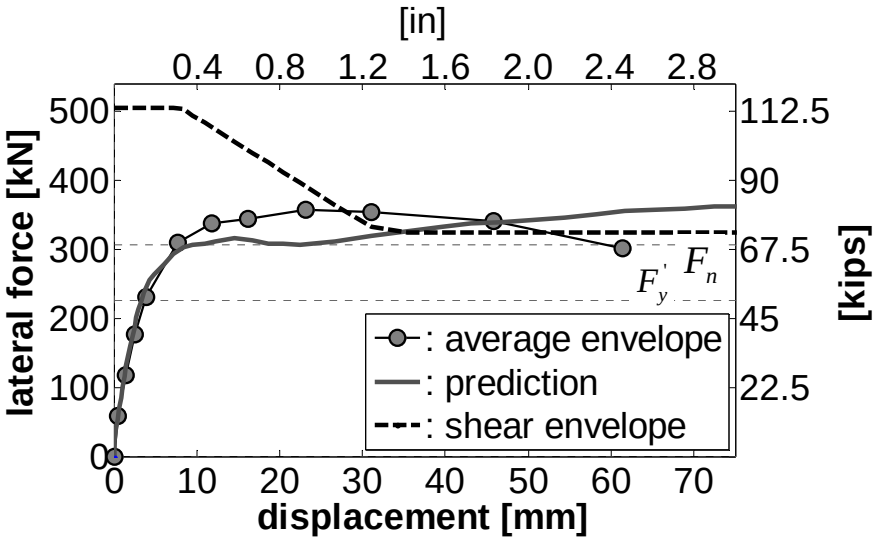

Figure 6.44 DSH-87C First peak envelope with shear strength envelope obtained using the theoretical force-displacement envelope

6.3.3 DSH-87C Curvature profiles

As mentioned before the gage length for the linear potentiometers in the base of the column includes a component to account for the strain penetration effect. For this specimen that component was found to be 86 mm (3.4 in). Figure 6.45 shows the match

between measured and predicted moment-curvature relation and Figure 6.46 shows the curvature profiles calculated at selected ductilities. It is noticed that up to ductility 1 the distribution of curvature is almost uniform along the column. For ductilities larger than 1 the curvatures start to concentrate mostly in the first cell.

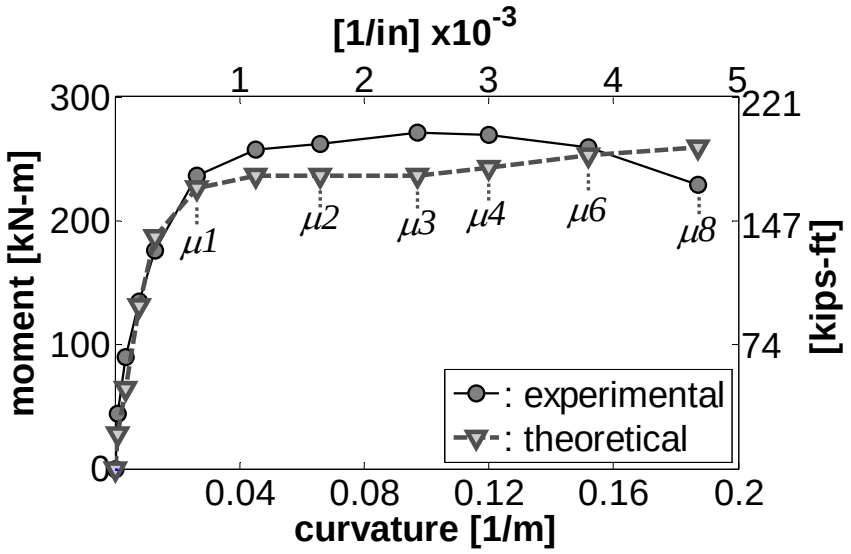

Figure 6.45 DSH-87C Moment curvature at column base

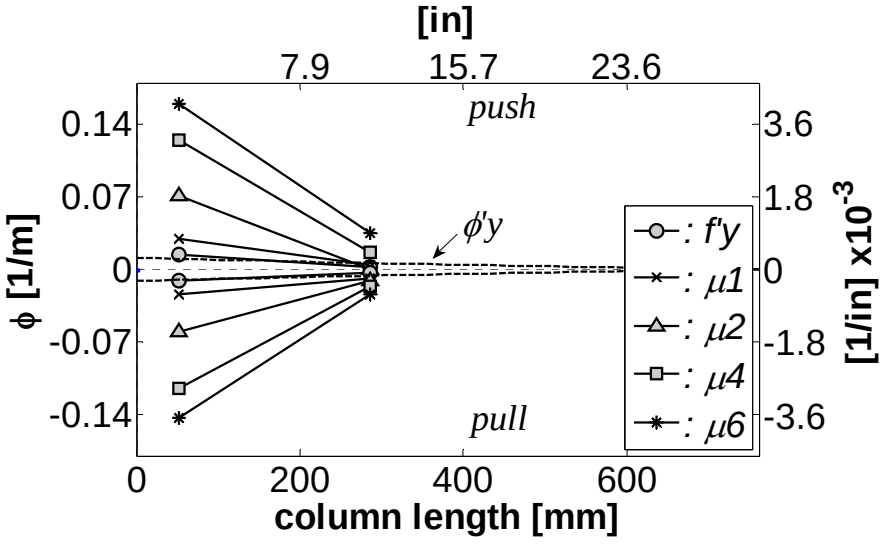

Figure 6.46 DSH-87C Curvature profiles

6.3.4 DSH-87C Equivalent plastic hinge length

Figure 6.47 shows the equivalent plastic hinge lengths obtained in the push and pull directions. Note that the average value obtained 256 mm (10.1 in) is the same value obtained for the room temperature specimen DSH-89A. This implies a reduction of ~10% in the expected hinge length as L_p is directly related with the yield stress of the longitudinal steel which increase ~10% when the temperature is reduced to -40°C. This reduction is very small when compared with the reduction in L_p obtained for the flexurally dominated cold specimens of 43% (Chapter IV).

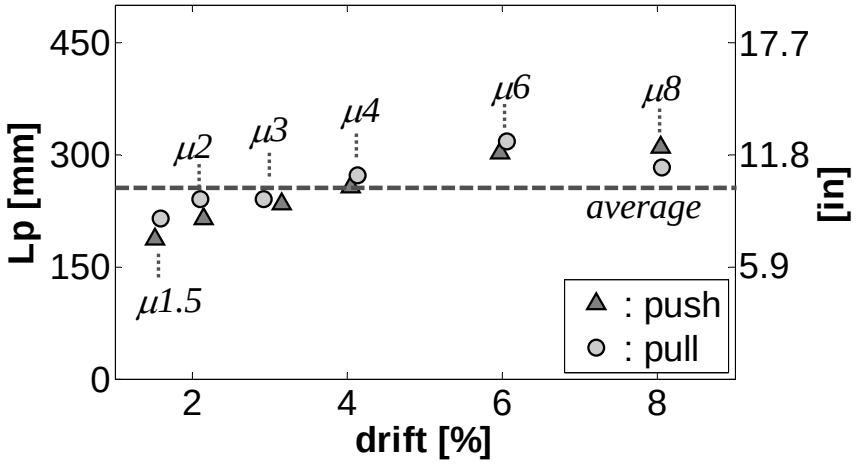

Figure 6.47 DSH-87C Equivalent plastic hinge length

6.3.5 DSH-87C Deformation components

Figure 6.48 shows the calculated shear and flexural components of deformation. It is seen that the sum of the flexural and shear components of deformation is in close agreement with the total deflection measured in the column; which implies that the data recorded by the lpot's is reliable. Note that the relative contribution of shear deformation to the total deflection increase as the lateral demand increase. Shear deformation is 12, 15, 20 and 31% of the total displacement at ductilities 3, 4, 6 and 8, respectively.

Figures 6.49 to 6.52 evaluate the theoretical models used to estimate shear and flexural deformations. It is noticed that the match between measured and predicted

displacements is very close up to ductility 6. At ductility 8 shear displacements are under predicted, this is not a major issue as it can be said that the specimen has already failed at this level of lateral demand.

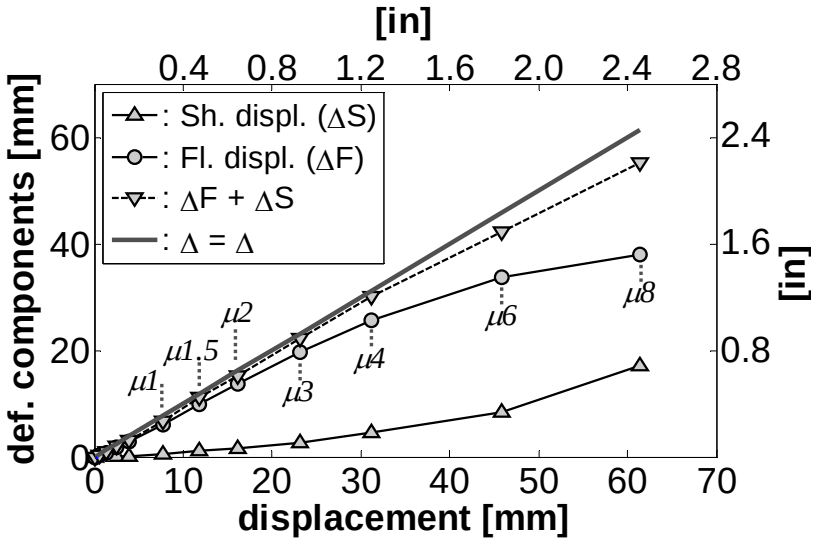

Figure 6.48 DSH-87C Deformation components

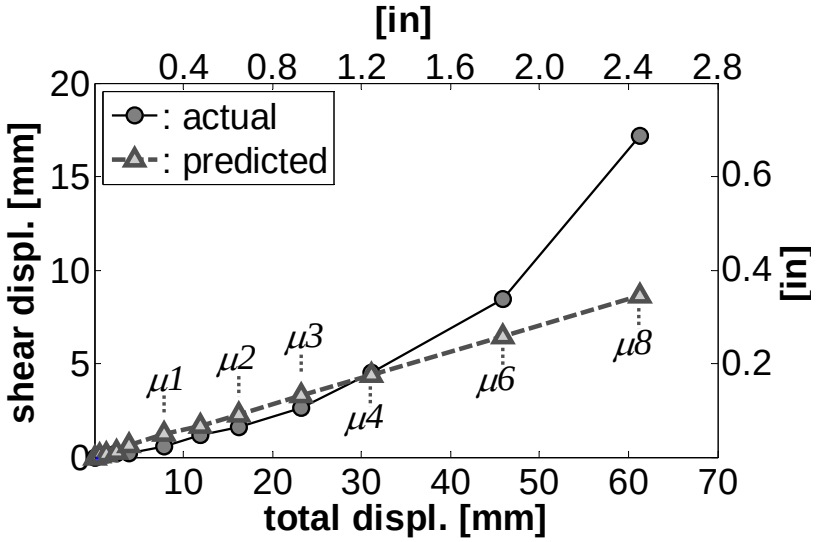

Figure 6.49 DSH-87C measured and predicted shear deformation components as function of the total displacement

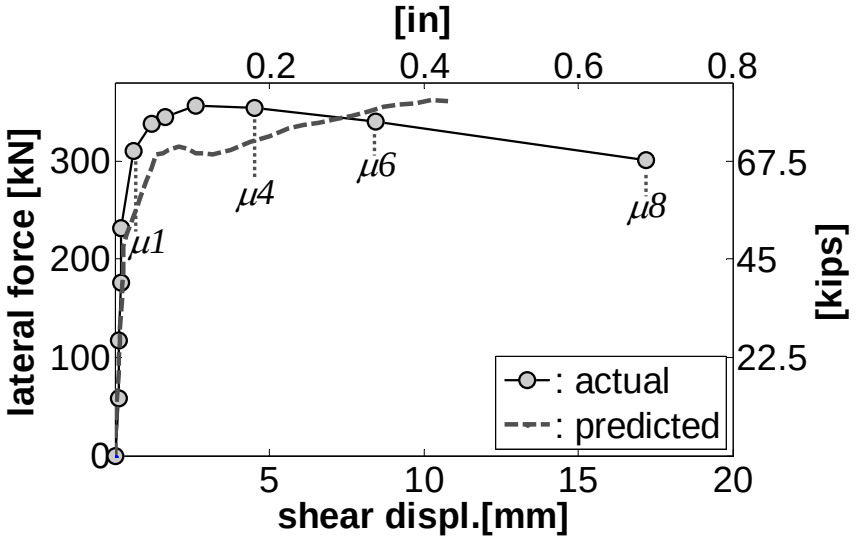

Figure 6.50 DSH-87C force vs. shear displacement envelope

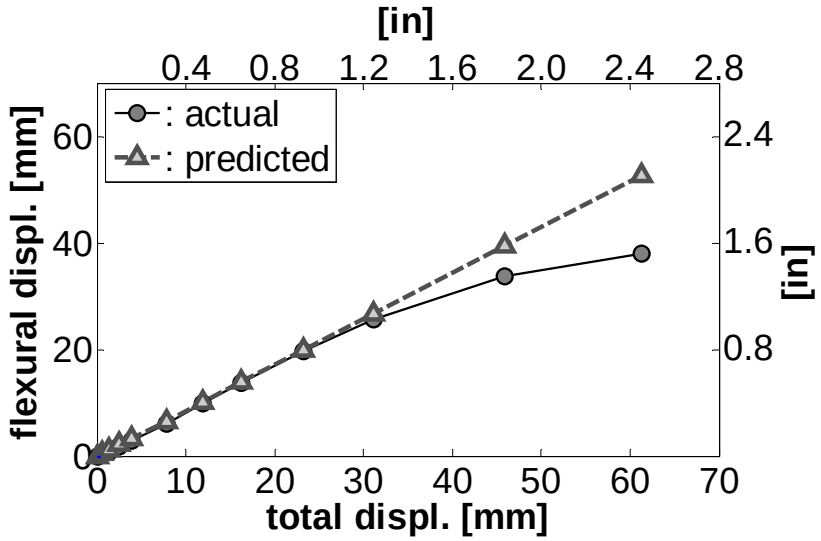

Figure 6.51 DSH-87C measured and predicted flexural deformation components as function of the total displacement

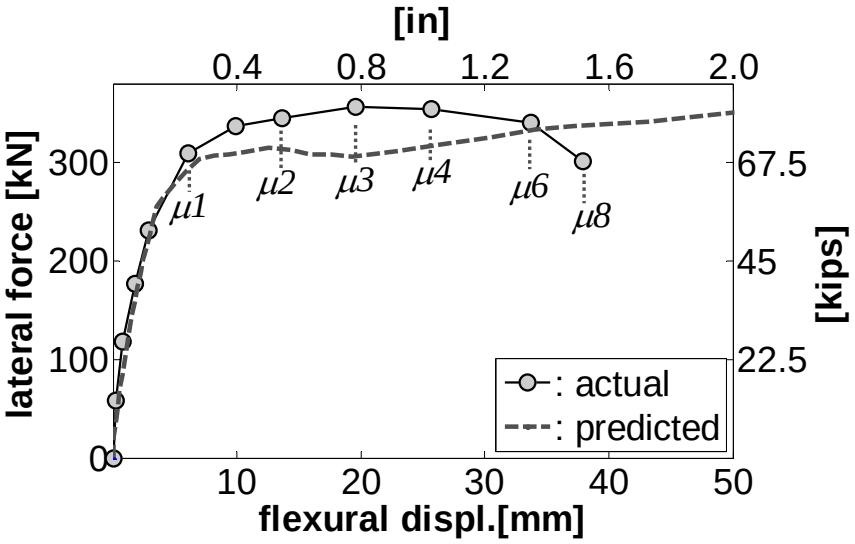

Figure 6.52 DSH-87C force vs. flexural displacement envelope

6.3.6 DSH-87C Strains on longitudinal steel

Figures 6.53 and 6.54 show the longitudinal strain profiles in the top and bottom bar, respectively. It was only possible to generate the strain profiles for low level of lateral demand because the strain data for higher levels was not reliable. Note that the shape of the profiles is different to the obtained at room temperature; in this case the maximum strains are recorded by the gauge placed closer to the base.

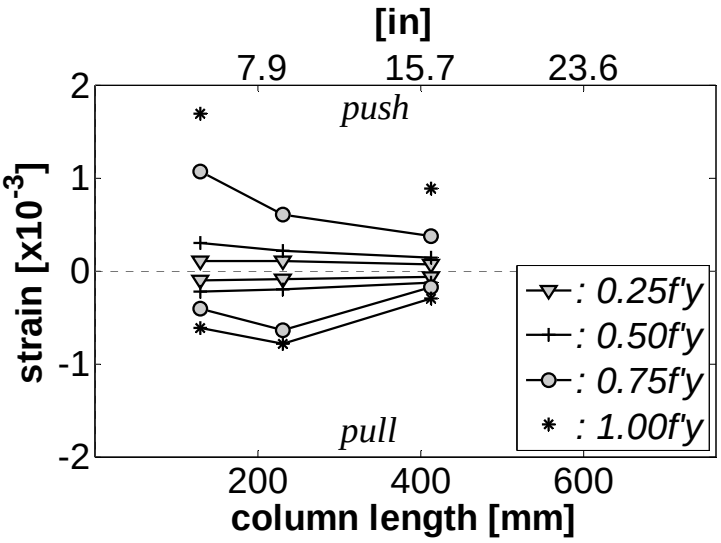

Figure 6.53 DSH-87C longitudinal strain profiles in top most bar

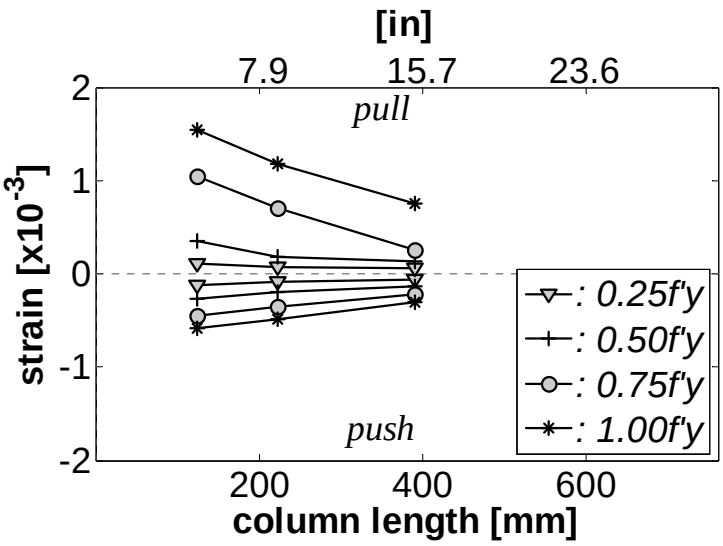

Figure 6.54 DSH-87C longitudinal strain profiles in bottom most bar

6.3.7 DSH-87C Strains on transverse steel

Unfortunately, from the 12 strain gages placed on the spiral of this specimen only one worked properly during a large period of time. Figure 6.55 shows the shear induced strain recorded by this gauge that was placed 245 mm from the base. It is seen that the maximum strain recorded was 0.0071 during the first pull at ductility 4, which is practically the same strain recorded in the room temperature specimen at this same level of ductility.

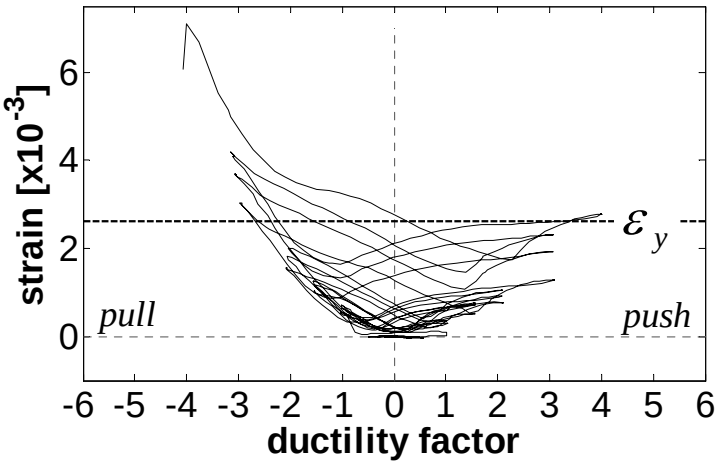

Figure 6.55 DSH-87C shear induced strain history 245 mm from the base

6.4 Comparison of units DSH-87A and DSH-87C

Figure 6.56 compares the hysteretic force displacement response of both specimens and Figure 6.57 the average first peak envelope. From these graphs it is noticed that:

- Elastic stiffness of the cold specimen is 56% larger than the measured for the room temperature unit.

- The cold specimen exhibited an increase of 20% in the flexural/shear strength when compared to the room temperature one.

- The cold specimen was able to sustain cyclic deformations 33% larger than the warm unit.

- Strength degradation associated with increasing levels of lateral demand started at ductility 3 for both specimens. However, from the three cycles average envelope in Figure 6.58 may be noticed that strength degradation over repetitive cycles at the same level of ductility is more severe in the warm unit.

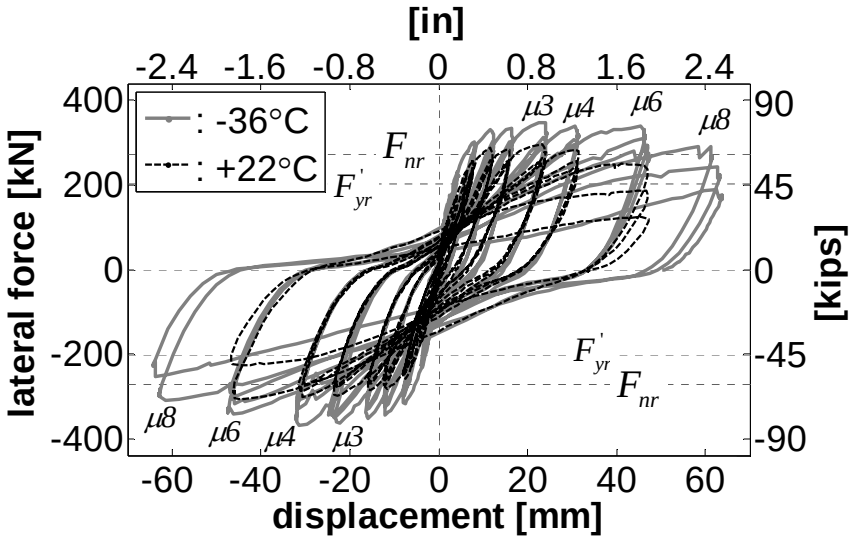

Figure 6.56 DSH-87A and DSH-87C hysteretic responses

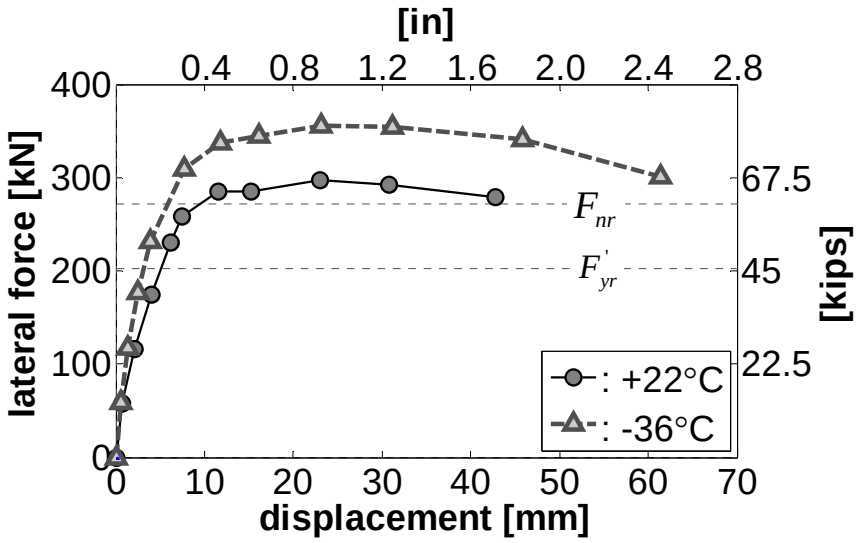

Figure 6.57 DSH-87A and DSH-87C average first cycle envelope

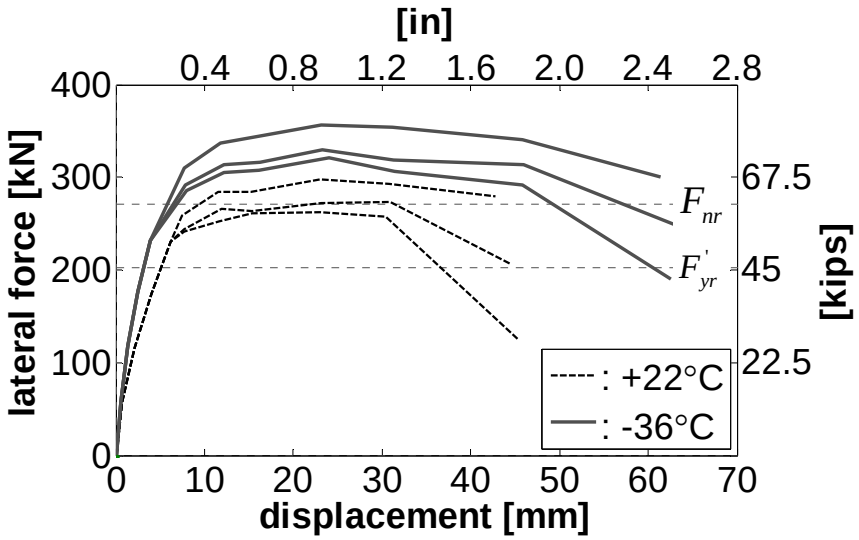

Figure 6.58 DSH-87A and DSH-87C three cycles envelope

Figure 6.59 presents the shear and flexural components of deformation for the cold and room temperature tests. It is seen that there was basically no change in the deformation components due to the low temperature.

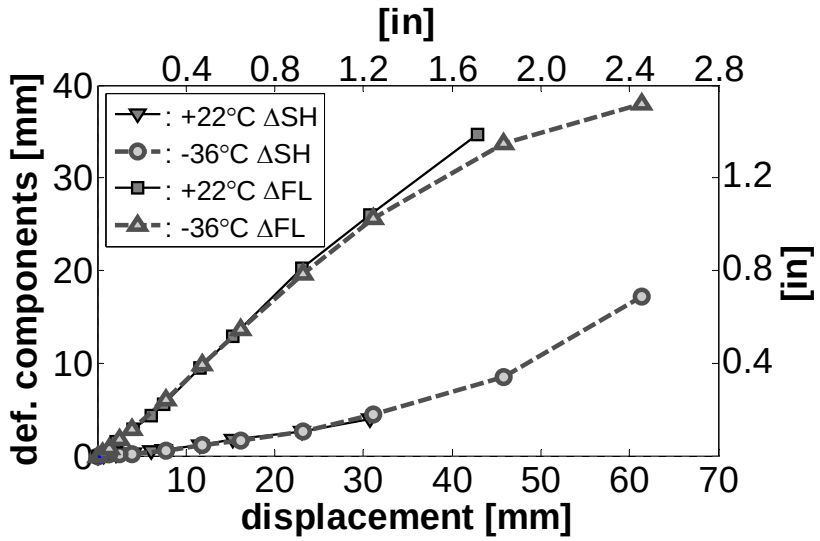

Figure 6.59 DSH-87A and DSH-87C three cycles envelope

Energy dissipating properties are analyzed in Figures 6.59 and 6.61. It is seen from these graphs that the energy absorbed and the hysteretic damping exhibited by both specimens is practically the same. From Figure 6.62 can be seen that the conventional expression (Dwairi 2007) used for estimate equivalent damping in direct-displacement based design (Priestley et al. 2007) applied also for short columns under freezing conditions.

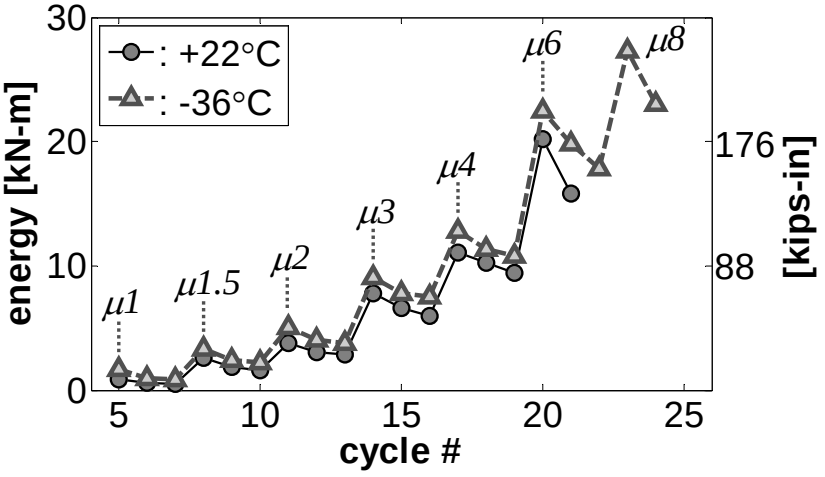

Figure 6.60 DSH-87A and DSH-87C hysteretic energy

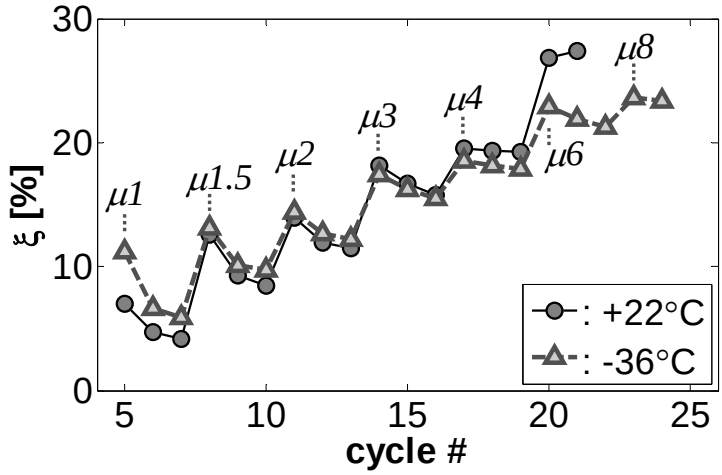

Figure 6.61 DSH-87A and DSH-87C hysteretic damping

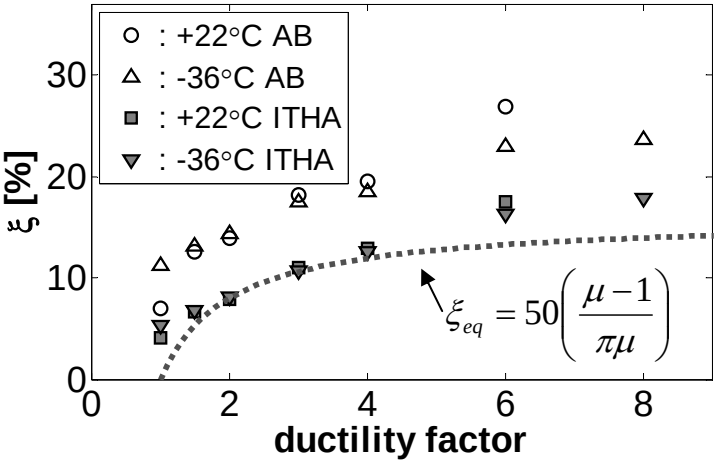

Figure 6.62 DSH-87A and DSH-87C corrected damping

Figure 6.63 and 6.64 examine the effect of low temperatures in the curvature distribution and equivalent plastic hinge length, respectively. It is seen that curvatures in the base of the column is slightly larger for the cold specimen. However, the increase is not as marked as the detected for the flexural dominated specimens in Chapters IV and V. Also, contrary to the results obtained in earlier chapters, no shortening of the equivalent plastic hinge length was noticed in the cold specimen (Figure 6.64).

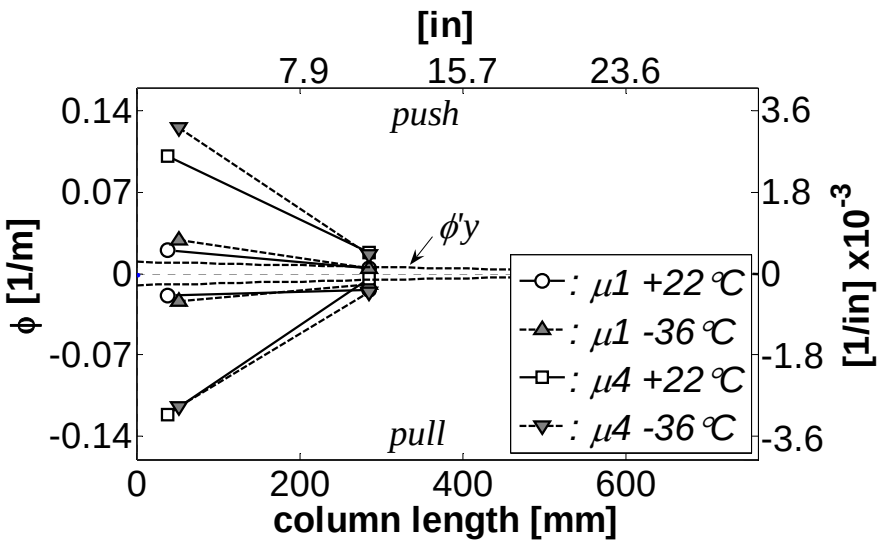

Figure 6.63 DSH-87A and DSH-87C curvature profiles

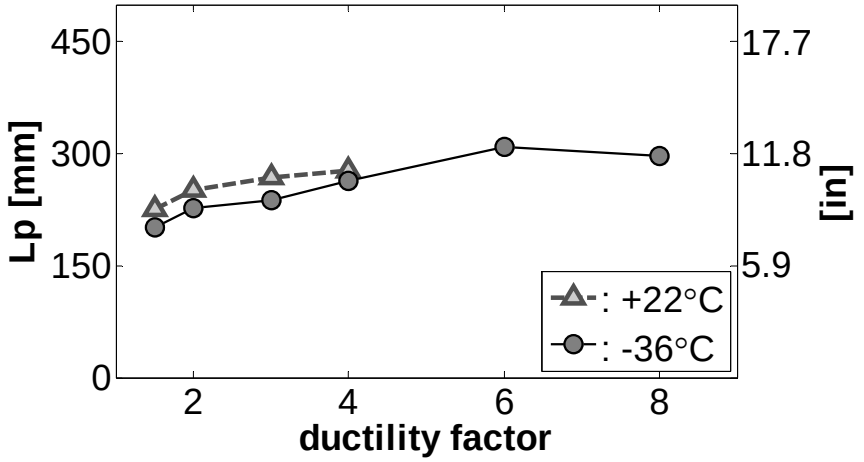

Figure 6.64 DSH-87A and DSH-87C equivalent plastic hinge lengths

Figure 6.65 shows the shear induced strain history recorded by strain gages placed in the spiral of the specimens at almost the same distance from the base ~270 mm (10.6 in). It is seen that strains on the transverse reinforcement of the room temperature specimen are activated earlier than in the cold specimen. This implies that the concrete at low temperatures was able to sustain larger shear stresses, presumably because the large adhesive forces associated with the ice surface that delays the propagation of cracks. This becomes evident by examining the condition of both specimens when subjected to the same level of lateral demand in Figure 6.66. It is noticed that after the cycles at ductility 2

there are more core cracks in the room temperature specimen than in the cold one. Finally, Tables 6.2 and 6.3 summarizes the results obtained during both tests.

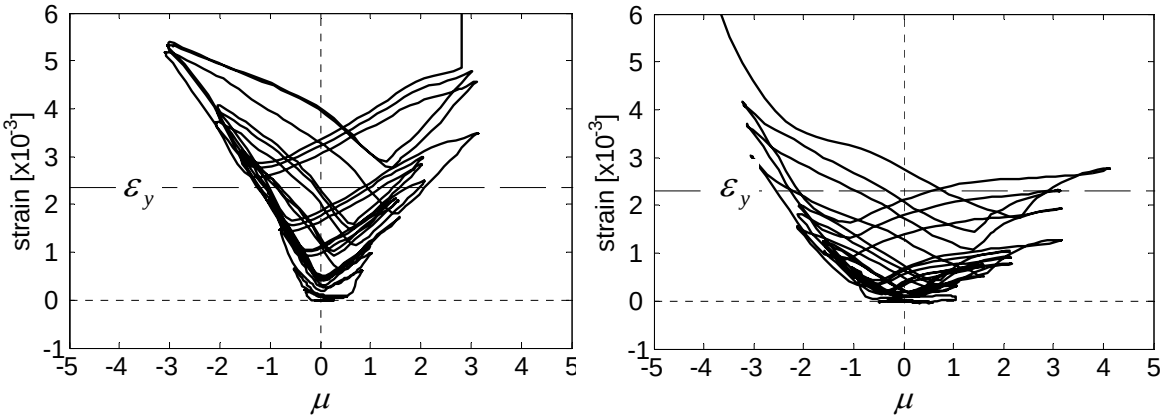

(a) DSH-87A [22°C/72°F] **(b)** DSH-87C [-36°C/-33°F]

Figure 6.65 DSH-87A and DSH-87C shear induced stain history

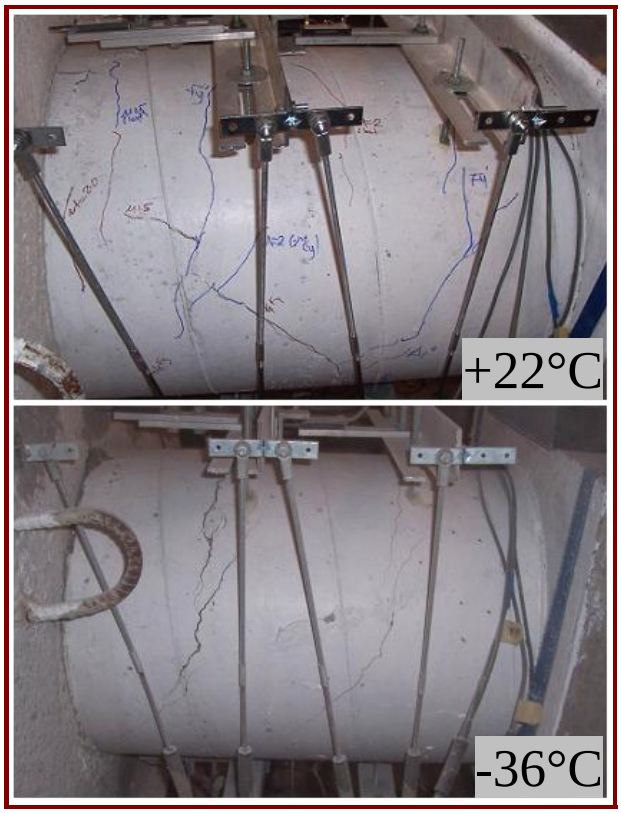

Figure 6.66 DSH-87A and DSH-87C after the cycles at ductility 2

Table 6.2 Summary of results obtained (Load control phase)

Cycle	Average Lat. Force [kN]	Average tip displacement [mm]		
		+22°C	-36°C	-36°C / +22°C
0.25fy'	58.0	0.7	0.5	0.72
0.5fy'	116.7	2.1	1.4	0.64
0.75fy'	175.4	4.0	2.5	0.61
fy'	231.0	6.1	3.9	0.64

Table 6.3 Summary of results obtained (Displacement control phase)

Cycle	Average Displacement [mm]	First cycle average lateral force [kN]		
		+22°C	-36°C	-36°C / +22°C
μ1	7.6	259.6	307.1	1.18
μ1.5	11.7	284.8	336.4	1.18
μ2	15.7	285.5	343.7	1.20
μ3	23.1	297.2	356.1	1.20
μ4	30.9	292.2	354.1	1.21
μ6	44.3	279.0	342.0	1.23
μ8	61.4	-	306.0	-

6.5 Room temperature specimen BSH-89A

This specimen was tested on March 27/2007. Figures 6.67 and 6.68 show the variations of temperature and axial load during the test. As for the other specimens, horizontal lines in Figure 6.68 represent the average applied axial load and the ±10% deviation.

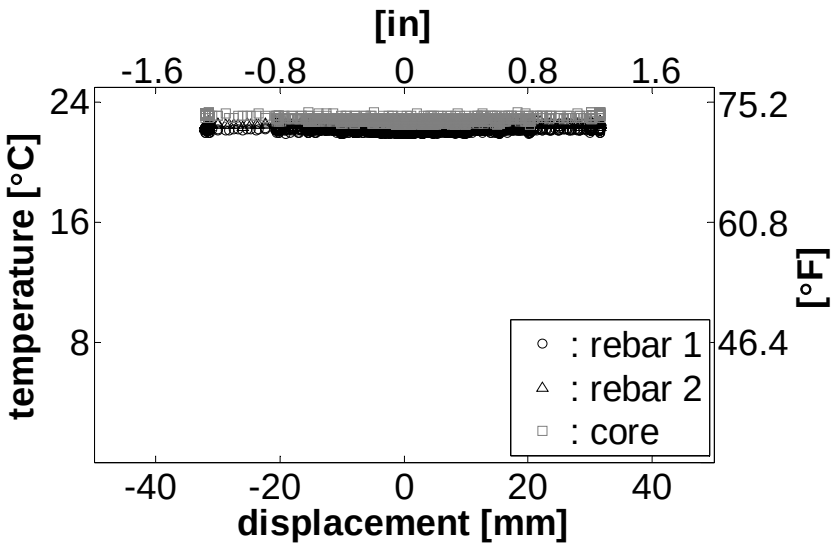

Figure 6.67 Temperature variations during the test of BSH-89A

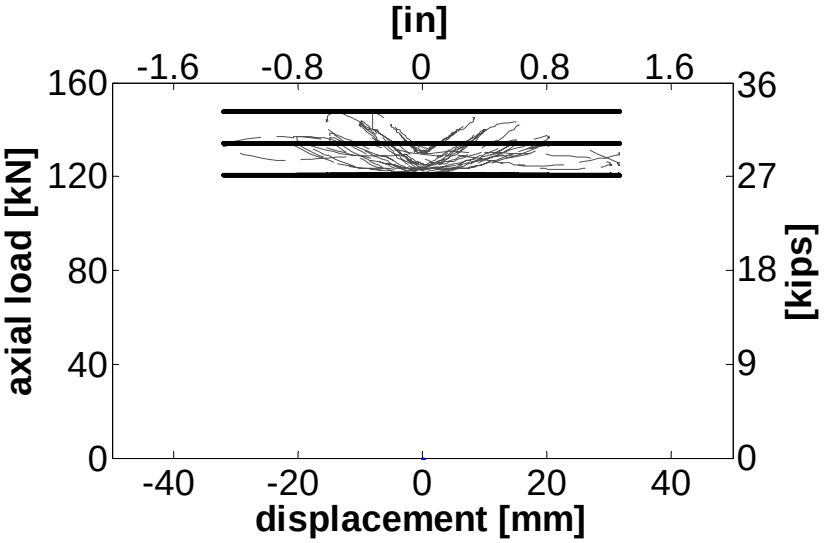

Figure 6.68 Axial load variations during the test of BSH-89A

6.5.1 BSH-89A Test observations

Figure 6.69 shows the specimen before the test. First two hairline cracks were flexural in nature and appeared in the specimen during the second cycle of force control 163 kN spaced 190 mm (7.5 in) between them and the column base as shown in Figure 6.70. At the next cycle of force control 246 kN (Figure 6.71) the first shear cracks

appeared inclined ~30° to the column axis. With the last cycle of force control 325 kN shear and flexural cracks keep growing in length (Figure 6.72).

With the cycles at ductility 1 a new minor shear crack appear between the already existing shear cracks (Figure 6.73). Also at this level of demand, a new flexural crack appeared at ~50 mm (2 in) from the load stub and the first signs of concrete crushing are noticed at the base of the column. During the cycles at ductility 1.5 a number of new small shear cracks appear and the main shear crack widened noticeably and extended from the base to the load stub of the column (Figure 6.74), during the first cycle at this level of ductility the column reached the maximum lateral load during the test.

At ductility 2 (Figure 6.75) shear cracks are all interconnected provoking spalling of the cover concrete at mid height of the column. At the first cycle of ductility 3 concrete damage is large, cover concrete is lost in a large percent of the column and the longitudinal and transverse steel are exposed (Figure 6.76). The test was stopped after the second push at ductility 3 due to severe strength degradation. Figure 6.77 shows the condition of the specimen after instrumentation removal.

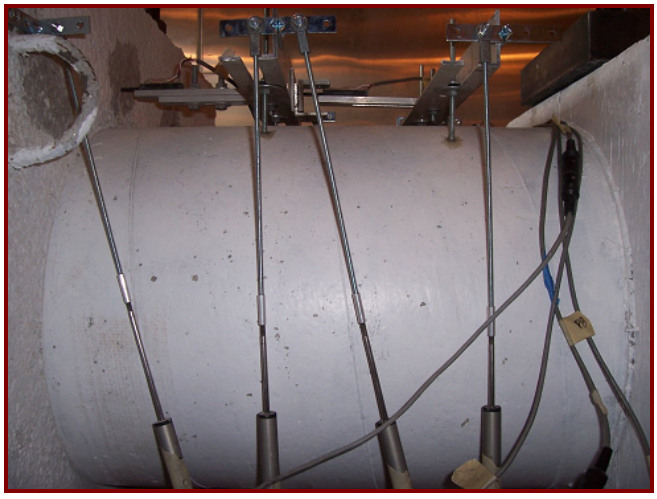

Figure 6.69 BSH-89A specimen before test

Figure 6.70 BSH-89A after the cycle at $f_y^i / 2$

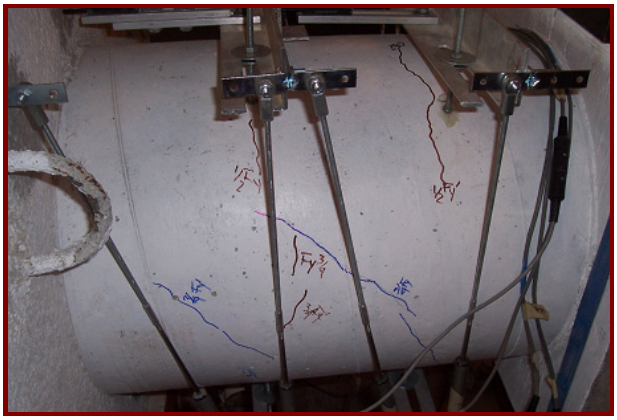

Figure 6.71 BSH-89A after the cycle at $3f_y^i / 4$

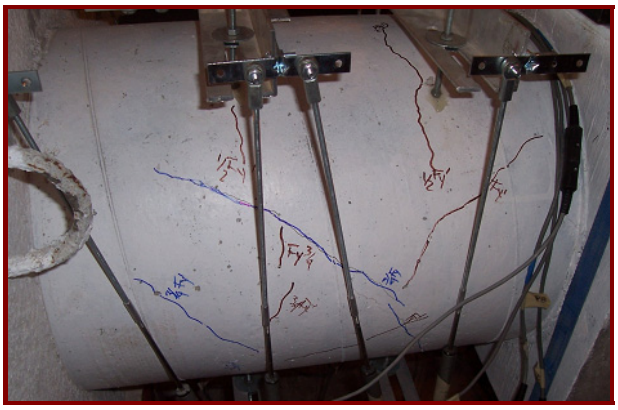

Figure 6.72 BSH-89A after the cycle at f_y^i

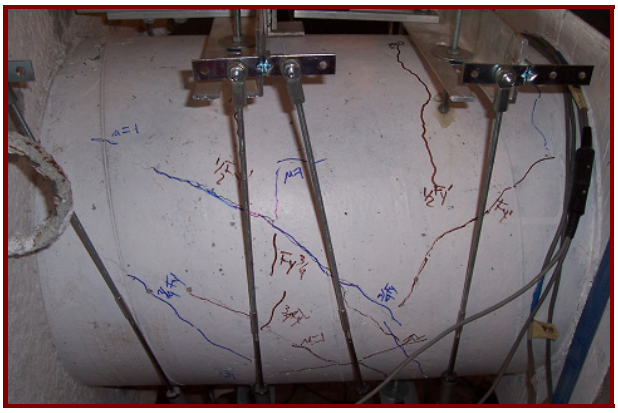

Figure 6.73 BSH-89A after the cycles at ductility 1

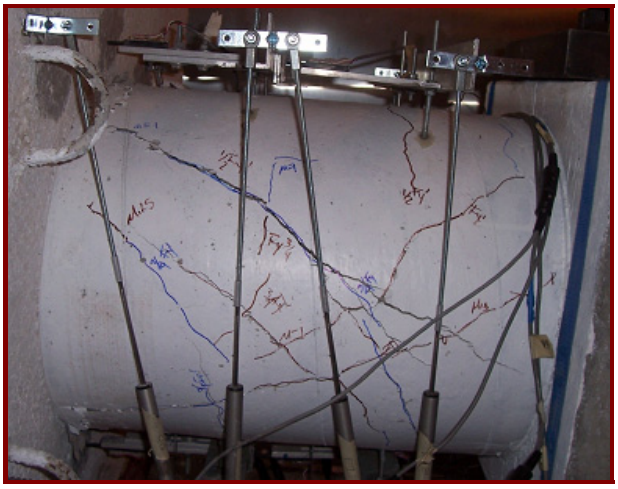

Figure 6.74 BSH-89A after the cycles at ductility 1.5

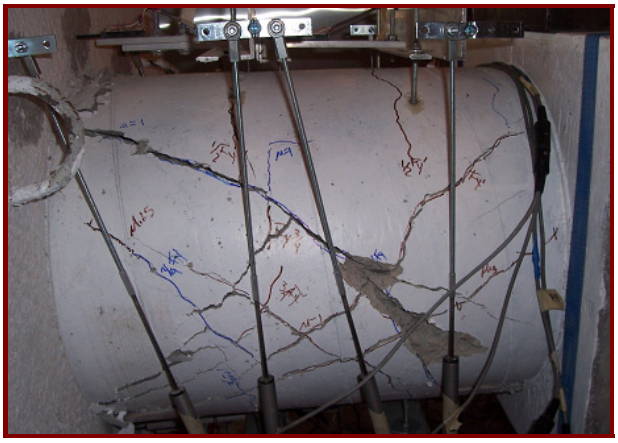

Figure 6.75 BSH-89A after the cycles at ductility 2

Figure 6.76 BSH-89A after the first cycle at ductility 3

Figure 6.77 BSH-89A after instrumentation removal

6.5.2 BSH-89A Force displacement response

The hysteretic force displacement response recorded during the test is displayed in Figure 6.78, this figure also shows the theoretical force displacement envelope and shear strength envelope. It is seen that the specimen reached its peak load at the first cycle of ductility 1.5, after this point strength degradation is noticeably but the column is still able to sustain lateral loads. However, for real earthquake conditions (high strain rates) it should be expected that the column fail at this level of demand (ductility 1.5). Figure 6.79 shows the first peak envelope along with the predicted response and shear

strength envelope, it is seen that the specimen was more flexible than expected and also exhibit slightly larger shear strength, this last presumably due to the closeness of the supports. As for the ductile shear specimens (DSH), the experimental response is also compared with the theoretical shear strength envelope calculated using the predicted force-displacement envelope ("completely blind prediction") and not the displacement recoded during the test (which was the approach used in Figures 6.78 and 6.79). Results obtained are displayed in Figures 6.80 and 6.81, noticed that the predicted behavior is still close to the actual response.

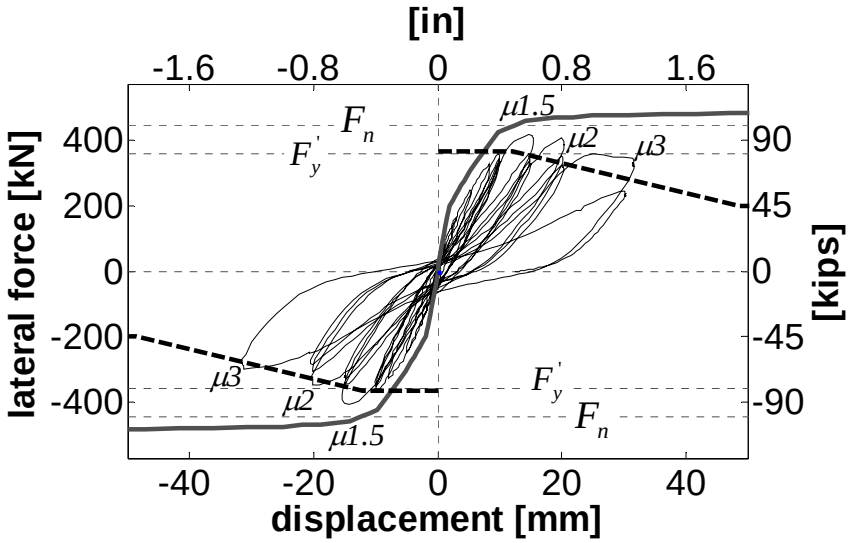

Figure 6.78 BSH-89A Force displacement response and theoretical shear strength envelope

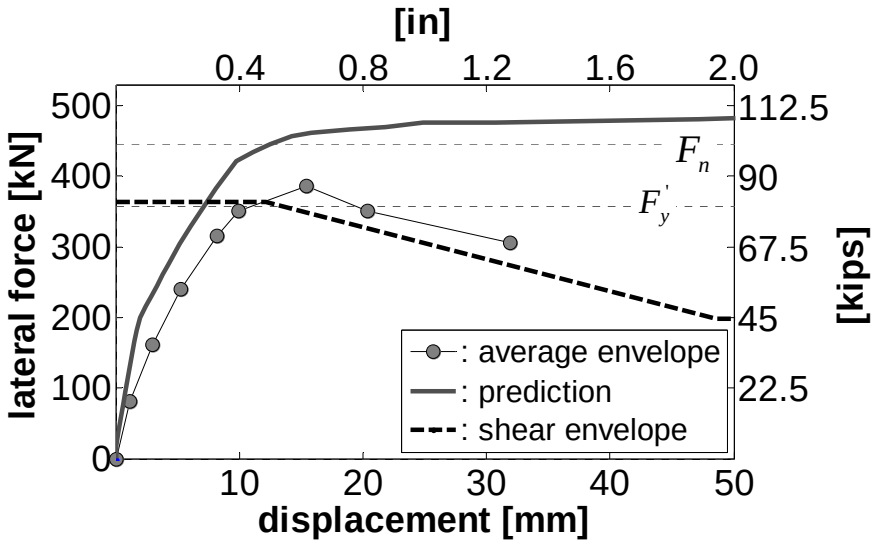

Figure 6.79 BSH-89A First peak envelope and theoretical shear strength envelope

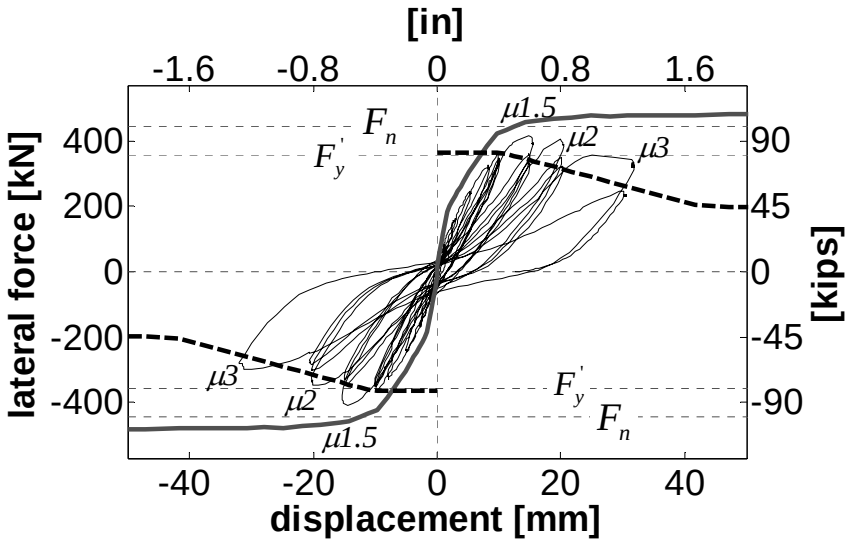

Figure 6.80 BSH-89A Force displacement response with shear strength envelope obtained using the theoretical force-displacement envelope

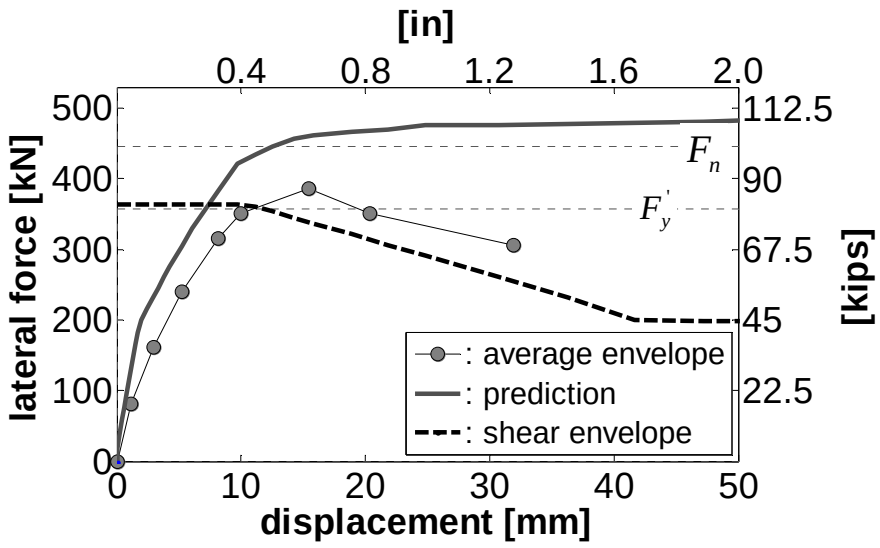

Figure 6.81 BSH-89A First peak envelope with shear strength envelope obtained using the theoretical force-displacement envelope

6.5.3 BSH-89A Curvature profiles

The component to account for the strain penetration effect in the gage length for the linear potentiometers in the base of the column was found to be 190 mm (7.5 in). Figure 6.82 shows the match between measured and predicted moment-curvature relation and Figure 6.83 shows the curvature profiles calculated at selected ductilities. As for the ductile shear specimens, it is noticed that up to ductility 1 the distribution of curvature is almost uniform along the column. For ductilities larger than 1 the curvature starts to concentrate mostly in the first cell.

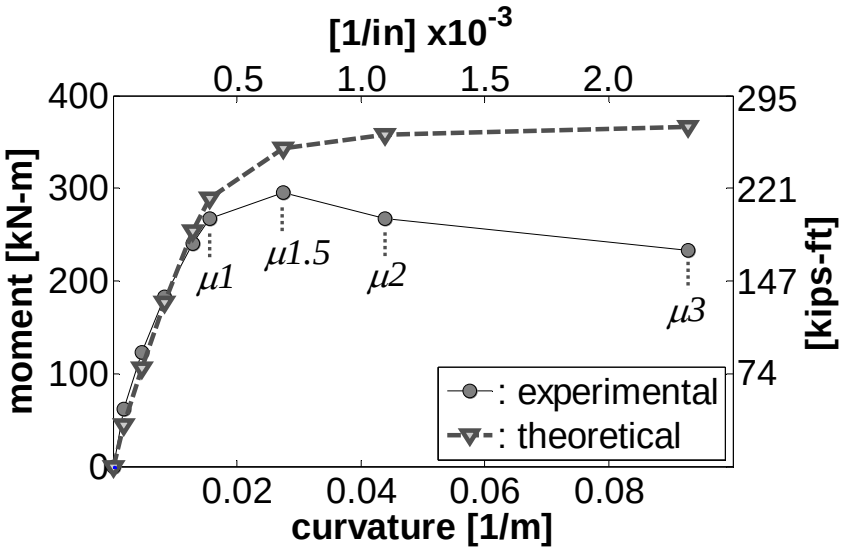

Figure 6.82 BSH-89A Moment curvature at column base

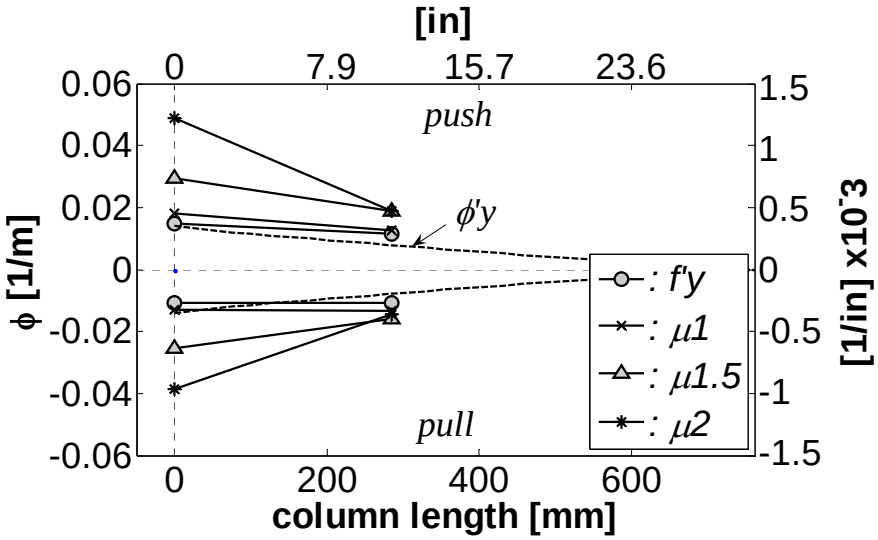

Figure 6.83 BSH-89A Curvature profiles

6.5.4 BSH-89A Equivalent plastic hinge length

Figure 6.84 shows the results obtained for the equivalent plastic hinge length in the push and pull directions. It is seen that the predicted value (with reduction factor of 0.59 obtained for the current test set up) $L_p = 0.59(0.044 * 558 * 28.7) = 416mm\ (16.3in)$ is ~30% larger than the average value measured $L_p = 317mm\ (12.5in)$.

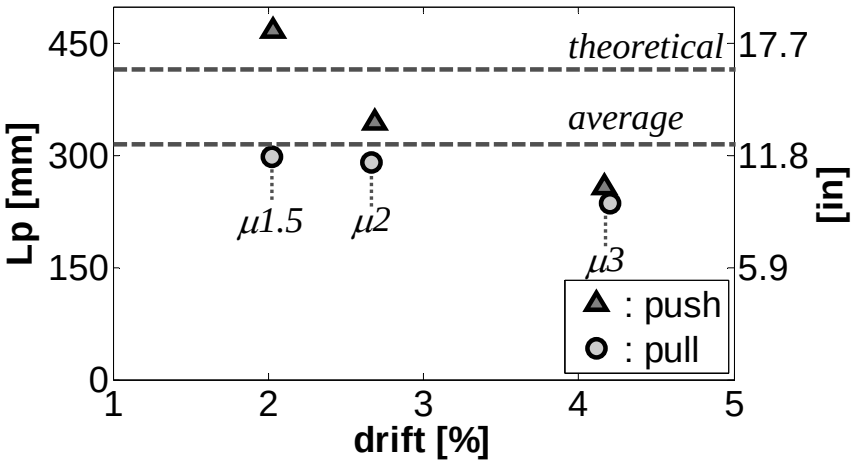

Figure 6.84 BSH-89A Equivalent plastic hinge length

6.5.5 BSH-89A Deformation components

As for the other shear specimens, the validity of the data recorded can be evaluated by comparison of the displacements recorded by the string potentiometer in the tip of the column with the summation of shear and flexural components calculated from the lpot's data. Figure 6.85 shows the results obtained, it is seen that the data from the linear potentiometers is valid up to ductility 2. After this point the summation of shear and flexural components is larger than the total defection measured. This most likely due to interference of the large concrete damage induced in the column at this point with the readings of the linear potentiometers. Theoretical models used to estimate shear and flexural deformations are evaluated by direct comparison with the deformation components recorded during the test. The results obtained are displayed in Figures 6.86 to 6.89, comparisons are performed as function of the total displacement and also as function of the applied lateral force. From Figure 6.86 can be noticed that measured shear displacements are below the displacements predicted by the theoretical model, it is believed that the predicted values are correct and the discrepancy is due to inaccuracy of the experimental data. This can be justified by inspection of Figures 6.85, 6.86 and 6.88: noticed from Figure 6.85 that the summation of shear and flexural components are always below the total deflection, as the flexural component is in close agreement with the predicted values (Figure 6.88), the only explanation is that the measured shear

components is below the actual shear deformation. For example at ductility 1.5, the summation of shear and flexural components is 12.3 mm and the measured tip displacement 15.4 mm. Now, if we use the theoretical shear deformation, the summation of components is 15.5 mm, practically the same value measured during the test. The deformation due to shear at ductilities 1.5 and 2 represent ~34% of the total deflection.

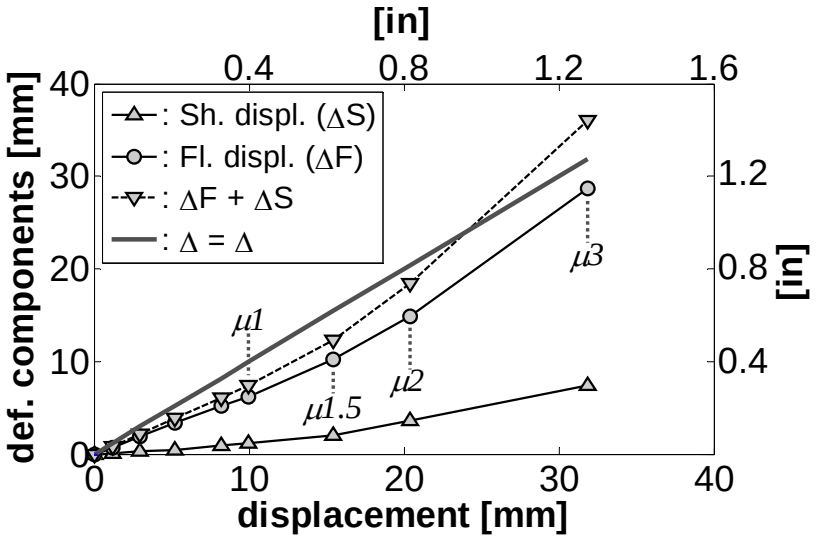

Figure 6.85 BSH-89A Deformation components

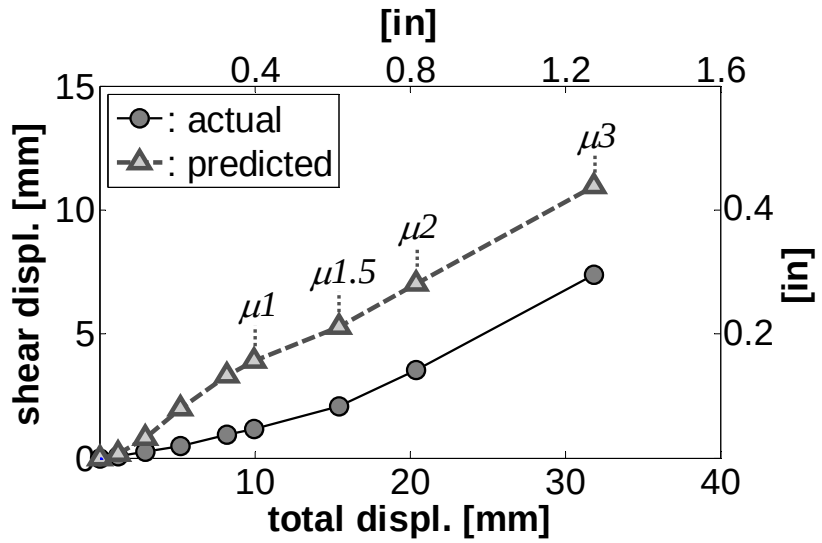

Figure 6.86 BSH-89A measured and predicted shear deformation components as function of the total displacement

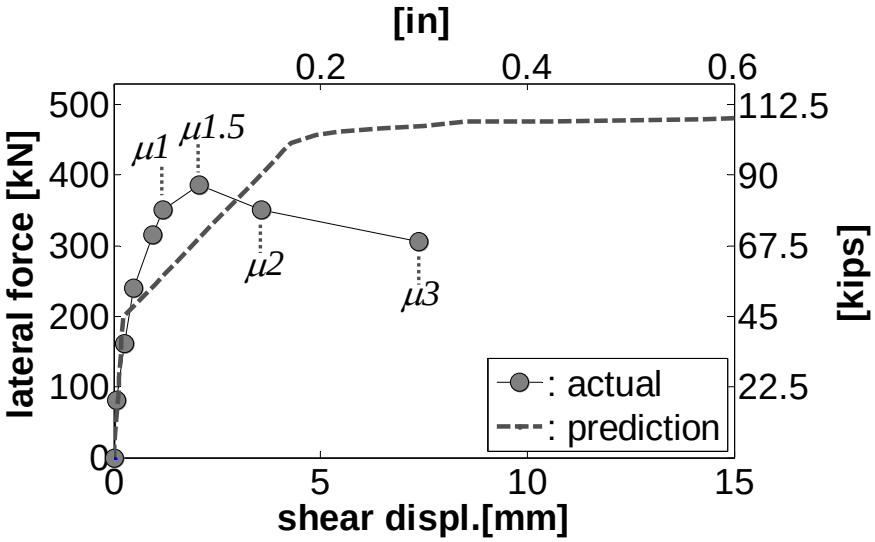

Figure 6.87 BSH-89A force vs. shear displacement envelope

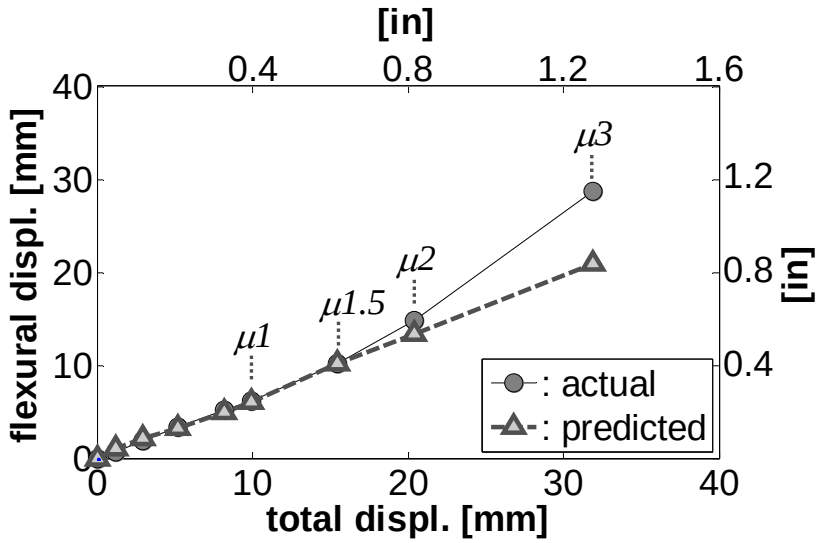

Figure 6.88 BSH-89A measured and predicted flexural deformation components as function of the total displacement

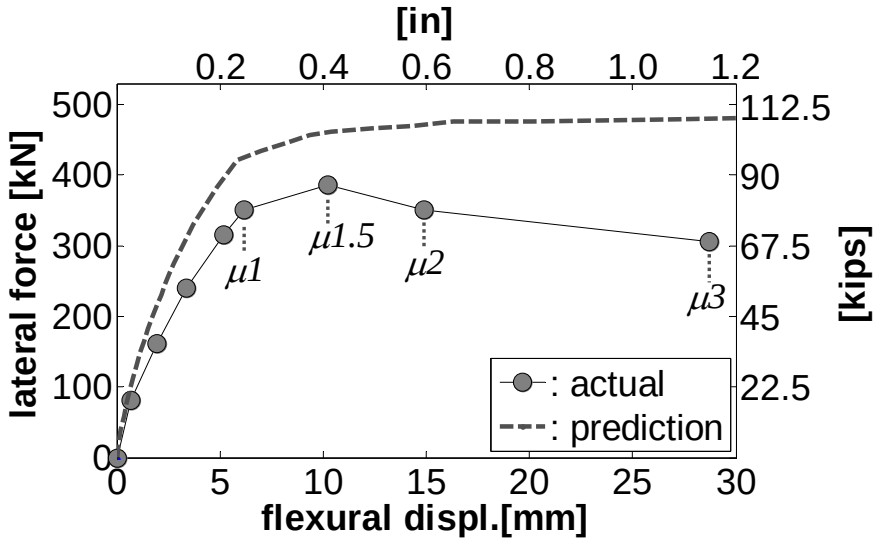

Figure 6.89 BSH-89A force vs. flexural displacement envelope

6.5.6 BSH-89A Strains on longitudinal steel

Figure 6.90 shows the strain profile of the top most bar. It is seen that over a distance 400 mm (15.7 in) from the base, the tensile strains in the bar increase almost uniformly. There was not enough information to generate the strain profile of the bottom bar.

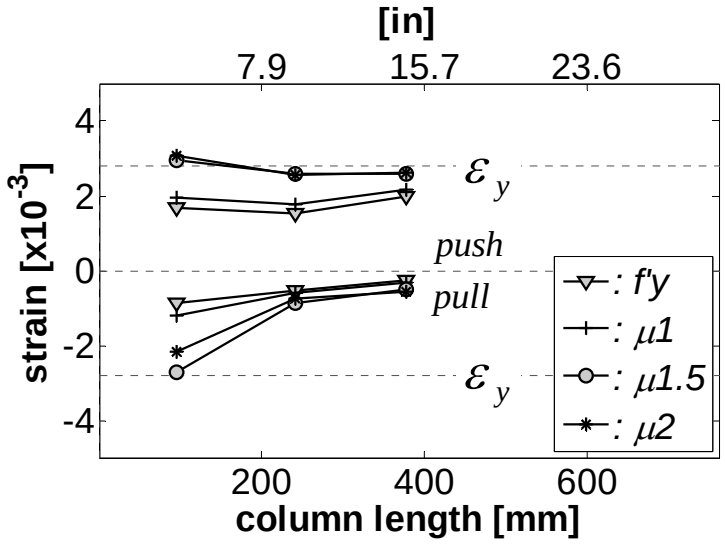

Figure 6.90 BSH-89A longitudinal strain profiles in top most bar

6.5.7 BSH-89A Strains on transverse steel

Figure 6.91 shows the strain profiles in the top face of the spiral, i.e. confinement induced strain. As expected larger strains are recorded in the pull direction when the concrete in the top face is in compression and dilates due to the Poisson effect. Maximum strains are recorded not by the gauge closest to the column base but by one placed 356 mm (14 in) from the base. There was not enough reliable data to generate the bottom face profile or the right side shear induced profile.

Figure 6.92 shows the shear induced strain profile for the left side of the spiral. Note that at ductility 1 the shear strain induced in the spiral has already exceeded twice the spiral yield strain. It is also seen that the larger strains are recorded by a gage placed 250 mm (10 in) from the base. Figure 6.93 show the strain history recorded by this gauge. Unfortunately, the strain gauge broke when reaching ductility 1.5, registering a maximum strain of 0.018, i.e. 7.6 times the spiral yield strain.

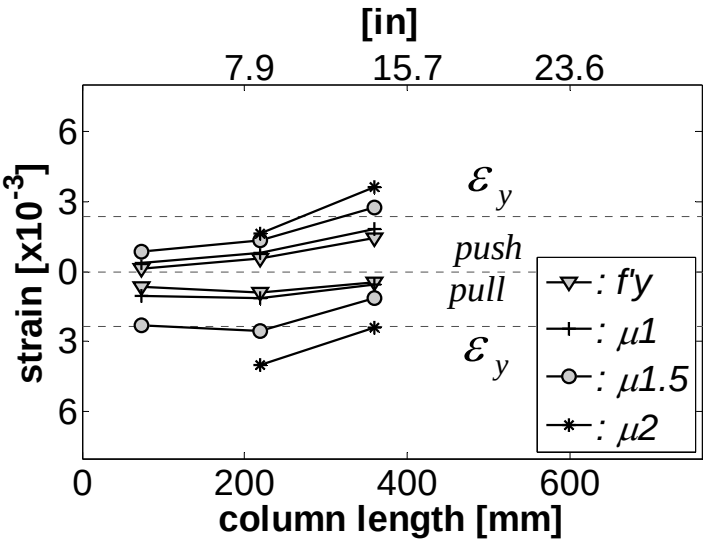

Figure 6.91 BSH-89A confinement induced strain profiles in top face of spiral

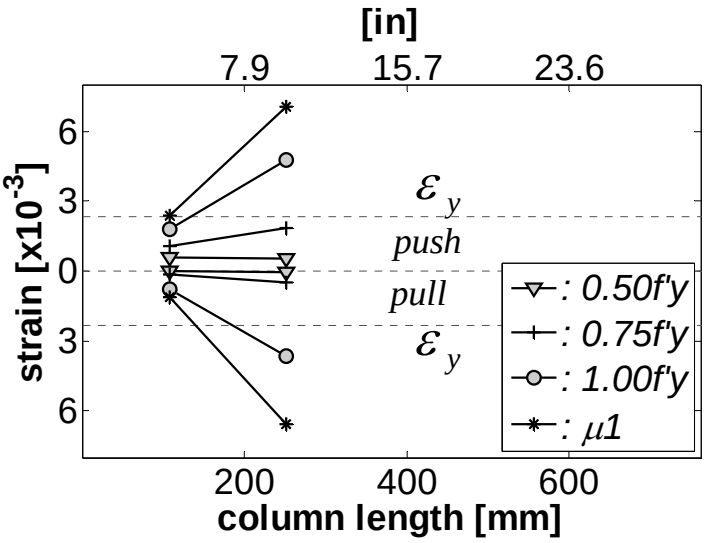

Figure 6.92 BSH-89A shear induced strain profiles in left face of spiral

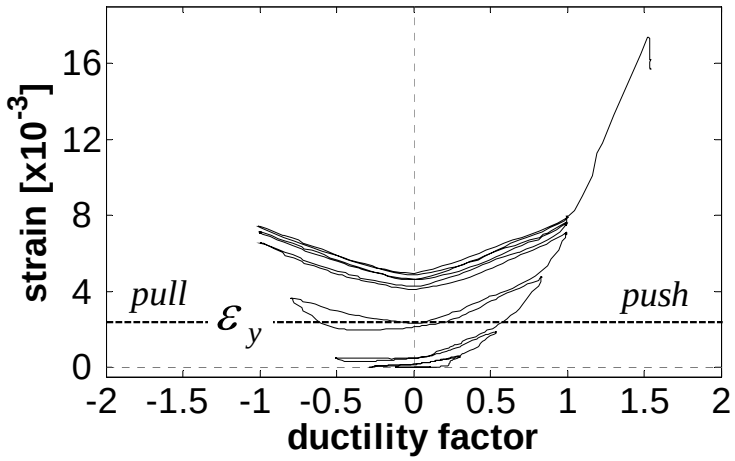

Figure 6.93 BSH-89A shear induced strain history 250 mm from base

6.6 Cold temperature specimen BSH-89C

This specimen was tested on April 16/2007. Figures 6.94 shows the variation of temperature during the test. Note that not the whole test was performed on freezing conditions. The maximum load capacity of the actuator was reached at the ductility 1.5 cycles and it was decided to stop the cold test at this point and finalize it next day at room temperature. More will be said about this in the next section. Figure 6.95 shows the axial load variations.

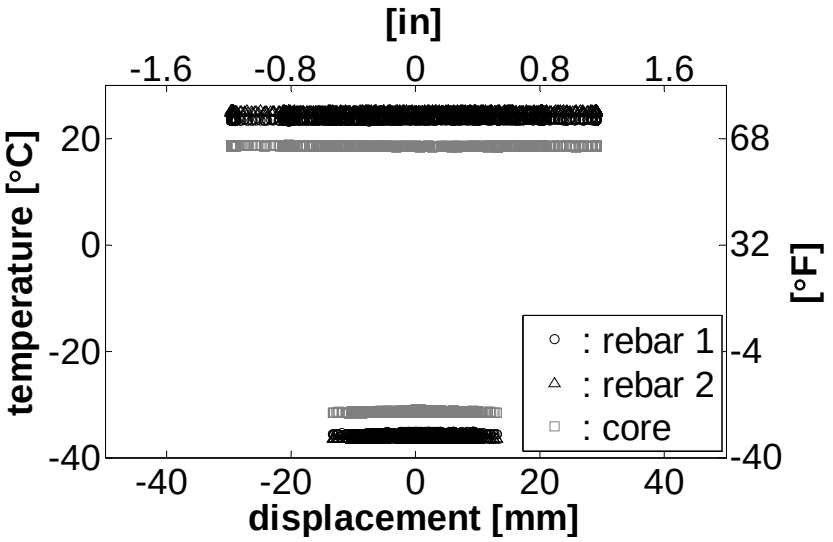

Figure 6.94 Temperature variations during the test of BSH-89C

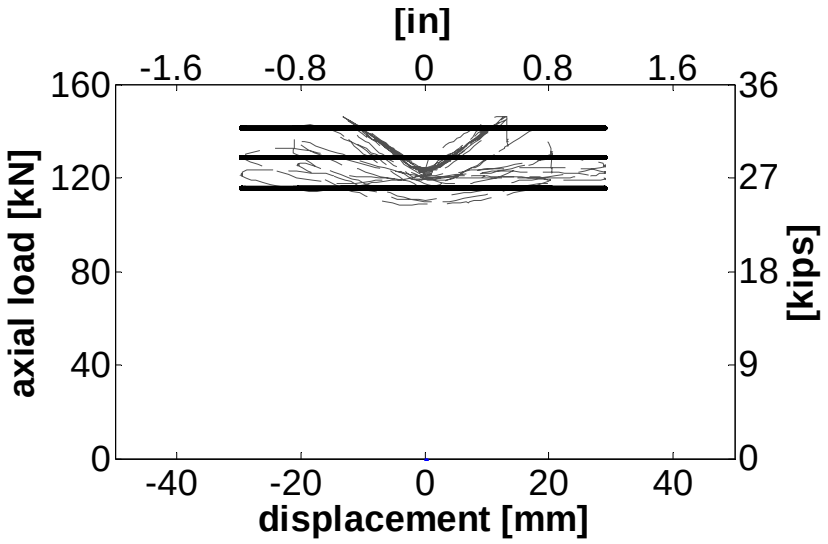

Figure 6.95 Axial load variations during the test of BSH-89C

6.6.1 BSH-89C Test observations

Figure 6.96 shows the specimen before the test. First hairline flexural crack appeared in the specimen during the third cycle of load control 246 kN at a distance ~150 mm (6 in) from the column base (Figure 6.97). With the last cycle of the force control phase 325 kN, a new hairline flexural crack developed at 150 mm (6 in) as shown in Figure 6.98.

First “shear only” cracks developed during the cycles at ductility 1 (Figure 6.99). When taking the specimen to ductility 1.5, the lateral force reached the actuator maximum load (500 kN / 112 kips). The only difference noticed in the specimen was an increase in the length of the existing shear and flexural cracks (Figure 6.100). After 3 cycles at this displacement there was not significant strength degradation and the test was stopped.

In order to verify that the increase in strength was effectively due to the cold temperature (and not perhaps to an initial larger concrete strength in this column) the test was continue next day at room temperature. The column was first subjected to one more cycle at ductility 1.5, the required lateral load was 414 kN (93 kips), no new cracks appeared with this cycle (Figure 6.101). The column failed due to brittle shear in the second cycle of ductility 2 (Figure 6.102) where a large increase in the width of the main shear cracks was noticed, peak load reached was ~ 105 kips. The column was taken to two cycles at ductility 3 (Figures 6.103 and 6.104) where the strength degradation and concrete damage due to the large dilation of the column was quite large. Figure 6.105 shows the condition of the specimen after the test, it is seen that transverse and longitudinal reinforcement is exposed in a large portion of the column.

Figure 6.96 BSH-89C before test

Figure 6.97 BSH-89C after the cycle at $3f_y^{'}/4$ (cold)

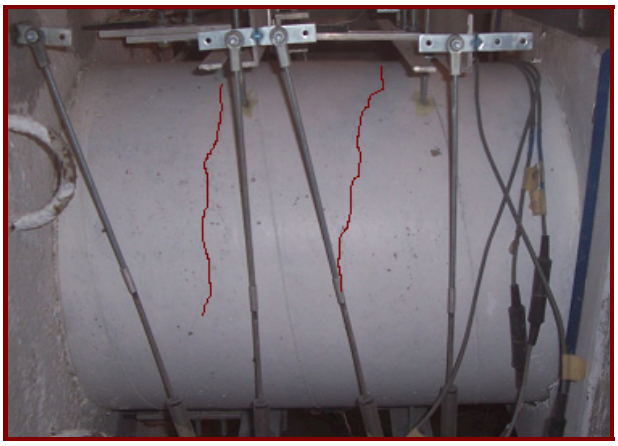

Figure 6.98 BSH-89C after the cycle at $f_y^{'}$ (cold)

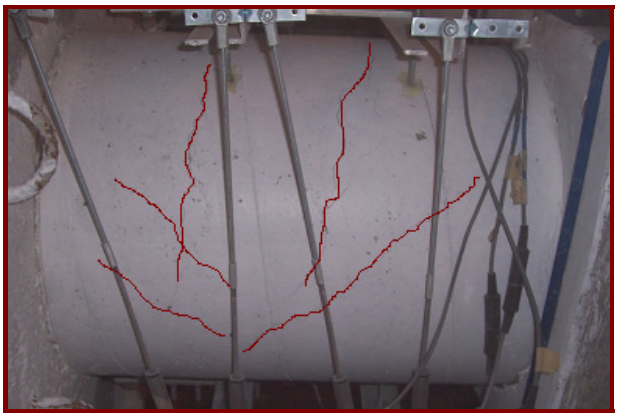

Figure 6.99 BSH-89C after the cycles at ductility 1 (cold)

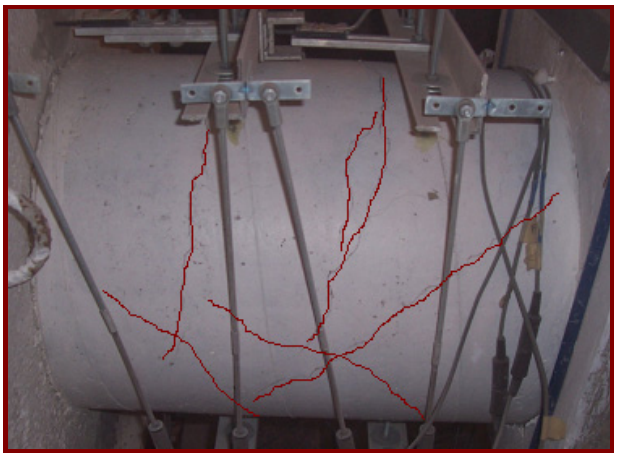

Figure 6.100 BSH-89C after the cycles at ductility 1.5 (cold)

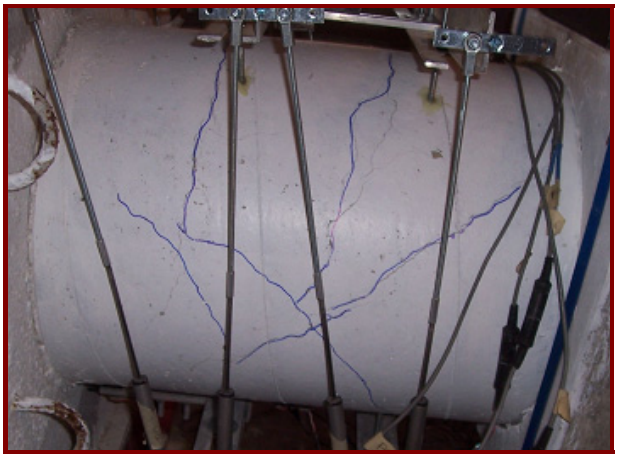

Figure 6.101 BSH-89C after a cycle at ductility 1.5 (ambient)

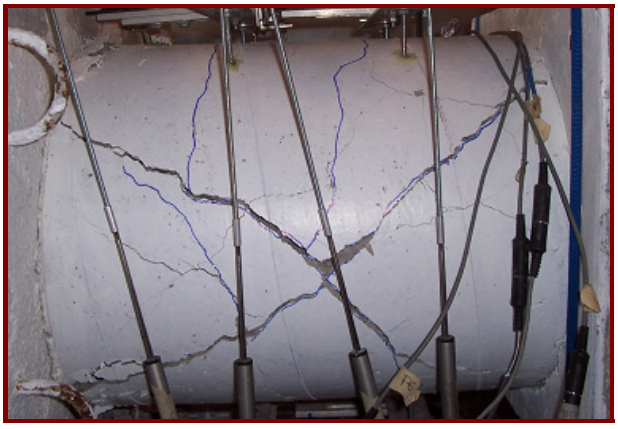

Figure 6.102 BSH-89C after the cycles at ductility 2 (ambient)

Figure 6.103 BSH-89C after the first cycle at ductility 3 (ambient)

Figure 6.104 BSH-89C after the second cycle at ductility 3 (ambient)

Figure 6.105 BSH-89C after instrumentation removal

6.6.2 BSH-89C Force displacement response

The hysteretic force displacement response recorded during the test is displayed in Figure 6.106, this figure also shows the theoretical force displacement envelope and shear strength envelope. Hysteretic loops in solid black lines correspond to the cold part of the test, i.e. up to the three cycles at ductility 1.5 when the actuator reached its maximum load. After this point the test was continued at room temperature, hysteretic loops at room temperature are displayed with a dashed line in Figure 6.106. It may be said that the specimen failed at the second cycle of ductility 2 where a strength lost of ~33% over the peak load reached in the first cycle at this ductility was observed. Figure 6.107 shows the average first peak envelope, note that there are two different loads that correspond to ductility 1.5. The larger load (500 kN) correspond to the cold part of the test and the smaller one (414 kN) to the room temperature part of the test, i.e. the effect of low temperatures was to increase in 20% the strength of the column. Note that that the improvement in shear strength at sub-freezing temperatures is larger than the predicted by the theoretical model.

Figures 6.108 and 6.109 are similar to Figures 6.106 and 6.107 but this time the shear envelope is calculated using the theoretical force-displacement envelope instead of the experimental response. Note that this will only change the displacements at which shear strength degradation starts and ends, and not the actual shear strength. It is seen from these two figures that the predicted model is still close enough to the actual response.

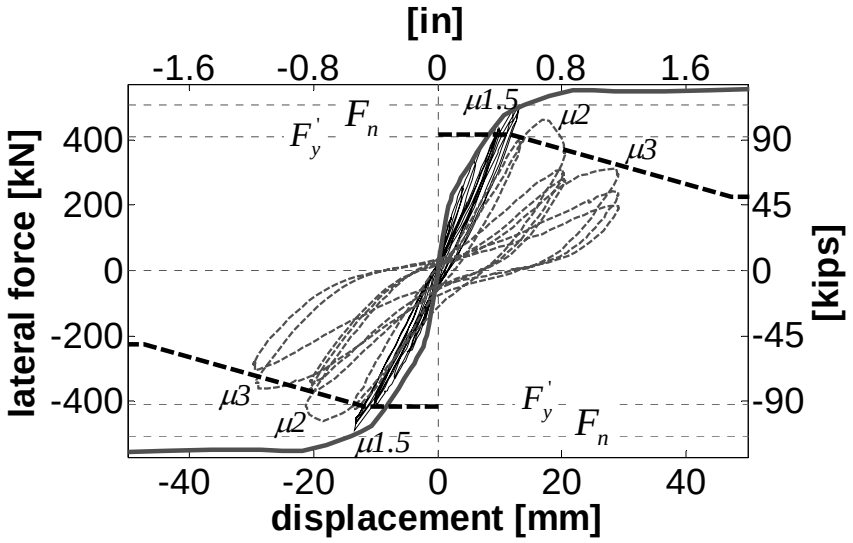

Figure 6.106 BSH-89C Force displacement response and theoretical shear strength envelope

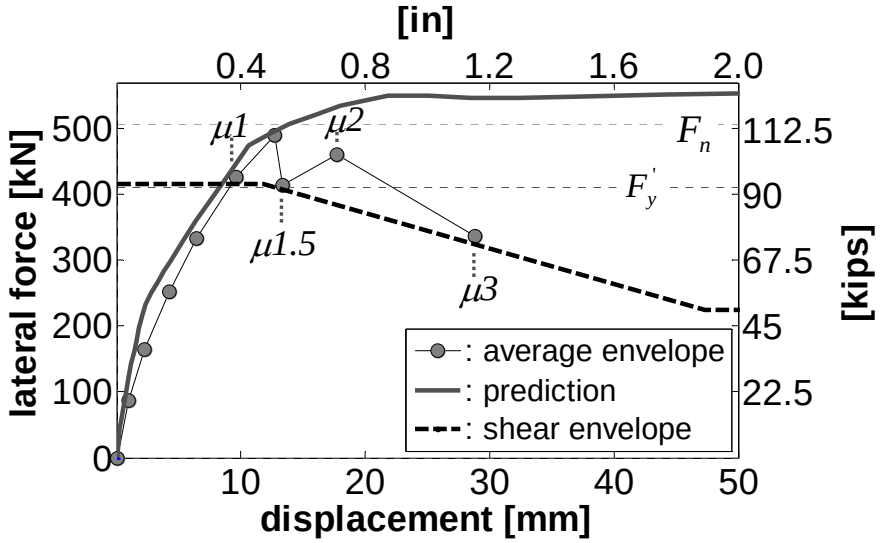

Figure 6.107 BSH-89C First peak envelope and theoretical shear strength envelope

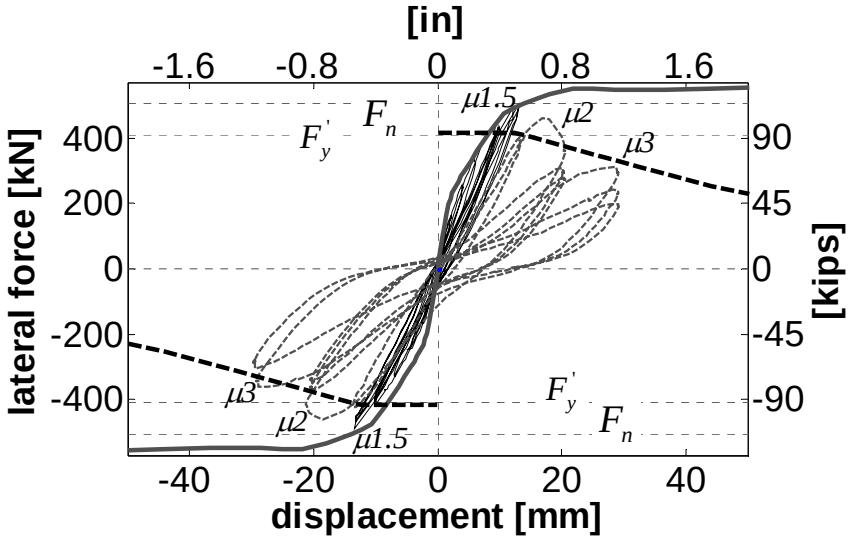

Figure 6.108 BSH-89C Force displacement response with shear strength envelope obtained using the theoretical force-displacement envelope

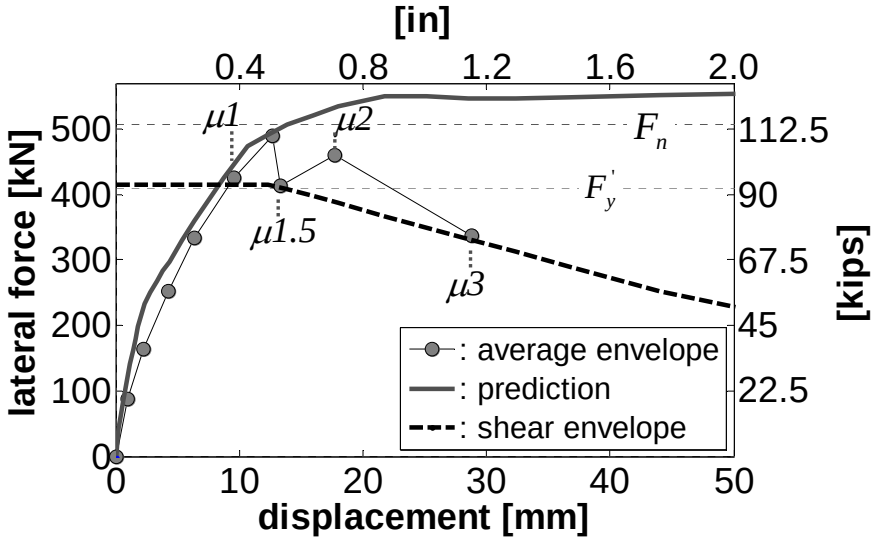

Figure 6.109 BSH-89C First peak envelope with shear strength envelope obtained using the theoretical force-displacement envelope

6.6.3 BSH-89C Curvature profiles

The component to account for the strain penetration effect in the gage length of the linear potentiometers in the base of the column was found to be 100 mm (4 in). Figure 6.110 shows the match between measured and predicted moment-curvature relation and

Figure 6.111 shows the curvature profiles calculated at selected ductilities. Dashed lines represent curvature profiles measured at room temperatures. Note that at ductility 1.5 cold and room temperature profiles are practically the same. As for the other three shear specimens, curvature distribution up to ductility 1 is mostly uniform along the column.

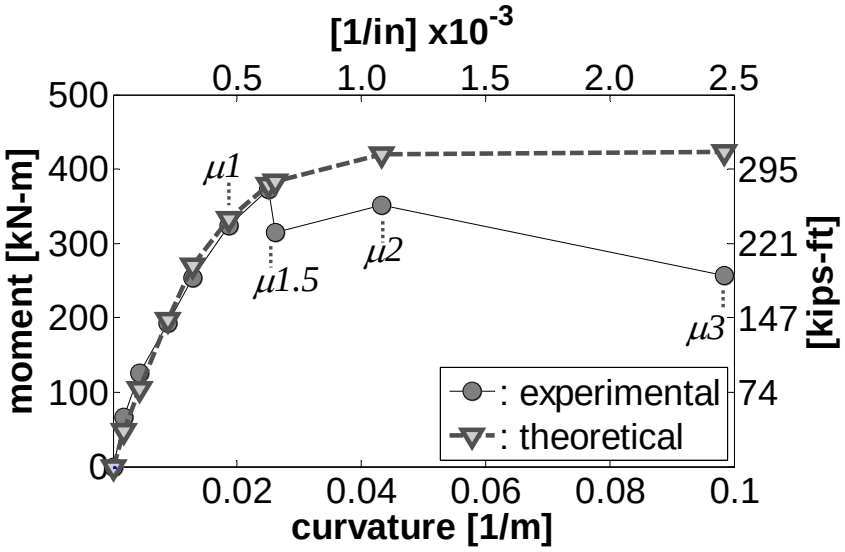

Figure 6.110 BSH-89C Moment curvature at column base

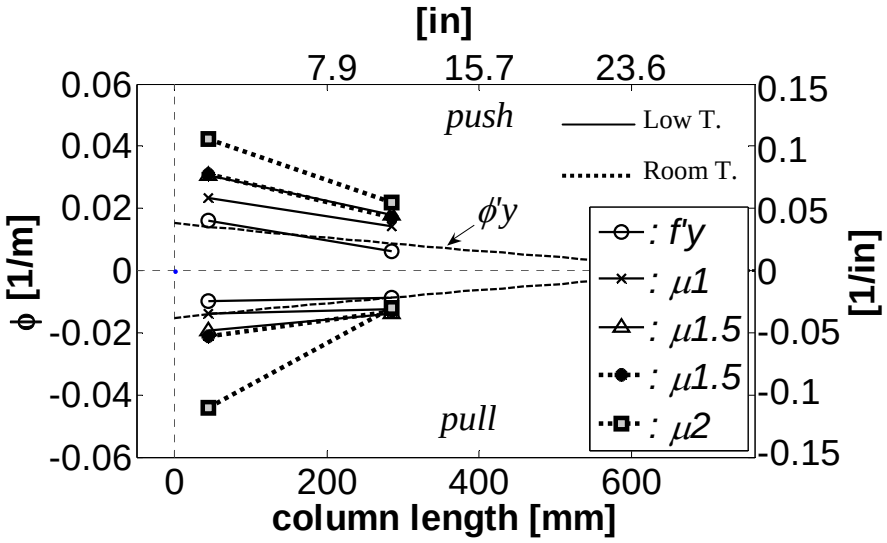

Figure 6.111 BSH-89C Curvature profiles

6.6.4 BSH-89C Equivalent plastic hinge length

As mentioned before, the cold test was stopped at ductility 1.5 so there is not enough data for calculation of an equivalent plastic hinge at low temperatures. Figure 6.112 shows the results obtained for the equivalent plastic hinge length in the room temperature part of the test. The average value obtained $L_p = 327mm\,(12.9in)$ is in agreement with the value obtained for the specimen BSH-89A $L_p = 317mm\,(12.5in)$.

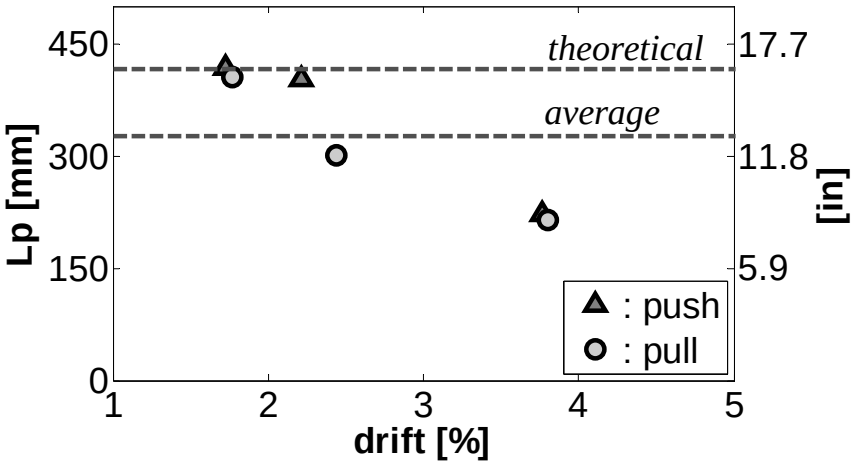

Figure 6.112 BSH-89C Equivalent plastic hinge length

6.6.5 BSH-89C Deformation components

The variation of flexural and shear components of column tip displacement with increasing drift is shown in Figure 6.113. This figure also compares the sum of the components with the displacement directly measured by a string potentiometer in the tip of the column. It is seen that shear components of deflection are negligible at low level of lateral demand, but when the shear cracks have fully developed at ductility 3 it increases to about 28% of the total deflection. The sum of flexural and shear components of displacement is in reasonably close agreement with the measured displacement, underestimating the true value in all cases.

Figures 6.114 to 6.117 compare the shear and flexural deformation components measured during the test with the deformations predicted by the theoretical models, the

comparison is done as function of the total displacement and also as a function of the applied lateral load. Predicted flexural deformations are very close to the measured values. In the case of the shear induced deflections the measured values are always below the predicted ones. As for specimen BSH-89A we believe the predicted shear deflections are right and the discrepancy is due to inaccuracies in the experimental data collected, perhaps due to interference of the concrete damage in the readings of the diagonal linear potentiometers.

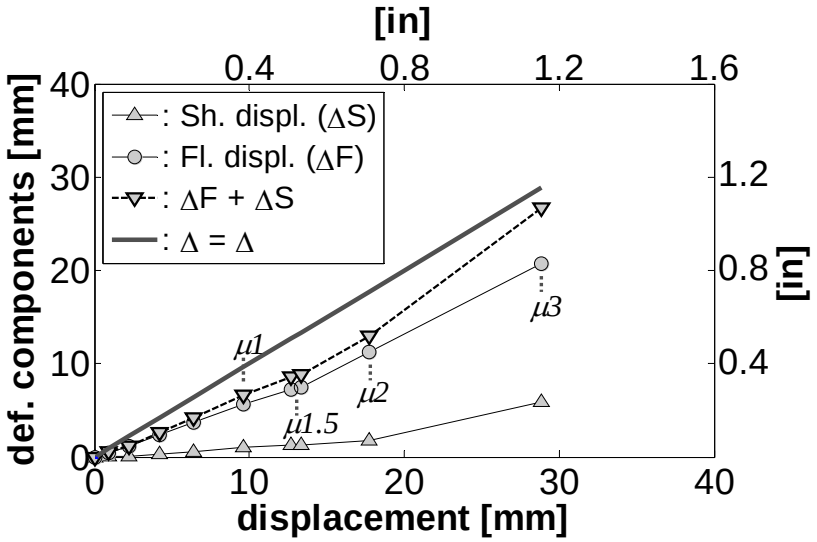

Figure 6.113 BSH-89C Deformation components

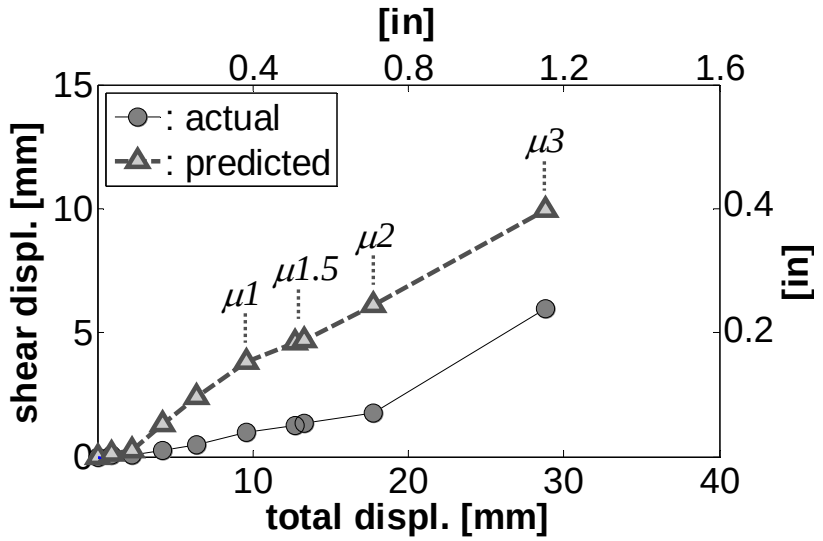

Figure 6.114 BSH-89C measured and predicted shear deformation components as function of the total displacement

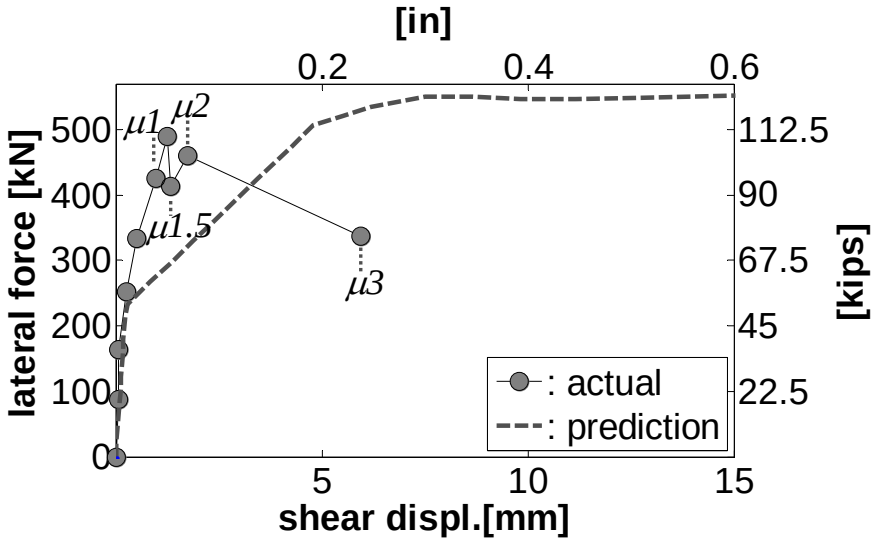

Figure 6.115 BSH-89C force vs. shear displacement envelope

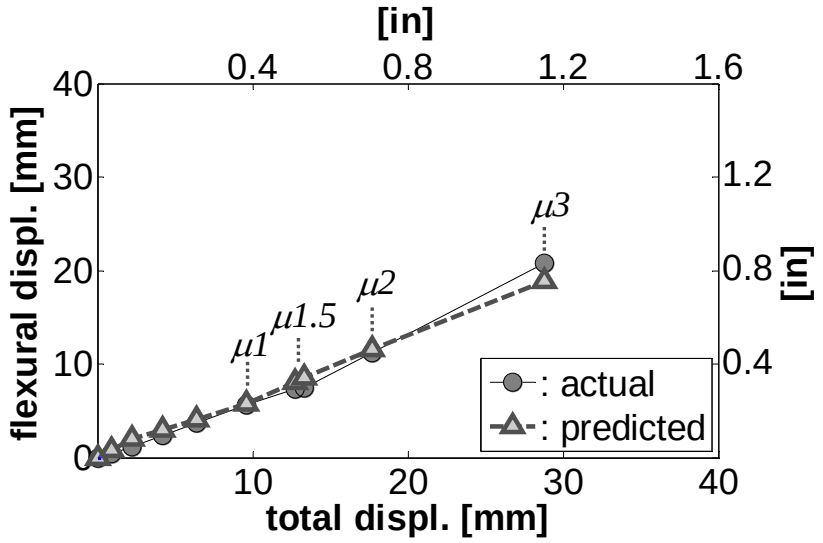

Figure 6.116 BSH-89C measured and predicted flexural deformation components as function of the total displacement

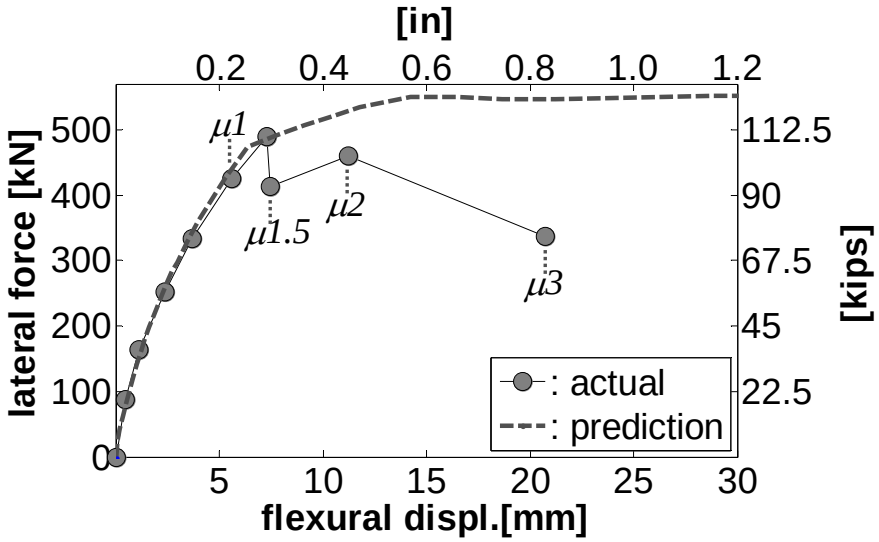

Figure 6.117 BSH-89C force vs. flexural displacement envelope

6.6.6 BSH-89C Strains on longitudinal steel

There was not enough reliable data to generate strain profiles of the longitudinal bars. Figures 6.118 and 6.119 present the strain history recorded by strain gages placed in the top and bottom bar, respectively. Strain histories are presented only up to ductility 1.5, i.e. the cold part of the test. Strain gauges in longitudinal bars did not work after this

point presumably due to the amount of water present in the specimen after the deicing process. It is seen from these graphs that at ductility 1.5 the main bars has barely reach the yield strain.

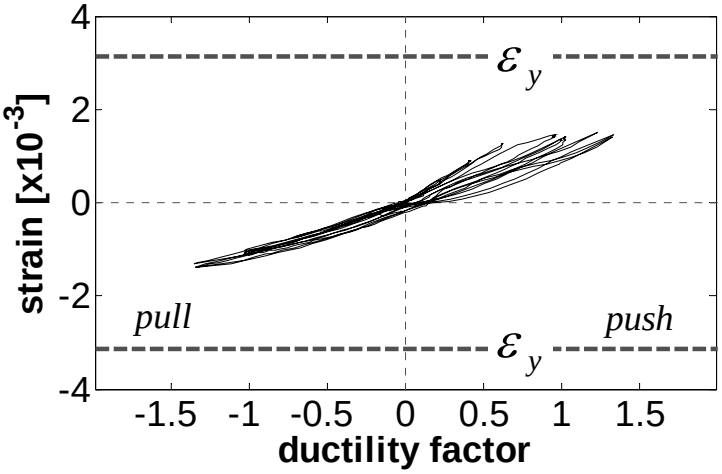

Figure 6.118 BSH-89C top bar strain history at 58 mm (2.3 in) from the base

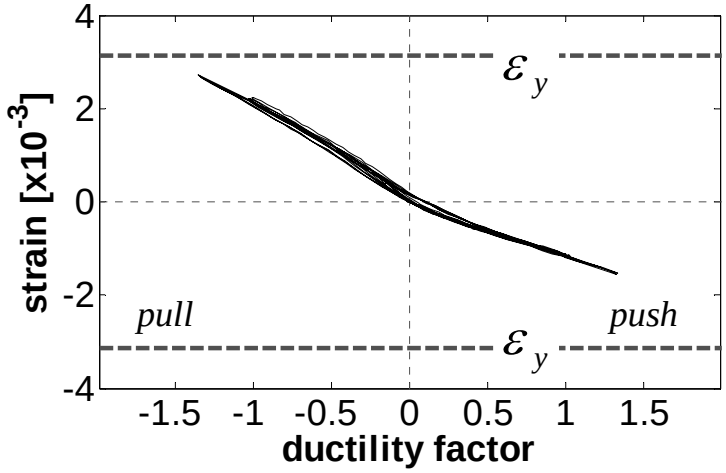

Figure 6.119 BSH-89C bottom bar strain history at 50 mm (2 in) from the base

6.6.7 BSH-89C Strains on transverse steel

Information collected from the strain gages placed in the spiral is presented in the form of strain histories as there was not enough reliable data to generate strain profiles. Figure 6.120 displays the strain history recorded by a strain gage placed on the top side of the spiral at 330 mm (13 in) from the base of the column. In this figure, the black solid

line represents the strain history registered during the cold part of the test (up to 1.5) and the dashed line represents the strain history recorded during the room temperature part of the test. Note that there is an increase in the strain when going from the low to room temperature condition due to thermal dilation of the steel. It seen that the spiral reached the yield strain during the cycles at ductility 2 and it increases to more than twice the yield strain during the first cycle at ductility 3.

Figure 6.121 shows the strain history recorded by a strain gage placed on the left side of the spiral at 42 mm (1.7 in) from the base of the column. As for Figure 6.120, the black solid line represents the strain history registered during the cold part of the test (up to 1.5) and the dashed line represents the strain history recorded during the room temperature part of the test. Note that the strains recorded are very low, barely reaching the yield strain. This is due to closeness of this point to the base of the column, as noticed in the others shear specimens the largest shear strains are developed in a region 250–350 mm (10 -14 in) away from the base. Unfortunately, strain gages placed in this zone did not work properly for this specimen.

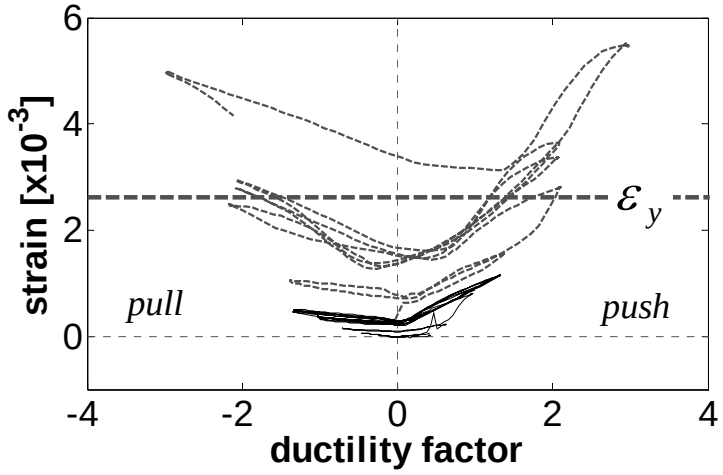

Figure 6.120 BSH-89C confinement induced strain history in top face of spiral at 330 mm (13 in) from the base

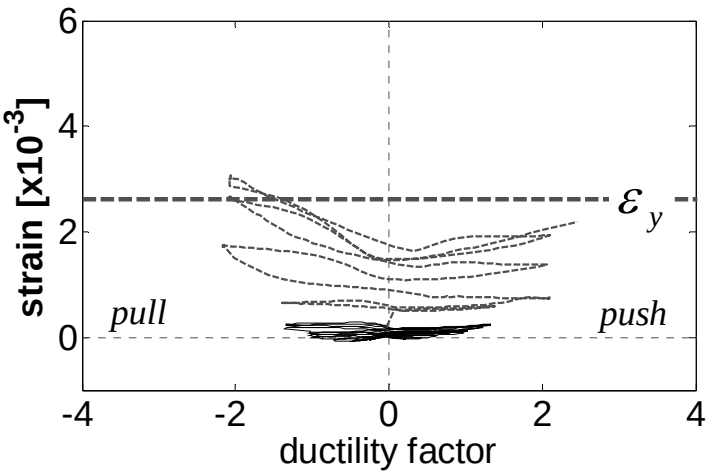

Figure 6.121 BSH-89C shear induced strain history in left face of spiral at 42 mm (1.7 in) from the base

6.7 Comparison of units BSH-89A and BSH-89C

Figure 6.122 compares the hysteretic force displacement response of both specimens and Figure 6.123 the average first peak envelope. From these graphs it is noticed that:

- Elastic stiffness of the cold specimen is 35% larger than the measured for the room temperature unit.

- The cold specimen exhibited an increase of 32% in the shear strength when compared to the room temperature one.

- Not much can be said regarding the displacement capacity and strength degradation of the specimens as the cold test was stopped at ductility 1.5 for the reason earlier explained.

- It is seen from Figure 6.124 that the strength degradation over cycles at the same level of ductility demand decreases at low temperatures.

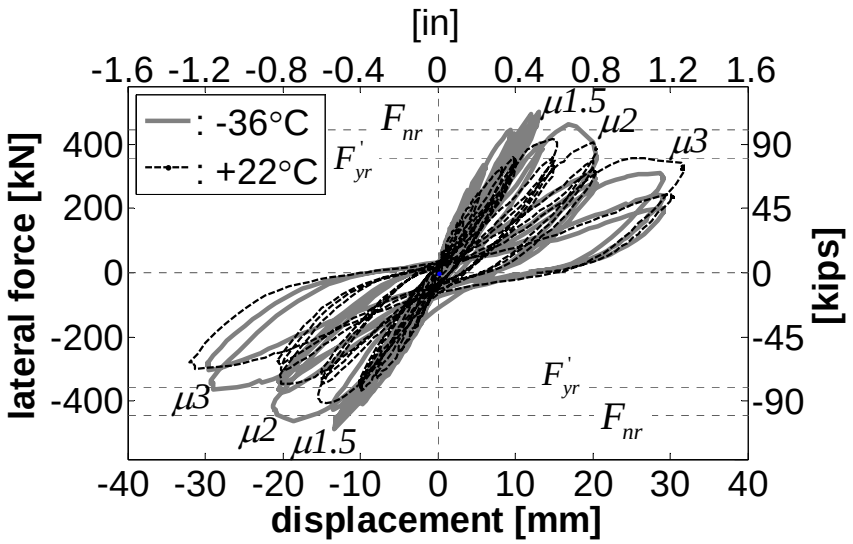

Figure 6.122 BSH-89A and BSH-89C hysteretic responses

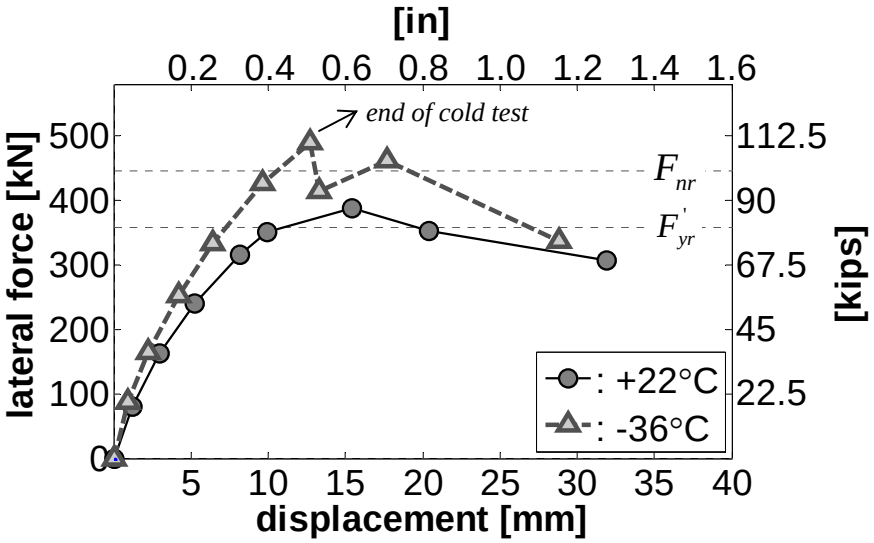

Figure 6.123 BSH-89A and BSH-89C average first cycle envelope

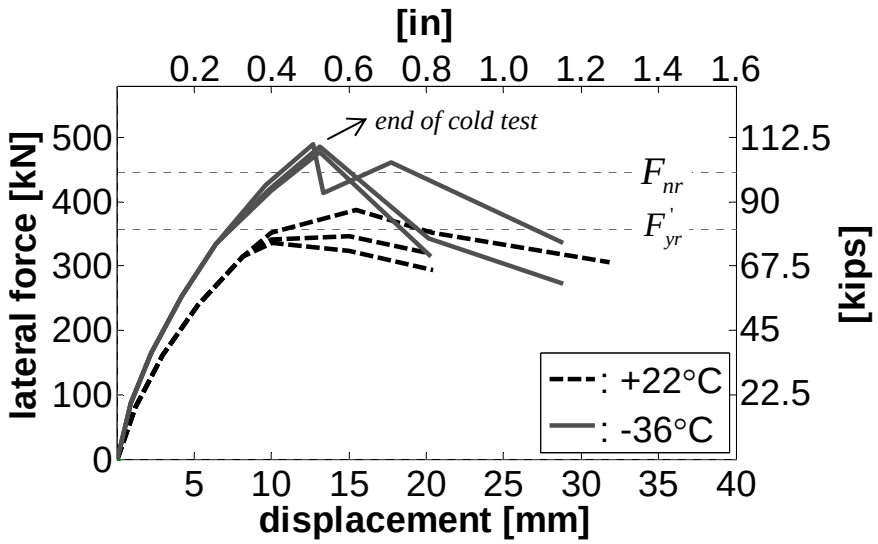

Figure 6.124 BSH-89A and BSH-89C three cycles envelope

Figure 6.1.25 presents the shear and flexural components of deformation for the cold and room temperature tests. It is seen that there was basically no change in the deformation components due to the low temperature.

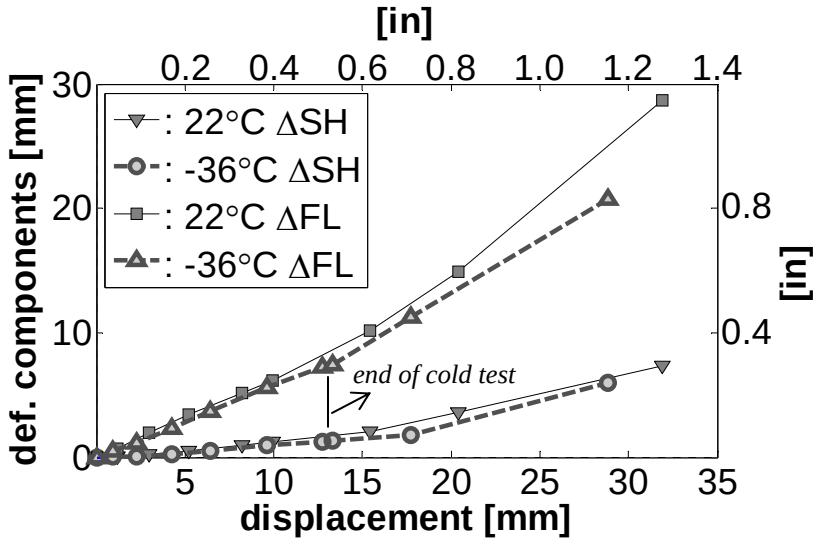

Figure 6.125 BSH-89A and BSH-89C three cycles envelope

Figures 6.126 and 6.127 analyze the energy dissipation properties of the units. It is seen from these graphs that up to ductility 1.5 the room temperature specimen exhibited better dissipation properties than the cold one, most likely because up to this

level of demand the cold specimen was responding mainly elastic (remember that target displacements are calculated based on room temperature material properties and the response of the room temperature specimen). However, these differences become minimal when the damping values are corrected to use in direct-displacement based design (Figure 6.128).

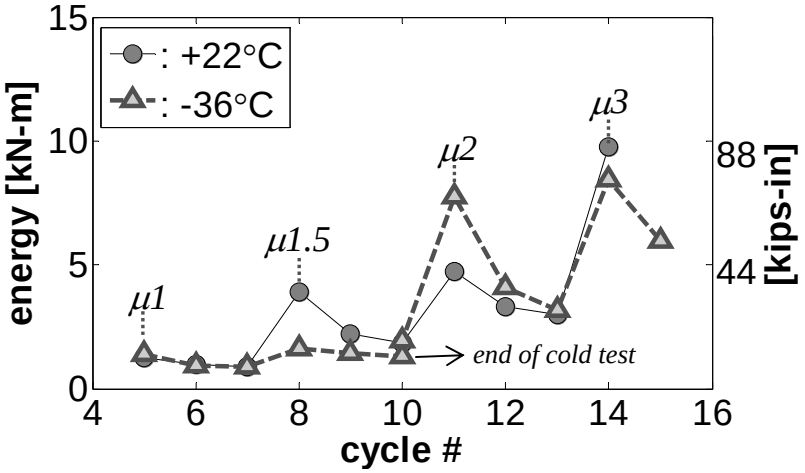

Figure 6.126 BSH-89A and BSH-89C hysteretic energy

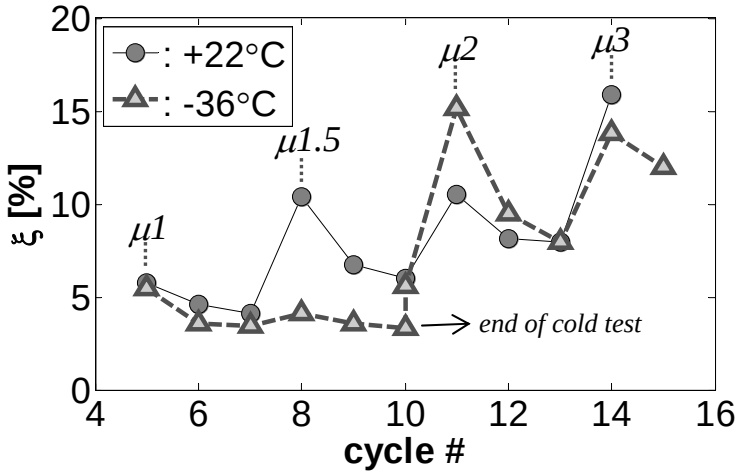

Figure 6.127 BSH-89A and BSH-89C hysteretic damping

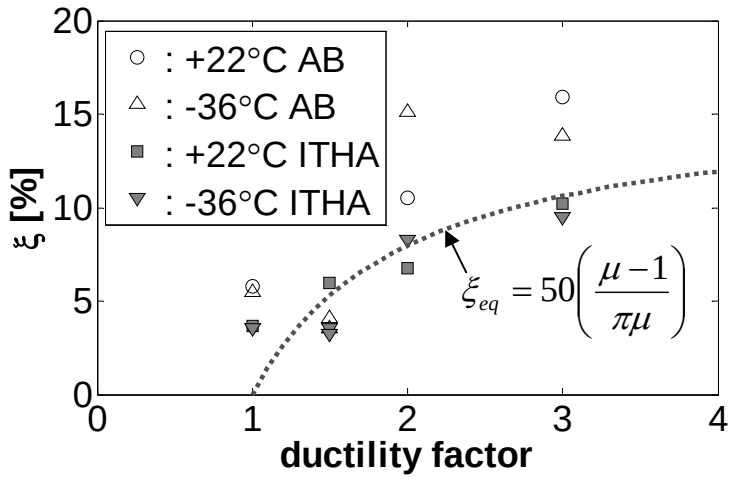

Figure 6.128 BSH-89A and BSH-89C corrected damping

From Figure 6.129 can be seen that low temperatures did not affect the curvature distribution of short shear dominated columns. As mentioned before there was not enough data to calculate an equivalent plastic hinge at low temperature conditions. Therefore, equivalent plastic hinge lengths displayed in Figure 6.130 correspond to room temperature conditions. However, this figure works to verify the validity of the lpot's data recorded during both tests.

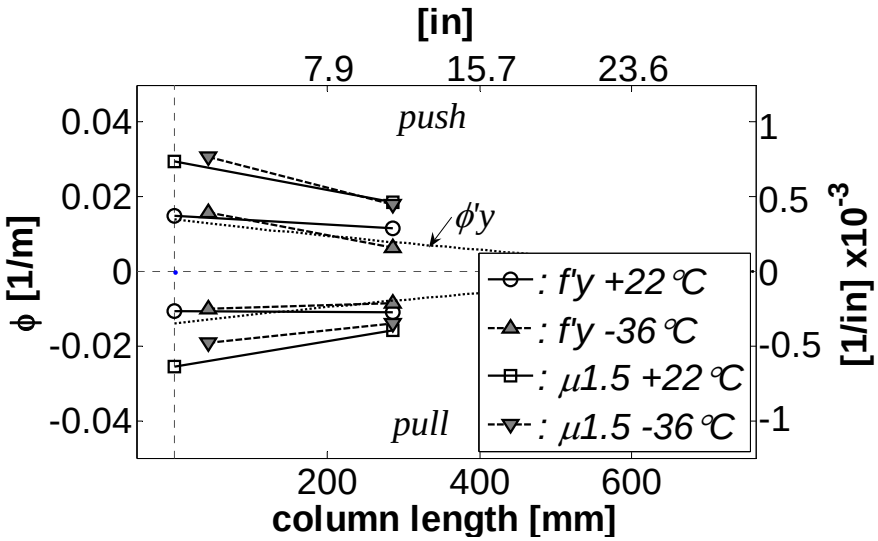

Figure 6.129 BSH-89A and BSH-89C curvature profiles

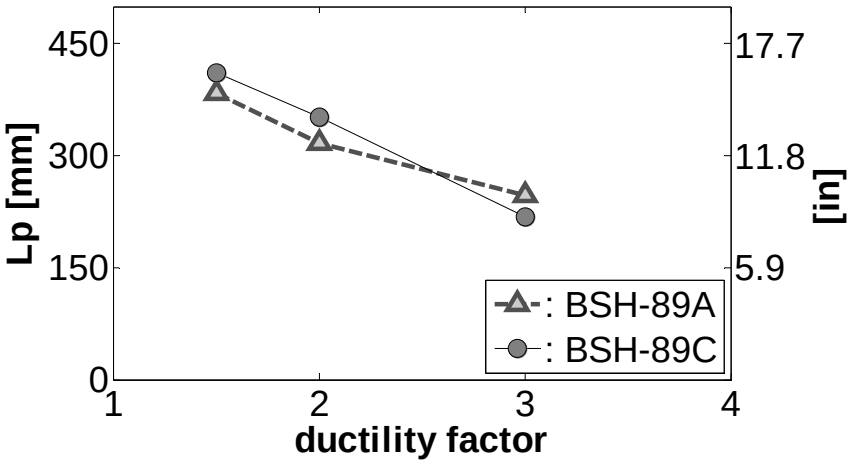

Figure 6.130 BSH-89A and BSH-89C equivalent plastic hinge lengths

Figure 6.131 shows the shear induced strain history recorded by strain gages placed in the spiral of the specimens at ~50 mm (2 in) from the column base. It is seen that up to ductility 1.5, the strains induced in the spiral of the room temperature specimen are three times larger than the strains measured in the cold test. This implies that up to this level of demand shear stresses in the cold specimen are mostly resisted by the concrete, i.e. the effect of low temperatures was to increase the shear strength of the concrete. This can be corroborated by looking at the condition of both specimens after the cycles at ductility 1.5 in Figure 6.132. Note that concrete damage is more severe in the room temperature unit. Finally, Tables 6.4 and 6.5 summarize the results obtained in both tests.

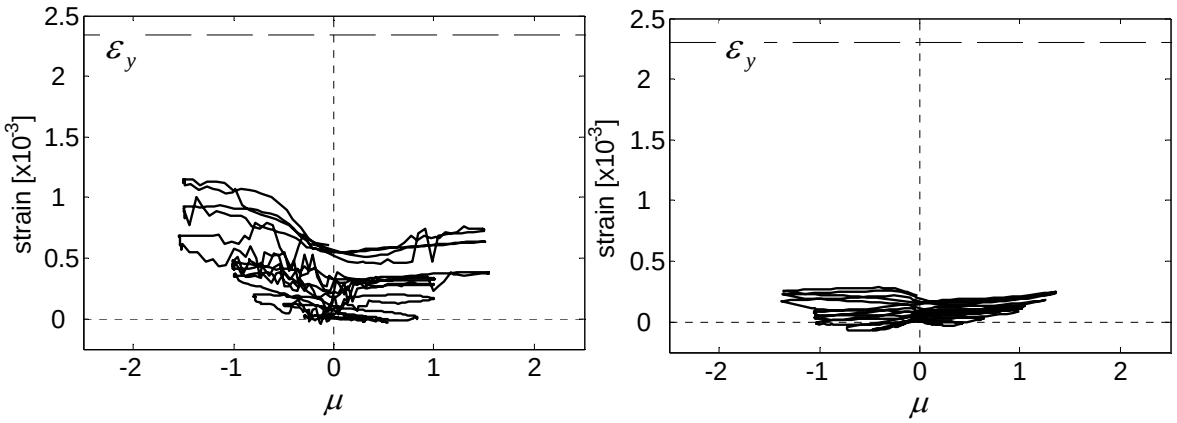

(a) BSH-89A [22°C/72°F] **b)** BSH-89C [-36°C/-33°F]

Figure 6.131 BSH-89A and BSH-89C shear induced stain history

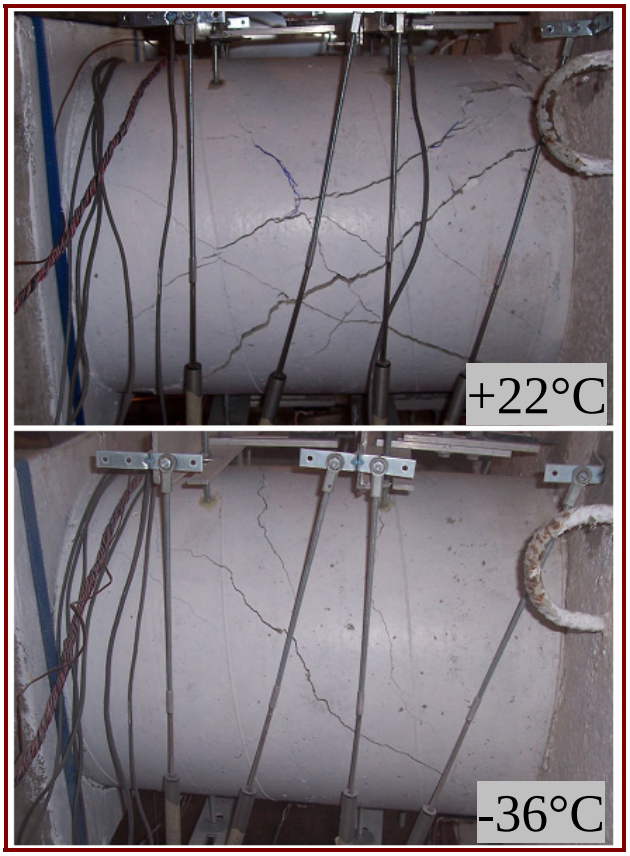

Figure 6.132 BSH-89A and BSH-89C after the cycles at ductility 1.5

Table 6.4 Summary of results obtained (Load control phase)

Cycle	Average Lat. Force [kN]	Average tip displacement [mm]		
		+22°C	-36°C	-36°C / +22°C
0.25fy'	84.1	1.2	0.9	0.73
0.5fy'	163.0	3.0	2.2	0.74
0.75fy'	246.1	5.5	4.1	0.74
Fy'	324.5	8.6	6.2	0.71

Table 6.5 Summary of results obtained (Displacement control phase)

Cycle	Average Displacement [mm]	First cycle average lateral force [kN]		
		+22°C	-36°C	-36°C / +22°C
μ1	9.8	347.5	429.4	1.24
μ1.5	14.1	378.0	500.0	1.32
μ2	19.1	361.1	445.6	1.23
μ3	30.4	312.6	313.1	1.00

6.8 Revised predictive models

Table 6.6 summarizes the predicted and experimental shear strengths for the four tests. It is seen that the predicted shear strengths are in close agreement with the shear strength measured during the test of room temperature specimens. However, the model underestimates the shear strengths of the cold units. As will be shown next through an analysis of the shear strength components, this is mainly cause to a major improvement in the concrete shear resisting mechanism at low temperatures that is not captured by the model.

Table 6.6 Predicted and experimental shear strengths

Test #	UNIT	T		Vth		Vexp		Vexp/Vth
		[°C]	[°F]	[kN]	[Kips]	[kN]	[Kips]	
1	DSH-87A	+22	+72	288	64.7	297	66.7	1.03
2	DSH-87C	-36	-33	325	73.0	356	80.0	1.10
3	BSH-89A	+22	+72	363	81.6	387	87.0	1.07
4	BSH-89C	-36	-33	416	93.5	500	112	1.20

6.8.1 Shear strength components

The total shear V_s carried by the transverse steel is usually calculated from the hoop strains measured at different heights of the column. As mentioned before, the majority of strain gages placed on the transverse steel of the cold units did not work properly. Therefore, average strains in the spirals were calculated from the shear deformations measured in the specimen and then used to calculate V_s at different level of lateral demand during the test. The axial load contribution to shear strength V_p is calculated as the lateral component of the compression strut as explained in Chapter II, the neutral axis depth at different levels of lateral demand is obtained from a moment-curvature analysis. The concrete contribution V_c is then obtained by subtracting from the total shear the other two components (V_s and V_p). Results obtained are displayed in Figure 6.133. Shown in this figure are also the shear force at which inclined flexure/shear cracking was first observed (V_{cr}) and the shear strength provided by the concrete according to the revised UCSD model (obtained with the corresponding temperature dependent material properties). It is seen that the concrete contribution V_c is largely increased in the units tested at sub-freezing temperatures, peak contributions increased by 30% and 34% in the DSH and BSH units, respectively. The predicted V_c is in close agreement with the exhibited by the room temperature units; however, it underestimates the improvement in the concrete shear resisting mechanism at to low temperatures (although low temperature material properties were used for the prediction).

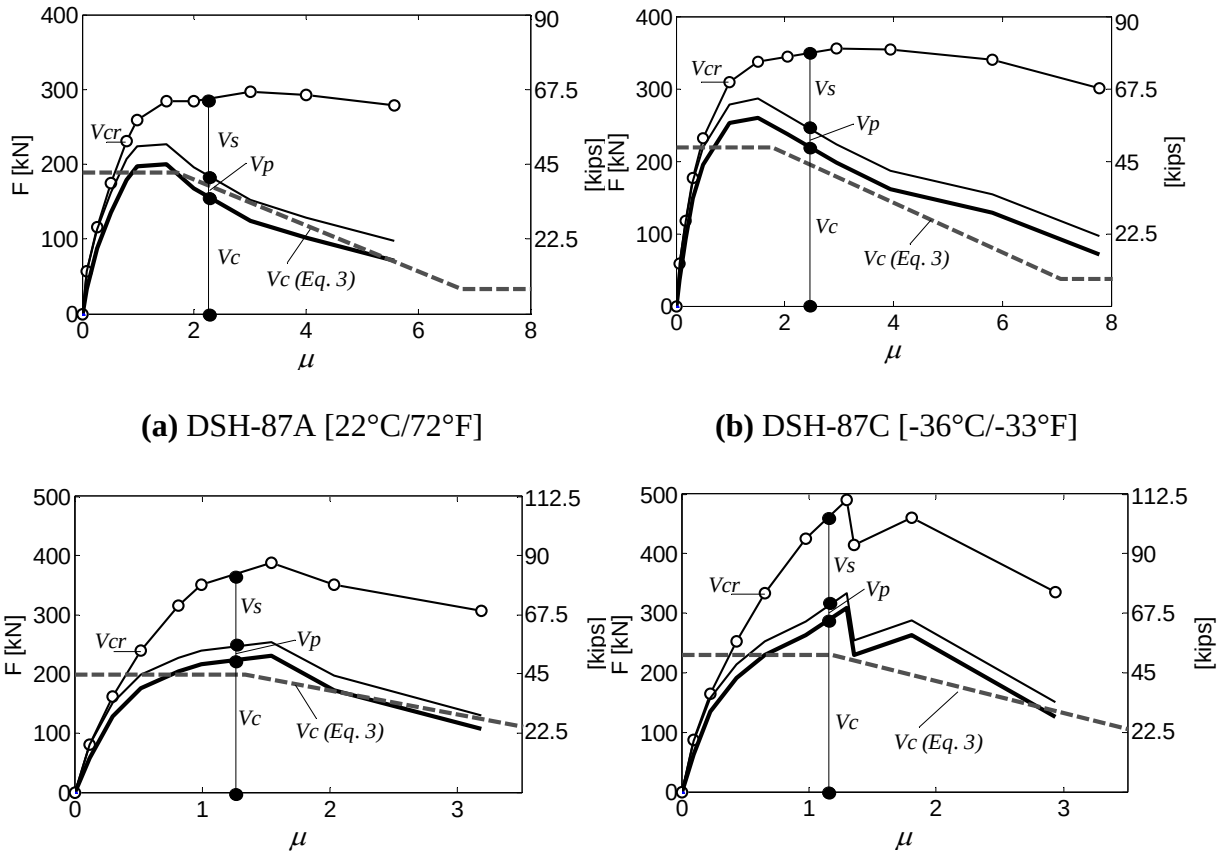

Figure 6.133 Column shear capacity components versus ductility.

6.8.2 Evaluation of shear design models

Shear strengths exhibited by the four units are also compared with the AASHTO design shear strengths calculated using the recommended LRFD guidelines for the seismic design of highway bridges. Equations 6.1 to 6.6 summarize the procedure recommended by AASHTO to calculate shear design strengths. Note that these equation are available in US customary units (kips, in) exclusively and are presented as such. In this model the shear column strength capacity (Eq. 6.1) is calculated as the summation of the shear capacities provided by the concrete V_c (Eq. 6.2) and the transverse steel V_s (Eq. 6.6). The effect of the axial load is considered when determining the shear strength of the

concrete (Eq. 6.3), concrete shear strength degradation associated with inelastic demands is taking into account by means of the factor α (Eq. 6.4).

$$\phi V_n = 0.85\left(V_c + V_s\right) \tag{6.1}$$

$$V_c = v_c A_e = v_c\left(0.8A_g\right) \tag{6.2}$$

$$v_c = 0.032\alpha\left(1+\frac{P}{2A_g}\right)\sqrt{f_c^{'}} \le \min(0.11\sqrt{f_c^{'}}, 0.047\alpha\sqrt{f_c^{'}}) \tag{6.3}$$

$$0.3 \le \alpha = \frac{(\rho_s f_{yh} \le 0.35)}{0.15} + 3.67 - \mu \le 3 \tag{6.4}$$

$$\rho_s = \frac{4A_{sp}}{D's} \tag{6.5}$$

$$V_s = \frac{\pi}{2}\left(\frac{A_{sp} f_{yh} D'}{s}\right) \tag{6.6}$$

In Equations 6.5 and 6.6, D' is the core diameter measured from spiral center. AASHTO design shear strengths are compared with the experimental results obtained in this research in Table 6.7, presented in this table are also the shear strengths obtained using the revised UCSD model for design. Note that these equations are intended for design and not assessment purposes. Design shear strengths were calculated using the appropriate temperature dependent material properties. For the AASHTO provisions, an average measured/model shear strength ratio of 1.74 was obtained for the room temperature units and 1.90 for the cold temperature units. In the case of the revised UCSD design model, average ratios of 1.48 and 1.61 were obtained for the room and cold temperature units, respectively.

Table 6.7. Experimental and design shear strengths

UNIT	T		Vexp		Vd1		Vd2		Vexp/Vd1	Vexp/Vd2
	[°C]	[°F]	[kN]	[Kips]	[kN]	[Kips]	[kN]	[Kips]		
DSH-87A	+22	+72	297	66.7	162	36.3	202	45.4	1.84	1.47
DSH-87C	-36	-33	356	80.0	181	40.7	229	51.5	1.97	1.55
BSH-89A	+22	+72	387	87.0	238	53.4	261	58.7	1.63	1.48
BSH-89C	-36	-33	500	112	271	60.9	299	67.2	1.84	1.67

Vexp = experimental shear strength, Vd1 = AASHTO design shear strength,
Vd2 = UCSD revised model design shear strength

6.9 Final discussion and concluding remarks

This chapter presented the experimental results from the testing of two pair of short shear dominated columns. One pair of columns was deigned to fail by shear at low level of ductility demand (brittle shear failure), while the other pair was designed to fail by shear at large levels of ductility demand (ductile shear failure). The only variable between columns of the same pair was the temperature of the specimen during the test; one of the columns was tested at normal room temperature conditions (~22°C, 72°F) while the other was tested under freezing conditions (~-36°C, -33°F). Specimens tested at low temperatures exhibited an increase in its shear strength; the amount of this increase was larger in the brittle shear units (32%) than in the ductile shear units (20%).

Even though it was shown in Chapters IV and V that flexural strength increases at low temperatures thus resulting in an increased shear demand, the shear capacity increases at an even higher proportion, thus delaying the onset of shear failure at low temperatures. In the case of the ductile shear units, the cold specimen sustained cyclic deformations 33% larger than the warm unit. The brittle shear cold test units couldn't be tested to failure because the maximum load of the actuator was reached. Nonetheless, based on the information collected up to μ1.5 and the condition of the specimen at this point, a similar behavior can be anticipated. Note that this is opposite to the found for flexurally dominated specimens in Chapters IV and V where a reduction in the displacement capacity of the members tested at low temperatures was identified. This reduction was attributed mainly to a reduction in the spread of plasticity and equivalent plastic hinge length of the cold flexural units; however, such reduction was not observed

in the case of the shear dominated members. It is believed that such reduction was not observed in the shear dominated members because the contribution of shear induced deformation into the total measured deflection was quite considerable (~30%), while for the flexurally members was negligible. Also, the reduced clear length of the column caused the shear and flexural cracks to cover the whole length of the column leaving no space for a possible reduction in the spread of plasticity of the columns tested at low temperatures.

Specimens tested at low temperatures also exhibited an increase of 56% (ductile units) and 35% (brittle units) in the elastic stiffness. A slightly reduction in the strength degradation over repetitive cycles at the same level of ductility was noticed when the specimens were tested at low temperatures. No major changes were noticed in the in the dissipation properties of the specimens tested at low temperatures.

The observed increase in shear strength of the columns tested at low temperatures was in some way expected as past research (Chapter I) have shown mechanical properties of plain concrete and reinforcing steel to improve at low temperatures. Current available models for assessment and design of shear strength in RC columns under seismic actions become conservative when the columns are exposed to sub-freezing temperatures even if the increase in concrete compressive strength and steel yield stress due to low temperatures are taking into account. It was shown that the assessment shear model was mainly underpredicting the contribution of the concrete shear mechanism, presumably because the concrete tensile and fracture properties are not taken directly into account by the method but through the compressive strength; however, past research has show tensile strength and fracture properties to improve at low temperatures at a proportion even larger than it does for the compressive strength (Lee et al. 1998).

CHAPTER VII

SEISMIC BEHAVIOR OF REINFORCED CONCRETE BRIDGE BENTS AT LOW TEMPERATURES

7.1 Introduction

Chapters IV to VI discussed the results obtained from the testing under cyclic reversals of 13 large scale circular bridge columns while subjected to room temperatures (~20°C, 68°C) and sub-freezing temperatures (~-40°C, -40°C), these results are used in this Chapter to model typical bridge bents used by the Alaska Department of Transportation (DOT). First, the results obtained from the experimental tests are summarized and used to calibrate a fiber-based lumped plasticity model capable of simulating the response of reinforced concrete (RC) circular columns to cyclic load reversals while subjected to sub-freezing temperatures. Once the simulation model is calibrated against the experimental results, it is used to analyze typical bridge bents used by the Alaska DOT. In order to determine the impact of sub-freezing temperatures on the seismic response of RC bridge bents, the bent models are subjected to inelastic lateral pushovers and to a series of incremental inelastic time history analyses using spectrum compatible records.

7.2 Review of experimental results

A total of 10 RC columns were tested as part of this research. In addition, three column tests conducted in a pilot study (Sloan 2005, Montejo et al. 2008a) were also re-analyzed. The test units being analyzed can be divided into three groups according to

their structural behavior: (1) Flexural-dominated ordinary reinforced concrete columns (Montejo et al. 2008b), (2) Flexural-dominated reinforced concrete filled steel tube columns (Montejo et al. 2008b) and (3) Shear-dominated ordinary reinforced concrete columns (Montejo et al. 2008c). The term ordinary reinforced concrete (ORC) columns refer to conventional circular RC columns in which transverse reinforcement is in the form of spirals. In reinforced concrete filled steel tube (RCFST) columns a steel tube is used as formwork during casting of the concrete. In the majority of the cases a gap is left between the steel tube and the beam–column joint or foundation, so that the steel tube is only providing shear and confinement strengths to the column, and not (in a direct way) flexural or axial strength, which are provided by the concrete and the longitudinal bars.

7.2.1 Flexural-dominated ordinary reinforced concrete column

Table 7.1 summarizes the properties of the four flexural units analyzed. Although Sloan (2005) tested four identical units at different temperatures, we are only presenting here the extreme temperature cases (20°C and -40°C). The primary differences between each pair of columns are the amount of longitudinal steel and axial load. A detailed analysis of the experimental results was previously presented in Chapter IV and by Sloan (2005). Figures 7.1 and 7.2 compare the average first cycle envelopes for the warm and cold units, along with the envelopes are the theoretical monotonic envelope calculated using the equivalent plastic hinge method (Priestley et al. 2007). Results obtained from the experimental program indicated that flexural-dominated ORC columns exposed to the combined effect of cyclic reversals and low temperatures exhibited an increase in the flexural strength accompanied by a reduction in the spread of plasticity; no effect of temperature on the energy dissipation properties was found. The increase in the flexural strength of the columns can be explained by the increase in the strength of plain concrete and steel reinforcement when exposed to sub-freezing temperatures. The amount of this increase was of 16% in the light reinforced columns and 14% in the heavy reinforced columns. The reduction on the spread of plasticity at low temperatures was evident from the condition of the specimens after the test and confirmed with the curvature profiles obtained during the tests and the calculation of equivalent plastic hinge lengths. The reduction in the hinge length caused an increase in the initial stiffness and a reduction in

the displacement capacity of the cold specimens; this was especially evident in the lightly reinforced units tested without axial load (Figure 7.1). It was proposed in Chapter IV to reduce the equivalent plastic hinge length by a factor of 0.57 as shown in Equation 7.1 (which was first introduced in Chapter IV as Equation 4.3). Theoretical predictions in Figures 7.1 and 7.2 were obtained using the reduced plastic hinge length for the cold units and the appropriate temperature-dependent material properties (Tables 2.5, 2.7 and 4.2). Identified in the theoretical predictions were the stages when the extreme tension reinforcement in the base of the column reached the yield strain, and strains of 0.015 and 0.07, which define the first yield, serviceability and damage control limits, respectively (Kowalsky, 2000). Note that the behavior of the cold units can be predicted if the appropriate low temperature material properties and the reduced equivalent plastic hinge length are used.

$$\begin{aligned} L_p &= kL + L_{sp} \geq 2L_{sp} && \textit{room temperatures} \\ L_p &= 0.57\left(kL + L_{sp} \geq 2L_{sp}\right) && \textit{subfreezing temperatures} \end{aligned} \qquad (7.1)$$

where:

$$L_{sp} = 0.022\, f_s d_{bl} \quad f_s \leq fy \quad (MPa)$$

$$k = 0.2\left(\frac{f_{su}}{f_y} - 1\right) \leq 0.08$$

In the above equations, L is the distance from the base to the inflection point, f_y is the expected longitudinal bar yield stress, f_{su} is the expected longitudinal bar tensile strength, f_s is the tensile stress in the longitudinal bars and d_{bl} is the diameter of the longitudinal bar.

Table 7.1 Flexural dominated ORC columns

UNIT	AVG. TEMP.	LONG. STEEL/ RATIO	TRANSVERSE STEEL/RATIO	AXIAL LOAD/ RATIO
SL-P20	74˚F 23˚C	8#5 1.0%	#3@64mm (2.5in) 1.1%	No
SL-M40	-40˚F -40˚C	8#5 1.0%	#3@64mm (2.5in) 1.1%	No
FL 89A	+22˚C +72˚F	8#9 3.1%	#3@60mm (2.4in) 1.2%	220kN (49kips) 6.2%
FL 89C	-36˚C -33˚F	8#9 3.1%	#3@60mm (2.4in) 1.2%	218kN (49kips) 4.8%

*For all units: Diameter: 457mm (18in) Cantilever length: 1651mm (65in)

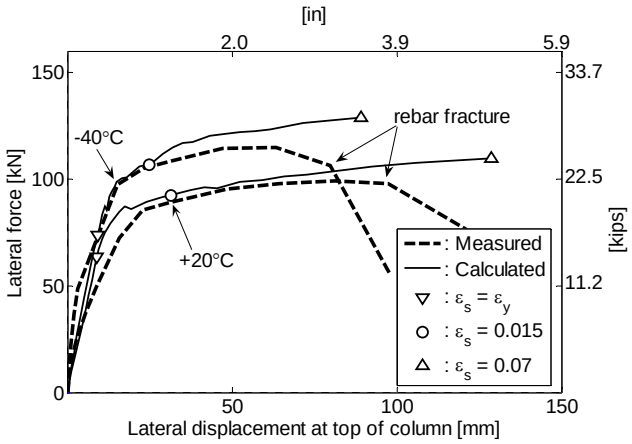

Figure 7.1 Average first cycle envelopes and theoretical envelopes for units SL-P20 and SL-M40.

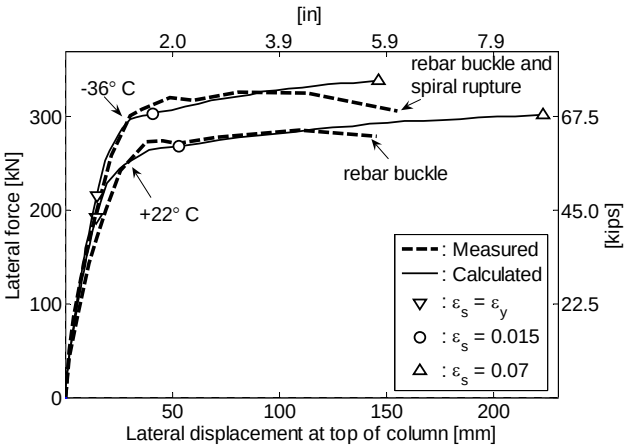

Figure 7.2 Average first cycle envelopes and theoretical envelopes for units FL-89A and FL-89C.

7.2.2 Flexural-dominated reinforced concrete filled steel tube columns

Table 7.2 shows the test matrix for the RCFST columns tested in this research. Main difference between pairs of identical columns was the amount and properties of the longitudinal steel. While one pair of columns was reinforced with 8#9 bars having a yield stress of 558 MPa (81 ksi), the other was reinforced with 8#7 bars with a yield stress of 442 MPa (64 ksi). Figures 7.3 and 7.4 show the average first cycle envelope along with the calculated monotonic envelope. A detailed analysis of the experimental data was presented in Chapter V. The effect of low temperatures on the seismic behavior of RCFST columns was found to be similar to that described for ORC columns, i.e. the cold specimens exhibited an increase in the initial stiffness and flexural strength when compared to the room temperature units. Low temperature average flexural strength increase on the RCFST columns was of 9%. Failure of the cold specimens was more brittle as it involves fracture of the longitudinal reinforcement which was not observed in the room temperature units. A significant reduction of the equivalent plastic hinge length of the RCFST columns when compared to the values obtained for ORC columns was detected. From the experimental results the following expression was proposed to calculate the equivalent plastic hinge length in RCFST columns:

$$L_p = 9.3 d_{bl} \frac{f_{su}}{f_y} + g \tag{7.2}$$

Where d_{bl} is the diameter of the bar and g the gap between the steel tube and the adjacent member, both in mm; f_y and f_{su} are the expected yield stress and expected tensile strength of the reinforcing bar, respectively. As no change in L_p was detected during the cold tests of the RCFST specimens compared to the room temperature tests, assessment of the behavior of this type of columns at low temperatures can be performed using the equivalent plastic hinge length predicted by Equation 7.2 without any correction for reduced temperatures. As for the flexural-dominated ORC columns, it is seen from Figures 7.3 and 7.4 that the response of RCFST columns subjected to low temperatures and lateral loads can be adequately predicted if the appropriate low temperature material properties and equivalent plastic hinge length are utilized.

Table 7.2 Flexural dominated RCFST columns

UNIT	TEMP.	LONG. STEEL/ RATIO	TRANSV. STEEL/ RATIO	AXIAL LOAD/ RATIO
RCFST 89A	22˚C 72˚F	8#9 3.1%	#3@60mm (2.4in) 9.5mm (3/8in) th. steel tube (1.2+8.5)%	231 kN (51.9 kips) 5.9%
RCFST 89C	-36˚C -33˚F	8#9 3.1%	#3@60mm (2.4in) 9.5mm (3/8in) th. steel tube (1.2+8.5)%	219 kN (49.2 kips) 3.3%
RCFST 87A	22˚C 72˚F	8#7 2.1%	#3@60mm (2.4in) 9.5mm (3/8in) th. steel tube (1.2+8.5)%	226 kN (50.8 kips) 5.7%
RCFST 87C	-36˚C -33˚F	8#7 2.1%	#3@60mm (2.4in) 9.5mm (3/8in) th. steel tube (1.2+8.5)%	231 kN (51.9 kips) 3.5%

*For all units: Diameter: 457mm (18in) Cantilever length: 1651mm (65in)

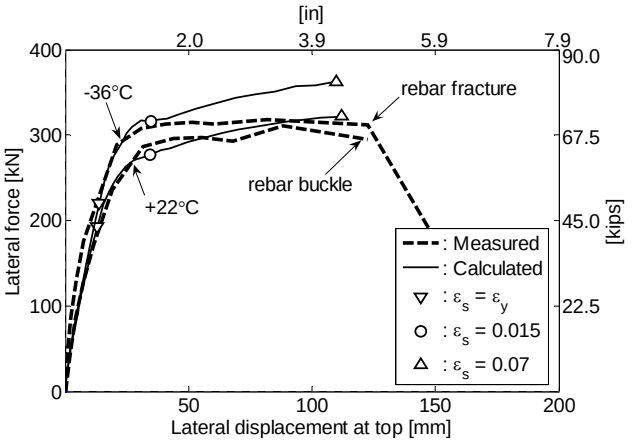

Figure 7.3 Average first cycle envelopes and theoretical envelopes for units RCFST-89A and RCFST-89C.

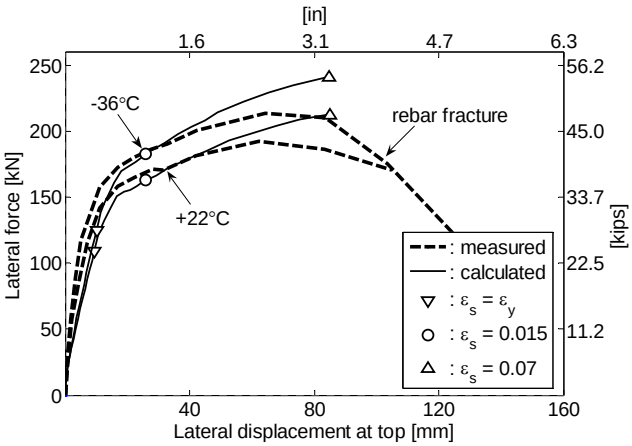

Figure 7.4 Average first cycle envelopes and theoretical envelopes for units RCFST-87A and RCFST-87C.

7.2.3 Shear-dominated reinforced concrete columns

The test matrix of the shear dominated columns tested in this research is displayed in Table 7.3. The units were detailed to fail by shear at low levels of ductility (brittle shear BSH units) and larger levels of ductility (ductile shear DSH units). Figure 7.5 shows the average first peak envelopes along with force-displacement prediction and the theoretical shear strength envelope (Kowalsky and Priestley, 2000). The point of shear failure (if any) is given by the intersection between the force-displacement response and the shear strength envelope. In general, it was found that specimens tested at low

temperatures exhibited an increase in its shear strength; the amount of this increase was larger in the brittle shear units than in the ductile shear units. It was shown in Chapter VI that the assessment shear model was generally underpredicting the contribution of the concrete shear mechanism, presumably because the concrete tensile and fracture properties are not taken directly into account by the method but through the compressive strength; however, past research (see literary review in Chapter I) has show tensile strength and fracture properties to improve at low temperatures at a proportion even larger than it does for the compressive strength. It is important to notice that although it has been shown that flexural strength increases at low temperatures, thus resulting in an increased shear demand, the shear capacity increases at an even higher proportion, thus delaying the onset of shear failure at low temperatures.

Table 7.3 Shear dominated reinforced concrete columns

UNIT	TEMP.	LONG. STEEL/ RATIO	TRANSVERSE STEEL/RATIO	AXIAL LOAD/ RATIO
DSH 87A	22˚C 72˚F	8#7 2.2%	#3@102mm (4in) 0.8%	142 kN 32 kips (3.7%)
DSH 87C	-36˚C -32˚F	8#7 2.2%	#3@102mm (4in) 0.8%	130 kN 29 kips (2.5%)
BSH 89A	22˚C 72˚F	8#9 3.8%	#3@145mm (5.7in) 0.6%	135 kN 30 kips (3.5%)
BSH 89C	-36˚C -32˚F	8#9 3.8%	#3@145mm (5.7in) 0.6%	135 kN 30 kips (2.6%)

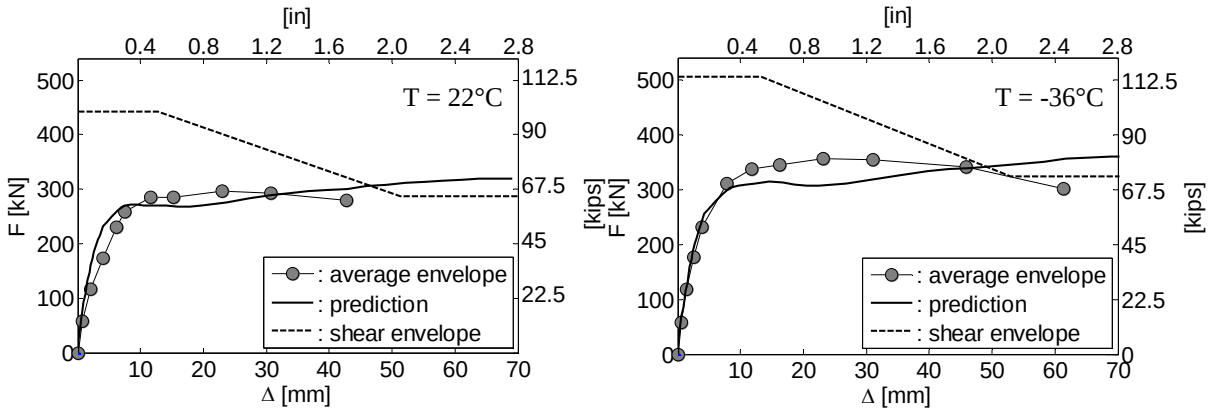

(a) DSH-87A **(b)** DSH-87C

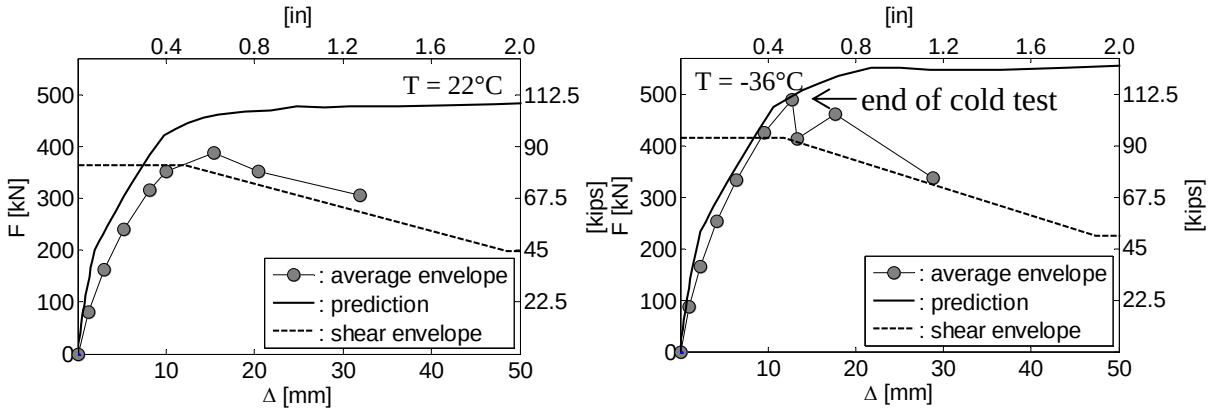

(c) BSH-89A **(d)** BSH-89C

Figure 7.5 Average first cycle envelopes, theoretical force-displacement envelopes and theoretical shear strength envelopes for the shear dominated units.

7.3 Finite element modeling of RC structures

Finite element modeling strategies for non-linear material response in beam-columns members can be classified in two main categories: lumped and distributed plasticity. In the lumped plasticity model the inelastic deformations are concentrated into rotational springs at the ends of a linear elastic element. This approach provides an efficient way of modeling and controlling plastic hinge formation. The drawback to concentrated plasticity models is that axial force-moment interaction and axial-force stiffness interaction are separate from the element behavior. Distributed plasticity models

provide a more general framework for non-linear frame analysis which allow plastic hinges to form at any location and account for axial force-moment interaction by integrating the force-deformation response at sections along the element length (Scott and Fenves, 2006). In distributed plasticity models the behavior at a section level is described by a fiber model. In the case of modeling the inelastic response of reinforced concrete members subjected to cyclic lateral loads, enhanced fiber beam-column elements have been developed over the last several years (Spacone et al. 1996a, b). Figure 7.6 exposes the differences abovementioned between lumped and distributed plasticity models.

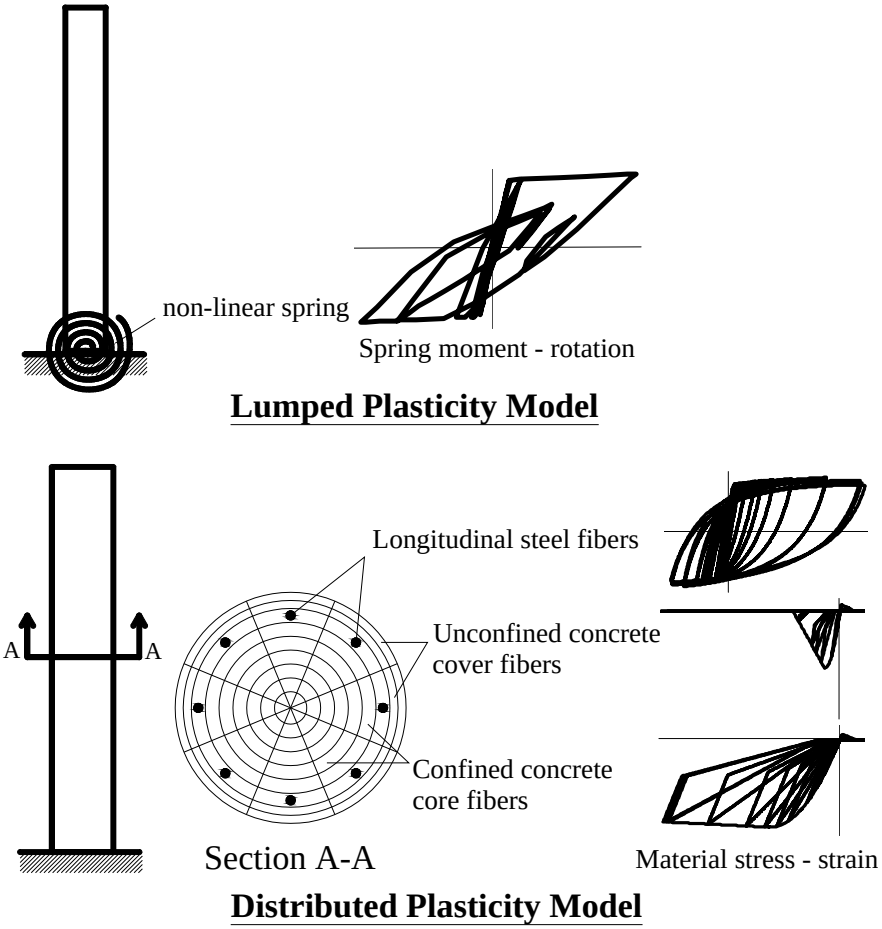

Figure 7.6 Average first cycle envelopes

Distributed plasticity beam column elements can be defined following a displacement or force based approach. Displacement-based elements followed the standard finite element approach, where the displacement fields along the element are

expressed as functions of the nodal displacements. As the assumed displacement field is approximate several elements per member are required to obtain a good approximation, especially in zones with high curvature gradients such as the potential plastic hinge zones in reinforced concrete members. In the force-based formulation the internal force fields are expressed as functions of the nodal force. It has been shown that force-based elements are exact within the framework of classical beam theory (Spacone et al. 1996a, b). Because of its precision, the main advantage of using force-based elements over displacement-based elements is then the ability to use one force-based element per structural member to simulate the non-linear behavior of a frame structure.

7.3.1 Fiber-based lumped plasticity model

It has been shown that both, force-based and displacement-based approaches cause localization of the response when the structural members exhibit elastic-plastic or strain-softening type behaviors, which is usually the case in RC members (Bazant and Planas 1998; Coleman and Spacone 2001). In the displacement-based approach inelastic curvatures are concentrated over a single displacement based element, in the case of force-based element the inelastic curvatures are localized at a single integration point. Figure 7.7 presents the response of a cantilever RC column to an increasing lateral displacement at the top, the column was modeled using force-based elements (a, b) and displacement-based elements (c, d). Shown in Figure 7.7 are the base shear and the base curvature response as a function of the lateral displacement. With force-based elements the column is modeled with a single element and increasing number of integration points (3, 5 and 8 IP), in the case of displacement-based elements the column is modeled using an increasing number of elements (3, 5 and 20 E). From Figure 7.7 it is seen that the force-displacement responses obtained in all the cases are in relatively close agreement in the elastic range and up to intermediate levels of ductility demand. However, at larger levels of ductility, an undesirable trend becomes apparent, as the number of integration points (in the case of force-based elements) or the number of elements (in the case of displacement-based elements) increases, the strength degradation of the column starts earlier. This can be explained by looking at the base curvature behavior in Figures 7.7 b and d. As the number of integration points or the number of elements increases, the

length of the first integration point or element (where the inelastic behavior is localized) decreases and larger curvatures are required to achieve a given target displacement. Larger strains are then imposed in the material fibers accelerating the material softening or failure.

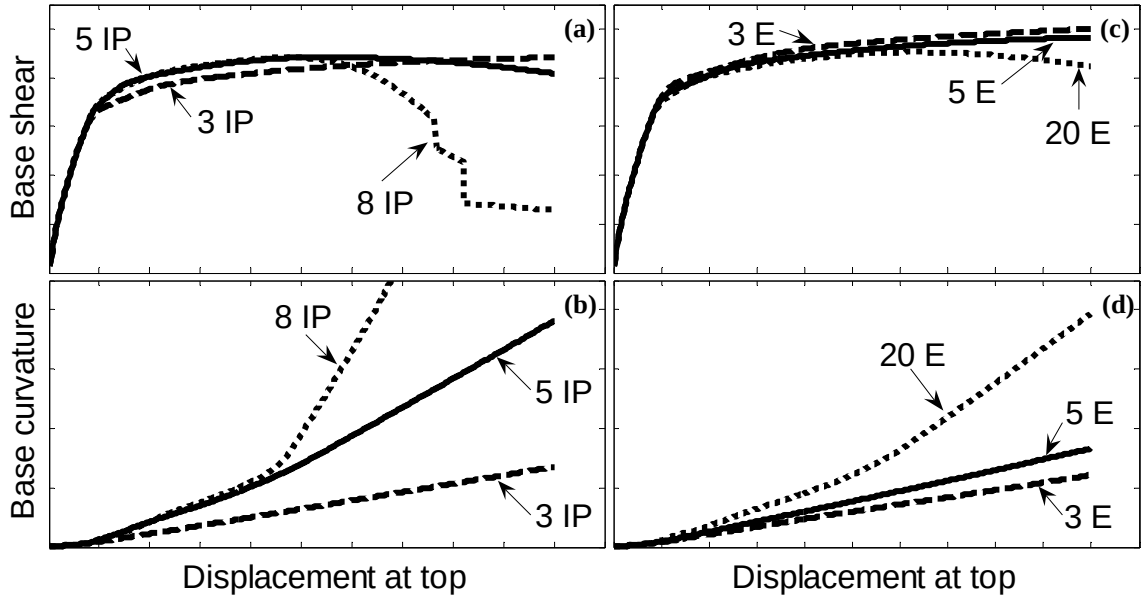

Figure 7.7 Strain localization problems in distributed plasticity models, force based elements with 3, 5 and 8 integration points (a, b) and displacement base elements with 3, 5 and 20 elements (c, d).

To address localization in force-based elements, Coleman and Spacone (2001) developed a constant fracture energy localization technique to maintain objective response for strain-softening behavior as the number of integration points changes. This regularization method, however, requires a modification of the stress-strain properties of the constitutive materials based on the number of integration points. Scott and Fenves (2006) developed a new element integration method that confines nonlinear constitutive behavior to plastic hinge regions of a specified length while maintaining numerical accuracy and objectivity. The section response between hinges is assumed linear elastic. The formulation utilizes the force-based fiber beam column element formulation and is available in the OpenSees software framework system (McKenna et al. 2000) as the *BeamWithHinges* element. As shown in Figure 7.8, the required inputs for this element are the material fiber properties and the plastic hinge length (L_p) for the distributed

plasticity part of the element, and the modulus of elasticity (*E*), inertia (*I*) and cross section area (*A*) for the elastic part.

In this research the force-based-fiber lumped plasticity model developed by Scott and Fenves (2006) is used for the non-linear bridge bents simulations. The model is first evaluated and calibrated using the experimental data presented in the previous chapters so that it is capable to accurate predict the response of ORC and RCFST columns exposed to cyclic lateral loads and low temperatures.

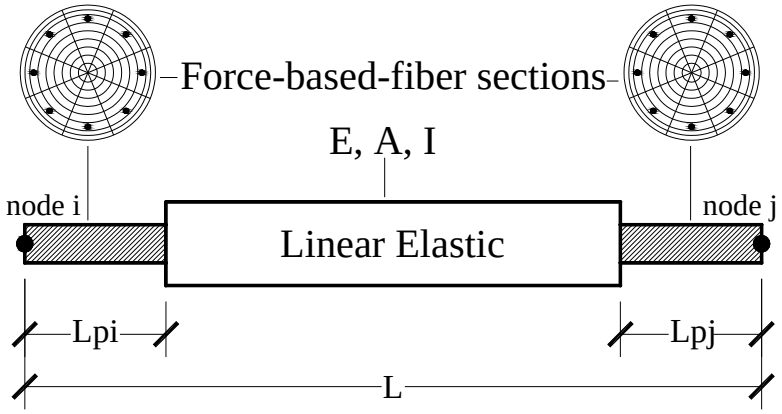

Figure 7.8 Force-based-fiber lumped plasticity element (Scott and Fenves, 2006)

7.4 Material Constitutive Relationships

When a fiber approach is used, separate material rules need to be specified for the reinforcing steel bars, unconfined concrete and confined concrete; material stress is assumed constant between integration points along the fiber segment. No prior moment-curvature analysis is required because the hysteretic response of the section is defined by the material properties, and hence does not need to be specified. Material models used in this research are described next; all models used are available in OpenSees.

7.4.1 Confined and unconfined concrete

Confined and unconfined concrete are modeled with the OpenSees *Concrete02* material. The input data required for this model: maximum compressive strength, strain at maximum strength, crushing strength and strain at crushing, were calculated as proposed by Mander at al. (1988) and previously described in Chapter II. Figures 7.9 and 7.10 shows the hysteretic stress-strain relationship for *Concrete02* and compares it with the monotonic Mander envelope.

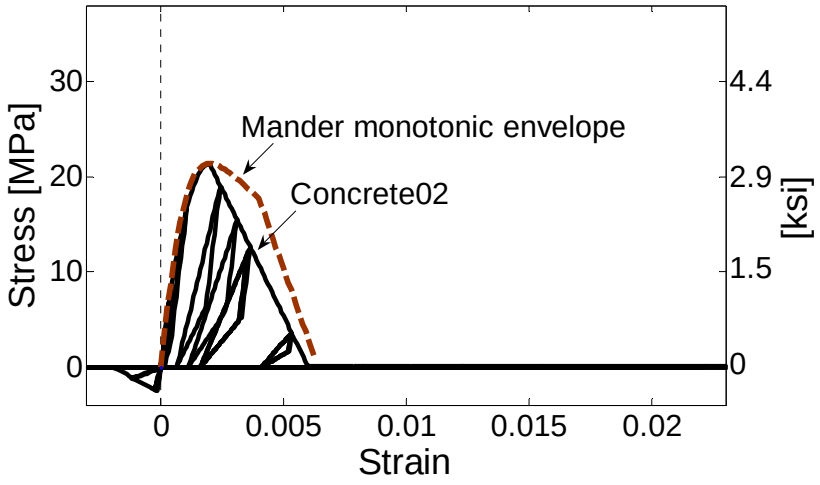

Figure 7.9 Hysteretic model for the unconfined concrete.

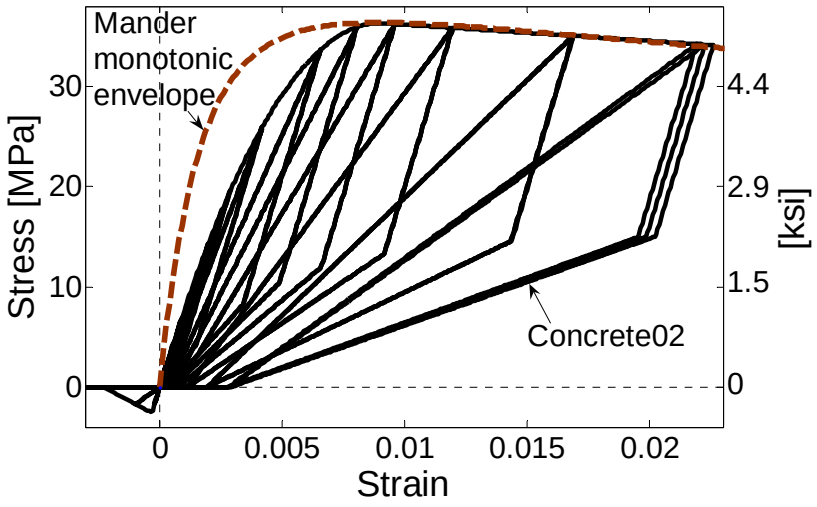

Figure 7.10 Hysteretic model for the confined concrete.

7.4.2 Reinforcing steel bars

Reinforcing steel bars are modeled using the *ReinforcingSteel* material (Mohle and Kunnath, 2006) which was specially intended to be used in a reinforced concrete fiber section as the steel reinforcing material. The Mohle and Kunnath (2006) steel constitutive model is based on the steel model proposed by Chang and Mander (1994). The model can be used to account for: isotropic hardening, diminishing yield plateau and degrading strength and stiffness due to cyclic reversals. Minimum input data required for this model are the yield and maximum stress, strain at maximum stress and the strain and tangent at the on-set of hardening. Figure 7.11 shows the general hysteretic behavior of the *ReinforcingSteel* material along with the monotonic envelope by Raynor (2002).

The degradation of strength and stiffness due to cycling is calculated according to the Coffin and Manson fatigue model through the factors α, C_f and C_d. The damage strain range constant, α, is used to relate damage from one strain range to an equivalent damage at another strain range and is constant for a material type. The ductility constant, C_f, is used to adjust the number of cycles to failure. A higher value of C_f translates to a larger number of cycles to failure. The strength reduction constant, C_d, controls the amount of degradation per cycle. A larger value for C_d will result in a lower reduction of strength for each cycle. Suggested values by Mohle and Kunnath (2006) for bars with a slenderness (ratio between the bar unsupported length and the bar diameter) of 6 are $\alpha = 0.506$, $C_f = 0.26$, $C_d = 0.38$. Berry (2006) calibrated the model constants using the experimental results from 20 specimens of the bridge-column database (Berry et al. 2004) in which bar fracture were reported, values recommended by Berry are $\alpha = 0.506$, $C_f = 0.26$, $C_d = 0.45$. In general these values are expected to change with the steel type, bar diameter and the confinement provided to the section. The calibration of the Coffin-Manson factors with the experimental data obtained in this research is presented in section 7.5.

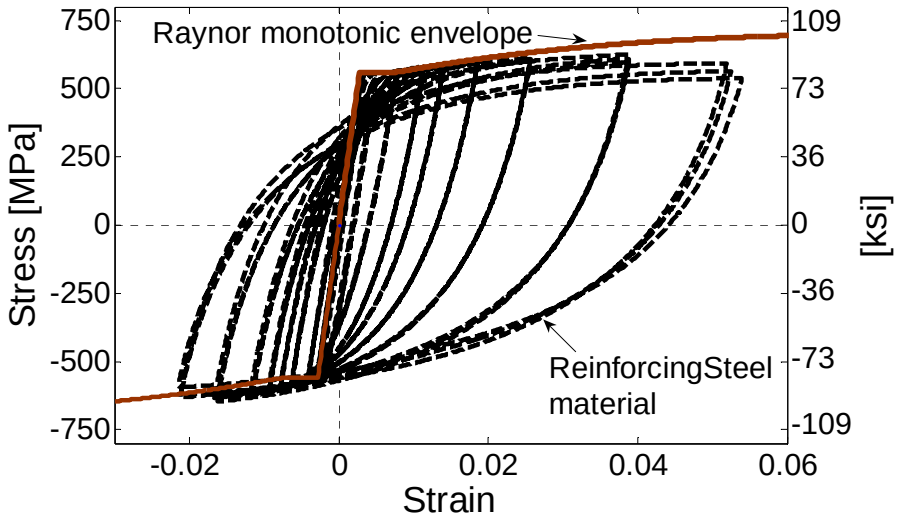

Figure 7.11 Hysteretic model for the reinforcing steel.

7.4.3 Steel tube in RCFST columns

As mentioned earlier in Chapter V, the RCFST columns tested in this research were designed to emulate typical bent columns of Alaska DOT bridges. As shown in Figure 7.12 (Figure 5.1 in Chapter V), the tests simulate the part of the column from the cap beam to the inflection point where the steel tube is providing only confining and shear strength to the column. The behavior of in-ground hinges, where the steel tube is providing flexural strength to the column, was not experimentally investigated in this project (ongoing research at NCSU is dealing with this topic). As there is not sufficient experimental data available to calibrate a material model that includes strength degradation, the steel tube is modeled using the same *ReinforcingSteel* material used to model the reinforcing bars but without including the strength degradation part.

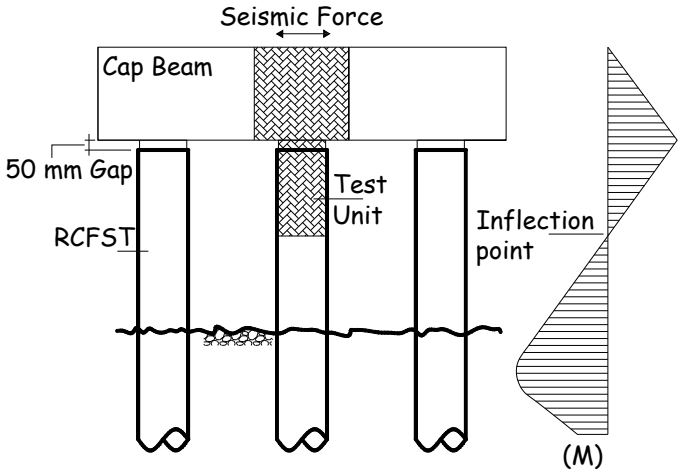

Figure 7.12 Prototype structure and its representative test model.

7.5 Calibration of the fiber based lumped plasticity model

The experimental results from the testing of the 8 flexural dominated units described in section 7.2 are used to calibrate the parameters of the fiber based plasticity model, more precisely the strength degradation parameters for the reinforcing steel. Concrete and steel material properties (strains and strengths) used for the non-linear cyclic simulation are the same used to generate the theoretical monotonic envelopes in Chapters IV to VI. Plastic hinge lengths used for the distributed plasticity part of the *BeamWithHinges* (Figure 7.8) element are those calculated from the experimental results and used to develop Equations 7.1 and 7.2. The elastic part of the element is modeled with the effective section inertia (EI_{eff}) which is calculated from the moment-curvature response of the section as the slope of the line from the origin to the point of first yield of the longitudinal steel. Table 7.4 summarizes the material properties and plastic hinge length used for the simulations.

Optimal values obtained for the factors α, C_f and C_d are displayed in Table 7.5. Notice from this table that in the case of the ORC columns (SL-P20, SL-M40, FL 89A and FL 89C), the values of α, C_f and C_d were kept constant for each pair of identical specimens. That is, for the ORC columns the effect of low temperatures was captured by just incorporating the increase in the strength of the constitutive materials and the reduction in the plastic hinge length. However, in the case of the RCFST columns where

no reduction in the plastic hinge length at low temperatures was incorporated, the values of α, C_f and C_d were needed to be change within identical columns to capture the brittle behavior of the cold specimens. In general the factor's values vary with the steel type, bar diameter and column transverse detailing. To limit the number of variables, the steel degradation factors are kept constant for all the simulations. The values used are those proposed by Berry (2006) $\alpha = 0.506$, $C_f = 0.260$ and $C_d = 0.45$.

The results obtained from the simulations are presented in Figures 7.13 to 7.20. For each unit the force-displacement hysteretic response, the average force-displacement first cycle envelope, the area-based hysteretic damping and the base curvature response were calculated and compared with the experimental results. It is noticed that both the global response (force-displacement) and the local response (base curvatures) obtained from the finite element model, are in close agreement with the experimental results. Regarding the dissipative properties, which were analyzed via area-based hysteretic damping, it is seen that they are generally overpredicted by the finite element model. The predicted hysteretic loops are fatter than the actual loops mainly because the model used does not capture the pinching due to bar slipping at the base. In flexural concrete members, strain penetration occurs along longitudinal reinforcing bars that are fully anchored into connecting concrete members, causing bar slips along a partial anchoring length and thus end rotations to the flexural members at the connection intersections. Ignoring the strain penetration in linear and nonlinear analyses of concrete structures may underestimate the member deflections and overestimate the stiffness, hysteretic energy dissipation capacities and section curvature (Zhao and Sritharan, 2007). Although a hysteretic model has been proposed to account for the strain penetration effect (Zhao and Sritharan, 2007), the implementation of this model in OpenSees still presents serious numerical instabilities and for such reason was not used in the simulations. The strain penetration effects on deflections, stiffness and curvature were accounted for by including the strain penetration length in the plastic hinge length used.

Table 7.4. Material properties and plastic hinge lengths used for the simulations

UNIT	TEMP.	CONCRETE COMPRESSIVE STRENGTH (f'_c)	LONG. BAR YIELDING STRESS (f_y)	LONG. BAR ULTIMATE STRENGTH (f_u)	PLASTIC HINGE LENGHT (L_p)
SL-P20	23˚C 74˚F	39.2 MPa 5.7 ksi	503 MPa 73 ksi	689 MPa 100 ksi	351 mm 13.8 in
SL-M40	-40˚C -40˚F	64.8 MPa 9.4 ksi	565 MPa 82 ksi	772 MPa 112 ksi	226 mm 8.9 in
FL 89A	+22˚C +72˚F	21.4 MPa 3.1 ksi	558 MPa 81 ksi	703 MPa 102 ksi	411 mm 16.2 in
FL 89C	-36˚C -33˚F	27.6 MPa 4 ksi	627 MPa 91 ksi	778 MPa 113 ksi	264 mm 10.4 in
RCFST 89A	22˚C 72˚F	26.2 MPa 3.8 ksi	558 MPa 81 ksi	703 MPa 102 ksi	226 mm 8.9 in
RCFST 89C	-36˚C -33˚F	44 MPa 6.4 ksi	627 MPa 91 ksi	778 MPa 113 ksi	226 mm 8.9 in
RCFST 87A	22˚C 72˚F	26.2 MPa 3.8 ksi	442MPa 64ksi	675MPa 98ksi	190 mm 7.5 in
RCFST 87C	-36˚C -33˚F	44 MPa 6.4 ksi	490 Mpa 71 ksi	741 MPa 108 ksi	190 mm 7.5 in

Table 7.5. Coffin-Manson fatigue model factors obtained from calibration of the experimental results

Bar type	#9 fy = 558 MPa ASTM A615				#7 fy = 442 MPa ASTM A615		#5 fy = 503 MPa ASTM A706	
Unit	*FL 89A*	*FL 89C*	*RCFST 89A*	*RCFST 89C*	*RCFST 87A*	*RCFST 87C*	*SL P20*	*SL M40*
C_f	0.34	0.34	0.37	0.3	0.37	0.3	0.22	0.22
α	0.51	0.51	0.51	0.51	0.48	0.48	0.48	0.48
C_d	0.45	0.45	0.45	0.36	0.45	0.36	0.30	0.30

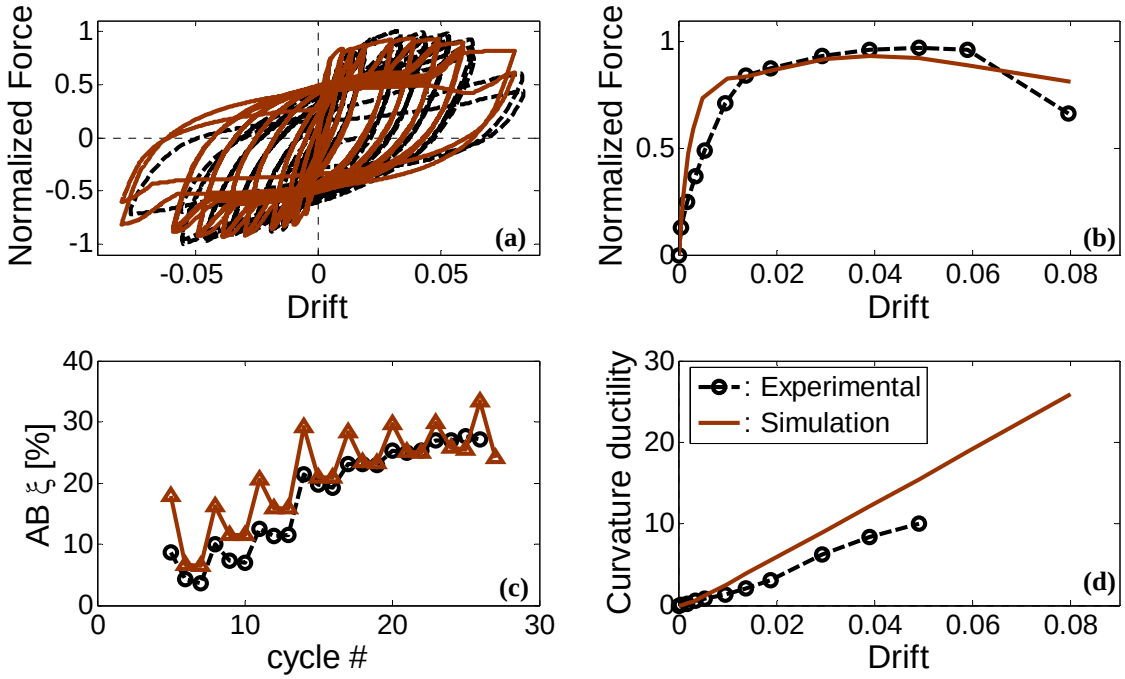

Figure 7.13 Experimental vs. simulated: (a) hysteretic response, (b) average first cycle envelope, (c) area based hysteretic damping and (d) base curvature ductility for SL-P20.

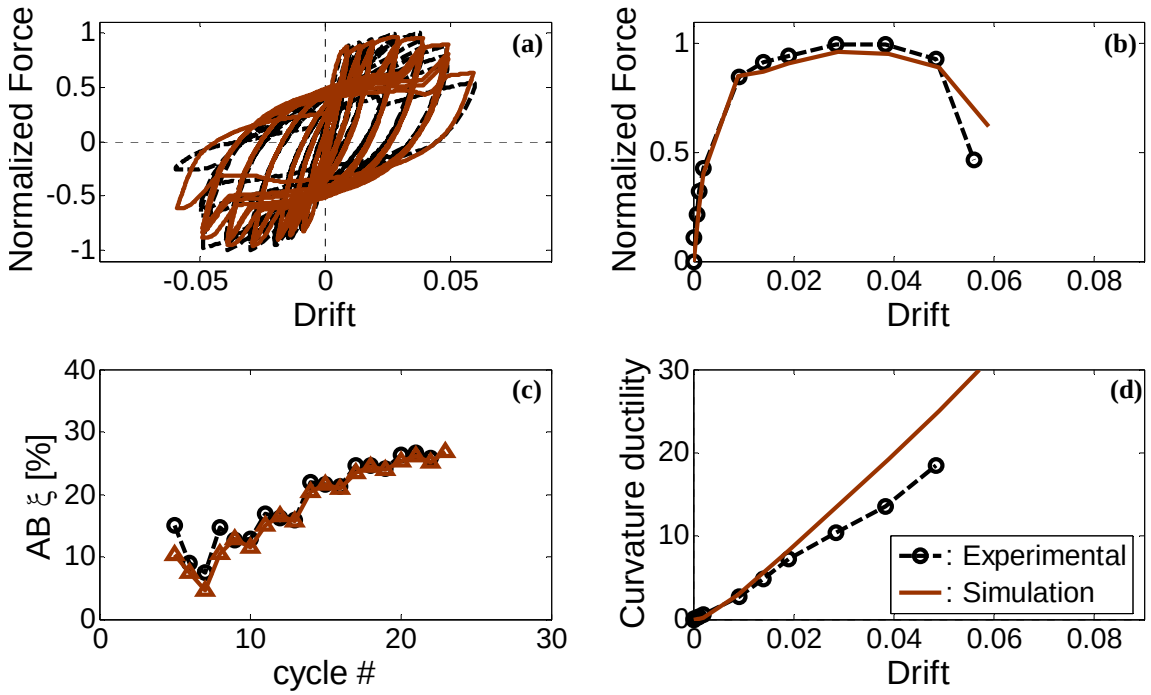

Figure 7.14 Experimental vs. simulated: (a) hysteretic response, (b) average first cycle envelope, (c) area based hysteretic damping and (d) base curvature ductility for SL-M40.

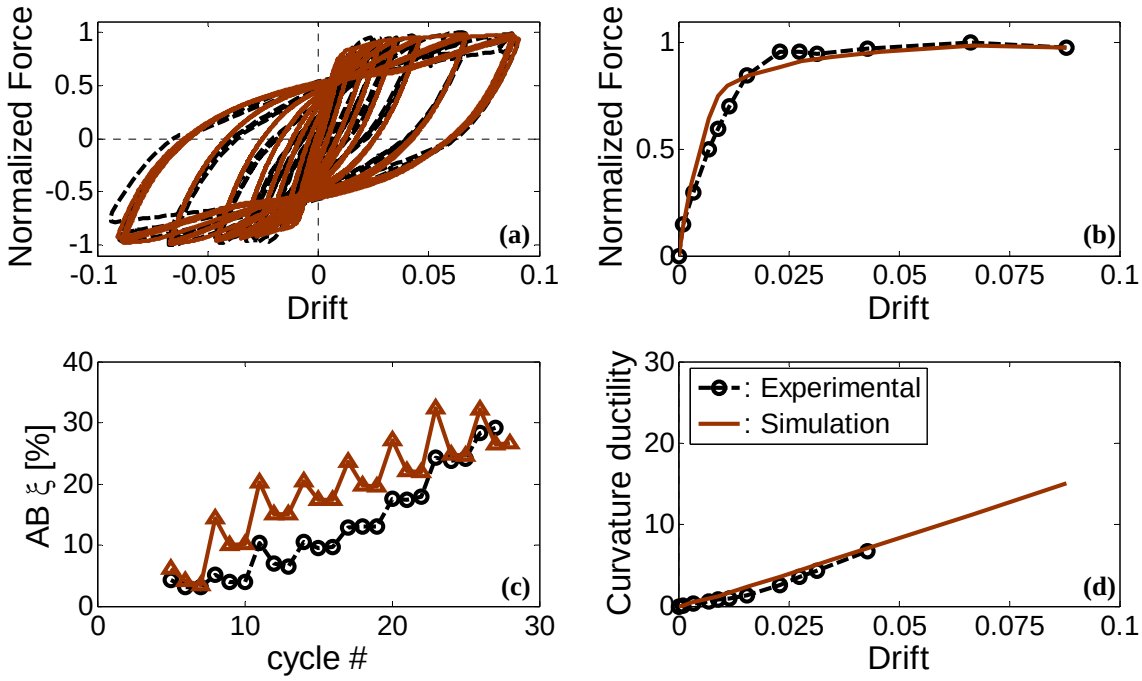

Figure 7.15 Experimental vs. simulated: (a) hysteretic response, (b) average first cycle envelope, (c) area based hysteretic damping and (d) base curvature ductility for FL 89A.

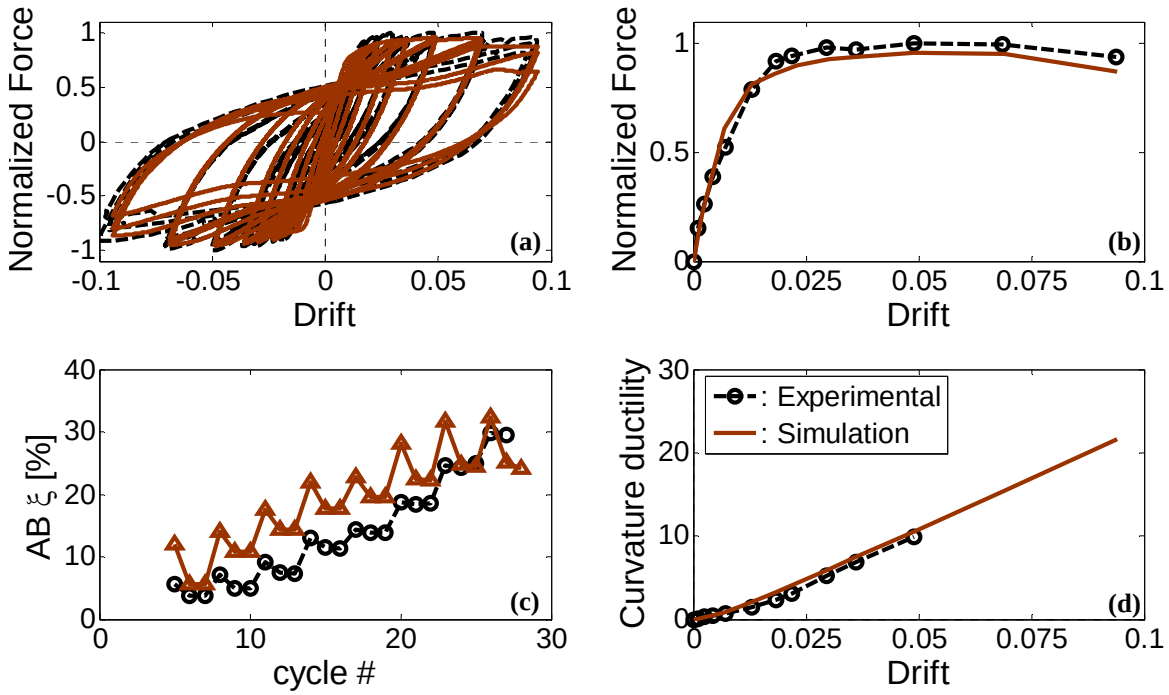

Figure 7.16 Experimental vs. simulated: (a) hysteretic response, (b) average first cycle envelope, (c) area based hysteretic damping and (d) base curvature ductility for FL 89C.

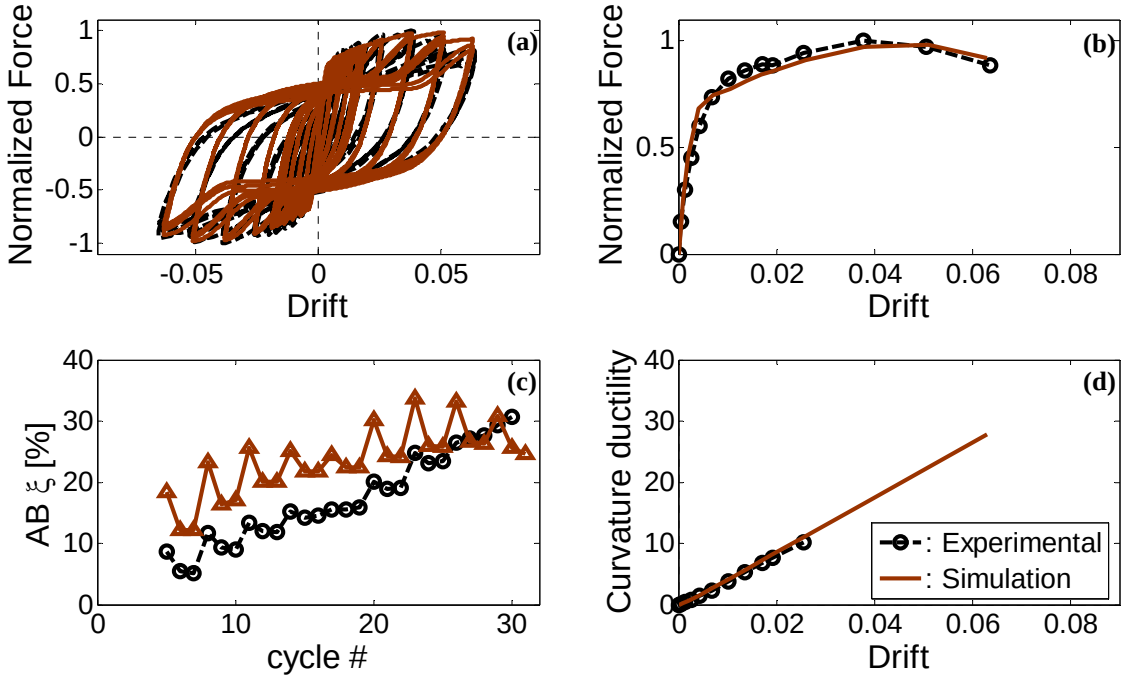

Figure 7.17 Experimental vs. simulated: (a) hysteretic response, (b) average first cycle envelope, (c) area based hysteretic damping and (d) base curvature ductility for RCFST 87A.

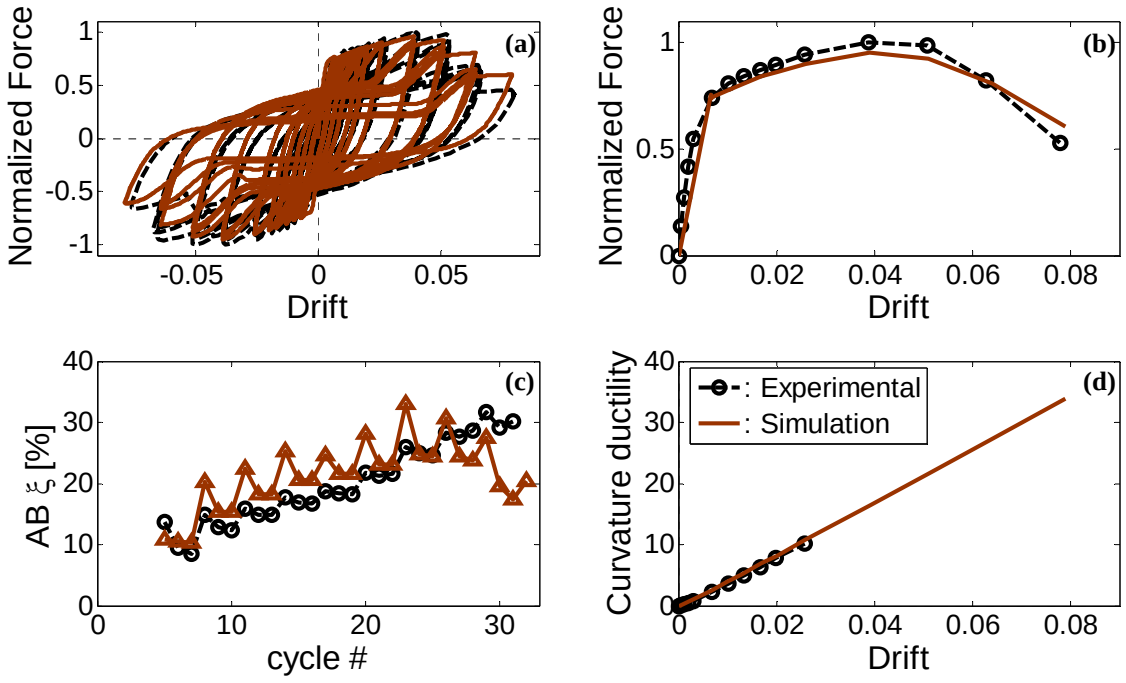

Figure 7.18 Experimental vs. simulated: (a) hysteretic response, (b) average first cycle envelope, (c) area based hysteretic damping and (d) base curvature ductility for RCFST 87C.

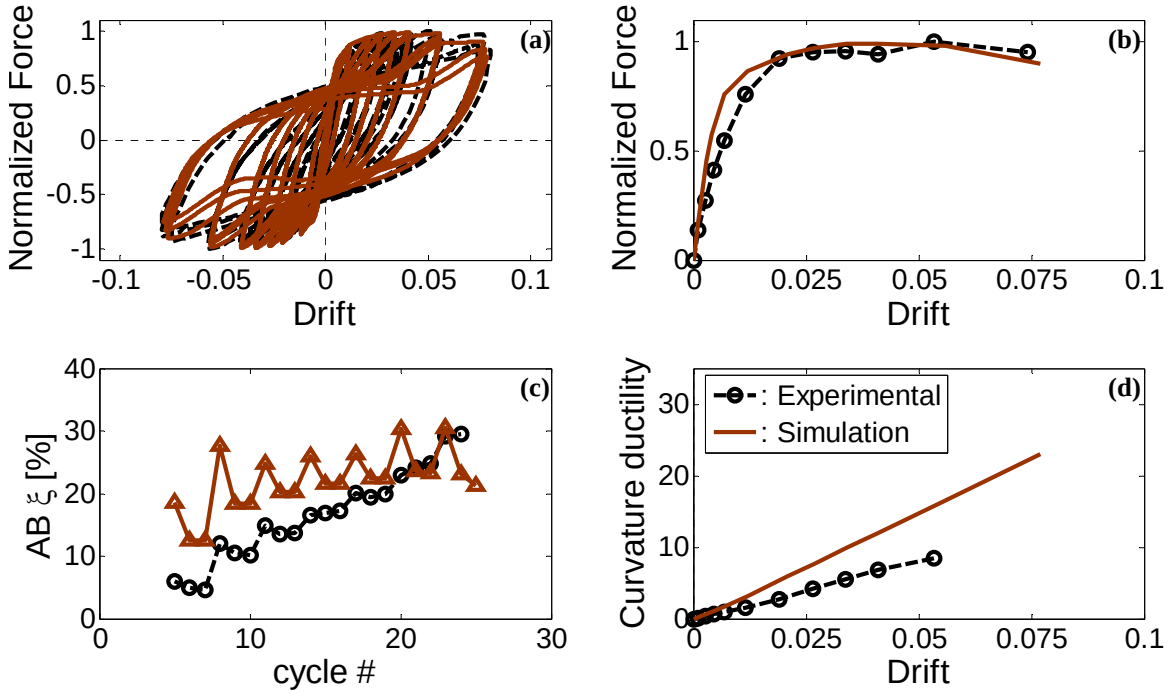

Figure 7.19 Experimental vs. simulated: (a) hysteretic response, (b) average first cycle envelope, (c) area based hysteretic damping and (d) base curvature ductility for RCFST 89A.

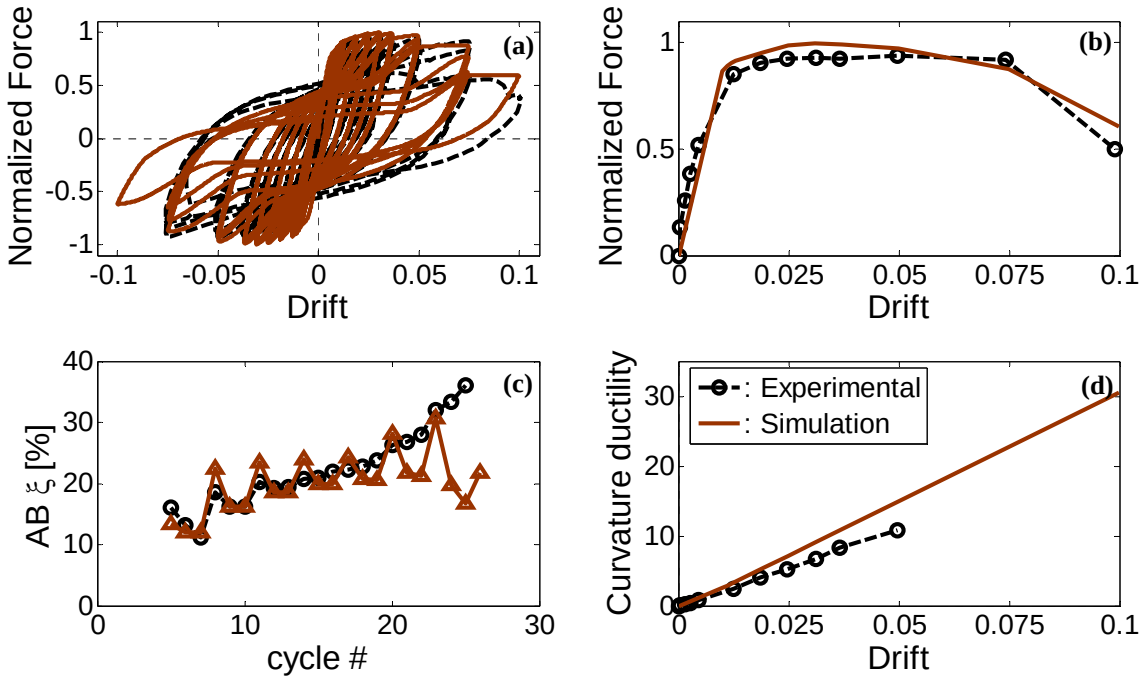

Figure 7.20 Experimental vs. simulated: (a) hysteretic response, (b) average first cycle envelope, (c) area based hysteretic damping and (d) base curvature ductility for RCFST 89C.

7.6 Equivalent plastic hinge lengths for RCFST columns

As mentioned in section 7.3.1 (Figure 7.8), the *beamWithHinges* element (Scott and Fenves, 2006) selected to model the bridge bent columns required the definition of an equivalent plastic hinge length (L_p) over which the inelastic deformations are concentrated. In the case of ordinary reinforced concrete columns (ORC), the value of L_p for warm or sub-freezing conditions can be obtained from Equation 7.1. When reinforced concrete filled steel tube columns (RCFST) are used, Equation 7.2 was obtained from experimental results of this research to define L_p in the top hinge (Figure 7.12), where a gap is left between the steel tube and the adjacent member. However, to the authors knowledge there is no expression available to define L_p when the steel tube is providing flexural strength to the column. This situation can occur in two different scenarios: (1) in-ground hinges of RCFST columns used as pile/columns (Figure 7.12) and (2) when the steel tube is specially connected to the adjacent member so it can develop its flexural capacity.

7.6.1 Equivalent plastic hinge length and depth to fixity of RCFST pile/columns

Reinforced concrete pile or drilled shaft bents are a type of bridge substructure in which the piles or columns are extended from the superstructure continuously below grade (Figure 7.12). Under lateral seismic loading, the location of the maximum moment and formation of the in-ground plastic hinge depend on the relative lateral stiffness of the pile to the soil and are expected at depth ranging from 1.5 to 4.5 times the diameter of the pile/column (Priestley et al. 1996, Chai 2002). The common seismic design practice is to simplify the soil-structure interaction problem by considering the piles or shafts within each bent to be fixed at an estimated depth below the ground surface. This simplification is made in an attempt to account for the flexibility that the soil adds to the bent while avoiding difficult soil modeling issues. Several procedures have been proposed for the estimation of an equivalent length to fixity, plastic hinge length, yield displacement and equivalent viscous damping (Davison and Robinson 1965, Chen 1997, Budek et al. 2000, Chai 2002, Suarez and Kowalsky 2007). However, all of these studies are based on experimental results or computer simulations of ordinary reinforced concrete columns/piles and no expressions or procedures to define the properties of the equivalent cantilever model are available in the case of RCFST columns/piles. To overcome this limitation an expression to define the diameter (D_{eq}) of an equivalent ORC column capable of replicate the behavior of a given RCFST column is developed in this research. Once the equivalent diameter is obtained any of the existing procedures can be used to determine the length to fixity, plastic hinge length, yield displacement and equivalent viscous damping.

As shown in Table 7.6, six different pile configurations were analyzed. Differences between each configuration included section diameter, height - diameter ratio (H/D), diameter - steel pipe thickness ratio (D/t), axial load ratio (ALR) and longitudinal reinforcement ratio (ρ). Non-linear pushover analyses were performed using OpenSees (McKenna et al. 2000), the columns were modeled using fiber-based distributed plasticity elements and the non-linear response of the soil was modeled using lateral springs with

appropriate p-y curves. Two different types of soils were used in the analyses: (1) Sand, with a unit weight of. 16.7 kN/m^3 and a friction angle of 30 degrees, and (2) Clay, with a unit weight of 17 kN/m^3 and undrained shear strength of 40 kPa. An iterative procedure was implemented to obtain the equivalent diameter: First, the responses (lateral deflections and moments profiles) of a RCFST pile/column and an ORC pile/column with the same section diameter and reinforcing steel are normalized to the maximum absolute value and compared. The diameter of the ORC pile/column is then increased (while keeping the soil springs stiffness constant) until an acceptable match with the normalized response of RCFST pile/column is reached. Comparisons of the responses is done at the same level of ductility demand ($\mu=1$), determined by the stage of lateral displacement at which the maximum curvature in the column reaches the section yield curvature. It was found that the equivalent diameter (D_{eq}) is directly related to the ratio of the effective stiffness (EI_{eff}) of the RCFST column and the ORC column of equal diameter as shown in Equation 7.3. It is seen from Equation 7.3 that the effective stiffness of the ORC pile was needed to be increased by a factor of 1.4, in part, to account for additional confinement provided by the soil to the cover concrete. The values of effective stiffness are calculated from the moment-curvature response of the sections as the slope of the line from the origin to the point of first yield of the longitudinal steel, in ORC columns, or first yield of the steel tube, in RCFST columns. Figures 7.21 to 7.26 show the results obtained for each of the cases presented in Table 7.6. Note that in the RCFST pile/columns the maximum moment location is deeper and the curvature is flatter than the exhibited by the ORC pile/columns, thus ultimate displacement capacity will be larger for RCFST than for ORC pile/columns.

$$D_{eq} = \left(\frac{(EI)_{eff}\, RCFST}{1.4(EI)_{eff}\, ORC} \right)^{1/4} \tag{7.3}$$

Table 7.6. RCFST column/pile configurations for inelastic pushover analyses

Case #	Soil	Diameter	D/t	H/D	ALR	ρ
1	Sand	610 mm (24 in)	68	4.9	6.7 %	3.3 %
2	Clay	610 mm (24 in)	68	4.9	6.7 %	3.3 %
3	Sand	914 mm (36 in)	48	6.6	3.8 %	1.4 %
4	Clay	914 mm (36 in)	48	6.6	3.8 %	1.4 %
5	Sand	1067 mm (42 in)	48	2.8	3.1 %	2.7 %
6	Clay	1067 mm (42 in)	48	2.8	3.1 %	2.7 %

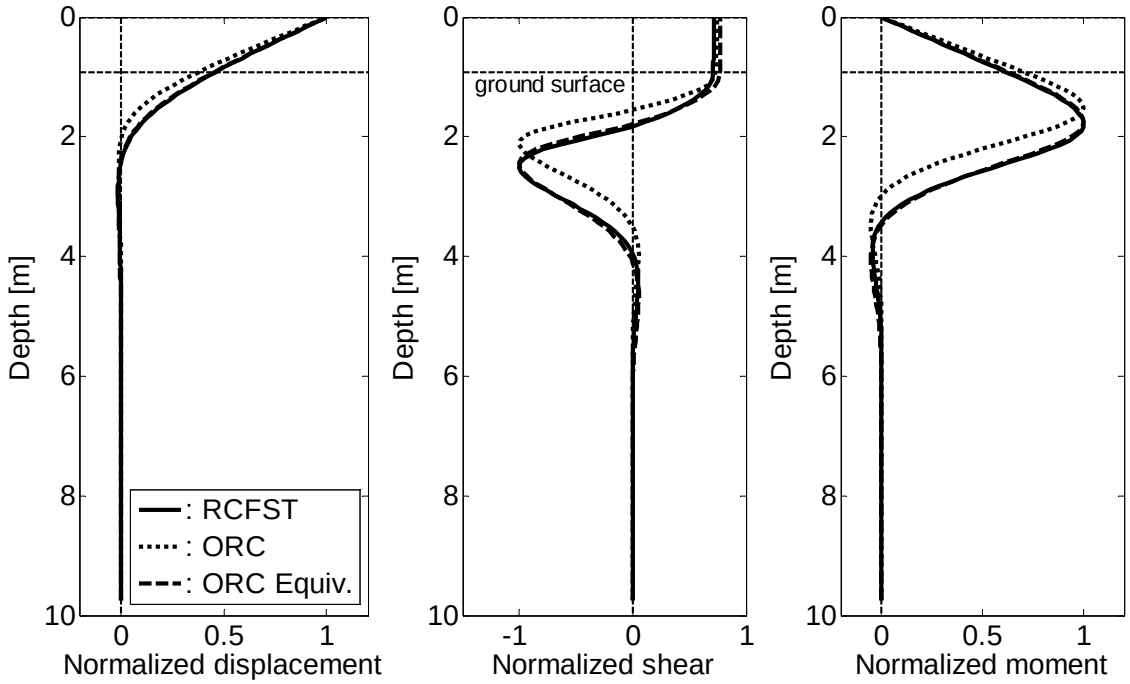

Figure 7.21 Normalized displacement, shear and bending moment diagrams for case 1 (Table 7.6)

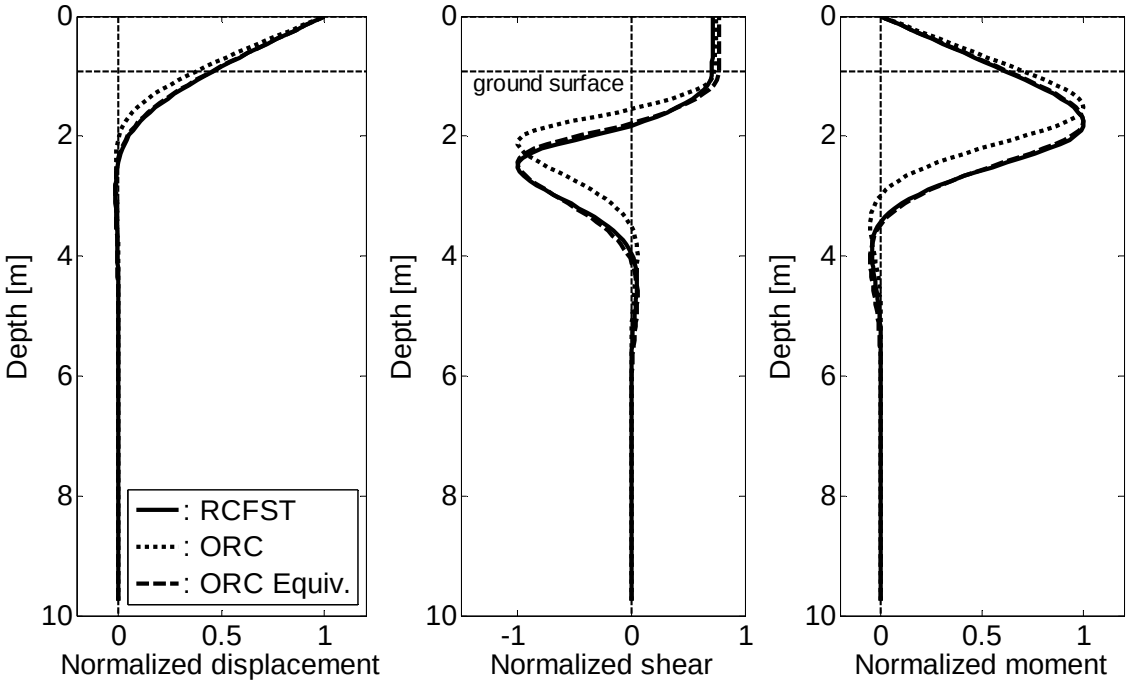

Figure 7.22 Normalized displacement, shear and bending moment diagrams for case 2 (Table 7.6)

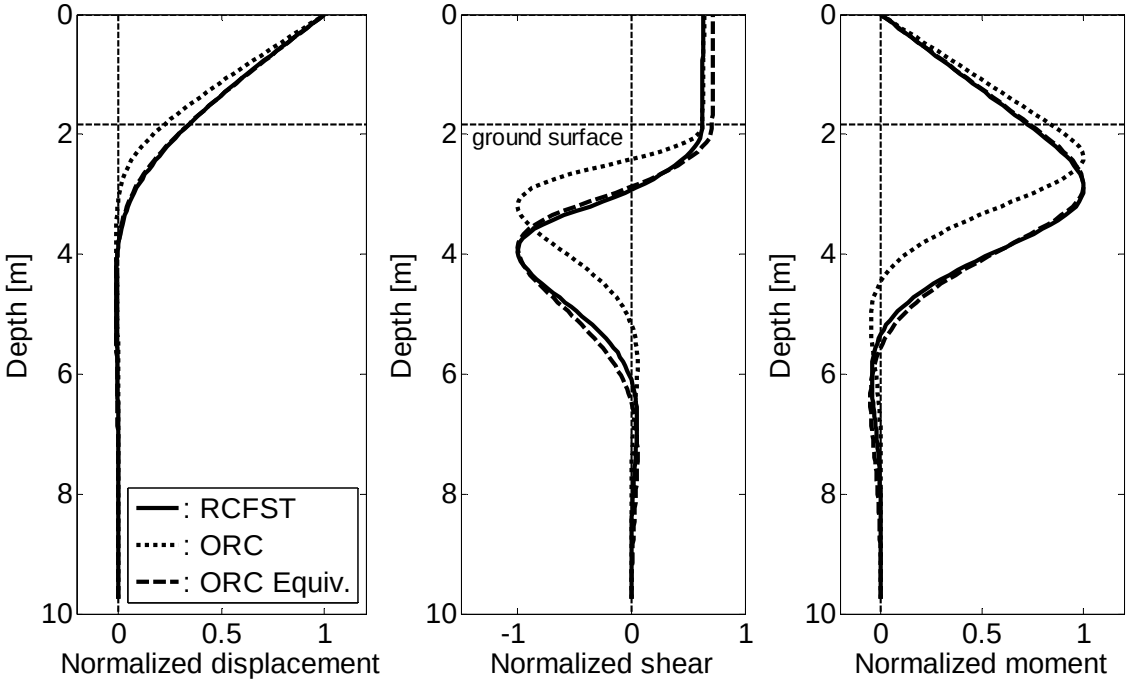

Figure 7.23 Normalized displacement, shear and bending moment diagrams for case 3 (Table 7.6)

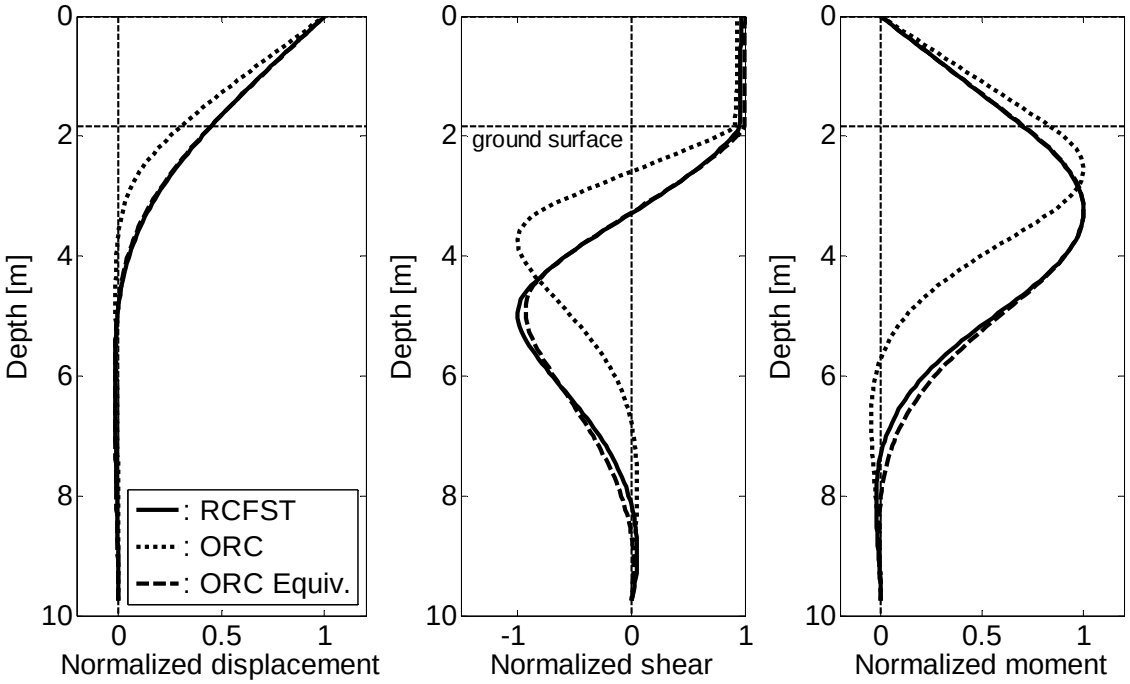

Figure 7.24 Normalized displacement, shear and bending moment diagrams for case 4 (Table 7.6)

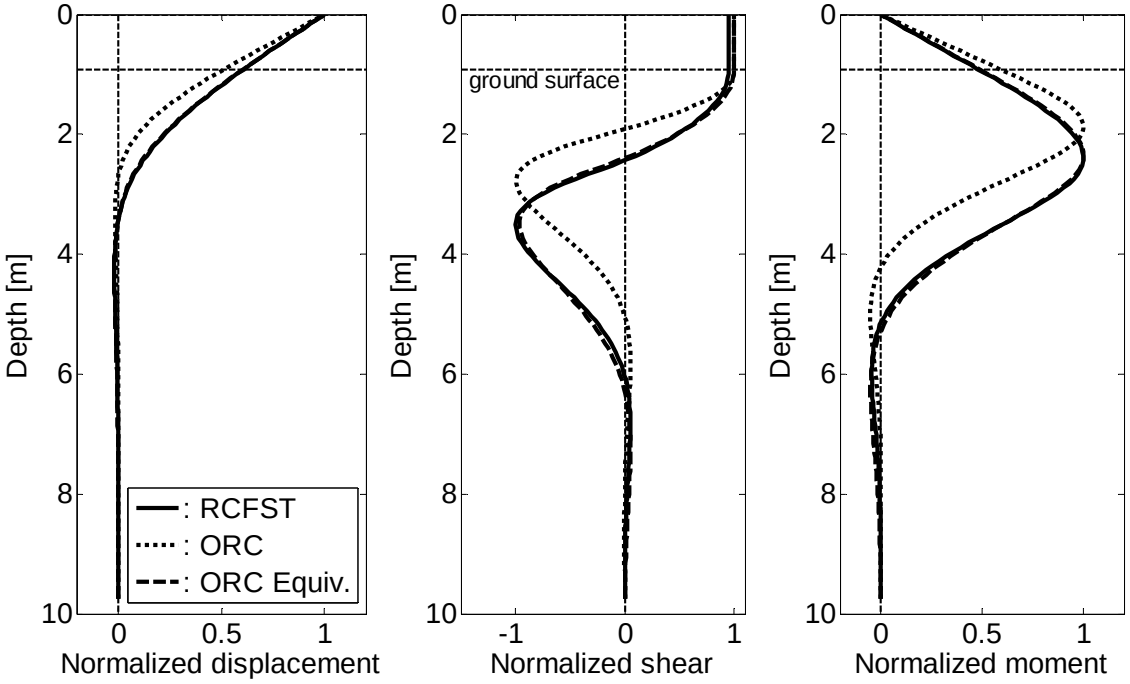

Figure 7.25 Normalized displacement, shear and bending moment diagrams for case 5 (Table 7.6)

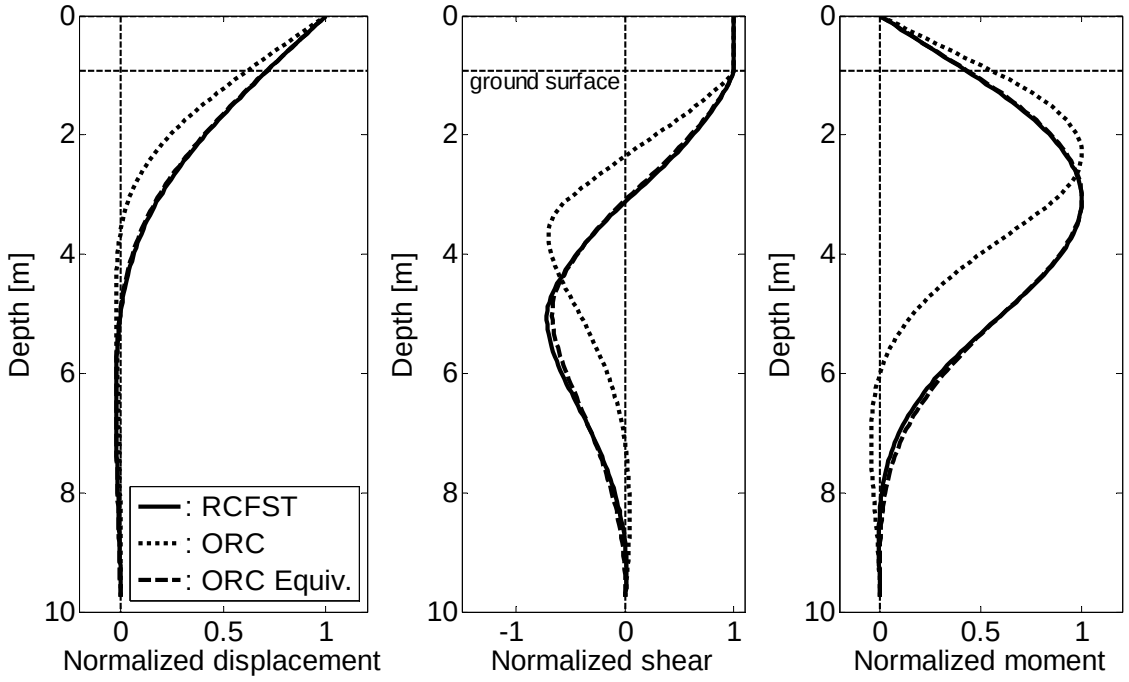

Figure 7.26 Normalized displacement, shear and bending moment diagrams for case 6 (Table 7.6)

7.6.2 Equivalent plastic hinge length of RCFST columns having fixed-based detail

When the pier is supported on a spread footing, the steel tube can be specially connected to the footing so it can develop its flexural capacity (Figure 7.27). Similar to the ORC columns (Equation 7.1), the equivalent plastic hinge length can be decomposed in two parts as shown in Equation 7.4. One is related to the strain penetration L_{sp} of the reinforcing bars into the footing and can be obtained using Equation 7.5 where f_{yb} is the yield stress of the longitudinal bars (Priestley et al. 2007). The other portion kL is function of the cantilever length of the column L and was found from a moment-curvature parametric study of different RCFST sections. Knowing the moment distribution along the column (Figure 7.27), the curvatures at all heights could then be read from the moment-curvature relationship of the section to produce the curvature distribution of the column, which is then integrated to provide the top displacement. The value of kL is obtained as the length over which the base curvature needs to be

concentrated (idealized curvature distribution in Figure 7.27) to obtain the previously calculated top displacement.

The variables analyzed in the parametric study were the amount and strain hardening ratio of the reinforcing bars $f_{ub}/f_{yb,}$ the ratio between column diameter and steel tube thickness D/t and the strain hardening ratio of the steel tube f_{ust}/f_{yst}. Figures 7.28 to 7.30 show the results obtained, it is seen that the strain hardening ratio of the steel tube dominates the equivalent plastic hinge length of the column. Equation 7.6 was obtained from the data presented in Figure 7.30.

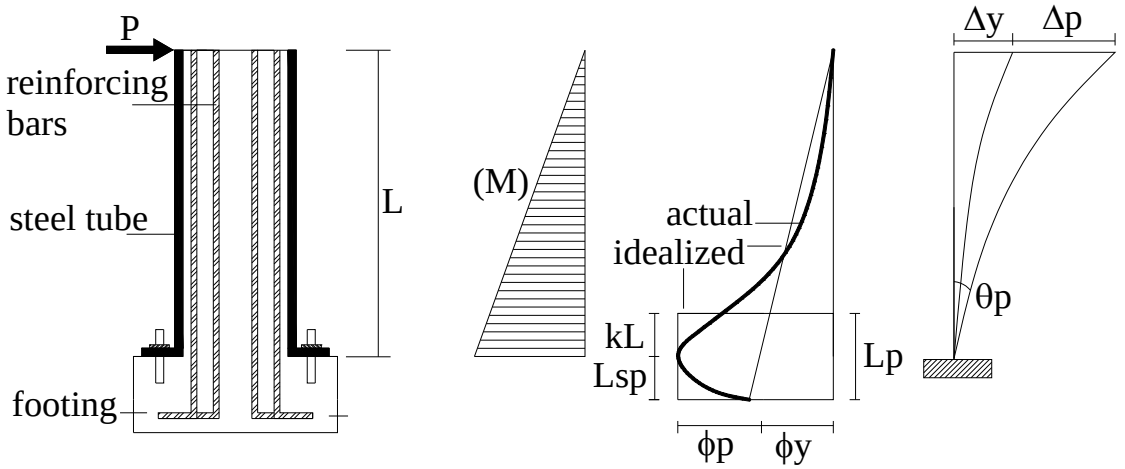

Figure 7.27 Equivalent plastic hinge length for RCFST columns having a fixed based detail

$$L_p = kL + L_{sp} \geq 2L_{sp} \tag{7.4}$$

$$L_{sp} = 0.022 f_{yb} d_{bl} \qquad (MPa) \tag{7.5}$$

$$k = 0.04\left(2.3\frac{f_{ust}}{f_{yst}} - 1\right) \qquad (MPa) \tag{7.6}$$

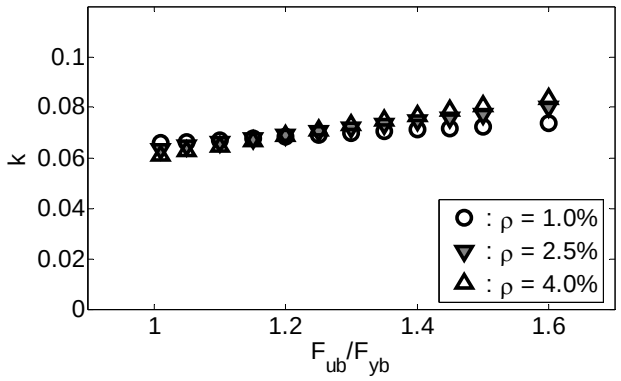

Figure 7.28 Effect of the amount and strain hardening ratio of the longitudinal reinforcement on the equivalent plastic hinge length of RCFST columns with steel tube fixed at the base

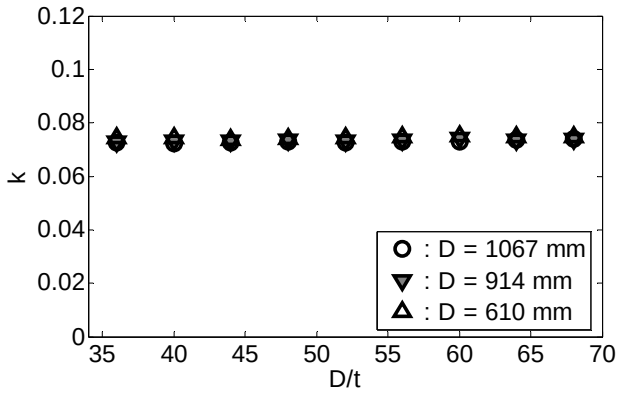

Figure 7.29 Effect of the column diameter – steel tube thickness ratio D/t on the equivalent plastic hinge length of RCFST columns with steel tube fixed at the base

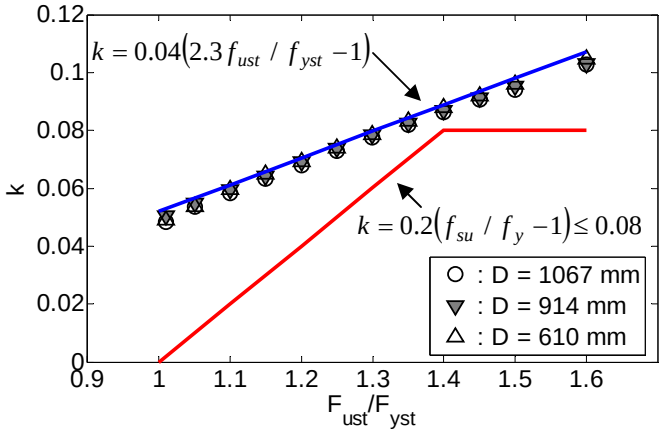

Figure 7.30 Effect of the strain hardening ratio of the steel tube on the equivalent plastic hinge length of RCFST columns with steel tube fixed at the base

7.7 Static and dynamic analyses generalities

The effect of sub-freezing temperatures on the seismic response of RC bridge bents will be analyzed by means of inelastic static pushover analyses and inelastic time-history analyses. Pushover analysis is used to track levels of strain and formation of plastic hinges to determine displacement limit states, which are initially given in terms of material strain. The limit strain definitions used in this research (Table 7.7) are those recommended by Kowalsky (2000) for ORC columns. In the case of RCFST the strain limits are adapted from the POLA (Port of Los Angeles) seismic design code (2004). Once the deformation limit states are obtained from the pushover analysis, an incremental non-linear time history analysis is performed to determine the seismic level of intensity required to reach each limit state. The elastic damping in all the dynamic simulations is represented by 0.5% tangent-stiffness proportional damping (Priestley et al. 2007).

Note that effect of seasonal freezing on the lateral response of continuous column/pile members has been already addressed in Suleiman et al. (2006) and Sritharan et al. (2007). Results obtained showed that the freezing soil incites a migration of the plastic hinge towards the surface, accompanied by a significant increase in the effective elastic stiffness and shear demand and a reduction in the displacement capacity. In this research we focused on the effect of the variation on the material properties and spread of plasticity at low temperatures on the seismic response of the piers. To avoid the soil-interaction effects, pier columns are assumed to be fixed at the base. Which may represent the case of columns supported by a spread footing or and oversized shaft, or column/pile columns if the height used is assumed to be the equivalent depth to fixity.

Table 7.7. Limit states definitions

Limit state	Concrete strain limit (ORC)	Concrete strain limit (RCFST)	Steel strain limit (rebar and tube)
Serviceability	-0.004	-0.008	0.015
Damage control	-0.018	-0.027	0.07

7.7.1 Seismic input

The seismic input for the non-linear time history analysis consists of 7 spectrum compatible records generated through adjustments of recorded accelerograms using wavelet theory (Suarez and Montejo, 2003, 2005). The seed accelerograms were selected from the 3551 records of the PEER NGA dataset (PEER 2006). Initial selection is conducted based on an approximate match to the spectral shape using the RMS of the difference in normalized spectral accelerations (Hancock et al. 2006) as shown in Equation 7.7.

$$\Delta SA_{RMS} = \sqrt{\frac{1}{N_p}\sum_{i=1}^{N_p}\left(\frac{PSA_o(T_i)}{PGA_o} - \frac{PSA_s(T_i)}{PGA_s}\right)^2} \tag{7.7}$$

where N_p is the number of periods, $PSA_o(T_i)$ is the pseudo spectral acceleration from the record at period T_i, $PSA_s(T_i)$ is the target pseudo spectral acceleration at the same period; and PGA_o and PGA_s are the peak ground acceleration of the accelerogram and the zero-period anchor point of the target spectrum, respectively. The target spectrum is obtained from the 2003 NEHRP seismic design provisions (FEMA 450) for a soil type C in Caribou Creek, Alaska – 99676. The records selected are presented in Table 7.8. Displacement and pseudo-acceleration response spectra are displayed in Figure 7.31 for the original linearly scaled records and in Figure 7.32 for the compatible records along with the target spectrum. Additional ground motion parameters for the compatible records are shown in Table 7.9.

Table 7.8. Earthquake records used to generate the spectrum-compatible accelerograms

	Earthquake	Station	NGA ID	M_w	CD (km)	Soil type
EQ1	Chi-Chi, Taiwan 1999	HWA058	2962	6.20	100.1	D
EQ2	Nenana Mountain, AK 2002	TAPS PumpStation#09	2093	6.70	104.7	D
EQ3	Imperial Valley, CA 1979	El Centro Array #5	0180	6.53	3.95	D
EQ4	Superstition Hills, CA 1987	CDMG 135	0721	6.54	18.2	D
EQ5	Northridge, CA 1994	Bell Gardens-Jaboneria	0951	6.69	44.1	D
EQ6	Northridge, CA 1994	Canoga Park-Topanga	0959	6.69	15.7	D
EQ7	Whittier Narrows, CA 1987	Playa Del Rey-Saran	0684	5.99	32.8	D

M_w: moment magnitude, CD: Closest distance

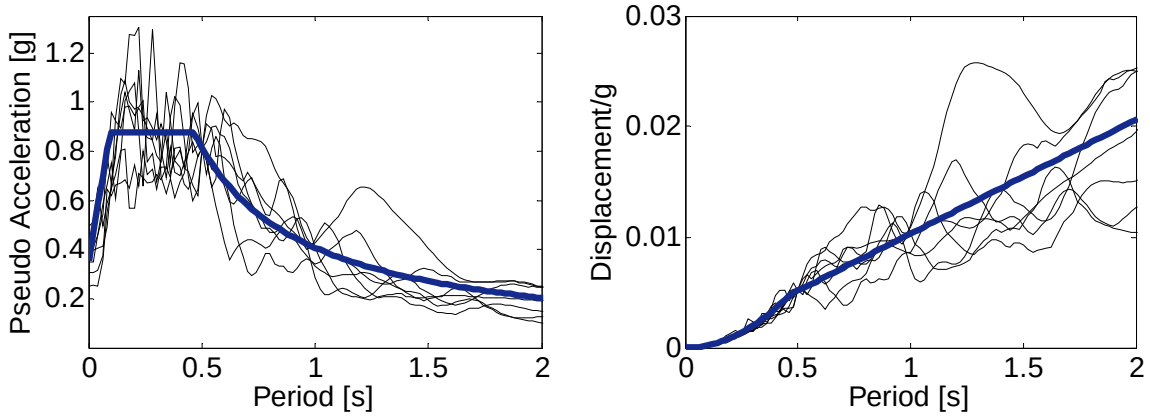

Figure 7.31 Displacement and pseudo-acceleration response spectra for the original records (scaled to match the target spectral amplitude at T=0.5 s) and the target spectrum

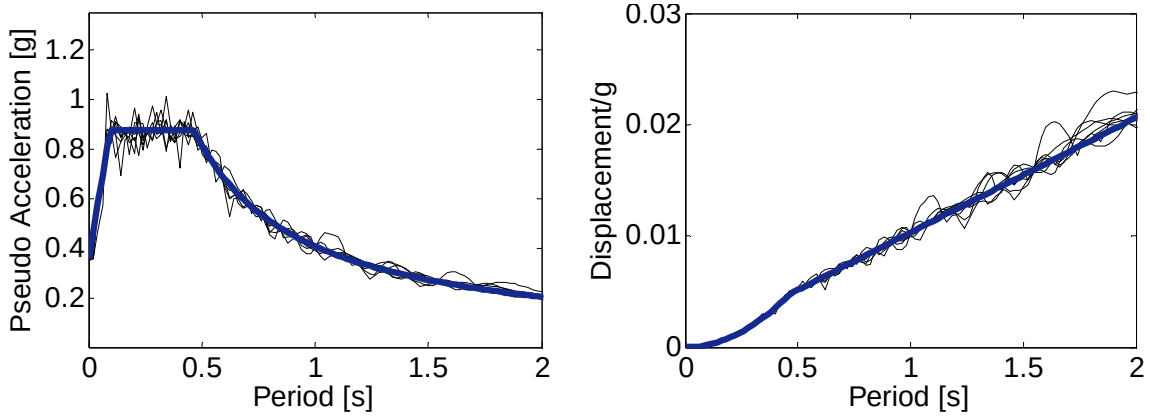

Figure 7.32 Displacement and pseudo-acceleration response spectra for the spectrum-compatible records and the target spectrum

Table 7.9. Ground motion parameters of the compatible records

Record	PGA (g)	PGV (cm/s^2)	PGD (cm)	Tm (s)	Du (s)	Ds (s)
EQ1	0.35	39.5	9.5	0.53	45.3	40.7
EQ2	0.35	32.0	8.3	0.48	37.3	31.8
EQ3	0.35	36.4	11.9	0.58	14.6	10.6
EQ4	0.35	39.1	11.6	0.49	23.3	17.6
EQ5	0.35	32.5	10.9	0.45	25.7	20.2
EQ6	0.35	32.8	9.8	0.51	18.0	13.9
EQ7	0.35	29.1	9.1	0.44	25.9	24.7

In table 7.9 PGA, PGV and PGD are the peak ground acceleration, velocity and displacement respectively. $Tm=\sum(C_i^2/f_i)/\sum C_i^2$ is the mean period, where C_i are the Fourier amplitudes, and f_i represent the discrete Fourier transform frequencies between 0.25 and 20 Hz. Du is the uniform duration calculated as the total time during which the acceleration is larger than 5% of PGA. Ds is the significant duration calculated as the interval of time over which 5% and 95% of the total Arias Intensity (AI) is accumulated. The Arias intensity is a measured of the accumulation of energy in the accelerogram represented by the integral of the square of the ground acceleration $AI=(\pi/2g)\int a^2(t)dt$.

7.8 Seismic behavior of single column bridge bents at low temperatures

Two different types of columns are analyzed, ordinary reinforced concrete columns (ORC) and reinforced concrete filled steel tube columns (RCFST). The columns are assumed to be in single bending, geometric properties of each configuration are displayed in Figures 7.33 and 7.34. Both columns have an outside diameter of 2.44 m (96 in) and are reinforced with 40#18 steel bars (ρ=2.2%). The only difference between the

two models is the presence of a 32 mm (1.25 in) steel tube in the RCFST column (D/t=76.8). Two different cantilever lengths are examined, L=12 m (L/D=4.9) and L=8m (L/D=3.3), axial load applied in all cases is 6675 kN (ALR=3.9%), calculated using room temperature concrete compressive strength). Two different scenarios are considered for each type of column, regular room temperature conditions (20°C) and sub-freezing conditions (-40°C). Material properties and plastic hinge lengths used for each scenario are summarized in Table 7.10. The concrete compressive strength for the cold specimens is obtained from Equation 7.8 (previous Equation 1.3 - Browne and Bamforth, 1981) for an average moisture content *w* of 4.3%. Yield and ultimate tensile stresses for steel bars and steel tube in the cold specimens are assumed to be 10% larger than for the room temperature units. Plastic hinge lengths are obtained using Equation 7.1 for ORC columns and Equation 7.4 for RCFST columns. Note that there is not an expression available to calculate the equivalent plastic hinge length at low temperatures of RCFST with fixed based detail. An ongoing research program at NCSU will shed some light on this aspect. However, as the response of this type of specimens is mainly controlled by the steel tube, no major change in the plastic hinge length is anticipated due to the low temperature effect. The analyses were performed keeping the same plastic hinge length used for the corresponding room temperature units.

$$\sigma_c(T) = \sigma_c(T_R) - Tw/12 \qquad 0^\circ C > T > -120^\circ C \qquad (7.8)$$

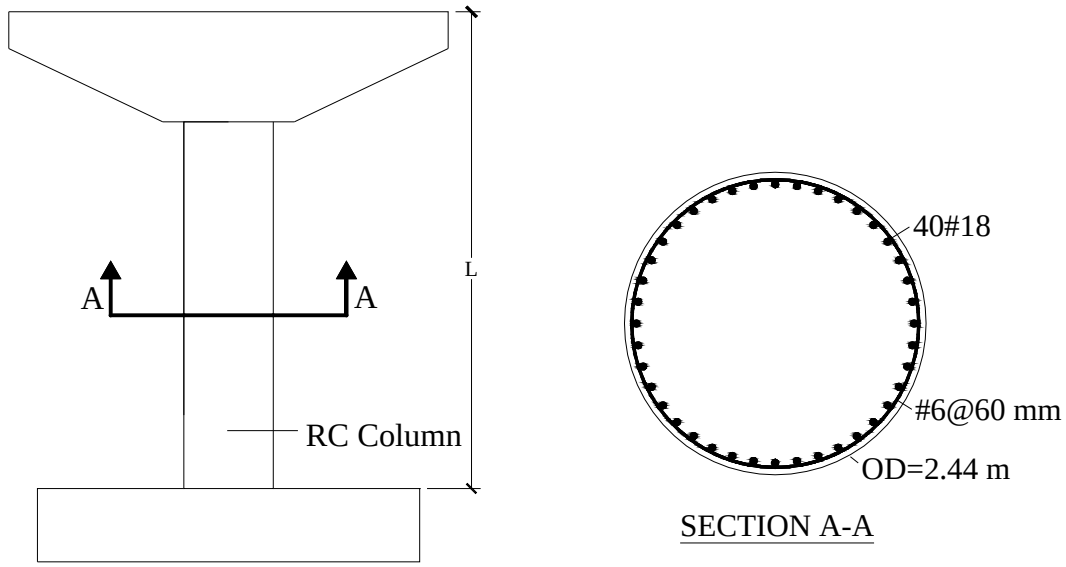

Figure 7.33 Single ORC column bridge bent

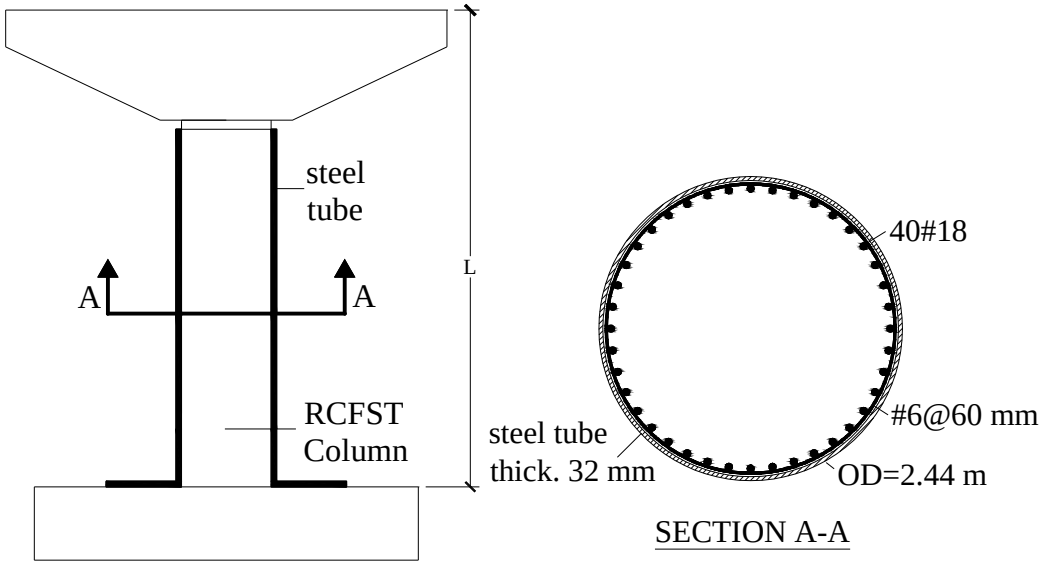

Figure 7.34 Single RCFST column bridge bent

Table 7.10. Material properties and plastic hinge lengths for the two different scenarios (Single-column pier)

Property \ Scenario	+20°C (+68°F)	-40°C (-40°F)
f'_c (MPa)	36.4	50.9
f_{yb} (MPa)	455.4	500.9
f_{ub} (MPa)	637.56	701.3
f_{yp} (MPa)	394.1	433.5
f_{up} (MPa)	492.6	541.9
L_p ORC (mm)	1531 (L=12m) 1211 (L=8m)	905 (L=12m) 722 (L=8m)
L_p RCFST $_{TOP}$ (mm)	N.A	N.A
L_p RCFST $_{BOT.}$ (mm)	1471 (L=12m) 1171 (L=8m)	1471 (L=12m) 1171 (L=8m)

7.8.1 Single ORC column bridge bents

Figure 7.35 shows the results of the static-non-linear pushover analyses for the single ORC column bridge bent for the warm and sub-freezing conditions when L/D=4.9. The deformation limit states presented in Table 7.11 were obtained from the strain limit states (Table 7.7) by tracking the concrete and steel strains during the pushover analyses. It is seen that at the sub-freezing condition the column exhibit an increase of ~15% on the

flexural strength and also a reduction in the deformation capacity. The serviceability and damage control limit states at low temperatures are reached at lateral displacements 87% and 73% the displacements required to reach the same limit states at room temperature conditions, respectively. At room temperature both limit states are controlled by the compressive strain in the concrete, while at low temperature the serviceability limit is controlled by the concrete and the damage control limit by the tensile strain in the steel bars.

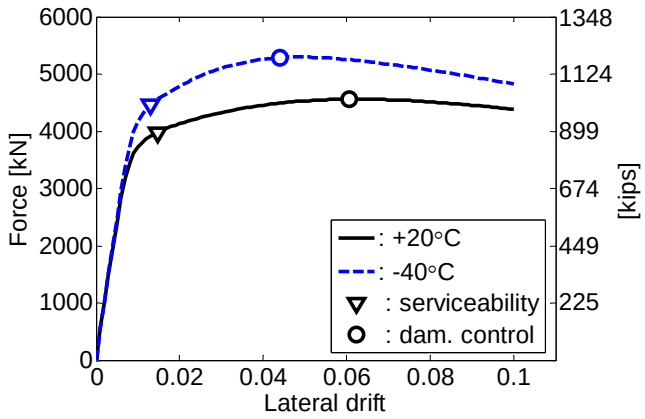

Figure 7.35 Single ORC column bent pushover results at warm and freezing conditions (L/D=4.9)

Table 7.11. Deformation limit states - single ORC bent at warm and freezing conditions (L/D=4.9)

Limit state	+20°C (+68°F) drift limit / required PGA	-40°C (-40°F) drift limit / required PGA
Serviceability	1.48% / 0.64g	1.30% / 0.61g
Damage control	6.06% / not reached	4.40% / not reached

In order to analyze the effect of low temperatures at several levels of lateral demand, the bents are subjected to spectral matched records (Tables 7.8 and 7.9) scaled

to various levels of intensity. This procedure is commonly known as incremental dynamic analysis IDA (Vamvatsikos and Cornell, 2002). The demand parameter and intensity measure selected are maximum absolute lateral drift (defined as the ratio between maximum displacement reached by the structure and the bent height) and peak ground acceleration (since the records were generated to match the same target spectrum, this intensity measure is representative of any spectral acceleration). Figures 7.36 to 7.38 show the results of the IDA analysis for L/D=4.9. It is seen from figure 7.38 that the average responses at both conditions is almost identical up to a PGA~0.6, where the serviceability limit is reached in both scenarios (Figures 7.36 and 7.37, Table 7.11). After this point, the structure behaves slightly more flexible in the warm condition. The structure was closer to reaching the serviceability limit at the freezing condition than at the room temperature condition; mainly because the drift required to reach this limit state is smaller in the freezing condition.

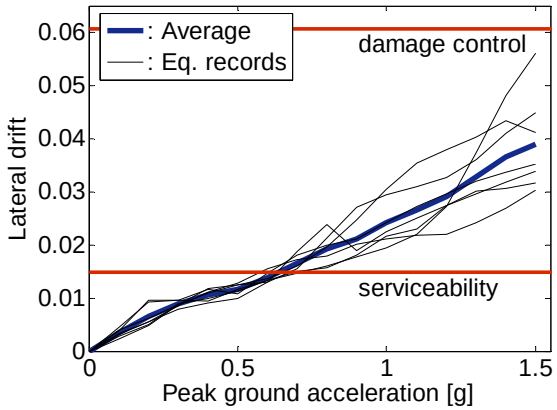

Figure 7.36 IDA curve for the single ORC column bent at warm conditions (L/D=4.9)

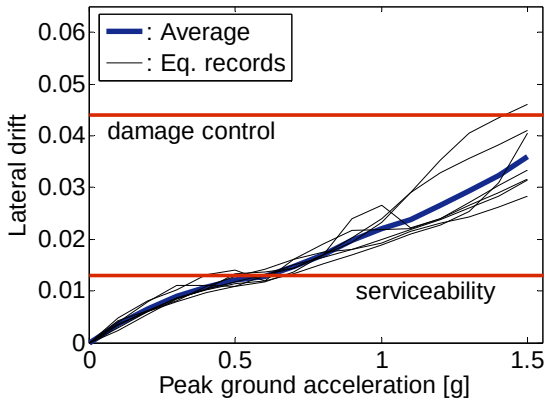

Figure 7.37 IDA curve for the single ORC column bent at freezing conditions (L/D=4.9)

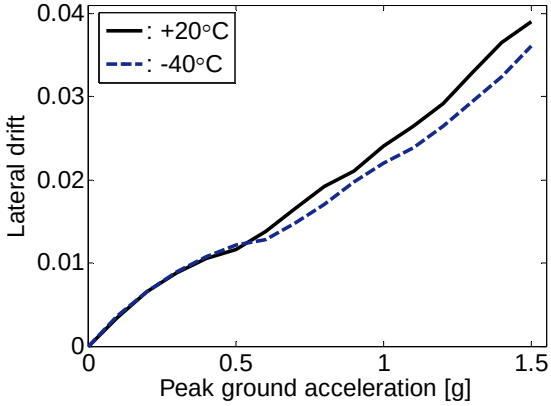

Figure 7.38 Average IDA curves for the single ORC column bent at warm and freezing conditions (L/D=4.9)

Results obtained when L/D=3.3 are presented in Figures 7.39 to 7.42 and in Table 7.12. From the pushover analysis (Figure 7.39, Table 7.12) it seen that the average increase in flexural strength at low temperature is ~12%. The lateral displacements demand required to reach the serviceability and damage control limit states at freezing conditions are 85% and 72% the displacements required to reach the same limit states at room temperature conditions, respectively. It was also noticed that the damage control limit changed from being controlled by the concrete strain for the bent at room temperatures to be controlled by the steel strain for the bent at low temperatures. Results obtained from the IDA analysis are quit similar to the results obtained for L/D=4.9. Maximum lateral responses are almost identical up to PGA~0.5 where the serviceability

limit is reached in both scenarios, after this point lateral displacements are slightly larger at the room temperature condition.

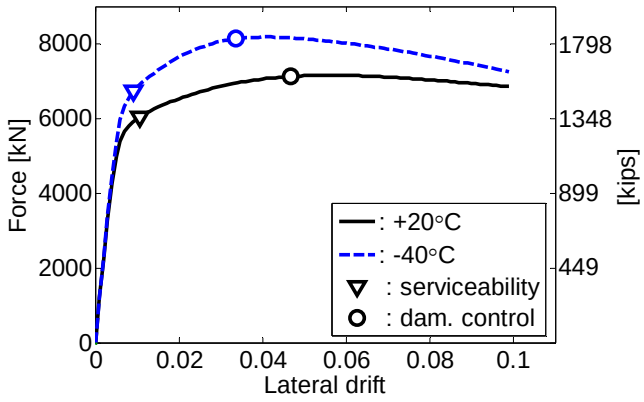

Figure 7.39 Single ORC column bent pushover results at warm and freezing conditions (L/D=3.3)

Table 7.12. Deformation limit states - single ORC bent at warm and freezing conditions (L/D=3.3)

Limit state	+20°C (+68°F) drift limit / required PGA	-40°C (-40°F) drift limit / required PGA
Serviceability	1.07% / 0.57g	0.92% / 0.48g
Damage control	4.68% / not reached	3.37% / not reached

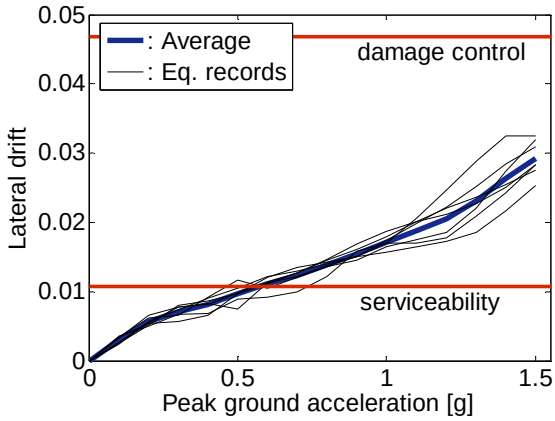

Figure 7.40 IDA curve for the single ORC column bent at warm conditions (L/D=3.3)

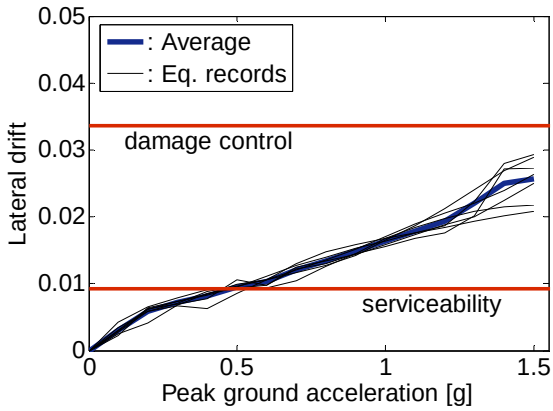

Figure 7.41 IDA curve for the single ORC column bent at freezing conditions (L/D=3.3)

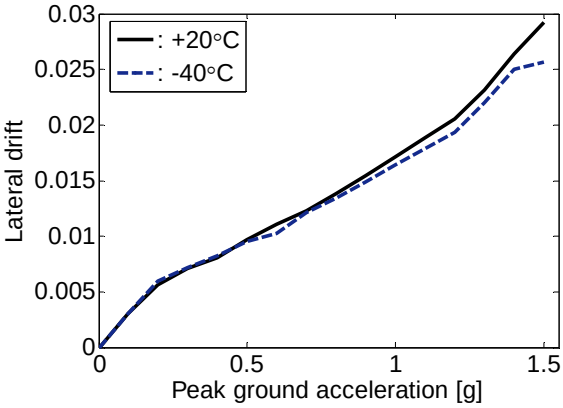

Figure 7.42 Average IDA curves for the single ORC column bent at warm and freezing conditions (L/D=3.3)

7.8.2 Single RCFST column bridge bents

Figure 7.43 and Table 7.13 show the results obtained from the pushover analysis of the single RCFST column bridge with L/D=4.9. The column exposed to low temperatures exhibits an increase in the flexural strength of 10%. Opposite to the ORC columns, in the case of RCFST columns the lateral deformations at which the limit states are reached did not change with the low temperatures, mainly because the plastic hinge length was kept constant for both scenarios. The serviceability and damage control limit states were controlled by the strain in the steel tube in all the single RCFST column bents analyzed in this research. Figure 7.44 to 7.46 show the results of the IDA analysis, it is seen that the dynamic response of this type of pier is not affected by the low temperatures and that the serviceability limit is barely reached.

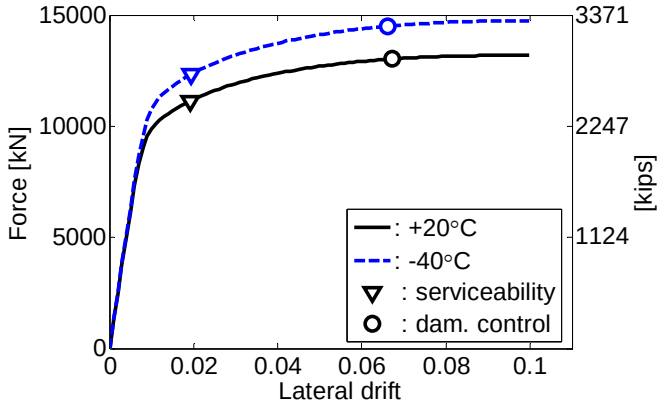

Figure 7.43 Single RCFST column bent pushover results at warm and freezing conditions (L/D=4.9)

Table 7.13. Deformation limit states - single RCFST bent at warm and freezing conditions (L/D=4.9)

Limit state	+20°C (+68°F) drift limit / required PGA	-40°C (-40°F) drift limit / required PGA
Serviceability	1.92% / ~1.5g	1.94% / ~1.5g
Damage control	6.72% / not reached	6.62% / not reached

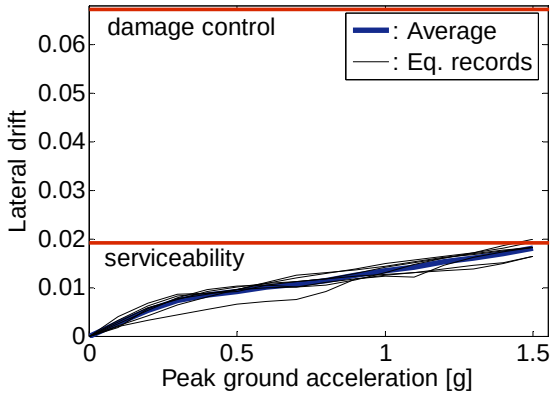

Figure 7.44 IDA curve for the single RCFST column bent at warm conditions (L/D=4.9)

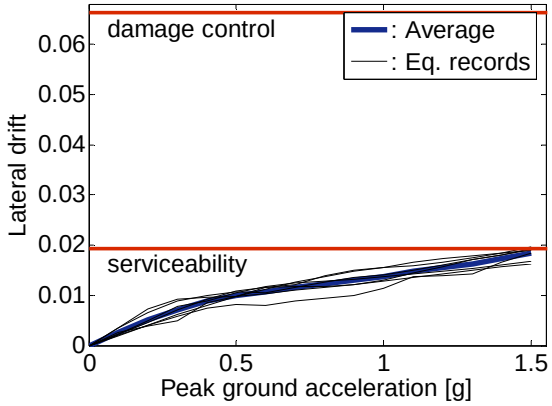

Figure 7.45 IDA curve for the single RCFST column bent at freezing conditions (L/D=4.9)

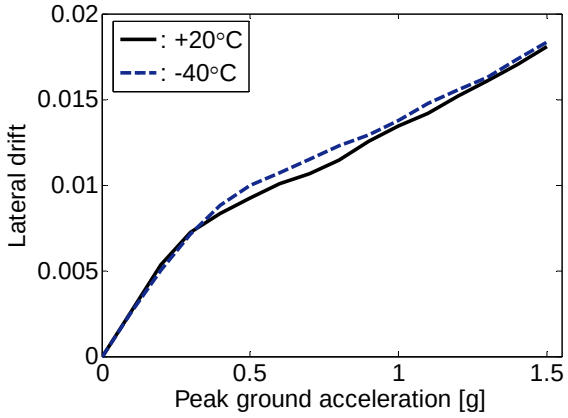

Figure 7.46 Average IDA curves for the single RCFST column bent at warm and freezing conditions (L/D=4.9)

Figures 7.47 and 7.50 and Table 7.14 show the results obtained from the static and dynamic analyses for the single RCFST column bridge with L/D=3.3. As for the column with L/D=3.3, it is seen that the only effect of the low temperatures in the behavior of the column is the increase on the flexural strength of the column (~10%) - no effect on the displacement capacity and dynamic response was identified.

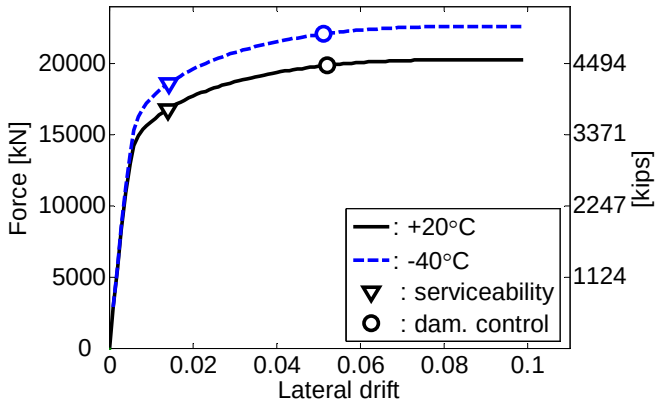

Figure 7.47 Single RCFST column bent pushover results at warm and freezing conditions (L/D=3.3)

Table 7.14. Deformation limit states - single RCFST bent at warm and freezing conditions (L/D=3.3)

Limit state	+20°C (+68°F) drift limit / required PGA	-40°C (-40°F) drift limit / required PGA
Serviceability	1.42% / not reached	1.42% / not reached
Damage control	5.22% / not reached	5.13% / not reached

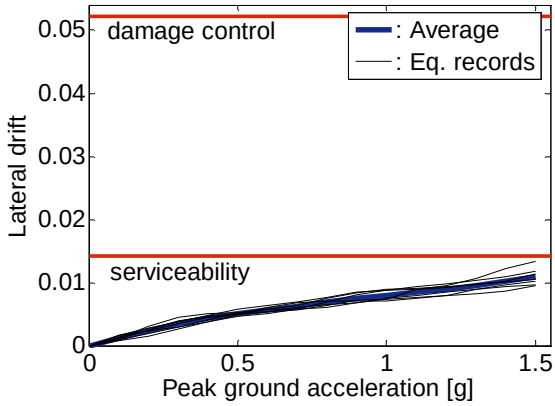

Figure 7.48 IDA curve for the single RCFST column bent at warm conditions (L/D=3.3)

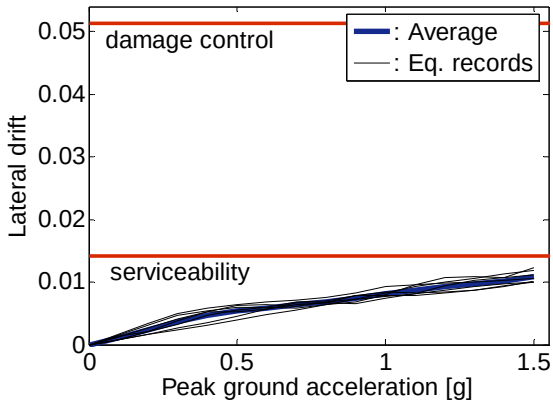

Figure 7.49 IDA curve for the single RCFST column bent at freezing conditions (L/D=3.3)

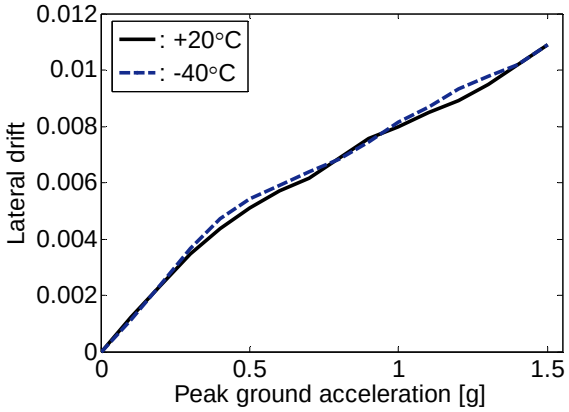

Figure 7.50 Average IDA curves for the single RCFST column bent at warm and freezing conditions (L/D=3.3)

7.9 Low temperature effect on the seismic behavior of multi-column RC piers

The Multi-column bents analyzed are shown in Figure 7.51 and 7.52. As for the single column piers, two different types of columns are used: ORC columns and RCFST columns. Four pile/columns with diameter 1.067 m (42 in) and reinforced with 30#10 bars (ρ=2.1%) compose the bridge bent, steel tube thickness in RCFST columns is 22 mm (7/8 in, D/t=48). A total dead load of 5300 kN (1191 kips) is distributed on the cap beam, the axial load in each column is then ~1325 kN (298 kips, ALR=4.1%). Two different column lengths are analyzed L=5.7 m (L/D=5.3) and L=7.5 m (L/D=7). Material properties values for the freezing and normal temperature values are the same used for the single column and are presented again in Table 7.15 along with plastic hinge lengths used in the simulations. Plastic hinge lengths on the bottom (in-ground hinges) of column/piles at room temperatures are usually calculated using the following equation, based on analysis by Chai (2002):

$$\frac{L_p}{D} = 1 + \frac{0.1\left(H - H_{CP}\right)}{D} \leq 1.6 \tag{7.9}$$

where H is the clear length of the column and H_{CP} is the distance from the top hinge to the point of contraflexure. In the case of steel piles POLA (2004) recommends $L_p=2D$.

Although experimental results by Sritharan et al. (2007) show the spread of plasticity to reduce at low temperatures, no expression is yet available to calculate the plastic hinge length at sub-freezing temperatures. It has been shown that in fixed-head pile columns the in-ground hinge will rarely govern the design since the column–top hinge typically forms first and has a shorter plastic hinge length (Priestley et al. 2007). Therefore, it was decided to use an average value of $L_p=1.2D$ for the in-ground plastic hinge length of ORC pile/columns and $L_p=2D$ for RCFST pile/columns.

The cap beam was initially modeled as a fiber-force-based element, analysis of the results obtained showed that the beam barely reach the moment required for first yield. It was then decided to model the cap beam as an elastic member with appropriate effective stiffness to reduce the computational effort.

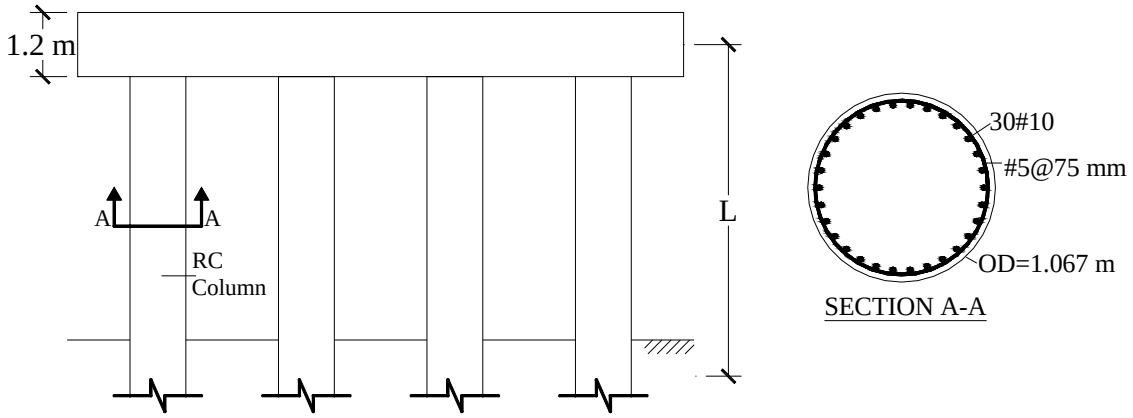

Figure 7.51 Multiple ORC columns bridge bent

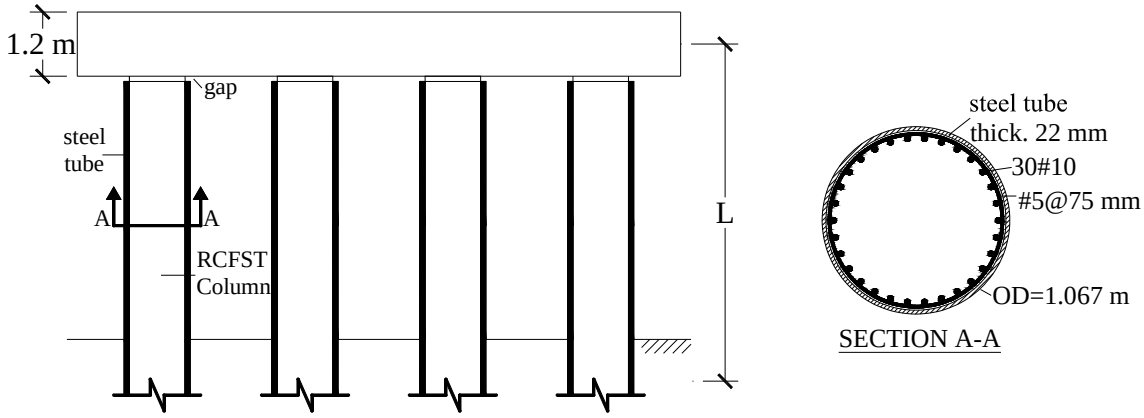

Figure 7.51 Multiple RCFST columns bridge bent

Table 7.15. Material properties and plastic hinge lengths for the two different scenarios (Multi-column pier)

Property \ Scenario	+20°C (+68°F)	-40°C (-40°F)
f'_c (MPa)	36.4	50.9
f_{yb} (MPa)	455.4	500.9
f_{ub} (MPa)	637.56	701.3
f_{yp} (MPa)	394.1	433.5
f_{up} (MPa)	492.6	541.9
L_p ORC $_{TOP}$ (mm)	641	402
L_p RCFST $_{TOP}$ (mm)	467	467
L_p ORC $_{BOT.}$ (mm)	1280	1280
L_p RCFST $_{BOT.}$ (mm)	2134	2134

7.9.1 Multi-ORC-column bridge bents

The results obtained from the pushover analyses of the multi-ORC-column bridge bents with L/D=5.3 are presented in Figure 7.52 and Table 7.16. The displacement required to reach the serviceability and damage control limit states at sub-freezing

temperatures are 94% and 76% the lateral displacements required to reach the same limit states at room temperatures, respectively. The increase in the flexural strength at low temperatures is ~12%. Serviceability and damage control limits were controlled by the concrete compressive strain in the top hinges for all the multi-ORC-columns analyzed in this research.

Results of the incremental non-linear dynamic analyses are display in Figures 7.53 to 7.55. As for the single column bents, it is seen that the dynamic behavior is practically the same at room and low temperatures up to the serviceability limit after which the room temperature bent behaves slightly more flexible. The damage control limit is not reach in any of the scenarios; however it is closer to being reached at low temperatures because the damage control lateral displacement is smaller than it is at room temperatures.

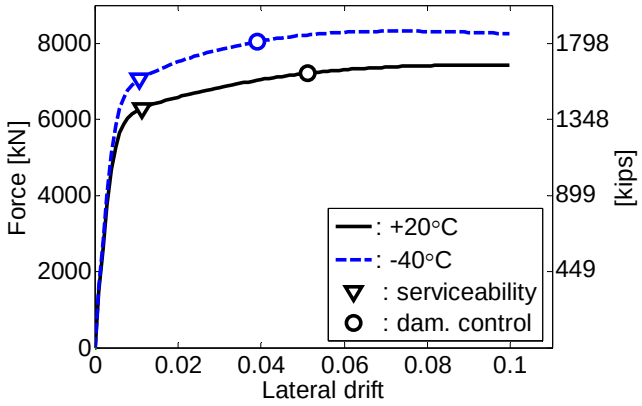

Figure 7.52 Multi ORC column bent pushover results at warm and freezing conditions (L/D=5.3)

Table 7.16. Deformation limit states - Multi ORC column bent at warm and freezing conditions (L/D=5.3)

Limit state	+20°C (+68°F) drift limit / required PGA	-40°C (-40°F) drift limit / required PGA
Serviceability	1.13% / 0.68g	1.07% / 0.69g
Damage control	5.11% / not reached	3.91% / not reached

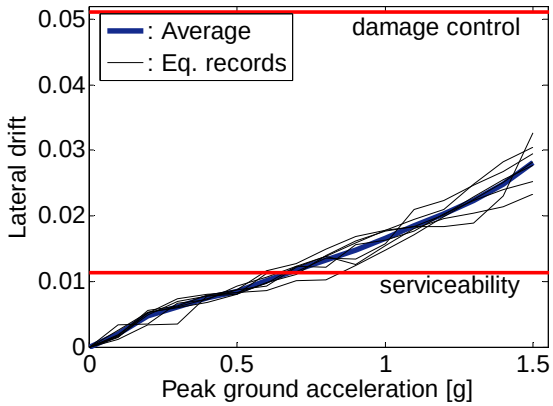

Figure 7.53 IDA curve for the multi ORC column bent at warm conditions (L/D=5.3)

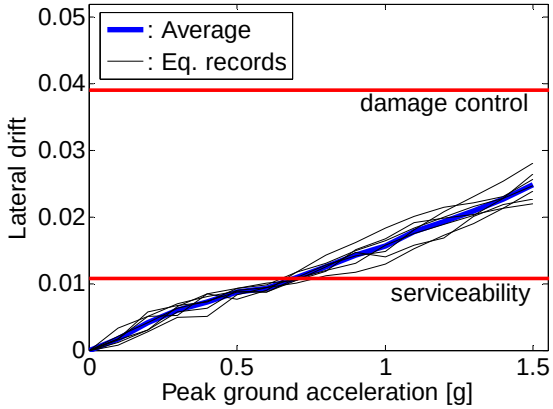

Figure 7.54 IDA curve for the multi ORC column bent at cold conditions (L/D=5.3)

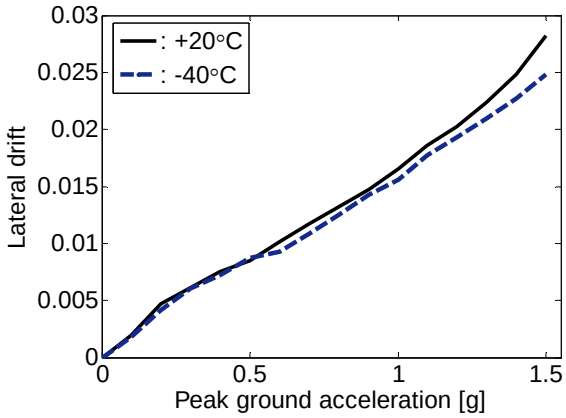

Figure 7.55 Average IDA curves for the multi ORC column bent at warm and freezing conditions (L/D=5.3)

Figures 7.56 to 7.59 and Table 7.17 present the results obtained form the static and dynamic analyses of the multi-ORC-column bent with L/D=7. It is seen that the results obtained follow the same trends discussed earlier for the bent with L/D=5.3.

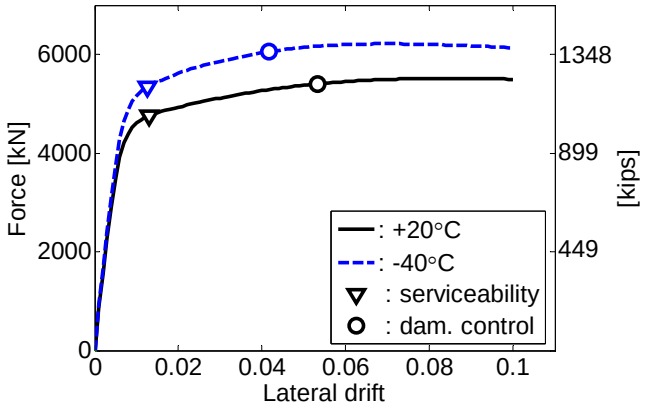

Figure 7.56 Multi ORC column bent pushover results at warm and freezing conditions (L/D=7)

Table 7.17. Deformation limit states - Multi ORC column bent at warm and freezing conditions (L/D=7)

Limit state	+20°C (+68°F) drift limit / required PGA	-40°C (-40°F) drift limit / required PGA
Serviceability	1.31% / 0.64g	1.26% / 0.59g
Damage control	5.33% / not reached	4.15% / not reached

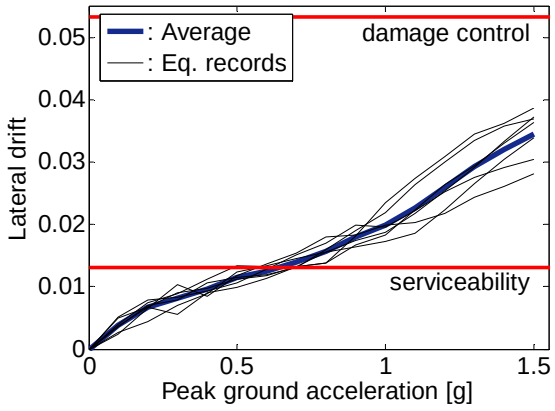

Figure 7.57 IDA curve for the multi ORC column bent at warm conditions (L/D=7)

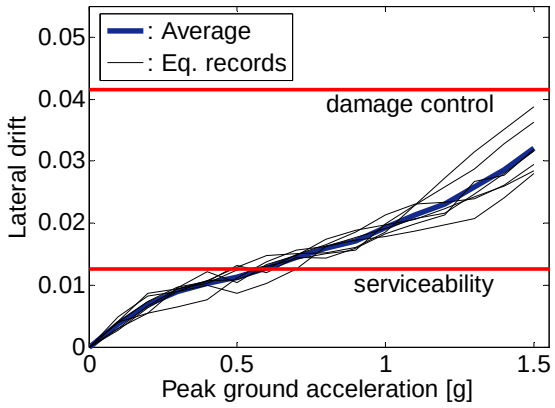

Figure 7.58 IDA curve for the multi ORC column bent at warm conditions (L/D=7)

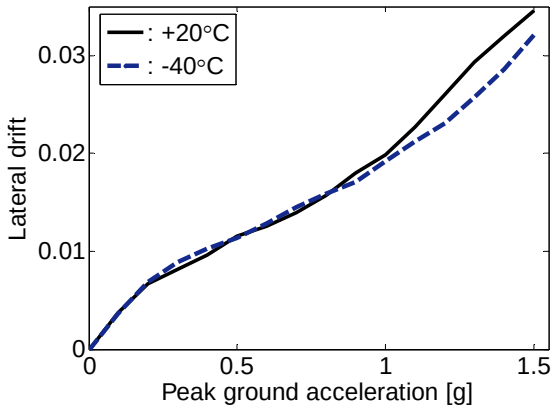

Figure 7.59 Average IDA curves for the multi ORC column bent at warm and freezing conditions (L/D=7)

7.9.2 Multi-RCFST-column bridge bents

Figure 7.60 and Table 7.18 show the results from the pushover analysis performed to the multi-RCFST-column bent with L/D= 5.3. It is seen that the bent exposed to low temperatures exhibits an increase in the flexural strength of ~9% when compared to the room temperature case. No effect of the low temperatures in the deformation limit states is identified. Both limit states are controlled by the steel bar tensile strain in the top hinges of the bent. Figures 7.61 to 7.63 show the results of the incremental dynamic analyses, it is seen that the dynamic response is practically the same at room and sub-freezing temperatures.

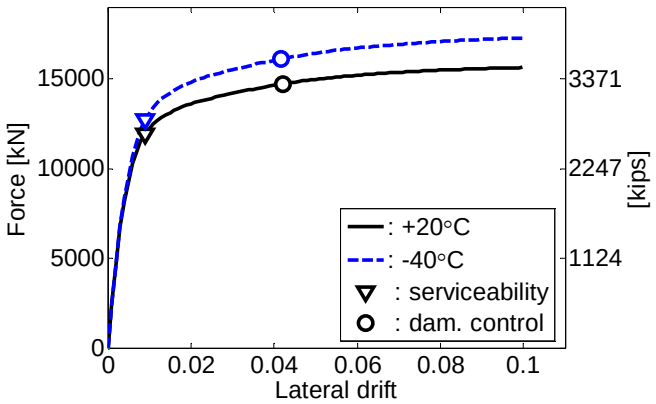

Figure 7.60 Multi RCFST column bent pushover results at warm and freezing conditions (L/D=5.3)

Table 7.18. Deformation limit states - Multi RCFST column bent at warm and freezing conditions (L/D=5.3)

Limit state	+20°C (+68°F) drift limit / required PGA	-40°C (-40°F) drift limit / required PGA
Serviceability	0.90% / 1.12g	0.90% / 1.12g
Damage control	4.21% / not reached	4.18% / not reached

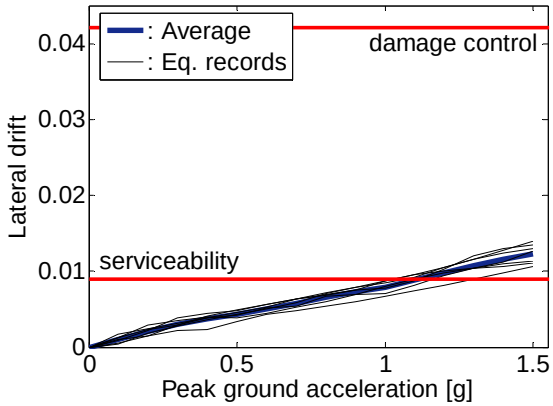

Figure 7.61 IDA curve for the multi RCFST column bent at warm conditions (L/D=5.3)

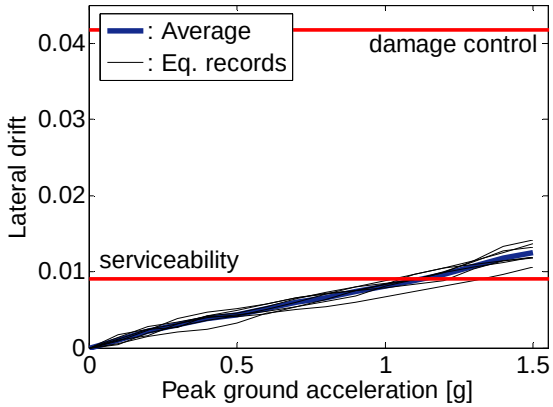

Figure 7.62 IDA curve for the multi RCFST column bent at freezing conditions (L/D=5.3)

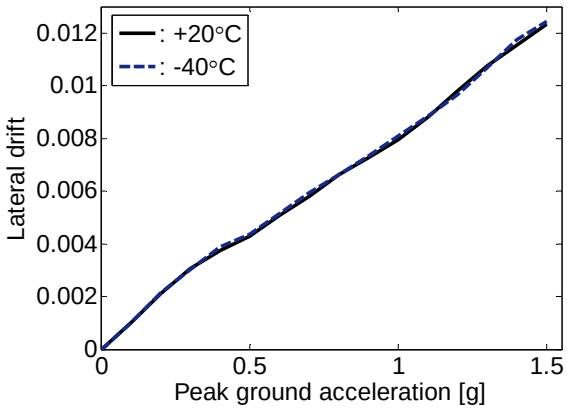

Figure 7.63 Average IDA curves for the multi RCFST column bent at warm and freezing conditions (L/D=5.3)

Figures 7.64 to 7.67 and Table 7.19 present the results obtained form the static and dynamic analyses of the multi-RCFST-column bent with L/D=7. It is seen that the results obtained follow the same trends discussed earlier for the bent with L/D=5.3.

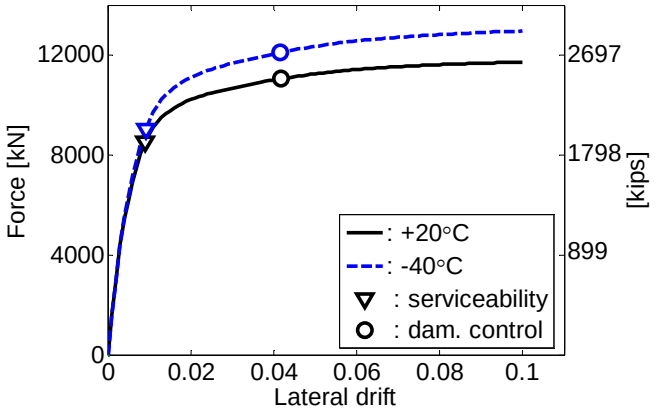

Figure 7.64 Multi RCFST column bent pushover results at warm and freezing conditions (L/D=7)

Table 7.19. Deformation limit states - Multi RCFST column bent at warm and freezing conditions (L/D=7)

Limit state	+20°C (+68°F) drift limit / required PGA	-40°C (-40°F) drift limit / required PGA
Serviceability	0.91% / 0.80g	0.80% / g
Damage control	4.18% / not reached	4.14% / not reached

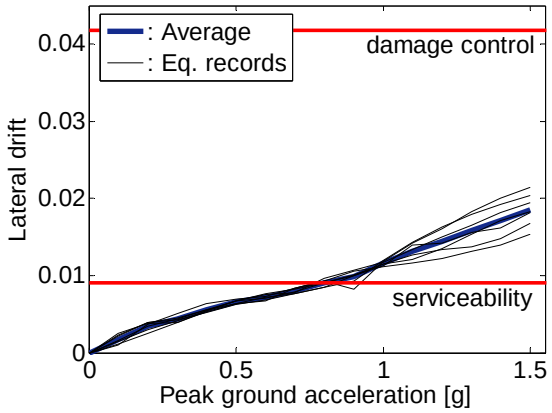

Figure 7.65 IDA curve for the multi RCFST column bent at warm conditions (L/D=7)

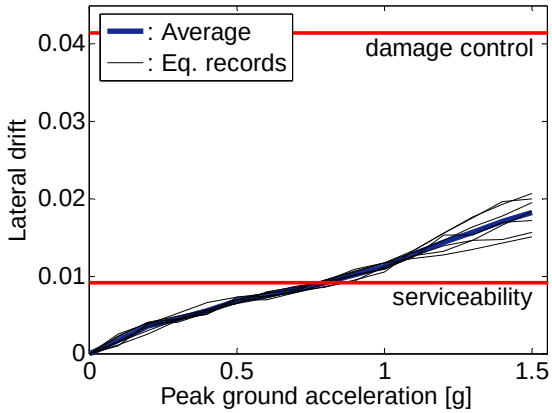

Figure 7.66 IDA curve for the multi RCFST column bent at cold conditions (L/D=7)

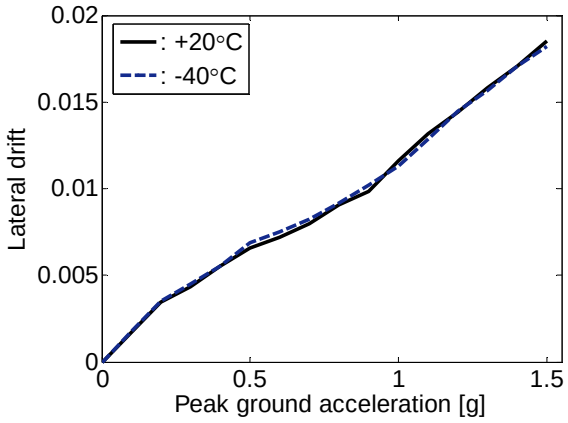

Figure 7.67 Average IDA curves for the multi RCFST column bent at warm and freezing conditions (L/D=7)

7.10 Parametric study

It has been shown that the response of reinforced concrete columns subjected to the combined effect of low temperatures and lateral loads can be properly estimated using moment curvature analysis along with the equivalent plastic hinge method if the appropriate temperature dependent material properties and plastic hinge length are used. A parametric study was performed with the aim of discovering trends that can assist with the seismic design of RC bridge columns in cold regions. The main objective was to find a simple way to calculate the reduction in ductility capacity and increase in strength observed at low temperatures.

In order to quantify the increase of flexural strength at low temperatures a series of moment curvatures analysis were performed. Three different section diameters were analyzed 457 mm (18 in), 914 mm (36 in) and 2440 mm (96 in). For each section diameter the axial load ratio was varied between 0% and 30%, and the longitudinal reinforcement ratio between 1% and 4%. A total of 95 section configurations were analyzed, for each configuration two moment-curvature analysis are performed, one with warm temperature (+20°C, +68°F) material properties and the other with low temperature (-40°C, -40°F) material properties. The low temperature overstrength is then defined as the ratio between the low and room temperature nominal moments (defined at a cover

concrete strain of 0.004). Concrete compressive strength and steel tensile strength were assumed to be, respectively, 40% and 10% larger than the employed for the room temperature condition. It is seen from Figures 7.68 and 7.69 that the low temperature flexural overstrength is not influenced by the amount of longitudinal steel or axial load. Figure 7.70 shows the overstrengths (sorted on ascending order) for all the 95 section configurations along with the overstrengths obtained from the flexural units tested in this research, it is seen that a low temperature flexural overstrength factor of 1.15 seems appropriate for the seismic design of RC columns exposed to sub-freezing temperatures.

Calculation of the reduction in displacement ductility capacity due to low temperatures requires the calculation of the force-displacement response of the member, which is extrapolated from the section (moment-curvature) analysis using the equivalent plastic hinge method. Material properties are the same as used for the overstrength factor analysis. Temperature dependent equivalent plastic hinge lengths are calculated using Equation 7.1. Two different section diameters were analyzed 914 mm (36 in) and 2440 mm (96 in). Other variables analyzed include: axial load ratio [0%-20%], longitudinal reinforcement ratio [1%-4%], transverse reinforcement ratio [0.4%-1.3%] and aspect ratio [L/D = 3-11]. For each member configuration the force-displacement response is calculated for room and low temperature conditions. The reduction in the ductility capacity at low temperatures is characterized by the ratio between the displacement ductilities at low and room temperatures at a given level of strain. Figures 7.71 and 7.72 show the reduction of displacement ductility at low temperatures as a function of concrete and steel strain, respectively. It is seen from these graphs that the reduction in ductility increases with the lateral demand. Equations 7.10 and 7.11 were obtained from the data presented in Figures 7.71 and 7.72 and can be used to estimate the low temperature ductility capacity reduction for a given concrete (ε_c) or steel strain (ε_s). For example, if concrete strains of 0.004 and 0.018 are specified as the strain limits for the serviceability and damage control limit states, using Equation 7.10 it is obtained that the displacement ductility at low temperatures at each limit state is, respectively, 84% and 70% the room temperature ductility. Alternatively, if the limit states are defined in terms of ductility instead of strains, Equation 7.12 (Figure 7.73) can be used.

$$\frac{\mu_{-40^oC}}{\mu_{+20^oC}} = 0.43\varepsilon_c^{-0.12} \tag{7.10}$$

$$\frac{\mu_{-40^oC}}{\mu_{+20^oC}} = 0.46\varepsilon_s^{-0.12} \tag{7.11}$$

$$\frac{\mu_{-40^oC}}{\mu_{+20^oC}} = 0.88\left(\mu_{+20^oC}\right)^{-0.17} \tag{7.12}$$

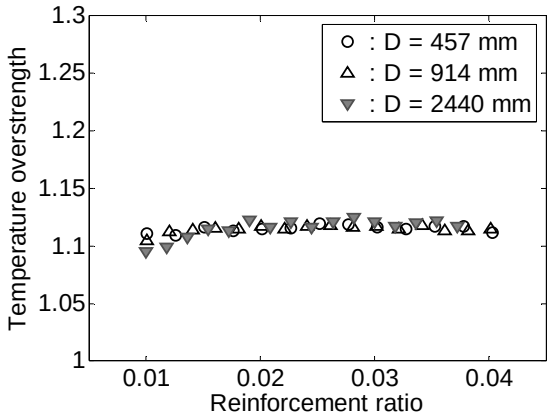

Figure 7.68 Effect of longitudinal reinforcement ratio on the low temperature overstrength of RC columns

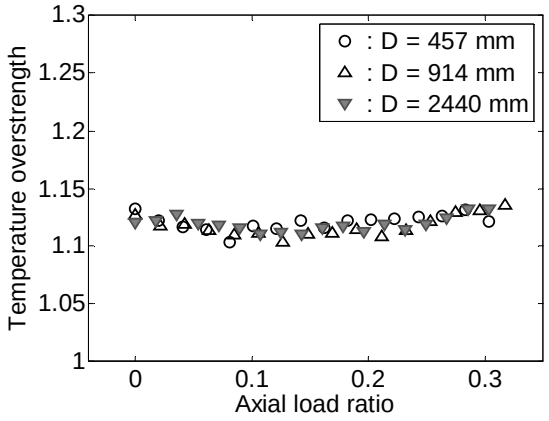

Figure 7.69 Effect of axial load ration on the low temperature overstrength of RC columns

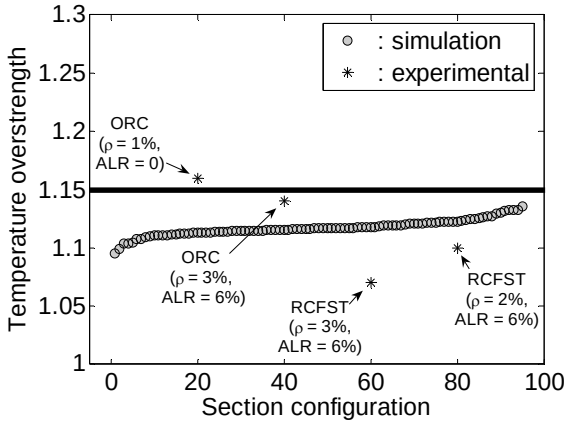

Figure 7.70 Proposed low temperature flexural overstrength for RC columns

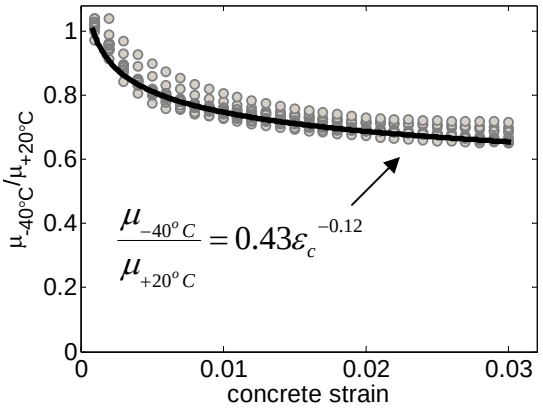

Figure 7.71 Reduced ductility at low temperatures as a function of the concrete strain

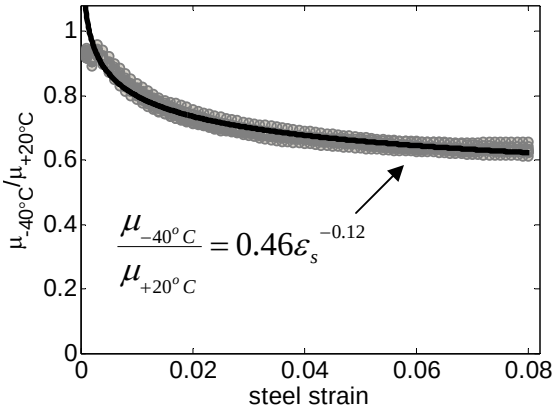

Figure 7.72 Reduced ductility at low temperatures as a function of the steel strain

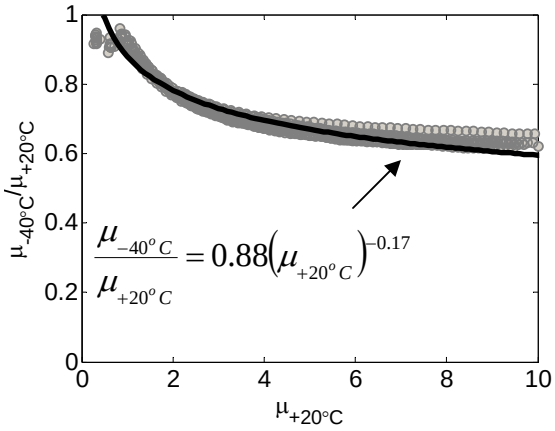

Figure 7.73 Reduced ductility at low temperatures as a function of the room temperature ductility

7.11 Final discussion and concluding remarks

With the objective of identifying the effect of low temperatures in the seismic response of RC bridge bents, this chapter presented the non-linear static and dynamic analysis of typical Alaska DOT RC bridge bents. To avoid strain localization problems, the bents were modeled using the fiber-based lumped plasticity elements developed by Scott and Fenves (2006) as implemented in OpenSees (McKenna et al. 2000). The model variables were calibrated using the experimental results previously presented in Chapters IV to VI.

Types of bents analyzed included single and multi column bents composed of ordinary reinforced concrete (ORC) columns and reinforced concrete filled steel tube (RCFST) columns. Each bent was analyzed under two different scenarios: room temperature conditions (+20°C, +68°F) and sub-freezing conditions (-40°C, -40°F). Each condition was simulated by changing the constituent material properties and the plastic hinge lengths. The columns were modeled fixed at the base to avoid the soil-structure interaction effect which has been already been shown by other researchers (Suleiman et al. 2006, Sritharan 2007) to largely affect the behavior of drilled shaft bents.

The results from the numerical simulations performed in this section can be summarized as follows:

- Bridge bents composed of one (single bending) or multiple ORC columns (double bending): the effect of low temperature was to increase the flexural strength of the bent by ~13% when compared to the strength exhibited at room temperature conditions. The serviceability limit at low temperatures was reached at approximately 86% of the level of lateral demand required to reach the same limit at room temperatures. The lateral displacement required to reach the damage control limit at low temperatures is ~73% of the lateral displacement required to reach the same limit at room temperatures. However, from the incremental dynamic analyses (IDA) it is seen that the level of seismic intensity required to reach the serviceability limit at low temperatures is only 8% smaller than the intensity needed to attain the same limit at room temperature. It is also noticed that the damage control limit is hardly reached in both scenarios.

- Bridge bents composed of a single RCFST column: An average increase of 10% in the flexural strength was identified in the bent exposed to low temperatures; however the deformation limit states remained constant. Note that it was assumed that no reduction in the plastic hinge length occurred in this type of configuration. This stills need to be corroborated by an ongoing experimental research at NCSU. Results from the IDA analyses show that this type of element will tend to remain almost elastic during a seismic event.

- Bridge bents composed of multiple RCFST columns: The bents exposed to low temperatures presented an increase of 9% on the flexural strength. Serviceability and damage control limit states are reached at the same level of lateral displacements. From the IDA analyses it is seen that the damage control limit state is not likely to be reached and that the serviceability limit is reached only at high levels of seismic intensity (PGA>1g). The limit states in this type of bents are largely controlled by the top hinges, specifically by the tensile strain in the steel longitudinal bars (as the concrete is very well confined by the steel tube). In any fixed-head pile column the in-ground hinge will rarely govern the design since the column top hinge typically form first, and has a shorter plastic hinge length. This situation is more pronounced in the case of RCFST pile/columns,

where the in-ground hinge has a moment capacity ~3-4 times the moment capacity of the top hinge (due to the direct contribution of the steel tube in the flexural strength of the in-ground hinge and not in the top hinge were a gap is left between the tube and the cap beam). Figure 7.74 shows the normalized moment-curvature response of the top and in-ground hinge of the multi RCFST column with L/D=5.3 when it is excited by one of the compatible records scaled to 1.2g (intensity at which the bent is expected to reach the serviceability limit, Table 7.18). It is seen that at this point the in-ground hinge remain almost elastic while the top hinge has already undergo several inelastic cycles. Elastic response below ground would help preclude the need for inspection of below ground hinges.

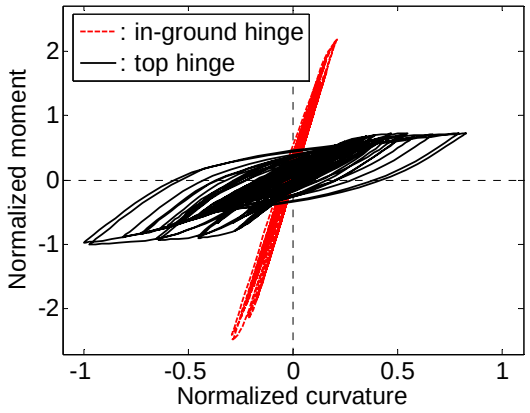

Figure 7.74 Behavior of in-ground and top hinges in fixed head RCFST pile columns

Finally, the chapter concludes with a parametric study that allowed generation of simple equations than can be used to estimate the reduction in ductility and flexural overstrength at low temperatures. The analysis model used in the parametric study was calibrated from the experimental tests conducted as part of this research.

CHAPTER VIII

CONCLUSIONS AND RECOMMENDATIONS

8.1 Summary and conclusions

An experimental and analytical study was undertaken to investigate the influence of sub-freezing temperatures on the seismic behavior of reinforced concrete bridge columns. The results obtained can be summarized as follows:

Low temperature effects on plain concrete and reinforcing steel: An extensive literary search presented in Chapter I identified a lack of information on the effects of sub-freezing temperatures on reinforced concrete structures with most of the research focused at the material level. Data extracted from previous research complemented with physical testing performed as part of this research provided trends in the mechanical properties of reinforcing steel and plain concrete. In general, it can be said that plain concrete and reinforcing steel exhibited a desirable behavior at low temperatures: a remarkable increase in strength without any loss in the deformation capacity. It was found that that the concrete compressive strength (f'_c) at low temperatures can be properly estimated using Equation 8.1 (previous Equation 1.3 - Browne and Bamforth, 1981) and depends on the moisture content (w). Concrete moisture content is related to the concrete pore volume which is governed by the age of the material, curing conditions, water/cement ratio and aggregates gradation. Moisture content of in-situ air dried concrete is usually in the range 2-5% and it will increase depending on the grade of exposure. According to Equation 8.1 for a concrete with room temperature compressive strength of 36 MPa (5.2 ksi) and 4.4% moisture content, the expected concrete

compressive strength at -40°C (-40°F) is 40% larger than the room temperature compressive strength.

$$f_c^{'}(T) = f_c^{'}(20^{\circ}C) - Tw/12 \qquad 0^{\circ}C > T > -120^{\circ}C \qquad (8.1)$$

Regarding the effect on reinforcing steel, it was found that the increase in yield (f_y) and maximum tensile strength (f_u) at low temperature can be estimated using Equation 8.2 (see Figure 1.9 on Chapter I). According to Equation 8.2, the reinforcing steel tensile strength at -40°C (-40°F) is 10% larger than the room temperature tensile strength. No significant effect of low temperatures on the deformation capacity of reinforcing steel or plain concrete was found. The reader is referred to Chapter I for information regarding the effect of low temperatures on additional material properties such as modulus of elasticity, fracture properties, concrete tensile strength and steel bond.

$$\begin{aligned} f_s(T) &= (1 - 0.004T) f_s(20°C) && 0^{\circ}C > T > -25^{\circ}C \\ f_s(T) &= 1.1 f_s(20°C) && -25^{\circ}C > T > -40^{\circ}C \end{aligned} \qquad (8.2)$$

Low temperature effects on flexural dominated RC members: Six half-scale circular reinforced concrete columns, designed to be flexural dominated, were tested under reversed cyclic loading while subjected to temperatures ranging from -36°C (-33°F) to 22°C (72°F). Four of the units tested were reinforced concreted filled steel tube (RCFST) columns and the other two were ordinary reinforced concrete (ORC) columns. Average axial load ratio applied to the units was 6% and the longitudinal reinforcement varied between 2% and 3%. In RCFST columns a steel tube is used as the formwork during casting of the concrete. In practice, a gap is left between the steel tube end and the beam–column joint or footing (if present); so that the steel tube is only providing shear and confinement strength to the column, and not (in a direct way) flexural or axial strength (which are provided by the concrete and the longitudinal reinforcement). In addition, three other columns tested at -40˚C (-40˚F), -20˚C (-4˚F) and 20˚C (68˚F) in a previous research at NCSU (Sloan, 2005) were reanalyzed, these units were lightly reinforced (ρ=1%) and tested without axial load. Detailed information on the flexural units tested, test setup and results obtained are presented on Chapters III to V.

Results obtained from the experimental program indicated that ORC columns exposed to the combined effect of cyclic reversals and low temperatures exhibit an increase in the flexural strength accompanied by a reduction in the spread of plasticity; no effect of temperature on the energy dissipation properties were found. The increase in the flexural strength of the columns was expected from the enhancement of the mechanical properties of plain concrete and steel reinforcement when exposed to sub-zero temperatures. The average increase in strength was about 15%. The reduction on the spread of plasticity with low temperatures was evident from the condition of the specimens after the test and confirmed with the curvature profiles obtained during the tests and the calculation of equivalent plastic hinge lengths. This reduction in the plastic hinge length caused an increase in the elastic stiffness and a reduction in the displacement capacity of the cold specimens. The effect of low temperatures was more notorious on the lightly reinforced columns tested without axial load. Based on the experimental results it was proposed (Chapter IV) to reduce the equivalent plastic hinge length by a factor of 0.57 as shown in Equation 8.3

$$\begin{aligned} L_p &= kL + L_{sp} \geq 2L_{sp} && \textit{room temperatures} \\ L_p &= 0.57\left(kL + L_{sp} \geq 2L_{sp}\right) && \textit{subfreezing temperatures} \end{aligned} \tag{8.3}$$

where:

$$L_{sp} = 0.022\, f_s d_{bl} \quad f_s \leq fy \quad (MPa)$$

$$k = 0.2\left(\frac{f_{su}}{f_y} - 1\right) \leq 0.08$$

In the above equations, L is the distance from the base to the inflection point, f_y is the expected longitudinal bar yield stress, f_{su} is the expected longitudinal bar maximum tensile stress, f_s is the tensile stress in the longitudinal bars and d_{bl} is the diameter of the longitudinal bar.

Analysis of the results obtained during testing of the RCFST specimens revealed a significant reduction of the equivalent plastic hinge length when compared to ORC

columns. The plastic hinge length plays a key role in the inelastic response of a column as it is where the inelastic rotation required to reach a target displacement (beyond yield) is accommodated. Thus, a short hinge length will imply larger inelastic demands in the hinge region that may compromise the displacement capacity of the column. Based on the experimental results obtained in this investigation, Equation 8.4 (previous Equation 5.2) was proposed to determine the equivalent plastic hinge length in reinforced concrete filled steel tube columns:

$$L_p = 9.3 d_{bl} \frac{f_u}{f_y} + g \tag{8.4}$$

where f_u is the ultimate stress of the longitudinal bar. As no change in L_p was detected during the cold tests of the RCFST specimens compared to the room temperature tests, assessment of the behavior of this type of columns at low temperatures can be performed using the equivalent plastic hinge length predicted by Equation 8.4 without any correction for reduced temperatures. The average increase of the flexural strength at low temperatures in RCFST columns was about 9%.

It was shown that the equivalent plastic hinge method can be used to estimate the response of members exposed to very low temperatures (Chapters IV and V) if the appropriate low temperature material properties (Equations 8.1 and 8.2) and equivalent plastic hinge lengths (Equations 8.3 and 8.4) are used .

Low temperature effects on shear dominated RC members: In order to determine the effect of low temperatures on the seismic behavior of shear dominated RC columns, two pairs of squat columns where tested under reversed cyclic loading. The only variable between columns of the same pair was the temperature of the specimen during testing: one of the columns was tested at room temperature 22°C (72°F) while the other was tested at -36°C (-33°F). Differences between each pair of identical columns were the ratios of transverse and longitudinal reinforcement which were designed with the aim of achieving shear failures at low ductility (brittle shear failure) and high ductility (ductile shear failure). Specimens tested at low temperatures exhibited an increase in its shear

strength; the amount of this increase was larger in the brittle shear units (32%) than in the ductile shear units (20%). Although flexural strength increases at low temperatures, thus resulting in an increased shear demand, the shear capacity increases at an even higher proportion, thus delaying the onset of shear failure at low temperatures. Current available models for assessment and design of shear strength in RC columns under seismic actions were evaluated (Kowalsky and Priestley 2000, AASHTO 2007) and found to be conservative when the columns are exposed to sub-freezing temperatures even if the increase in concrete compressive strength and steel yield stress due to low temperatures are taking into account. The reader is referred to Chapter IV for a more detailed presentation of the results obtained from the testing of the shear columns.

Low temperature effects on the dynamic behavior of RC bridge bents: In Chapter VII the results obtained from the experimental tests were used to calibrate a fiber-based lumped plasticity model capable of simulating the response of RC columns to cyclic load reversals while subjected to sub-freezing temperatures. Once the model was calibrated with the experimental results, it was used to model typical bridge bents used by the Alaska DOT. Types of bents analyzed included single and multi column bents composed of ordinary reinforced concrete (ORC) columns reinforced concrete filled steel tube (RCFST) columns. Each bent was analyzed under two different scenarios: room temperature conditions (+20°C, +68°F) and sub-freezing conditions (-40°C, -40°F). Each condition was simulated by changing the constituent material properties and the plastic hinge lengths. Performance limit states were initially established in terms of material strain and an inelastic pushover analysis were performed in each model to determine the corresponding displacement limit states. Once the deformation limit states are calculated, an incremental non-linear time history analysis using spectrum compatible records is performed to determine the seismic level of intensity required to reach each limit state.

In the case on bents composed of ORC columns it was found that the serviceability limit at low temperatures is reached at ~86% the level of lateral demand required to reach the same limit at room temperatures in the case of single column bents and 95% in the case on multi-column bents. The lateral displacement required to reach the damage control limit at low temperatures is ~73% the lateral displacement required to

reach the same limit at room temperatures for single and multi-column bents. The seismic behavior at room and low temperatures was almost identical until the serviceability limit is reached, after this point the bent at room temperatures behaves slightly more flexible.

No reduction in the displacement capacity was noticed in the bents composed of RCFST columns. However, it was noticed that in multi-RCFST-column bents the limit states are largely controlled by the reinforcing bar strain in the top hinge with the in-ground hinge remaining almost elastic.

8.2 Design recommendations

Seismic design of reinforced concrete bridges is generally based on the principles of capacity design, where a strength hierarchy is established in the bridge to ensure that damage is controllable, and occurs only where the designer intends (Priestley et al., 1996). Special importance is then placed on the ***ductility*** of the structural members selected to develop plastic hinges, which should be specially detailed in order to sustain large inelastic deformations. All other members should be design to remain elastic while resisting the ***overstrength*** moments coming from adjacent members. It has been shown that RC members exposed to low temperatures and cyclic loads exhibit an increase in strength and a reduction in the ductility capacity, in Chapter VII (section 7.10) a parametric study was performed in order to quantify those effects. The following recommendations are based on the results obtained from the parametric study, the inelastic pushovers and the cyclic tests performed in this research:

Low temperature flexural overstrength: It is recommended to use a low temperature overstrength factor (LTOF) of **1.15**. This factor must be applied when determining the moment that the column will transmit to the cap beam or footing (if present) and to calculate the design shear force in the column. The LTOF should be applied in addition to any material overstrength conventionally used.

Low temperature reduction in ductility capacity: It was found that the reduction in ductility due to low temperatures increases with the lateral demand. Equations 8.5 and 8.6 (previous Equations 7.10 and 7.11) can be used to estimate the low temperature

ductility capacity reduction for a given concrete (ε_c) or steel strain (ε_s). For example, if a steel strain of 0.01 is specified as the strain limit for the serviceability condition, using Equation 8.6 it is obtained that the low temperature displacement ductility at the serviceability condition is 80% the room temperature ductility. Alternatively, if the limit states are defined in terms of ductility instead of strains, Equation 8.7 (previous Equation 7.12) can be used.

$$\frac{\mu_{-40^oC}}{\mu_{+20^oC}} = 0.43\varepsilon_c^{-0.12} \tag{8.5}$$

$$\frac{\mu_{-40^oC}}{\mu_{+20^oC}} = 0.46\varepsilon_s^{-0.12} \tag{8.6}$$

$$\frac{\mu_{-40^oC}}{\mu_{+20^oC}} = 0.88\left(\mu_{+20^oC}\right)^{-0.17} \tag{8.7}$$

If a displacement based design approach (Priestley et al. 2007) is used, the effect of low temperatures can be directly taken into account by using the appropriate temperature-dependent material properties (Equations 8.1 and 8.2) and equivalent plastic hinge lengths (Equation 8.3).

Note that all the design recommendations are given based on a low temperature of -40°C (-40°F), as all of the tests were performed at approximately this temperature. The proposed equations can be conservatively used for the design of RC columns exposed to temperatures between 0 and -40°C.

8.3 Suggestions for further studies

- In most of the specimens tested in this research the length of the equivalent plastic hinge was controlled by the strain penetration length. Larger specimens need to be tested at freezing conditions to verify and to calibrate the proposed reduction in the equivalent plastic hinge length

- More low temperature tests at a material level are needed. Notice that most of the specimens tested failed by buckling and then rupture of the reinforcing steel due to low cycle fatigue. Other researchers have indicated that when employing detailing practices for potential plastic hinge regions to ensure large displacement capacities, the critical failure mode is likely to be caused by low cycle fatigue of the longitudinal reinforcing bars (Mander et al. 1994, El-Bahy et al. 1999, Brown and Kunnath 2004). No studies that explicitly examine the effect of low temperature on the low-cycle fatigue behavior of reinforcing bars were identified during the literature search.

- An experimental research is required to completely characterize the seismic behavior of RCFST pile/columns. The tests performed in this research evaluate only the behavior of the top hinge (gap region adjacent to the cap beam), although this hinge will form first and control the limit states when a multi-column bent is subjected to in-plane excitation, in ground hinges can be developed in the case of single-column bents or out-of-plane excitation of multi-column bents. An on-going experimental research at NCSU will shed some light on this respect. However, the soil-structure interaction of this type of columns still needs to be addressed. To the author knowledge, all of the studies addressing the seismic/non-linear soil-structure interaction problem are based on experimental results or computer simulations of ordinary reinforced concrete columns/piles and no expressions or procedures to define, for example, the properties of the equivalent cantilever model are available in the case of RCFST columns/piles. An analytical approach was developed in this research (section 7.6.1) to determine the equivalent diameter for an ORC pile/column capable of replicate the behavior of a given RCFST pile/column. The proposed methodology needs to be verified by experimental tests. Furthermore, the effect of seasonal freezing that has been shown to largely impact the soil-structure interaction of ORC pile/column (Sritharan, 2007) needs to be evaluated for this type of bents.

REFERENCES

Aboutaha R.S. and Machado R. Seismic Resistance of Steel Confined Reinforced Concrete Columns. *The Structural Design of Tall Buildings*, Vol. 7, 251-260, 1998

Aboutaha R.S. and Machado R. Seismic Resistance of Steel-Tubed High Strength Reinforced-Concrete Columns. *ASCE Journal of Structural Engineering*, Vol. 125, No. 5, 1999

ACI Committee 318, *Building Code Requirements for Structural Concrete and Commentary – ACI* 318-R95, American Concrete Institute, Detroit, 1995

Association of State Highway and Transportation Officials (AASHTO), *Guide Specifications for LRFD Seismic Bridge Design*, NCHRP Project 20-07, Task 193, National Cooperative Highway Research Program, Transportation Research Board, 2007.

ASTM A706, *Standard Specification for Low-Alloy Steel Deformed and Plain Bars for Concrete Reinforcement*, Annual Book of ASTM Standards, American Society for Testing and Materials, 2006

Bazant, Z. P. and Planas, J. *Fracture and Size Effect in Concrete and other Quasibrittle Materials*. CRC Press, Boca Raton, FL, 1998.

Berner D., Gerwick B.C. and Polivka M. Static and Cyclic Behavior of Structural Lightweight Concrete at Cryogenic Temperatures. *Temperature Effects on Concrete*, ASTM STP 858, 1985

Berry M.P, Parish, M and Eberhard, M.O. *PEER Structural Performance Database*. Pacific Earthquake Engineering Research Center, Berkeley, CA, 2004

Berry M.P. and Eberhard M.O. Practical Performance Model for Bar Buckling. *ASCE Journal of Structural Engineering.* Vol. 131, No. 7, 2005

Berry M.P. *Performance Modeling Strategies for Modern Reinforced Concrete Bridge Columns*. PhD Thesis, Department of Civil and Environmental Engineering, University of Washington, 2006

Brown, J., and Kunnath, S. K. Low-cycle fatigue failure of reinforcing steel bars. *ACI Materials Journal*, Vol. 101, No. 6, 2004

Browne R.D. and Bamforth P.B. The Use of Concrete for Cryogenic Storage; A Summary of Research Past and Present. *1st International Conference on Cryogenic Concrete*, New Castle, 1981

Budek A.M., Priestley M.J.N. and Benzoni G. Inelastic Seismic Response of Bridge Drilled Shaft. *ASCE Journal of Structural Engineering*, Vol. 126, No. 4, 2000

Cantin R. and Pigeon M. Durability and Mechanical Properties at Low Temperatures of Steel-Fiber Reinforced Concrete. *Proceedings of the 2nd International Conference on Concrete under Severe Conditions*, Norway, 1998.

Chai Y.K., Priestley, M.J.N. and Seible, F. Seismic Retrofit of Circular Bridge Columns for Enhanced Flexural Performance. *ACI Structural Journal*, Vol. 88, No. 5, 1991

Chai, Y.H. Flexural Strength and Ductility of Extended Pile Shafts I: Analytical Model. ASCE Journal of Structural Engineering. Vol. 128, No. 5, 2002

Chang G. and Mander J. Seismic Energy Based Fatigue Damage Analysis of Bridge Columns: Part I Evaluation of Seismic Capacity, *NCEER Technical Report 94-0006*, 1994

Chen Y. Assessment on Pile Effective Lengths and Their Effects on Design. *Computers & Structures*, Vol. 62, No. 2, 1997

Chopra A.K. and Goel R.K. Direct Displacement Based Design: Use of Inelastic vs. Elastic Spectra. *Earthquake Spectra*, Vol. 17, No. 1, 2001

Coleman, J. and Spacone, E. Localization Issues in Force-Based Frame Elements. *ASCE Journal of Structural Engineering*, Vol. 127, No. 11, 2001.

Davison M.T. and Robinson K.E. Bending and buckling of partially embedded piles. *Proceedings of the 6th International Conference of Soil Mechanics and Foundation Engineering*, Montreal, Canada, 1965

Dubey A. and Banthia N. Influence of Sub-Zero Temperature on Fracture Properties of Plain and Synthetic Fiber Reinforced Concretes. *Proceedings of the 2nd International Conference on Concrete under Severe Conditions*, Norway, 1998.

Dwairi H. and Kowalsky M.J. Equivalent Viscous Damping in Support of Direct Displacement Based Design. *Journal of Earthquake Engineering*, Vo. 11, No. 4, 2007

El-Bahy, A., Kunnath, S. K., Stone, W. C., and Taylor, A.W. Cumulative seismic damage of circular bridge columns: Benchmark and low-cycle fatigue test. *ACI Structural Journal*, Vol. 96, No. 4, 1999

Elices M. and Planas J. Measurement of Tensile Strength of Concrete at very Low Temperatures. *ACI Structural Journal*, Vol. 79, No. 3, 1982

Elices M. Cryogenic Prestressed Concrete: Fracture Aspects. *Theoretical and Applied Mechanics*, Vol. 7, 1987.

Elices M., Corres H. and Planas J. Behavior at Cryogenic Temperatures of Steel for Concrete Reinforcement. *ACI Structural Journal*, Vol. 83, No. 3, 1986

Filiatrault A. and Holleran M. Stress-Strain Behavior of Reinforcing Steel and Concrete under Seismic Strain Rates and Low Temperatures. *Material and Structures*, Vol.34, No.5, 2001

Frankenstein S. and Tuthill A.M. Ice Adhesion to Locks and Dams: Past Work; Future Directions? *Journal of Cold Regions Engineering*. Vol. 16, No. 2, 2002

Goto Y. and Miura T. Experimental Studies on Properties of Concrete Cooled to about Minus 160°C. *Technology Reports Tohoku University*, Vol. 44, No. 2, 1979

Grant D.N., Blandon C.A. and Priestley M.J.N. *Modeling Inelastic Response in Direct Displacement Based Design*, Report 2005/03, IUSS Press, Pavia, 2005.

Hancock J., Watson-Lamprey J, Abrahamson, N.A., Bommer, J.J., Markatis, A., McCoy, E. and Mendis R. An Improved Method of Matching Response Spectra of Recorded Earthquake Ground Motion Using Wavelets. *Journal of Earthquake Engineering*, Vol. 10, Special Issue 1, 2006

Jacobsen, L. S. Steady forced vibrations as influenced by damping. *ASME Transactions*, Vol. 52, No. 1, 1930

Kasami H., Tanaka Y., Kishima Y. and Yamane S. Properties of Concrete at Very Low Temperatures. *1st International Conference on Cryogenic Concrete*, New Castle, 1981

King D.J., Priestley M.J.N., and Park R. *Computer Programs for Concrete Column Design.* Research Report 86/12, Department of Civil Engineering, University of Canterbury, New Zealand, 1986

Kowalsky M.J. and Priestley M.J.N. Improved Analytical Model for Shear Strength of Circular Reinforced Concrete Columns in Seismic Regions. *ACI Structural Journal*, Vol. 97, No. 3, 2000

Kowalsky M.J. Deformation Limit States for Circular Concrete Reinforced Bridge Columns. *ASCE Journal of Structural Engineering*, Vol. 126, No. 8, 2000.

Kowalsky M.J. Priestley M.J.N and Seible F. *Shear Behavior of Lightweight Concrete Under Seismic Conditions*. Report No. SSRP-95/10. Department of Applied Mechanics and engineering Sciences, University of California, San Diego, 1995.

Lee G.C., Shih T.S. and Chang, K.C. Mechanical Properties of Concrete at Low Temperature. *ASCE Journal of Cold Regions Engineering*, Vol.2, No.1, 1988

Lee G.C., Shih T.S. and Chang, K.C. Mechanical Properties of High-Strength Concrete at Low Temperature. *ASCE Journal of Cold Regions Engineering*, Vol.2, No.4, 1988

Mander J.B., Priestley M.J.N., and Park R. Theoretical Stress-Strain Model for Confined Concrete. *ASCE Journal of Structural Engineering*, Vol. 114, No. 8, 1988

Mander, J. B., Panthaki, F. D., and Kasalanati, A. Low-cycle fatigue behavior of reinforcing steel. *ASCE Materials Journal*, Vol. 6, No. 4, 1994

Marshall A.L. Cryogenic Concrete. *Cryogenics*, November 1982

Maturana P., Planas J. and Elices M. Evolution of Fracture Behavior of Saturated Concrete in the Low Temperature range. *Engineering Fracture Mechanics*, Vol. 35. No. 4/5, 1990

McKenna F., Fenves G.L., Scott M.H. and Jeremic, B. *Open System for Earthquake Engineering Simulation – OpenSees*,2000 http://opensees.berkeley.edu

Mohle J. and Kunnath S. Reinforcing steel. *OpenSees User's Manual*, 2006 http://opensees.berkeley.edu

Montejo, L.A and Kowalsky, M.J. *CUMBIA – Set of Codes for the Analysis of Reinforced* Concrete Members. CFL Technical Report No. IS-07-01. Department of Civil, Construction and Environmental Engineering, North Carolina State University, Raleigh, 2007

Montejo, L. A., Sloan, J. E., Kowalsky, M. J. and Hassan, T. Cyclic Response of Reinforced Concrete Members at Low Temperatures. *ASCE Journal of Cold Regions Engineering*, in press, 2008a.

Montejo, L. A., Kowalsky, M. J. and Hassan, T. Seismic Behavior of Flexural Dominated Reinforced Concrete Bridge Columns at Low Temperatures. *ASCE Journal of Cold Regions Engineering*, submitted for publication, 2008b.

Montejo, L. A., Kowalsky, M. J. and Hassan, T. Seismic Behavior of Shear Dominated Reinforced Concrete Columns at Low Temperatures. *ACI Structural Journal*, submitted for publication, 2008c.

Moyer M.J. and Kowalsky M.J. Influence of Tension Strain on Buckling of Reinforcement in Concrete Columns. *ACI Structural Journal*, Vol. 100, No. 1, 2003

Nasser K.W. and Evans G.A. Low Temperatures Effects on Hardened Air Entrained Concrete. *Behavior of Concrete under temperature Extremes*, ACI SP-39, 1973

Ohlsson U., Daerga P.A.and Elfgren L. Fracture Energy and Fatigue Strength of Unreinforced Concrete Beams at Normal and Low Temperatures. *Engineering Fracture Mechanics*, Vol. 35. No. 1/2/3, 1990

Okada T. and Iguro M. Bending Behavior of Prestressed Concrete Beams under Low Temperatures. *Journal of the Japan Prestressed Concrete Engineering Association*, Vol.20, 1978

Pacific Earthquake Engineering Research Center PEER. Next Generation Attenuation of Ground Motions NGA database, http://peer.berkeley.edu/nga/index.html, 2006

Paulay T. and Priestley, M.J.N. *Seismic Design of Reinforced Concrete and Masonry Buildings*. John Wiley and Sons, New York, 1992

Pile Driving Contractors Association (PDCA), Installation Specification for Driven Piles, PDCA Spefication 102-07, 2007

POLA, *Code for Seismic Design Upgrading and Repair of Container Wharves*, Port of Los Angeles, San Pedro,2004.

Priestley M.J.N. and Park. Strength and Ductility of Concrete Bridge Columns Under Seismic Loading. *ACI Structural Journal*, Vol. 84, No. 1, 1987

Priestley M.J.N., Calvi G.M., Kowalsky M.J. *Direct Displacement Based Seismic Design of Structures.* IUSS Press, Pavia, Italy, (In preparation), 2007

Priestley M.J.N., Seible F., Xiao Y. and Verma R. Steel Jacket Retrofitting of Reinforced Concrete Bridge Columns for Enhanced Shear Strength-Part 1: Theoretical Considerations and Test Design. *ACI Structural Journal*, Vol. 91, No. 4, 1994.

Priestley M.J.N., Seible F., Xiao Y. and Verma R. Steel Jacket Retrofitting of Reinforced Concrete Bridge Columns for Enhanced Shear Strength-Part 2: Test Results and Comparison with Theory. *ACI Structural Journal*, Vol. 91, No. 5, 1994.

Raynor D.J., Lehman D.L. and Stanton J.F. Bond Slip Response o Reinforced Bars Grouted in Ducts. *ACI Structural Journal*, Vol. 99, No. 5, 2002.

Robalino P.J. *Shear Performance of Reinforced Lightweight Concrete Square Columns in Seismic Regions*. MS Thesis, Department of Civil Construction and Environmental Engineering, North Carolina State University, 2006

Rostàsy F.S and Push U. Strength and Deformation of Lightweight Concrete of Variable Moisture Content at Very Low Temperatures. *The International Journal of Cement Composites and Lightweight Concrete*, Vol. 9. No. 1, 1987.

Rostàsy F.S and Sprenger H. Strength and Deformation of Steel Fibre Reinforced Concrete at Very Low Temperature. *The International Journal of Cement Composites and Lightweight Concrete*, Vol. 6. No. 1, 1984.

Rostàsy F.S. and Wiedemann G. Stress Strain Behavior of Concrete at Extremely Low Temperature. *Cement and Concrete Research*, Vol. 10, 1980.

Sanford R.J. *Principles of Fracture Mechanics*. Prentice Hall, Upper Saddle River, NJ, 2003

Scott, M.H. and Fenves, G.L. Plastic Hinge Integration Methods for Force-Based Beam-Column Elements. ASCE Journal of Structural Engineering., Vol. 132, No. 2, 2006.

Sehnal Z.A., Kronen H. and Marshall A.L. Factors Influencing the Low Temperature Strength of Concrete. *2nd International Conference on Cryogenic Concrete*, The Netherlands, 1983

Shih T.S., Lee G.C and Chang K.C. High-Strength Concrete-Steel Bond Behavior at Low Temperature. *Journal of Cold Regions Engineering*, Vol. 2, No. 4, 1988

Sloan J.E. *The Seismic Behavior of Reinforced Concrete Members at Low Temperature*. MS Thesis, Department of Civil Construction and Environmental Engineering, North Carolina State University, 2005

Spacone E., Filipou, F.C. and Taucer, F.F. Fibre Beam-Column Model for Non-Linear Analysis of RC Frames: Part I. Formulation. *Earthquake Engineering and Structural Dynamics*, Vol. 25, 1996.

Spacone E., Filipou, F.C. and Taucer, F.F. Fibre Beam-Column Model for Non-Linear Analysis of RC Frames: Part II. Applications. *Earthquake Engineering and Structural Dynamics*, Vol. 25, 1996.

Sritharan S., Suleiman M.T. and White D. Effects of Seasonal Freezing on Bridge Column-Foundation-Soil Interaction and Their Implications. *Earthquake Spectra*, Vol. 23, No. 1, 2007

Suarez V. and Kowalsky M.J. Direct-Displacement-Based Seismic Design of Drilled Shaft Bents with Soil-Structure Interaction. *Journal of Earthquake Engineering*, Vol. 11, 1010-1030, 2007

Suarez, L.E. and Montejo L.A. Generacion de Registros artificiales Compatibles con un Espectro de Respuesta Mediante la Transformada Wavelet. *Proceedings of II Congreso Nacional de Ingeniería Sísmica*, Medellín, Colombia, 2003.

Suarez, L.E. and Montejo L.A. Generation of Artificial Earthquakes Via the Wavelet Transform. *International Journal of Solids and Structures*, Vol. 42, No. 21-22, 2005.

Suleiman M.T., Sritharan S. and White D. Cyclic Lateral Load Response of Bridge Column Foundation Soil Systems in Freezing Conditions. *ASCE Journal of Structural Engineering*, Vol. 132, No. 11, 2006.

Vamvatsikos, D. and Cornell, C.A. Incremental dynamic analysis. *Earthquake Engineering and Structural Dynamics*, Vol. 31, 2002.

Vandewalle, L. Bond between a Reinforcement Bar and Concrete at Low Temperatures. *Proceedings of the International Conference on Concrete under Severe Conditions*, Saporo, Japan, 1995.

Zhao, J. and Sritharan, S. Modeling of Strain Penetration Effects in Fiber-Based Analysis of Reinforced Concrete Structures. *ACI Structural Journal*, Vol. 104, No. 2, 2007.